TU Delft

Delft University of Technology

Receptivity of Swept Wing Boundary Layers to Surface Roughness
Diagnostics and extension to flow control

Zoppini, G.

DOI
10.4233/uuid:edfbbf98-2530-463b-94d0-43dee5435786

Publication date
2023

Document Version
Final published version

Citation (APA)
Zoppini, G. (2023). *Receptivity of Swept Wing Boundary Layers to Surface Roughness: Diagnostics and extension to flow control*. [Dissertation (TU Delft), Delft University of Technology].
https://doi.org/10.4233/uuid:edfbbf98-2530-463b-94d0-43dee5435786

Important note
To cite this publication, please use the final published version (if applicable).
Please check the document version above.

Copyright
Other than for strictly personal use, it is not permitted to download, forward or distribute the text or part of it, without the consent of the author(s) and/or copyright holder(s), unless the work is under an open content license such as Creative Commons.

Takedown policy
Please contact us and provide details if you believe this document breaches copyrights.
We will remove access to the work immediately and investigate your claim.

This work is downloaded from Delft University of Technology.
For technical reasons the number of authors shown on this cover page is limited to a maximum of 10.

Receptivity of Swept Wing Boundary Layers to Surface Roughness

Diagnostics and extensions to flow control

Receptivity of Swept Wing Boundary Layers to Surface Roughness

Diagnostics and extensions to flow control

Dissertation

for the purpose of obtaining the degree of doctor
at Delft University of Technology,
by the authority of the Rector Magnificus prof. ir. T.H.J.J. van der Hagen,
Chair of the Board for Doctorates,
to be defended publicly on
Thursday 7 September 2023 at 10:00 hours

by

Giulia ZOPPINI

Master of Science in Aeronautical Engineering,
Politecnico di Milano, Milan, Italy,
born in Vicenza, Italy.

This dissertation has been approved by

promotor: Dr. M. Kotsonis
promotor: Dr. D. Ragni

Composition of the doctoral committee:

Prof. Dr. Ir. Rector Magnificus,	chairperson
Dr. M. Kotsonis,	Delft University of Technology, promotor
Dr. D. Ragni,	Delft University of Technology, promotor

Independent members:

Prof. Dr. E.B. White,	Texas A&M University, United Stated of America
Dr.-Ing. M.J. Kloker,	University of Stuttgart, Germany
Dr. S. Cherubini,	Politecnico di Bari, Italy
Dr. M. Costantini,	DLR, Germany
Prof. Dr. Ir. L.L.M. Veldhuis,	Delft University of Technology

Reserve member:

Prof. Dr. F. Scarano,	Delft University of Technology

Keywords: Swept wing boundary layer, receptivity, transition, crossflow instability, laminar flow, surface roughness

Printed by: Rijnja, Den Haag

Front & Back: Oil flow visualization of flow topology incurred by the application of multiple discrete roughness elements array in a swept wing boundary layer.

Copyright © 2023 by G. Zoppini

ISBN 978-94-6366-719-7

An electronic version of this dissertation is available at
http://repository.tudelft.nl/.

Choose a job you love
and you will never have to work
a day in your life.

Confucius

Acknowledgements

This PhD thesis summarizes a four-year journey that combined meticulous and demanding research with moments of pure joy and light-heartedness. I owe my joy and success to the incredible individuals who accompanied and participated in this journey.

First and foremost, I extend my heartfelt gratitude to my promotor, Marios. His constant support, boundless enthusiasm, and unconditional trust have shaped my professional and personal growth. From the early stages of my research, Marios has consistently provided valuable insights and an endless stream of new ideas. His emphasis on enjoying our PhD life, both inside and outside the office, has been one of the suggestions that mostly defined my journey.

I am also grateful to my second promotor, Dani, a continuous source of energy and knowledge who offered an incredible and sometimes favourably biased support to this project. Beyond his technical contributions, his open frankness and relentless determination have helped me navigate many complex (and personal) decisions.

Furthermore, I want to express my gratitude to Theo, my closest ally in numerous battles against DaVis bugs, as well as in the pursuit of the craziest vector resolution to characterize a 1.2mm thick boundary layer. Together, we tackled complex set-ups, collected extensive datasets, and shared insightful discussions. He has been a great colleague and friend, taking me through both tough and fun.

Working alongside the three of you I experienced first-hand the collaborative spirit that represents the best part of life in academia. Thank you all for being incredible mentors and colleagues.

I would also like to express my sincere appreciation to the members of my doctoral committee for their time and effort in reviewing this document. Their valuable questions and suggestions have enriched this research.

Special appreciation is extended to Emiel and Stefan, the technicians who provided unwavering support in the low-speed lab. Their invaluable assistance and dedication in maintaining a functional and welcoming lab environment are truly admirable. Their prompt responsiveness to any (caused or occurred) malfunction deserves recognition, as do our delightful lunch time conversations.

A dedicated acknowledgement goes to Colette, whose dedication and involvement are a fundamental contribution for the smooth functioning of our section. From the very beginning to the finalization of this thesis, her guidance and help have been invaluable.

Of fundamental importance to survive the long lab hours was the vibrant community of the aerodynamics section. Thank you Kaisheng, Sven (official Summary translator), Beto, Jordi, Marina, Yifu, Giulio, Parisa, Ata, Tyler, Alessandro, Edoardo, Gabriel, Luis, Constantin, Jane, Christoph, Kushal, Adrian, Thomas, Ilda, Kherlen, Luuk, Babak, Haris, Renzhi, Wencan, Adrian and Mengie for enriching my academic

journey and social life. Our intellectual collaborations, stimulating discussions, and diverse perspectives have broadened my horizons and sharpened my research and work. Our social activities have provided a much-needed break from academic routines, and I am grateful for the friendships formed and the collaborative spirit that fuelled our times together.

During my PhD project I had the chance to work with Aaron on the development of his MsC thesis. Despite the numerous technical challenges we faced, collaborating with him was truly rewarding: I sincerely appreciate the opportunity he provided me to grow both as a researcher and supervisor.

Life outside the lab would not have been the same without the support of my international friends. Defying the limitations imposed by the pandemic, Silvia (with the crazy ideas and plans), Davide (with challenging fighting games of philosophical discussions), Donato (with panzerotti and not with raggeton), Ale (with ass'e mazza), Ezgi (with the party life), and Carolina (with the Portuguese additions) were always there to inject fun, companionship, and laughter into my life. Meeting Marina during my first days in the Netherlands was a stroke of luck, and with the addition of Ricardo, we supported each other first as house mates and then as friends. A strong bond also formed with Silvia, whose positivity and energy have been an anchor, as were her attempts to food/alcohol poison us all. With my last change of housing I met Rishabh, who not only welcomed all of us uncountable times, but also gave amazing contributions to the craziest events we organized. Another constant throughout these years has been Kaisheng: we supported each other in the lab while always embracing new social challenges resulting in a wonderful friendship and a chaperoned trip to his country. At last, a more recent addition to this group, Giulio, has become a trusted travel, dining, and card games companion. To all of you, I am grateful for the shared experiences and the bond we have formed.

Of course, I cannot leave out the usual suspects. Friends of a lifetime, Giulia and Greta, have remained close and supportive despite the increasing geographical distance between us. Good luck with your new endeavours! The constant presence of Ludo and Mari over endless phone calls and short trips has also been fundamental in making me feel less distant from home, even if it sometimes resulted in unhealthy levels of chips consumption. I am then always grateful to my Italian friends, who made every moment spent together special and worth cherishing.

Lastly, I want to express my deepest gratitude to my family and Ale, who have been my number one supporters from the very beginning. Their endless patience in listening to my tedious doubts, engaging in serious discussions and decision making, and offering guidance has been remarkable. Despite being there every step of the way, they let me find my own path without ever imposing their own wishes upon me. I hope that, with this document, they might gain a better understanding of how I spent these transformative years.

To each and every person who has crossed my path during this journey goes a heartfelt thank you for contributing to my growth and happiness being an integral part of this wonderful ride.

Contents

Summary xiii

Samenvatting xv

1 Introduction 1
- 1.1 Introduction. . . . 2
- 1.2 The Boundary Layer 3
  - 1.2.1 Boundary Layer Transition. . . . 4
  - 1.2.2 Crossflow Instabilities 6
- 1.3 CFI Receptivity to Freestream Turbulence 8
- 1.4 CFI Receptivity to Surface Roughness 9
  - 1.4.1 Distributed Surface Roughness. . . . 9
  - 1.4.2 Isolated Discrete Roughness Elements. . . . 10
  - 1.4.3 Discrete Roughness Elements Arrays 13
- 1.5 The Near-DRE Flow 16
  - 1.5.1 Transient Growth Mechanisms. . . . 18
  - 1.5.2 Transient Growth in Roughness Wake Flows 20
- 1.6 CFI suppression via Surface Roughness 22
- 1.7 Motivation, Objectives and Thesis Outline 24

2 Methodology 27
- 2.1 Experimental set-up 28
  - 2.1.1 Wind Tunnel and Swept Wing Model 28
  - 2.1.2 Coordinate Reference Systems 29
- 2.2 Surface Roughness Configurations 30
  - 2.2.1 Distributed Roughness Patches (DRP) 30
  - 2.2.2 Isolated Discrete Roughness Element (IDRE). . . . 32
  - 2.2.3 Discrete Roughness Elements (DRE) Arrays 33
- 2.3 Measurement Techniques. . . . 37
  - 2.3.1 Infrared (IR) thermography 37
  - 2.3.2 Hotwire Anemometry (HWA) 39
  - 2.3.3 Planar Particle Image and Particle Tracking Velocimetry (PIV and PTV) 42
  - 2.3.4 Tomographic Dual-pulse PTV (3D-PTV) 46
  - 2.3.5 Measurements Uncertainty Quantification 48
- 2.4 Boundary Layer Stability Solutions 50
  - 2.4.1 Linear and Non-Linear Parabolized Stability Equations 50

3 Receptivity of Stationary CFI to DRE Amplitude and Location 53
- 3.1 Introduction. . . . 54

3.2 Experimental Set-up and Methodology . . . 55
3.2.1 Numerical Stability Solution . . . 55
3.2.2 DRE Arrays Configurations . . . 55
3.2.3 IR Thermography . . . 56
3.2.4 Planar PIV Configuration . . . 56
3.3 Steady Perturbations Characteristics . . . 57
3.3.1 Transition Behavior as Function of Forcing Amplitude and Location . . . 57
3.3.2 Mean Flow Development . . . 60
3.3.3 Stationary Crossflow Instabilities Growth . . . 61
3.4 Unsteady Perturbations Characteristics . . . 68
3.5 Near-DRE Flow Topology . . . 72
3.6 Concluding Remarks . . . 77

4 The Near-element Flow of a Near-Critical IDRE 79
4.1 Introduction . . . 80
4.2 Experimental Set-up and Methodology . . . 80
4.2.1 IDRE Configurations . . . 81
4.2.2 IR Thermography . . . 81
4.2.3 HWA Configuration . . . 81
4.3 Stationary Flow Topology . . . 82
4.3.1 Base Flow Evolution . . . 83
4.3.2 Steady Disturbances . . . 85
4.4 Unsteady Perturbations Characteristics . . . 88
4.4.1 Unsteady Perturbation Fields . . . 89
4.4.2 Spectral and Intermittency Analysis . . . 92
4.5 Concluding Remarks . . . 97

5 The Near-element Flow Topology of a DRE Array 99
5.1 Introduction . . . 100
5.2 Experimental Set-up and Methodology . . . 101
5.2.1 DRE Arrays Configuration . . . 101
5.2.2 Tomographic Dual-Pulse PTV . . . 102
5.3 Critical Near-Element Flow . . . 104
5.3.1 Stationary Disturbance Topology . . . 104
5.3.2 Spectral Analysis and Transient Growth . . . 109
5.3.3 Algebraic Growth in Disturbance Energy and Scalability . . . 113
5.3.4 Variations of Forcing Wavelength . . . 117
5.4 Super-critical Near-Element Flow . . . 122
5.5 Concluding Remarks . . . 129

6 Stationary CFI Suppression via Multiple DRE Forcing 133
6.1 Introduction . . . 134
6.2 Experimental Set-up and Methodology . . . 135
6.2.1 DRE Arrays Configurations . . . 135
6.2.2 DRP Configurations . . . 136
6.2.3 IR Thermography . . . 138

6.2.4 Planar Dual-Pulse PTV 138
6.3 Effect of Multiple DRE Arrays Forcing 139
6.3.1 Effect of Multiple DRE Arrays on Transition 139
6.3.2 Linearity of the Disturbances Superposition 140
6.3.3 Sensisitivity to DRE Arrays Parameters 144
6.4 Effect of DRP Patches Forcing. 146
6.4.1 Effect of DRP on Transition and CFI 146
6.4.2 Effect of DRP chord location 149
6.5 Effect of DRE Arrays Forcing in the Presence of DRP 149
6.5.1 Effect of a Reference DRE Array Superposition to a DRP . . . 149
6.5.2 Effect of Multiple DRE Arrays Superposition to DRP Patches 151
6.6 Concluding Remarks 153

7 Conclusions and Recommendations **155**
7.1 Conclusions and Recommendations 156
7.2 Outlook: Spanwise Invariant Roughness Configurations 158

Bibliography **165**

A Appendix A **177**
A.1 Introduction. 177
A.2 Methodology 177
A.3 Results and Discussion 178

Bibliographical Note **183**

List of Publications **185**

Summary

The research presented in this thesis focuses on the receptivity to surface roughness of swept wing boundary layers dominated by crossflow instabilities (CFI), providing insights into how surface roughness can be used to passively control the developing instabilities. Discrete roughness elements (DRE) arrays and distributed randomized roughness patches (DRP) are employed to investigate the physical phenomena governing receptivity and their impact on CFI onset. The supporting data combine numerical solutions of linear and non-linear stability theory with advanced experimental flow diagnostics.

This booklet is divided into three main parts. The first part investigates the flow mechanisms dominating the receptivity of stationary CFI to the amplitude and location of DRE arrays. The relation between the external forcing configuration and the initial instability amplitude is investigated, along with scaling principles allowing for the up-scaled reproduction of the swept wing leading-edge configurations, which provide experimentally observable configuration.

The second part of this research explores the stationary CFI receptivity to specific up-scaled roughness configurations, including both isolated discrete roughness elements and DRE arrays. These roughness elements are applied at relatively downstream chord locations to enhance the experimental resolution of the near-roughness flow field.

The isolated discrete roughness elements ensure strong boundary layer forcing, which helps to outline the relation between the near-element instability onset and the rapid transitional process. In contrast, the applied DRE arrays configurations provide boundary layers dominated by the development of CFI. In such scenarios, high-magnification tomographic particle tracking velocimetry identifies the dominant near-element stationary instabilities precursor to CFI. Specifically, the presence of transient growth and decay mechanisms in the near-roughness flow region is outlined, exploring their role in the receptivity process and in the CFI onset. This investigation results in the first conceptual map describing the receptivity of swept-wing boundary layers to a wide range of DRE array amplitudes.

Lastly, the acquired knowledge of the near-element flow topology is employed in the final part of this work to develop a passive laminar flow control technique for stationary CFI cancellation. This technique is based on the destructive interference of the velocity disturbances introduced by a streamwise series of optimally arranged DRE arrays. The performed measurements confirm a reduction in the developing CFI amplitude accompanied by a delay of the boundary layer transition. The compatibility of the proposed technique with the control of CFI developing in a realistic free-flight scenario is as well investigated.

Samenvatting

Het onderzoek dat in dit proefschrift wordt gepresenteerd, richt zich op de gevoeligheid van grenslagen van vleugels die worden gedomineerd door dwarsstroominstabiliteiten (DSI) voor oppervlakteruwheid, en biedt inzicht in hoe oppervlakteruwheid kan worden gebruikt om de ontwikkelende instabiliteiten passief te controleren. Er worden discrete ruwheidselementen (DRE) en verdeelde willekeurige ruwheidsoppervlakten (WRO) gebruikt om de fysische fenomenen die de vroege stadia van transitie beheersen en hun impact op DSI te onderzoeken. De ondersteunende gegevens combineren numerieke stabiliteitsberekeningen met geavanceerde experimentele stromingsdiagnostiek.

Dit proefschrift is verdeeld in drie hoofdonderdelen. Het eerste deel onderzoekt de stromingsmechanismen die de gevoeligheid van stationaire DSI voor de amplitude en locatie van rijen van DRE domineren. De relaties tussen de externe krachten en de initiële instabiliteitsamplitude worden onderzocht, samen met schalingsprincipes die de reproductie van de kenmerken van de stroming aan de voorkant van de vleugel mogelijk maken door middel van een experimenteel observeerbare opgeschaalde kracht.

Het tweede deel van dit onderzoek bespreekt de gevoeligheid van stationaire DSI voor specifieke opgeschaalde ruwheidsconfiguraties. Geïsoleerde discrete ruwheidselementen en DRE-rijen worden bestudeerd. Beiden worden aangebracht op relatief stroomafwaartse koordelocaties om de experimentele resolutie van het stromingsveld rond de ruwheid te verbeteren.

Ten slotte wordt de verworven kennis van de stromingstopologie achter het element gebruikt in het laatste deel van dit werk om een passieve laminaire stromingsregelingstechniek te ontwikkelen doormiddel van het annuleren van stationaire DSI. Deze techniek is gebaseerd op de destructieve interferentie van de grenslaagverstoringen die door stroomafwaarts opeenvolgende DRE-reeksen worden geïntroduceerd. De uitgevoerde metingen bevestigen dat optimaal gerangschikte DRE-reeksen de zich ontwikkelende DSI-amplitude kunnen verminderen en de grenslaagovergang kunnen vertragen. Ook wordt onderzocht of de voorgestelde techniek compatibel is met de controle van DSI die zich ontwikkelen in de praktijk.

1

Introduction

The first chapter of this thesis provides an introduction to boundary layer stability and transitional processes, with a dedicated focus on swept wing boundary layers affected by crossflow instabilities. In particular, the correlation between the development of crossflow instabilities and the wing surface roughness is explored, outlining the knowledge gap motivating the present research.

1

1.1. Introduction

Boundary layer stability and transition to turbulence have been among the major research topics throughout the last century. Particular efforts have been devoted to the analysis of the complex physical phenomena involved, whose complete characterization remains nowadays a major challenge. Besides its scientific relevance, what contributed to keeping a high interest in this subject is its practical impact on the aeronautical engineering and industry. In fact, the transition from a laminar to a turbulent regime significantly modifies the BL flow properties. Specifically, turbulent boundary layers are characterized by three-dimensional (3D) velocity fluctuations and randomized fluid motion, which enhance the flow mixing and heat transfer in the wall vicinity. These effects are accompanied by a strong increase in skin friction, which in a modern transport aircraft is responsible for about half of the total drag force [6]. Therefore, extending the portion of laminar flow developing on an aeroplane wing would significantly improve its aerodynamic efficiency. Such a result can be achieved by implementing laminar flow control (LFC) techniques capable of shifting the BL transition location towards the wing trailing edge [6, 72, 135]. In particular, a drag reduction of 10% can be achieved by applying LFC to the aircraft's swept wing, while 4.5% drag reduction is obtained by controlling the boundary layer development on tail and nacelles surfaces [99]. Nonetheless, a complete understanding of the flow mechanisms driving the BL transition is required to successfully predict aerodynamic performances and develop reliable LFC techniques.

The enhancement of the wing aerodynamic efficiency would reduce the fuel consumption required for civil aviation flights, leading, in turn, to higher economic competitiveness and reduced environmental impact. For example, with 60% of the aerodynamic surfaces wetted by laminar flow, the total drag can be reduced of more than 16% with respect to an uncontrolled configuration [146]. Such an increase in aerodynamic efficiency would correspond to fuel savings in the order of 29% accompanied by an overall weight reduction of 17% at take off [26, 81, 159]. These aspects are becoming increasingly important in our modern society, as the use of aeroplanes as a transport mean is steeply increasing [3]. The fields mainly interested by operational growth are related to passenger and cargo transport, which nowadays is mostly performed by aeroplanes equipped with swept wings. The wide application of swept wings along with the complexity of the characteristic flow phenomena, make the study of the developing BL stability and transition process scientifically and technologically compelling.

In particular, on swept wings the combined effect of the sweep angle and pressure gradient results in the development of a three-dimensional (3D) BL, for which the main mechanism responsible for turbulent transition is the generation, growth and breakdown of crossflow instabilities (CFI) [137, 154]. These are strongly affected by freestream turbulence and wing surface roughness [16, 137], which fundamentally condition the instabilities onset through the receptivity process [107]. Due to the numerous parameters involved in this process (e.g. the BL stability, the external disturbances) and the limited geometrical size of the BL in the region of interest (hardly accessible for experimental measurements), the physical phenomena driving the receptivity process have not been fully characterized yet. Nonetheless, the

understanding of the onset mechanisms of CFI (and so of receptivity) are fundamental for the implementation of more effective LFC techniques tailored for swept wing applications.

In this context, the present thesis aims at investigating the development and stability of swept wing boundary layers, focussing on the characterization of the receptivity process. In particular, clarifying the correlation between external forcing and the onset of the instabilities eventually responsible for the BL transition, will provide insights for the development of more efficient LFC. In the following sections an overview of the BL instabilities, transitional process and interaction with external disturbances is reported, in order to illustrate the framework of the presented research.

1.2. The Boundary Layer

The term boundary layer (BL) was first introduced by Prandtl [114] to indicate the small flow region characterized by non-negligible viscous effects developing in the proximity of an aerodynamic body. Specifically, on the solid surface of the body, the fluid is at relative rest, hence the fluid velocity retains a null value (i.e. no-slip condition). However, at an infinite distance from the body (i.e. outside the boundary layer) the fluid particle velocity coincides with the freestream speed. Therefore, the BL can be associated with the flow region in which the velocity distribution reduces from the inviscid freestream value to a null value at the body surface. Given the reduced velocity of the fluid particles, in the BL region the inertial forces are comparable to the viscous forces, even for fluids of low viscosity such as air. As such, the inviscid flow assumption typical of numerous theoretical and numerical solvers does not hold within the BL. For this reason, despite its limited wall-normal extent, the boundary layer region can have a great impact on the external inviscid flow development.

The pioneering experiments conducted by Reynolds [126] observed dye dispersion in a pipe flow, and proved that the BL can develop either in a laminar or turbulent state (figure 1.1). The nature of the developing BL depends on the ratio between the inertial and viscous forces, represented by the Reynolds number (Re, [126]). Typically, laminar BL develops at low Re where viscous forces prevail and evolves as a wall-parallel, smooth flow. On the contrary, turbulent BL develops at higher Re where inertial forces are dominant and involve 3D chaotic fluid motions of various scales. The turbulent BL is described by a *fuller* velocity distribution profile, indicating that the velocity variations in the wall vicinity are stronger than for a laminar BL developing in the same flow conditions. This effect can be related to the wall skin friction τ, which is proportional to the fluid viscosity (μ) and the slope of the velocity profiles at the wall, namely $\tau = \mu \, \partial u/\partial y \, |_{wall}$. Accordingly, turbulent BL flows develop higher wall skin friction, resulting in enhanced aerodynamic drag, turbulent kinetic energy mixing and heat transfer. Hence, in the commercial aeronautical sector, an increase of the spatial length of the laminar BL region on a wing surface is highly desirable, as it relates to the possibility of reducing the skin friction drag and improving the wing aerodynamic efficiency [72].

However, not all industrial applications share this goal, as the higher kinetic energy associated with turbulent BL flows gives them an increased resistance to flow separation. More specifically, BL separation occurs when the work performed by the fluid

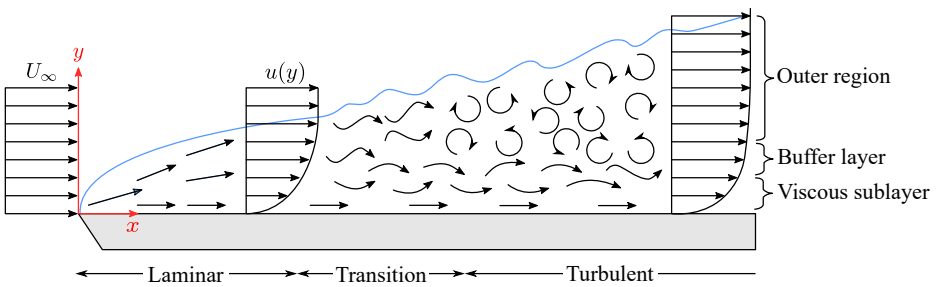

Figure 1.1: Schematic of BL evolution over a flat plate with wall-normal velocity distributions (y-axes is magnified) [104].

against the pressure gradient (i.e. $\int \partial p/\partial x$ dx, with p being the chordwise pressure distribution and x being the streamwise direction) exceeds the initial kinetic energy of the flow. This means that the lower kinetic energy associated with streamlines in the BL is not sufficient to overcome the adverse pressure gradient. Consequently, the BL flow separates from the surface of the aerodynamic body and is accompanied by a partial reversal of the velocity and wall-shear profiles. This leads to increased wake drag and significant lift reduction. Boundary layer separation can occur both for laminar or turbulent BL flows. However, under comparable flow conditions, turbulent BLs can withstand higher adverse $\partial p/\partial x$ propagating further downstream before separating. This aspect is taken advantage of in numerous industrial and aeronautical applications (such as high-lift devices, delta wings or golf balls), in which the development of a turbulent BL is artificially promoted.

1.2.1. Boundary Layer Transition

Boundary layer transition indicates the process that drives an initially laminar BL to a turbulent regime. Already from the first experiments conducted by Reynolds [126], the Re number for which the flow undergoes transition (i.e. critical Reynolds number, $\mathrm{Re}_{\mathrm{crit}}$) is found to depend on numerous flow parameters and external disturbances. Additionally, the transitional process of a BL can occur through different mechanisms, leading to various transitional scenarios as indicated by Morkovin [107].

Independently of the specific roadmap the transitional process is initiated by the receptivity process [107], which provides the initial characteristics for the BL instabilities development (such as their onset amplitude and frequency) based on the external disturbances. Among the various disturbances affecting the BL development and transition, surface roughness, wall temperature and free-stream disturbances are critical. Furthermore, a fundamental role is played by the pressure distribution on the wing surface (p) and particularly by the pressure gradient ($\partial p/\partial x$), which can either amplify or dampen the introduced instabilities.

For low amplitudes of the external disturbances, the receptivity process leads to the onset of BL instabilities with relatively small initial amplitude. These can

[1]Source: `https://www.istockphoto.com/nl/foto/wierookrook-gm1254789800-366874603?phrase=incense+smoke`

(a)

(b)

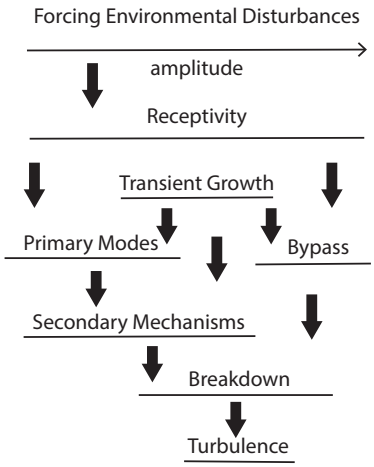

Figure 1.2: (a) Natural convection of air above a smoldering incense stick[1]. (b) Schematic of roadmaps leading to BL transition to turbulence [107].

be described within a modal framework (i.e. through the linear superposition of orthogonal modes, [98, 100]), and consequently follow an exponential growth process in time or space. The primary mode nature depends on the specific flow scenario considered, with the most common examples represented by Tollmien-Schlichting (TS) waves for two-dimensional (2D) boundary layers [9] or CFI for 3D boundary layer scenarios [16, 137]. The exponential growth of the primary modes eventually distorts the BL flow features, leading to the onset of secondary instability mechanisms characterised by rapid disturbance growth. These induce strong 3D and non-linear interactions among developing modes, driving the primary structures' breakdown to turbulence. This transitional path corresponds to *Path A* in Morkovin's map (figure 1.2(b)), and within this modal framework the prediction of the transition location can be based on the evolution of the least stable mode [122].

Different transitional scenarios can be observed when the intensity of the external disturbances is gradually increased. In particular, in numerous configurations transient growth [144] plays a relevant role in the instabilities onset. Transient growth is a non-modal mechanism related to the linear interaction of damped non-orthogonal eigenmodes [144], as further detailed in section §1.5. In simple terms, it can be described as a brief but intense algebraic growth process that rapidly enhances the amplitude of the disturbances emerging from the by receptivity. Depending on the resulting disturbance amplitudes, the occurring transitional process can differ. For sufficiently low external disturbance levels, both non-modal and modal growth can occur. In this scenario, the occurrence of transient growth provides a higher initial amplitude for the primary modes, before initiating their modal evolution and eventual breakdown (*Path B*). For higher external disturbance intensity, the initially linear modal amplification is overtaken by transient growth, following *Path C*. The transition

is then initiated by the development of the secondary instabilities, their growth and their breakdown. Finally, further increasing the intensity of the external disturbances, the transitional scenario can be due to *bypass transition*, indicating that the modal amplification is effectively bypassed by the excessively strong amplification of the initial disturbances (i.e. *Path D* and *E)*.

1.2.2. Crossflow Instabilities

Transitional scenarios following *Paths A* or *B* are typical for low disturbance environments dominated by modal growth of the BL instabilities. Specifically, the research presented in this work focuses on the investigation of swept wing BLs characterized by favourable pressure gradients ($\partial p/\partial x < 0$). These conditions are representative for the leading edge region of swept wings in a free-flight environment, and are characterized by the onset and amplification of CFI which become the inviscid instability mechanism dominating the boundary layer development. Accordingly, in the following discussion, the origin and main characteristics of CFI are presented. More complete reviews on the nature of CFI can be found in Bippes [16], Saric *et al.* [137], Wassermann & Kloker [177]. Additionally, numerous experimental [e.g. 117, 123, 136, 154, 184] and numerical studies [e.g. 19, 77, 84, 91, 100] have been dedicated to the investigation of the CFI development.

The origin of CFI relates to the inherent 3D flow topology of a swept wing BL [98, 137]. Specifically, due to the freestream velocity decomposition associated with the wing sweep angle, at the wing leading edge a spanwise velocity component (W) arises. Therefore, in the inviscid region outside the BL the streamlines initially develop as tangent to the leading edge and W itself, but are rapidly curved due to the presence of the streamwise velocity component U and the favourable pressure distribution ($\partial p/\partial x < 0$). The resulting inviscid streamlines represent the locii of points along which the forces acting on the flow, i.e. the force associated with the pressure gradient and the one corresponding to the centripetal acceleration, are balanced. When moving towards the wing surface through the viscous BL flow, the streamwise velocity component u_s and the associated momentum decrease. Thus, the centripetal force component reduces, while the pressure gradient contribution is left unaltered. This results in an imbalance of the forces acting on the flow, which is compensated for by the crossflow (CF) velocity component (w_s) developing orthogonally to the inviscid streamline in the centripetal direction. Obeying the no-slip condition at the wall and the inviscid force balance at the BL edge, the CF velocity profile is null at these two locations. Therefore, within the BL wall-normal extent w_s features a point of finite maximum and an inflection point (respectively yellow and green in figure 1.3) The latter acts as a source and driver of an inviscid instability mode [i.e. CFI, 7, 98, 137], developing in the form of a set of spanwise periodic co-rotating vortices almost aligned with the freestream velocity.

CFI develop as stationary vortices, situated at essentially fixed locations along the wing span, or travelling waves, moving along the spanwise and streamwise direction. As further discussed in section §1.3, the nature of the primary instability mode, along with its onset conditions are selected by receptivity, i.e. the process through which external disturbances enter the BL and drive the onset of the instabilities [107]. In

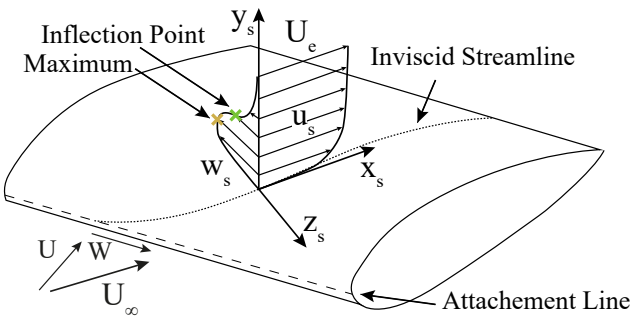

Figure 1.3: Sketch of crossflow velocity developing on a wing, adapted from Zhou *et al.* [191]

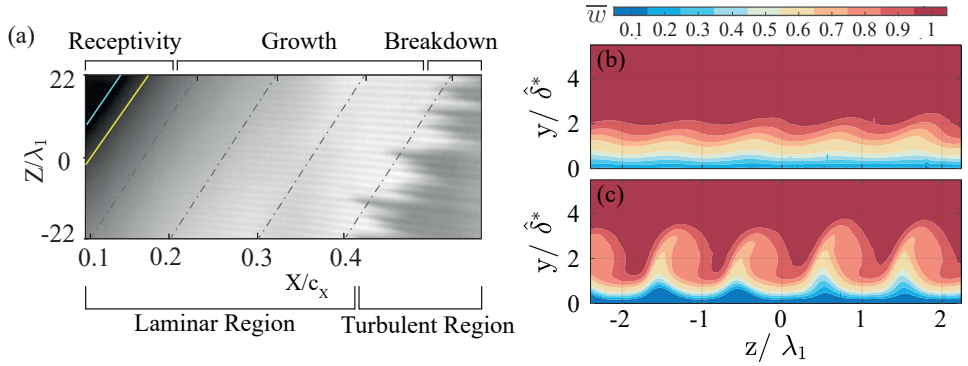

Figure 1.4: (a) Infrared (IR) thermography image of stationary CFI transition pattern on a 45° swept wing at Re_{c_X}=2.17 $\times 10^6$installed in the TU Delft LTT facility. Freestream direction (X) and vertical direction (Z); flow comes from the left. (b, c) Contours of spanwise velocity fields acquired with particle image velocimetry (PIV) for the same IR conditions at (b) x/c=0.25 and (c) x/c=0.35. [199]

particular, early experimental works outlined that flow configurations comparable to those encountered in free-flight, i.e. characterized by low T_u[30, 128], are dominated by the onset and evolution of stationary CFI, which represent the main focus of this research.

A 3D boundary layer dominated by stationary CFI is initially affected by weak disturbances, mostly developing in the spanwise and wall-normal velocity components. Surface flow visualization and infrared thermography imaging (an example of which is reported in figure 1.4(a)), show that the primary instability structures associated with stationary CFI manifest as a sequence of streaks almost aligned with the freestream direction and periodically distributed along the wing span [16, 42, 135, 137]. These streaks represent the footprint of the stationary CF vortices, modulating the BL velocity and consequently the wall skin friction and heat fluxes (figure 1.4(b)). Additionally, the CF vortices initiate a streamwise momentum redistribution process, where low-momentum fluid is displaced from the wall vicinity toward the upper regions of the BL, while high-momentum fluid is transferred toward the wing surface.

The initially weak instabilities follow an exponential growth process, accompanied by increasingly strong streamwise momentum redistribution. Once the CFI reach sufficiently high amplitudes, the BL modulation and the momentum redistribution process are strong enough to distort the BL, modifying the corresponding stability characteristics (figure 1.4(c)). Specifically, the strong spanwise modulation of velocity and momentum produces strong velocity shears in the spanwise and wall-normal directions. These are highly susceptible to secondary instability mechanisms of Kelvin-Helmholtz nature, which typically appear once the primary stationary structures saturate in amplitude [19, 100, 154, 175, 184]. These high-frequency secondary instabilities undergo an explosive growth process ultimately causing the breakdown of the primary structures and the onset of turbulent flow. The transition front appears in figure 1.4(a), as the limit between the brighter (i.e. laminar) and the darker (i.e. turbulent) region of the image. As typical for transition dominated by stationary CFI, it exhibits a jagged trend along the spanwise direction [42, 137].

Of major interest to this research, is the characterization of the receptivity process determined by the interactions between the external disturbances and the onset and development of the primary stationary CFI. The investigation of boundary layers receptivity to external disturbances, finds its roots in the early studies dedicated to surface roughness and freestream turbulence effects on 2D (i.e. unswept) BL flows [58, 106, 163]. However, with the advancement of transonic jet transport the research interest shifted towards the investigation of 3D boundary layers, pertinent to swept wing configurations. Early works [16, 17, 44] indicated that in these scenarios freestream turbulence level and surface roughness are the main initiators of CFI. Accordingly, the receptivity to these two parameters is further detailed hereafter.

1.3. CFI Receptivity to Freestream Turbulence

Receptivity to a wide range of freestream turbulence (T_u) values, was thoroughly investigated by Deyhle & Bippes [44] and Bippes [16], measuring the velocity disturbances evolution on a swept flat plate. One of the fundamental outcomes of this investigation is the distinction between high turbulence environments ($T_u/\mathbf{U}_\infty > 0.2\%$, where $\mathbf{U}_\infty$ is the freestream velocity), in which travelling CFI dominate the BL stability and transition; and low-turbulence environments ($T_u/\mathbf{U}_\infty$ <0.15%) in which stationary CFI are the dominant disturbance. Additionally, acoustic pressure fluctuations were not found to cause any measurable variation or trigger additional instabilities of crossflow nature, proving that these are mostly insensitive to the acoustic content of the freestream flow [117].

Generally, an increase in T_u corresponds to an increase of the initial amplitude of the travelling modes, while causing a decay in the amplitude of stationary CFI [16, 44]. Accordingly, for mild increases of $T_u/\mathbf{U}_\infty$ ($\simeq$0.08-0.15%) a transition delay is observed with respect to lower T_u scenarios, likely due to the interaction between stationary and travelling modes. Further T_u growth destabilizes the BL and causes transition advancement due to the excessive enhancement of the travelling CFI amplitudes. These observations were later confirmed by naphthalene flow visualization and hotwire anemometry (HWA) measurements performed on a swept wing model by Dagenhart & Saric [41] and White *et al.* [181]. More recently, Kurian *et al.* [82] conducted a

series of experiments replicating the configurations measured by Bippes [16], while extending the investigated parameter space to turbulence levels between 0.23% and 0.53%. The BL receptivity to T_u was found to be linear in this range, affecting the travelling CFI amplitude and non-linear evolution, but not their growth rate.

An additional feature of the receptivity process, already identified by these early studies, appears to be mode selection. Namely, the dominant spatial wavelength characterizing the CFI periodicity along the wing span results from the BL receptivity to both freestream turbulence intensity and surface roughness. However, Kurian *et al.* [82] outlined that for the investigated range, T_u variations do not affect the establishment of the dominant mode wavelength. This result is confirmed by Downs & White [47], investigating the interaction between coexisting stationary and travelling CFI for T_u of 0.16-0.2. Their results outline that the initiation of the travelling mode by freestream turbulence is enhanced by the presence of the surface roughness [16, 181]. However, the opposite effect is not occurring, as for the considered parameters range, the initiation of the stationary mode is almost insensitive to the small changes in T_u.

1.4. CFI Receptivity to Surface Roughness

Early receptivity investigations outlined that the onset and development of stationary CFI are mostly sensitive to the surface roughness distribution [47, 117, 137]. Specifically, three types of surface roughness are typically investigated in relation to CFI receptivity: distributed surface roughness patches (DRP), isolated discrete roughness elements (IDRE) and discrete roughness elements (DRE) arrays. Their characteristics and the main related findings are discussed hereafter.

1.4.1. Distributed Surface Roughness

The first works dedicated to the investigation of CFI evolution and transition, performed numerous flow visualizations on swept flat plates or swept wings to incur the global flow features of the developing BL [16, 41, 42, 135, 137]. These investigations showed that the natural transition front features a jagged trend along the wing span (as visible in the example reported in figure 1.4(a)). Its features are locally induced by the model surface finishing and the resulting surface roughness distribution [44, 109, 117], which excite a narrow band of instability modes through receptivity. Within the excited band, small variations of the developing modes' spanwise wavelength can affect the local instability growth, resulting in underlying small differences in the instability amplitude which locally correspond to transition advancement or delay (i.e. peaks and valleys in the transition front). To limit these effects many experimental and numerical works apply an artificial forcing in the form of arrays of discrete roughness elements (DRE) periodically distributed along the wing span, as further discussed in section §1.4.3.

Investigations dedicated to the characterization of the flow topology incurred by distributed roughness in swept flat plates, attracted growing interest in recent years [48, 49, 75, 125]. In the majority of these investigations the wing surface roughness is modelled by applying suitably manufactured distributed roughness patches (DRP). The resulting flow scenario can be representative of the random deposition of material

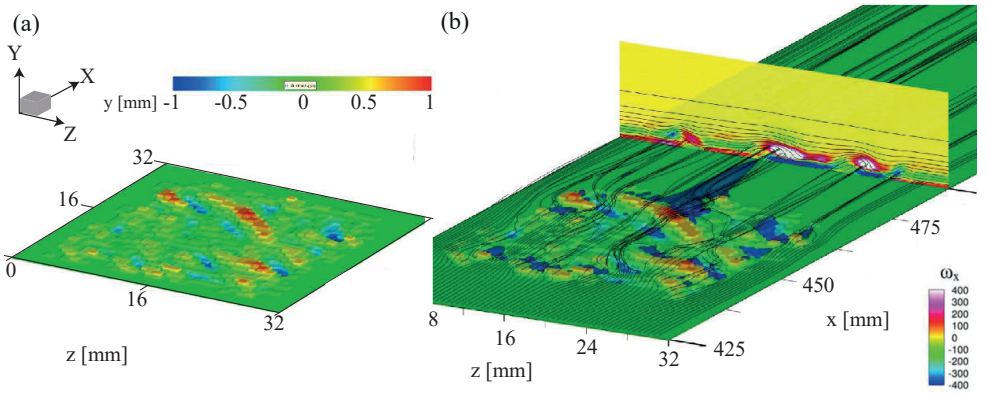

Figure 1.5: (a) Randomly distributed roughness coloured by peak amplitude for a test case DRP [48]; (b) Flow field over a DRP: streamlines and downstream flow field slice coloured by streamwise vorticity and contoured by 10% velocity increments [49].

on the wing surface, as well as of the formation of small valleys due to debris impacts. The incurred flow topology outlines that the local DRP higher peaks are the main drivers for the origin of low speed, high vorticity and high shear regions forming in the vicinity of the roughness patch itself (figure 1.5, [48, 49]). Moreover, the individual peak shape appears to be responsible for the topology of the near-peak flow field: a pair of counter-rotating vortices forms if the peak shape resembles a symmetrical DRE, while a single vortex develops if the peak resembles an asymmetric element placed at an angle in the flow field [48]. Additionally, minimal changes in the developing CFI amplitude and development are observable when the DRP is modified by removing the embedded valleys [48, 50]. This opened the way to investigations in which the applied DRP only protrude from the wing surface, given their easier manufacturing.

Finally, the considered investigations outline another interesting aspect of the distributed roughness application. Specifically, DRP composed of only the highest peaks obtained by removing the surrounding foothills, lead to enhanced BL velocity disturbances. The beneficial effect given by the presence of the foothills is defined as *roughness shielding* [155]. This effect can be attributed to the enhanced thickness of the BL developing over a DRP [48, 75], as well as to a process of energy redistribution driven by the presence of the distributed roughness [49, 79]. Further discussion on the roughness shielding technique is reported in section §1.11.

1.4.2. Isolated Discrete Roughness Elements

The application of an isolated discrete roughness element (IDRE) on the wing surface can be representative of the flow scenario induced by localized material deposition on the wing (such as an insect strike) or by a protruding rivet. The flow topology and transitional process dominating such a configuration have been widely investigated in 2D (i.e. un-swept) boundary layers, however, a comprehensive characterization of their behaviour in 3D boundary layers is still missing.

Investigations by Deyhle & Bippes [44] indicated that an IDRE applied in a 2D

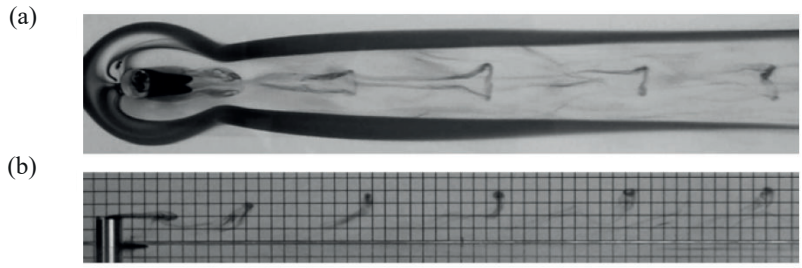

Figure 1.6: Potassium permanganate visualization of the flow field incurred by an IDRE in a 2D BL. (a) Top view and (b) side view with 5 mm grid background [25].

boundary layer, effectively introduces localized velocity disturbances in the BL which are highly effective at exciting CFI [117]. However, an excessively large isolated 3D roughness element applied on the wing surface can drive the transitional process via the initiation and spreading of a turbulent wedge [10, 58, 76, 147]. Therefore, early studies outlined how the geometry and dimensions of the IDRE play a crucial role in the onset and development of flow disturbances in the element wake and ensuing transition. As such, numerous works [76, 164] focussed on determining whether a given roughness geometry would give rise to turbulent flow, resulting in the definition of the roughness Reynolds number as a predicting parameter ($\mathrm{Re_k}=\frac{k\times|\mathbf{u}(k)|}{\nu}$ with $|\mathbf{u}(k)|$ BL velocity at the element height k and ν kinematic viscosity). In particular, $\mathrm{Re_k}$ proved to be a useful indicator for the distinction between *super-critical* and *critical* amplitude forcing configurations[2]. However, this geometrical parameter does not provide a satisfactory characterization of the flow mechanisms and instabilities ultimately responsible for the BL transition to turbulence.

The flow topology aft of IDREs has been widely investigated in 2D boundary layers [10, 58, 93, 147]. Detailed description of the flow features developing immediately aft of the element can be found in section §1.5, while the experimental and numerical characterization of the HSV evolution and the transitional process is treated hereafter. Specifically, Baker [10] performed HWA measurements on the HSV legs and identified velocity fluctuations occurring with frequency peaks corresponding to the unsteady shedding processes initiated by the roughness element. Additionally, the work by Klebanoff *et al.* [76] outlined that the onset of turbulent flow occurs at a finite chordwise distance from the roughness element location, even for high $\mathrm{Re_k}$ geometries. Further investigation of these aspects confirmed that the transitional process induced by IDREs is likely initiated by high-frequency instabilities of Kelvin-Helmoltz type, shed by the high shear layer regions forming along the perimeter (i.e. top and sides) of the roughness element wake [1, 24, 80, 93]. The periodic shedding process corresponds

[2]Throughout this booklet the definition of *super-critical* amplitude forcing configurations applies to forcing cases with sufficiently high roughness amplitude to induce flow transition in its vicinity, preventing the development of modal instabilities. *Critical* amplitude forcing configurations, instead, induce a set of instabilities in the roughness vicinity that develop into stationary modal CFI downstream, which ultimately drive the BL flow transition to turbulence. Finally, *sub-critical* amplitude forcing configurations originate weak CFI that leave the transitional process unaffected.

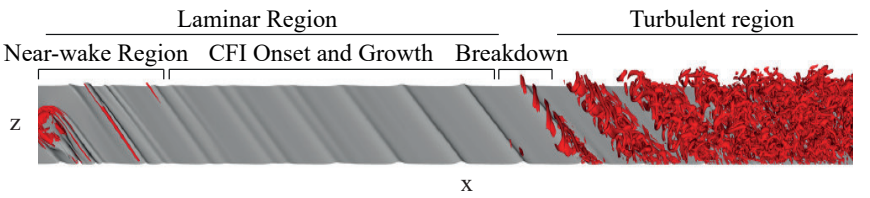

Figure 1.7: Chordwise flow field evolution incurred by a critical IDRE in a 3D boundary layer from non-linear DNS. Iso-contours of streamwise velocity (grey), and vortical structures extracted via λ_2 (red) [22].

to Strouhal numbers (based on the element height, the local flow velocity and the dominant shedding frequency) of St_k=0.05-0.4, with a monotonic increase of the intensity of primary fluctuations (and their harmonics) for increasing Re_k (up to Re_k=1000). In addition, works by Bucci *et al.* [24, 25], showed that the tonal behaviour (corresponding to the element shedding) observed in the element vicinity, can either be driven by the amplification of a local instability mode [24] or by the quasi-resonance of a marginally stable mode. Such mode would originate from background noise or external disturbances and can be enhanced by the roughness element geometry [25]. The occurring behaviour is strongly related to multiple geometrical and freestream parameters, among which Re_k, k/d, k/δ^* and T_u [24]. In 3D boundary layers, the pressure gradient and sweep angle may also play an additional and relevant role, as they significantly affect the BL stability and evolution.

Finally, the near-wake velocity deficit forming immediately aft of the element is observed to evolve into a far-wake accelerated region surrounded by low-speed flow [75, 93]. Depending on the roughness geometry and BL scales, this process can either enhance the initial disturbances initiating the turbulent wedge, or it can result in disturbances decay, stabilizing the BL. In the former scenario, a cascading configuration of low- and high-speed streaks is initiated in correspondence of the wedge-edges, destabilizing its evolution, enhancing its spreading and the onset of turbulence [13, 36, 80]. The latter scenario, instead, has given space to numerous transient growth and flow stability investigations [e.g. 35, 52, 93, 183].

Despite the wide body of literature dedicated to the effect of IDREs in 2D boundary layers, considerably fewer recent works directly investigate such effects in 3D boundary layer scenarios [e.g. 16, 137, 154]. Most of the available works have been dedicated to the analysis of the mechanisms dominating the wedge origin and downstream development [117], as the low- and high-speed streaks cascade driving the spanwise expansion of the wedge edges [13, 80]. By measuring the BL evolution aft of the IDRE, Radeztsky *et al.* [117] identified a single low-speed streak developing downstream with an inclination with respect to the freestream flow and behaviour typically pertaining to the evolution of CF vortices. Similar results were obtained from the DNS by Brynjell-Rahkola *et al.* [22], as shown by figure 1.7. Moreover, also in the 3D scenario the wall-normal and spanwise shear layers developing on the element edges are identified as responsible for initiating the instabilities dominating the transitional process. This suggests that the near-element flow topology as well as the instability origin for

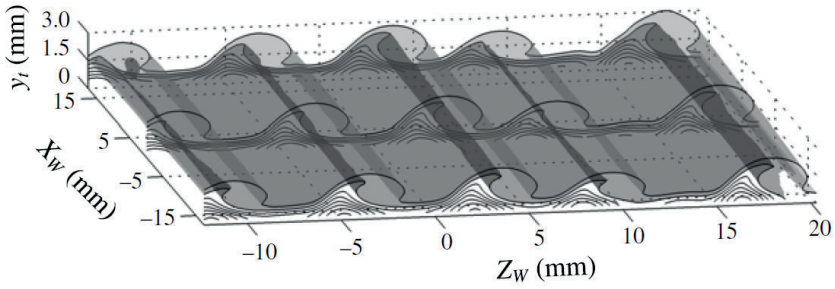

Figure 1.8: Time-averaged velocity magnitude along the CF vortex axis measured with tomographic PIV [154]. The local origin coincides with x/c=0.45 and Z=0. The semi-transparent iso-surfaces correspond to local velocity values of 0.9 and $0.8\mathbf{U}_\infty$. The flow is presented as seen from upstream.

IDRE in 2D and 3D boundary layers are strongly comparable [84]. Accordingly, the modal CFI that usually dominates the transitional scenario of smooth swept wings [16, 117, 137], appears to have little effect on the near-element flow development. Nonetheless, the aforementioned DNS investigations observe a significant asymmetry in the downstream evolution of the near-wake flow features, related to the presence of a CF velocity component in the baseflow [34], as further discussed in section §1.5.

1.4.3. Discrete Roughness Elements Arrays

Given the strong receptivity of CFI to the distributed roughness features or IDRE, numerous experimental and numerical works apply an artificial forcing in the form of arrays of cylindrical discrete roughness elements (DRE) periodically distributed along the wing span [117, 123, 136, 154]. Such arrays are typically applied in correspondence with the first neutral point of the most unstable CFI mode (according to numerical stability solutions [98, 100]), usually located in the vicinity of the leading edge. The inter-spacing (i.e spanwise wavelength λ) and height (k) of DREs are fundamental towards conditioning the developing instabilities wavelength and onset amplitude, although a predicting relation between the array geometry and CFI onset still has to be defined. Nonetheless, the presence of a DRE array enhances the spanwise uniformity of the BL by focusing the developing instabilities on a single CFI mode. Specifically, the mode selection process driven by receptivity results in a BL dominated by a monochromatic CFI with spanwise periodicity (i.e. the dominant mode spanwise wavelength) corresponding to the inter-spacing of the elements (figure 1.8). This simplifies the investigation of CFI-dominated BL, making the baseflow as well as the observed flow instabilities more repeatable and comparable within the literature framework.

The investigations by Reibert *et al.* [123] were among the first to document the effect of a DRE array on a swept wing BL. An array of 6μm height elements inter-spaced at a distance equivalent to the wavelength of the most unstable CFI mode (λ_{crit}) was applied close to the swept wing model leading edge. HWA measurements of the flow field showed that the CF vortices appear at a fixed wavelength, identical to the DRE inter-spacing. This configuration produces an almost spanwise invariant BL, leading

to transition through the formation of a relatively uniform (yet jagged) transition front. Moreover, the spatial amplification factors characterizing the dominant mode evolution along the chord, grow monotonically up to a saturation level. The obtained trends showed that for sufficiently high elements, the modifications of the measured forcing configuration do not affect the saturation amplitude value. White *et al.* [181] reported similar conclusions, however, despite measuring very similar configurations they achieved somewhat different values of saturation amplitude. This suggested that the saturation amplitude does not achieve a universal value nor it follows a universal scaling rule, as also appears from the results described by Bippes [16]. Furthermore, Reibert *et al.* [123] analysed the effect of inter-spacing the array elements at a distance equivalent to three times the wavelength of the dominant CFI mode λ_{crit} (i.e. the most unstable mode). In this forcing scenario, the CFI mode with wavelength λ_{crit} still dominates the flow, although also its super-harmonics (i.e. modes with smaller wavelengths) are excited.

A numerical study conducted by Tempelmann *et al.* [166] replicated the experimental case of Reibert *et al.* [123] through DNS and parabolised stability equations (PSE). The obtained results qualitatively confirm the main findings of the experimental work. However, the numerically computed amplitudes appear to be 2.5 times smaller with respect to the experimental ones, as also observed in other numerical works [67]. This can be attributed to numerous aspects, among which the presence of imperfections in the experimental set-up and the local features of the model surface finishing. The work by Tempelmann *et al.* [166] is among the first to investigate the BL receptivity to the DRE array location, albeit for a limited parameter range. Their main conclusions outline that the application of the DRE array in the vicinity of the forced mode neutral point introduces CFI with a stronger initial amplitude. A downstream shift of the array location corresponds, instead, to a mild decrease of the identified initial amplitude.

With the set of experiments carried out on a swept wing, Saric *et al.* [136] again observed a transition advancement when applying critical (i.e. inter-spaced at $\lambda = \lambda_{\text{crit}}$) or super-critical (i.e. inter-spaced at $\lambda > \lambda_{\text{crit}}$) wavelength arrays. However, none of these studies registered the presence of sub-harmonics of the forced mode in the flow, which led to investigating the sub-critically spaced DRE arrays, namely with an inter-spacing of the elements corresponding to $\lambda < \lambda_{\text{crit}}$. Saric *et al.* [136] showed that such arrays produce a boundary layer dominated by the CFI mode corresponding to the forced λ and its super-harmonics. The initial growth of these modes inhibits the growth of the most unstable CFI mode, increasing the extension of the laminar flow region. Therefore, the artificial forcing of sub-critically spaced DRE arrays was proposed as a means to stabilize the BL behaving like a passive LFC technique, and attracting the interest of numerous numerical [100, 145, 175] and experimental [47, 82, 138] works.

Specifically, the sub-critical wavelength forcing was investigated through DNS studies. The DNS baseflow is artificially deformed at the numerical domain inlet, introducing a wall-normal velocity component with finite amplitude and fixed sub-critical spanwise periodicity [upstream flow deformation, i.e. UFD, 175]. This technique focuses the energy and phase of the developing instabilities on the forced

CFI mode, inhibiting the development of the critical primary mode through non-linear interactions and mean flow distortion (MFD). Additionally, various DNS investigations [19, 67, 100, 175] characterised the sub-critical forcing effect on secondary CFI instabilities. In particular, Hosseini *et al.* [67] reproduced the experimental set-up of Saric *et al.* [136], observing that the sub-critical forcing is capable of weakening and delaying the appearance of secondary instabilities, delaying the BL transition [175].

Hunt & Saric [70] conducted an experimental investigation with a similar set-up to the work by Saric *et al.* [136], albeit in a lower T_u environment. The effect of the critically-spaced DRE on the swept wing flow was found to be significantly weaker, and only by increasing the amplitude of the DRE, instabilities of comparable amplitude and evolution could be observed. Differently from what was reported by previous investigations [32, 123], measuring the stationary CFI amplitudes Hunt & Saric [70] observed a dependence on the height of the element with a linear scaling for the tested roughness amplitude range (12μm to 47μm). Hence, the BL appears to be more sensitive to modifications of the DRE geometry in lower turbulence environments. Additionally, the work by Downs & White [47] investigated the role (and interaction) of natural roughness, critical and sub-critical DRE forcing at various turbulence levels. An increase in T_u is observed to correspond to a transition advancement for the first two cases but leaves the flow features mostly unaffected when combined with the sub-critical forcing case. Moreover, the sub-critical wavelength forcing proves to be a control technique quite robust to random background surface roughness while it is more sensitive to T_u modifications. This confirms that LFC performed through sub-critical wavelength forcing may not be robust to freestream turbulence variations.

Other attempts to incur the correlation between DRE forcing and freestream turbulence have been performed in environments with higher Re number. Specifically, in-flight measurements performed by Carpenter *et al.* [30] and Woodruff *et al.* [188] outline a peculiar behaviour of the critical wavelength forcing arrays in the free-flight scenario: no effect could be identified on the flow or transition for DRE amplitudes below a critical threshold. Reaching the critical amplitude value, a significant upstream advancement in the transition location, almost 15% of the chord, is observed. The sub-critical wavelength arrays prove once again to be highly sensitive to environmental modifications, as they only show transition delay under specific disturbance configurations and for a small subset of the considered cases. The most recent in-flight experiments on transition delay through sub-critical wavelength DRE further tackled this limit [138]. Despite the numerous flights successfully conducted, only one of the tested sub-critical forcing configurations showed a significant increase in laminar flow, the others having a negligible effect or even causing a transition advancement. Moreover, no significant correlation could be traced between the transition front location and the DRE chord location of the application, other than the arrays placed close to the attachment line causing a relevant transition advancement [138, 166]. This unexpected result may be due to a not yet defined interaction between the roughness effects and the freestream parameters, principally the turbulence level. This outlines once again the high sensitivity of the BL flow, especially of stationary CFI, to the receptivity process, exposing the need for a more in-depth study of its role in the instability onset.

1

Despite the large body of experimental receptivity studies conducted to date, an estimation of the onset instability amplitudes ensuing from receptivity is still incomplete. To gain these insights, the characterization of the very initial phases of receptivity, linked to the development of near-element flow, is necessary. This aspect is addressed in the following section, reporting a short review of the main works dedicated to the investigation of this topic.

1.5. The Near-DRE Flow

The above-surveyed works highlight the importance of near-wake development in the analysis of CFI receptivity to surface roughness, exposing the need for a more in-depth study of the near-element flow features to characterize the instability onset. However, the investigation of the near-element flow is extremely challenging both in experimental and numerical scenarios, being principally limited by two factors. On the one hand, due to the diverse and disparate scales of the flow phenomena involved, the near-element flow region is posing considerable challenges for state-of-art flow measurement techniques. As an example, the investigation presented in this work is performed on a swept-wing model of more than 1m chord and span developing a BL characterized by $\delta_{99} \simeq$1.4mm at 15% chord [153]. On the other hand, despite being mostly affected by surface roughness, numerous other parameters (such as freestream turbulence, local pressure gradient, and possible non-modal interactions in the element vicinity) are also involved in the receptivity process. These aspects complicate the implementation of numerical prediction tools capable of thoroughly simulating the near-element flow features. Lastly, a unifying feature that further increases the challenge in understanding these processes is the high three-dimensionality of the local flow as shown by Kurz & Kloker [83, 84].

Notwithstanding the intricacies of the problem, the DNS investigations conducted by Kurz & Kloker [83, 84] and Brynjell-Rahkola *et al.* [23], provide a detailed description of the DRE near-element flow topology. These works identified the dominant flow structures and their behaviour both for 2D and 3D boundary layer flows (figure 1.9). In both critical and super-critical amplitude forcing scenarios a recirculation region is identified immediately aft of the element. This is accompanied by the formation of a complex set of vortical systems that develops around the element. Specifically, a pair of counter-rotating HSV legs, originating from the roll-up of the BL streamwise vorticity upstream of the element, develop from the element's flanks. In turn, these HSV legs induce a weaker inner pair of counter-rotating vortices (IV) through the lift-up effect [87]. The development of such vortical systems compares well to the flow field incurred by an isolated discrete roughness element or a DRE array in 2D boundary layers [1, 46, 132]. Furthermore, an extensive analysis of the near-wake flow stability is carried out by Loiseau *et al.* [93] and Cherubini *et al.* [35], numerically investigating the flat plate flow configuration experimentally measured by Fransson *et al.* [56]. However, the downstream evolution of the vortical structures in the far-wake of the roughness element shows significant differences between the 2D and 3D boundary layers. Namely, Kurz & Kloker [84] showed that the presence of the CF velocity component in the swept wing baseflow leads to a loss of flow symmetry, as the resulting flow field is dominated by the crossflow direction of rotation. Accord-

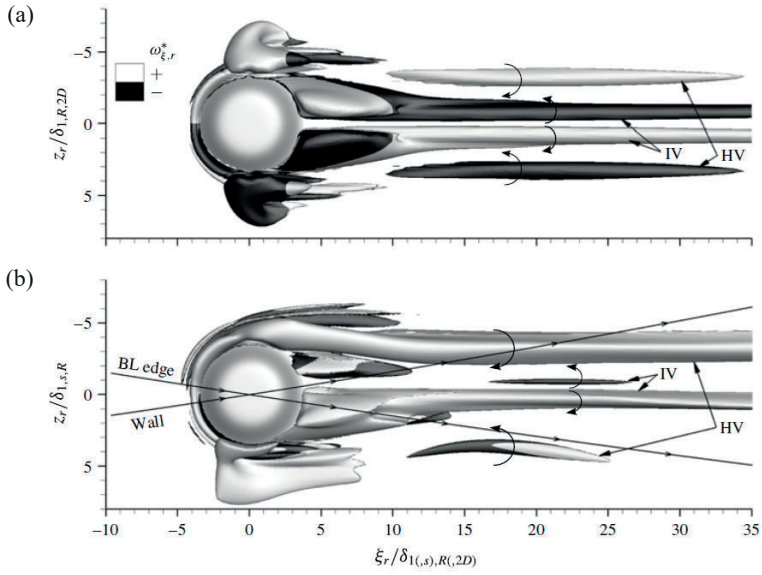

Figure 1.9: Near-wake vortex systems induced by a DRE with inner (IV) and outer (HV) vortex systems in (a) 2D, (b) 3D baseflow. Vortices are visualised by iso-surfaces of λ_2, the shading indicates positive or negative values of the vorticity along the CF vortex axis [84].

ingly in 3D boundary layers vortical structures co-rotating with the CFI (defined as co-crossflow structures for the sake of brevity) are sustained in their downstream evolution, while the counter-rotating structures are damped. As a result, only one leg of each vortical system is sustained in the flow field either initiating the development of modal instabilities or driving the laminar breakdown of the streak structures and the onset of turbulence (i.e. causing bypass transition). The latter case typically occurs in the presence of super-critical forcing configurations featuring high-amplitude DRE. Due to the strong local wall-normal and spanwise shears, near-wake unsteady instabilities (often of Kelvin-Helmholtz type) with excessive initial amplitude and rapid local growth develop and trigger transition in the element vicinity, effectively bypassing the development of modal CFI [52, 76, 124].

The occurring flow scenario can be satisfactorily predicted based on the roughness Reynolds number, i.e. $\mathrm{Re_k}$ [58, 123]. Specifically, for low $\mathrm{Re_k}$ (i.e. $\mathrm{Re_k}$<200 for the experimental set-up employed in this booklet) the sustained HSV leg is amplified past the element far-wake and develops in a modal stationary crossflow vortex. For higher $\mathrm{Re_k}$ the recirculation region forming aft of the element is strong enough to amplify unsteady disturbances in the wake-induced shear layer, which provide the first seed for unsteady laminar breakdown [1, 76, 197]. As such these near-wake instabilities persist and grow in the wake flow field, contaminating the laminar flow regions and initiating the BL transition to turbulence shortly downstream of the element location [23, 84]. Previous investigations showed that comparable behaviour characterizes 2D boundary layers forced by IDRE or DRE arrays [e.g. 24, 33, 52, 76].

Building upon the near-element flow evolution described beforehand, a distinction between near- and far-wake flow is introduced. Throughout this booklet, the term *near-wake* is generally used to indicate the flow region in which the near-element flow features (i.e. the HSV and IV) are developing. The *far-wake* region, instead, corresponds to the flow region in which modal instabilities develop in BL forced by critical roughness amplitudes, or to the region of laminar breakdown and turbulence onset for higher (super-critical) roughness amplitudes. Further clarifications of this definition can be found in Chapter 5.

Despite the significant insights on the near-element flow topology and instability development offered by the discussed DNS studies, the characterization of the DRE-CFI onset relation is yet to be defined. This is particularly evident in the lack of dedicated experimental studies of these effects. Nonetheless, a wider body of literature is dedicated to the investigation of the near-wake features induced by roughness elements in 2D boundary layers [e.g. 24, 35, 165, 183]. In particular, many of the reported works identify transient growth as a fundamental mechanism occurring in the near-wake region, relating the downstream onset of modal instabilities (i.e. critical behaviour) or the occurrence of bypass transition (i.e. super-critical behaviour) to the initial algebraic growth of the near-wake disturbances. Furthermore the highly three-dimensional flow developing in the near-wake of critical and super-critical roughness elements has been widely investigated through global stability analysis [e.g. 43, 84, 93]. However, in their numerical investigation Kurz & Kloker [84] outlined that the instability mechanism dominating the bypass transition scenario is not necessarily a global instability. Rather depending on Re_{k}, it can develop as a purely convective instability in the element near-wake, further accommodating the possible presence of transient mechanisms in the near-wake flow.

Given the similarities of the near-element flow fields between 2D and 3D boundary layer cases, it can be expected that transient growth mechanisms might be active also in the latter. Therefore, the following section is dedicated to the introduction of the transient growth concept.

1.5.1. Transient Growth Mechanisms

Transient growth is a linear instability mechanism driving the algebraic amplification of initially small amplitude disturbances which exponentially decay shortly downstream [e.g. 39, 90, 95, 144]. This phenomenon typically occurs in shear layers that are otherwise stable to modal instabilities (according to numerical stability solutions). Transient growth mechanisms govern the linear superposition of individually stable non-orthogonal disturbance modes [e.g. 95, 144]. Therefore, the occurrence of such mechanisms in the element's near-wake (and consequently in the initial phases of the receptivity process) would relate to the presence of non-modal flow interactions. From a mathematical standpoint, the occurrence of transient growth can be related to the non-normal nature of the Orr-Sommerfeld/Squire operator, which encompasses a set of non-orthogonal eigenmodes as stability solutions of the wall-normal velocity and vorticity equations [144]. The disturbance resulting from the linear superposition (i.e. vectorial sum) of individually decaying non-orthogonal eigenmodes [65, 98, 100] can experience algebraic growth. This is a linear growth process, typically brief

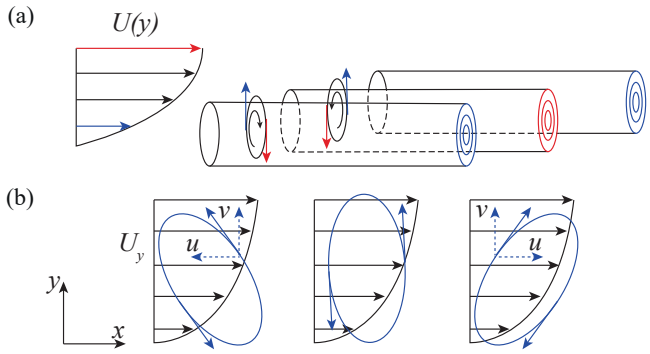

Figure 1.10: Schematic illustration of (a) the lift-up effect, with low- (blue lines) and high- (red lines) velocity streaks; and (b) the Orr mechanism [95].

albeit intense, which is rapidly hindered by the exponential decay of the energy associated with the dominant eigenmodes [63, 144]. The process encompassing the initial algebraic growth and the consecutive viscous dissipation driving the exponential decay is named transient growth [124, 144, 183].

From a physical point of view, the transient growth process can be related to the presence of a lift-up mechanism [figure 1.10(a), 87]. This typically occurs in flow fields dominated by instabilities in the form of streamwise structures [63, 124, 183]. Generally, a flow disturbance developing as a streamwise vortex transfers momentum across the BL. This induces mild modifications of the wall-normal velocity component (v) while initiating a strong streamwise velocity disturbance (i.e. streak) [74]. The original vortical structures may be locally stable and undergo exponential decay. Nonetheless, the increased disturbance energy associated with the streamwise momentum redistribution (i.e. the lift-up effect) can exceed the streaks' energy decay, thus leading to transient growth [20, 39, 87]. Once the original vortical structures are sufficiently weak (damped by the viscous diffusion effects), the streamwise velocity disturbances reduce and follow an exponential decay.

Another physical mechanism responsible for non-modal growth in shear flows, is the Orr mechanism [figure 1.10(b), 27, 112]. Specific flow scenarios can be characterized by the presence of instabilities developing as flow structures tilted against the mean shear. These structures can re-align to the mean shear by initially extracting energy from the baseflow through Reynolds stress production, rising to an upright position. Successively, these structures lose the acquired energy to the baseflow while aligning to the mean flow vorticity.

Transient growth mechanisms have been widely studied in the temporal framework (i.e. considering the instabilities growth in time) for incompressible 2D boundary layers. Numerical investigations performed within the parallel-flow approximation [27, 60, 64, 89, 121] in agreement with experimental studies [20, 59, 76], outlined the fundamental role of streak structures in transient growth processes. In particular, within the numerical investigation framework, streamwise vortex structures are typically defined

as *optimal disturbances* for the transient growth phenomena, as they maximize the ratio between the disturbance kinetic energy at the final and initial growth stages [53]. This is true also for numerical scenarios including non-parallel flow effects [4, 96]. In addition, Tumin & Ashpis [172] found that the non-modal growth process is typically destabilized by an adverse pressure gradient, while a favourable pressure gradient has the opposite effect.

The presence of a transient mechanism in 3D boundary layers has as well been investigated, with the first dedicated studies still tackling non-modal effects in a temporal framework. Breuer & Kuraishi [20] and Corbett & Bottaro [39] experimentally and numerically proved that 3D boundary layers can effectively sustain significant transient growth. Additionally, they identified that the optimal disturbances in this scenario are still associated with vortical structures almost aligned with the inviscid streamline. These vortices evolve into velocity streaks further downstream, driven by the lift-up effect. Given the topological resemblance between the algebraically growing disturbances and the most unstable CFI eigenmode, Corbett & Bottaro [39] outlined that in 3D boundary layers modal and non-modal disturbance growth can coexist. Hence, transient growth can be a complementary phenomenon to exponential amplification, providing the onset conditions for the modal disturbances development [20, 39]. The latter results are valid also for transient growth mechanisms developing in a spatial framework (i.e. instabilities growing in space), as proved by the development of dedicated numerical solvers [28, 29].

1.5.2. Transient Growth in Roughness Wake Flows

Considering the presented literature framework, the stationary flow topology incurred by a DRE in a 3D boundary layer is defined as sub-optimal for algebraic growth processes [28, 39, 183]. In fact, the near-wake region is dominated by the presence of the counter-rotating streamwise-oriented HSV and IV legs, leading to the formation of high- and low-speed streaks. These structures are found to be subject to and to sustain transient growth possibly resulting from the combined effect of the lift-up and Orr mechanisms [20, 39, 87]. The occurrence of a transient growth process drives the amplitude growth of the near-wake disturbances, which combined with the presence of a recirculation region in the element wake, can enhance the strong shear layers and unsteadiness characterizing the near-wake flow [20, 39]. Accordingly, in a critical $\mathrm{Re_k}$ scenario, the near-wake streak structures can initially undergo transient growth while evolving into modal CFI shortly downstream [20, 39, 93, 95]. However, in higher external disturbance environments (i.e. super-critical $\mathrm{Re_k}$), an explosive transient growth process can occur in conjunction with the presence of enhanced shears and excessive amplitude of the velocity streaks developing in the near-wake region. Thus, the breakdown of the laminar structures is initiated shortly downstream of the element, leading to increased flow unsteadiness and the onset of turbulence through bypass transition [4, 124].

In particular, experimental investigations conducted by White & Ergin [182], White *et al.* [183] showed that in DRE-forced 2D boundary layers algebraic growth is a fundamental mechanism in the near-wake flow evolution. The analysis of the Fourier spatial spectral energy distribution indicates that the observed transient process is

mainly sustained by the third and fourth harmonics of the dominant stationary mode (corresponding to the wavelength forced by the applied DRE array). The modal energy associated with such harmonics grows algebraically immediately aft of the element, followed by exponential decay shortly after while scaling with Re_k^2 in the transient flow region. These results have been confirmed by the DNS investigation by Fischer & Choudhari [54], albeit overestimating the modal energy measured in the experiments. Furthermore, previous investigations dedicated to 2D boundary layers receptivity characterized the near-wake of DRE of various shapes (i.e. square, hump, micro-ramp, and cylinders) and size (represented by the height-to-diameter ratio of the considered geometries) [e.g. 133, 190]. Both these parameters appear to affect the near-wake velocity field to such an extent that differences could be observed in the spanwise frequency spectra incurred by the various geometries. Accordingly, already the modification of the roughness height-to-diameter (k/d) ratio can affect the identified transient growth phenomena and consequently the onset of modal CFI [183]. However, White *et al.* [183] describe relatively simple modelling functions, based on the element geometry and the chordwise location of the modal energy peak. The proposed models approximate well the observed transient energy growth of the harmonic modes, as further discussed in Chapter 5.

Transient growth mechanisms may affect the near-wake development also in 3D boundary layers, driving the receptivity process and determining the initial amplitude for the modal instabilities development [20, 39, 165]. However, no experimental observation of these flow phenomena is yet available. The available literature framework shows that the receptivity process of forcing cases with sub-critical forcing amplitude (i.e. originating weak CFI that only marginally affect the transitional process) can be approximated by a direct geometrical dependence of the initial modal amplitude on the DRE geometry. This applies to forcing configurations in which the initial CFI amplitudes scale with the element geometry either represented by the simple element height (k, [145, 166]) or by a geometrical parameter such as Re_k (expressing a dependence on k^2). The former cases feature very low forcing amplitude configurations (i.e. k lower than 10% of the local BL displacement thickness, [70, 166]). The latter, instead, includes the results by Kurz & Kloker [83] outlining that the receptivity process of roughness elements with height lower than 30% of the local BL displacement thickness is described by a receptivity coefficient that linearly depends on k (hence the initial amplitude of the modal CFI relates to k^2). This behaviour is particularly evident for configurations with varying DRE aspect ratio (k/d, e.g. increasing height for a constant DRE diameter), while the initial amplitude sensitivity to the element height is reduced for constant aspect ratio geometries [83]. Evidently, the complexity of receptivity under variations of a multitude of governing parameters (such as roughness height, diameter, location etc.) complicate the deterministic definition of specific receptivity regimes. Nonetheless, to classify these receptivity regimes in intuitively accessible terms, throughout this booklet the aforementioned configurations are grouped under the *k-dependent receptivity* definition as they are represented through a direct relation with k showing only minor dependence on the effective DRE shape. It must be stressed here that k-dependent receptivity does not exclude dependence on other parameters (such as diameter or geometrical shape),

rather denotes the dominant influence of roughness height on the conditioning of the initial modal amplitudes. Higher amplitude elements follow a receptivity process with no clearly outlined dependence on the external forcing geometry. Therefore, a clear receptivity model for the characterization of the critical amplitude cases considered in the present work is still missing. Additionally, super-critical amplitude forcing configurations feature high-amplitude DRE inducing strong local wall-normal and spanwise shears. Hence, the near-wake flow receptivity can be dominated by different mechanisms relating to bypass transition rather than CFI development. This would further explain the difficulties encountered in literature when trying to directly correlate, either numerically or experimentally, the external forcing disturbances with an estimation of the initial amplitude of the modal instabilities.

Considering the relevance of the near-element flow features in clarifying the receptivity process, the near-wake flow analysis along with the investigation of the presence of transient mechanisms and the characterization of their role in the CFI onset and development, are among the main objectives of the present work.

1.6. CFI suppression via Surface Roughness

As previously mentioned, in numerous aeronautical applications it is desirable to sustain the laminar BL for the longest possible chord extent to reduce the developed skin friction drag. Some of the more common LFC techniques have already been introduced in the previous sections, such as the sub-critical wavelength forcing or the roughness shielding. These aspects are briefly re-considered and extended in the following discussion, outlining various instability control and suppression mechanisms investigated in past works. All the considered LFC mechanisms strongly rely on the boundary layer receptivity to roughness (or similar wall-forcing conditions). Therefore, detailed understanding of the receptivity process can offer valuable insights for the further development of tailored LFC techniques.

The sub-critical wavelength forcing technique discussed in section §1.4.3 and exemplified in figure 1.11(a) for an experimental application, proved effective in controlling CFI developing in wind tunnel environments [136]. However, successive works demonstrated that the sub-critical wavelength forcing is highly sensitive to the external flow conditions, exerting reduced control capabilities in a free-flight environment [138]. The investigation of comparable flow scenarios by means of DNS and UFD techniques provided comparable results. However, by focussing the developing disturbances on a single CFI mode, UFD succeeds in fixing the spanwise position and phase of the developing CF vortices with respect to the wing surface. Therefore, the application of UFD or sub-critical wavelength forcing can improve the performance of LFC techniques based on the destructive interference between velocity disturbance systems [176]. In particular, DNS investigations showed that the application of a series of successive spanwise rows of suction orifices can successfully control the BL development if the constructive interference of the 3D disturbances induced by each row is minimized [103]. Additionally, the combination of UFD with classical BL suction provides an optimal arrangement of the suction holes location with respect to the developing CFI [57]. This allows for the application of optimally located, strong, localized suction to already non-linear CFI configurations,

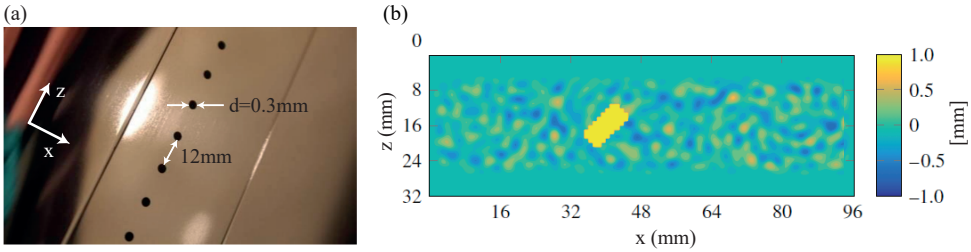

Figure 1.11: (a) Sample of DRE array applied to wing model to investigate sub-critical roughness as a passive control technique [70]. (b) Sample roughness configuration combining distributed roughness (DRP) and isolated rectangular roughness element for roughness shielding investigations [79]. Colourscale based on roughness height [mm].

successfully inhibiting the onset of secondary instabilities [57]. Nonetheless, the practical implementation of BL suction remains technically complicated and costly.

In the context of the receptivity to distributed surface roughness (section §1.4.3), Sharma *et al.* [155] defined the beneficial effect given by the presence of the DRP foothills as roughness shielding. This phenomenon has been widely investigated as the result of the superposition of IDREs and DRP patches in 2D boundary layers, as shown in figure 1.11(b) [12, 79, 162]. These investigations showed that the presence of the sole DRP induces smaller disturbances when compared to the flow field incurred by the IDRE or the combination of the two roughness systems. Moreover, minimal differences were identified between the last two configurations regarding the emerging disturbances' amplitude, energy and overall development. Additionally, these works showed that two IDREs opportunely applied at subsequent chord locations on the wing surface, can effectively reduce the amplitude of the incurred disturbances and delay the BL transition with respect to the single DRE forcing. Finally, the simultaneous presence of the DRP and the IDRE leads to a redistribution of the energy from longer towards shorter wavelengths [49, 79]. This is explained by considering that the momentum transfer process brings high-speed fluid towards the bottom of the BL, where the flow structures must conform to the topographical modes embedded in the distributed roughness patch. As such, the beneficial effect of the shielding can not be attributed to a simple superposition of effects, but relates to a modification of the baseflow field characteristics [49, 79].

The concept of instabilities suppression has also been applied to Tollmien-Schlichting (TS) waves in 2D boundary layers. Comparably to CFI, TS modes developing on a flat plate or a swept wing, initially grow independently from each other [73, 143, 148]. As such, the linear superposition of artificially generated TS instabilities is not expected to introduce significant mode coupling. Previous investigations [78, 92, 105, 170], successfully attenuated the linearly growing TS instabilities by superimposing artificially generated mono-frequency disturbances with properly adjusted amplitude and phase shift. Further development of this approach, led to the application of digital transfer functions continuously adapted by a control system to determine the corrected phase shifts leading to TS damping [11, 86, 116, 169]. In recent studies, multiple sensor-actuator systems have been applied in streamwise and spanwise

arrangements. This allows for performing the wave attenuation procedure at different locations, progressively suppressing the remaining disturbances further delaying transition [160, 161].

The application of roughness shielding and the instabilities suppression techniques developed for 2D boundary layer scenarios, open interesting possibilities for the attenuation of stationary CFI developing in swept wing BLs. Based on these and the results of the current research, a novel flow suppression technique capitalizing on destructive interference is introduced in this booklet.

1.7. Motivation, Objectives and Thesis Outline

The research presented in this thesis, focuses on the experimental investigation of 3D boundary layers receptivity to surface roughness. Particular attention is devoted to the characterization of the flow field in the vicinity of the applied roughness elements, in order to gain a deeper understanding of the physical phenomena dominating the receptivity process and their effect on the CFI onset and development. The successful characterization of the receptivity process provides insights into how surface roughness interacts with the onset and initial development of the dominant instabilities, enabling the design of more effective laminar flow control techniques for the control or suppression of CFI.

The first part of this work is dedicated to a parametric study, aiming at better understanding the flow mechanisms dominating the receptivity of stationary CFI to the amplitude and location of DRE arrays. The investigated forcing configurations are manufactured in-house, and the incurred flow fields are measured by infrared (IR) thermography and planar particle image velocimetry (PIV). This investigation is performed with two main objectives:

- Establish whether height-based metrics (such as Re_k) can be used to predict the initial instability amplitude incurred by a given DRE array configuration.
- Outline effective scaling principles to reproduce the swept wing leading-edge flow features through an experimentally observable up-scaled forcing configuration.

Specific up-scaled roughness configurations are the subject of the second part of this research. Critical and super-critical IDREs and DRE arrays are applied at relatively downstream chord locations (i.e. x/c=0.15), enhancing the experimental resolution of the near-element flow field. HWA and high-magnification tomographic particle tracking velocimetry (PTV) are employed to acquire the steady and unsteady near-element flow topology. Three main objectives can be formulated:

- Characterize the steady and unsteady flow mechanisms driving the onset of BL instabilities in an IDRE-forced scenario.
- Determine the nature of the dominant instabilities as well as their role in the receptivity and transitional processes in the various considered scenarios.
- Investigate the presence of transient mechanisms in the element near-wake, detailing their receptivity to external conditions and their role in the CFI onset.

The completion of these objectives results in the production of the first conceptual *receptivity map* describing the receptivity of swept wings boundary layers to a wide range of DREs amplitudes.

The final part of this work is dedicated to the development of a passive LFC technique based on the destructive interference of the velocity disturbances introduced by streamwise successive DRE arrays. Specifically, optimally arranged DRE arrays are applied on the wing surface, introducing velocity disturbance systems that destructively interact. The performed IR and planar PTV measurements confirm that these configurations can reduce the developing CFI amplitude, delaying the BL transition. Two main objectives can be identified for this investigation:

- Evaluate the effectiveness of a fundamental linear superposition mechanism in controlling the development of CFI, delaying the BL transition.
- Verify the suitability of the proposed technique in controlling CFI developing in a realistic free-flight scenario (i.e. with enhanced distributed surface roughness).

This booklet is organized into seven main chapters, divided as follows. Chapter 2 describes the main acquisition and processing techniques employed throughout this research. Chapter 3 presents the parametric investigation of the BL receptivity to DRE arrays amplitude and chord location. Chapter 4 outlines the investigation of near-critical IDRE near-element flow features, while Chapter 5 details the analysis of the near-element flow topology for the application of a critical and super-critical DRE array. Chapter 5 also provides a detailed description of the receptivity process, outlining the first conceptual map of 3D boundary layers receptivity to DREs amplitudes. Finally, Chapter 6 introduces the proposed CFI suppression technique, detailing the observed results and limitations. To conclude, Chapter 7 reports the main findings and the remaining research questions.

2

Methodology

The work presented in this thesis, mainly derives from experimental data. Therefore, this chapter provides a description of the facilities and experimental techniques employed, along with an introduction of the main data post-processing techniques applied. Furthermore, a brief description of the numerical boundary layer solution and of the linear and non-linear stability solver employed is provided, as they contributed to the design of the experimental campaigns and to the data analysis.

2.1. Experimental set-up

Hereby, the wind tunnel facility and wing model employed in the investigations are briefly introduced. More complete reviews can be found in Serpieri [152] and Rius Vidales [129].

2.1.1. Wind Tunnel and Swept Wing Model

All measurements presented in this booklet are conducted in the low-speed Low Turbulence wind Tunnel (LTT), an atmospheric closed-loop low turbulence subsonic tunnel extensively described by Dobbinga & van Ghesel Grothe [45]. The LTT is located at the TU Delft Aerodynamics laboratories and features a 1.25×1.80×2.6m (i.e. height, width and length) test section. Owing to the seven dedicated anti-turbulence screens and the large contraction ratio (17:1), the test section flow features low freestream turbulence levels. Specifically, for freestream velocities between 25-60m/s turbulence intensities of $T_u/\mathbf{U}_\infty \simeq 0.025\%$ are reached in the 2Hz-5000Hz bandpass range [152]. Furthermore, background acoustic emissions of the tunnel are not relevant for the transition of CFI-dominated BL [44, 117].

The employed wind tunnel model is an in-house designed, constant-chord swept wing (M3J), whose geometry and characteristics are detailed by Serpieri [152]. The swept wing main geometrical parameters are reported in table 2.1, while a sketch of the wing model is shown in figure 2.1. The wing was purposely designed and widely used to investigate the physics of primary and secondary CFI and LFC techniques [129, 152]. Its geometry derives from a modification of the NACA 6-series airfoil (66018), and features a favourable pressure gradient and accelerating flow up to x/c≃0.65. The flow over the model pressure side is measured by two rows of 46 chordwise distributed pressure taps, located at 24% and 76% of the wing span (locations sketched as green lines in figure 2.1(a)). The measured pressure distribution (described by the pressure coefficient C_p) and the corresponding pressure gradient ($\partial C_p/\partial x$) are shown in figure 2.1(b). These quantities are used to estimate the chordwise velocity distribution at the BL edge, necessary input for the BL numerical solution as discussed in section §2.4. To prevent the development of strong unsteady flow separation, during the measurements the BL over the wing suction side is forced to a turbulent state by applying a tripping wire in the leading edge vicinity. Moreover, even without the application of side wall-liners, this wing model behaves closely to an infinite-span wing, developing a spanwise invariant flow [153].

The experimental measurements described in this work, are mostly performed at an angle of attack α=-3.36° and a reference freestream Reynolds number Re_{c_x}=2.17 $\times 10^6$, corresponding to a freestream speed of $\mathbf{U}_\infty \simeq$25m/s. At these conditions, the favourable pressure distribution and the low T_u level allow stationary CFI to dominate the BL stability and transition [16, 137]. Due to the high sensitivity of stationary CFI to surface roughness, the model surface is carefully polished ensuring a low and consistent roughness level monitored using a Mitutoyo SJ-310 surface profilometer [153]. The resultant root-mean-square (rms) roughness of the wing surface is R_q = 0.2μm [153, 167]. The BL developing with these surface roughness configuration is considered as *natural* (or clean) as no external roughness forcing is applied to condition its evolution. This aspect is further treated in Chapter 3.

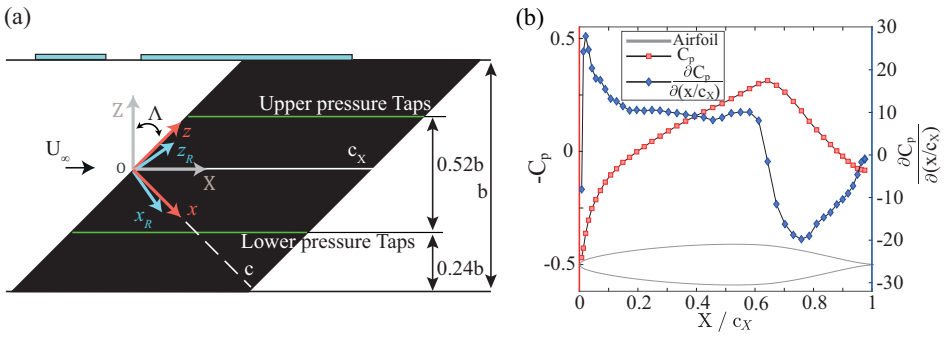

Figure 2.1: (a) M3J swept wing diagram with coordinate systems: tunnel-attached (grey, XYZ); wing-attached (red, xyz); CF vortex aligned (light blue $x_R y_R z_R$). Y-axes, y-axes and y_R axes are all directed towards the reader. Light-blue rectangles represent windows cut in the tunnel ceiling. (b) M3J airfoil geometry (aligned to the freestream direction X), pressure coefficient and pressure gradient distribution measured by the lower and upper arrays of pressure taps at α=-3.36°, Re_{c_X}=2.17 $\times 10^6$.

Parameter	Λ [°]	AR [-]	b [m]	c_X [m]	c [m]	S [m^2]	R_q [μm]
Value	45	1.01	1.25	1.27	0.9	1.58	0.20

Table 2.1: Geometric parameters of the M3J swept wing model [153]. Wing sweep angle (Λ), wing aspect ratio (AR), wing span along Z (b), wing chord along X (c_X), wing chord along x (c), wing surface (S), background wing surface roughness (R_q).

2.1.2. Coordinate Reference Systems

Given the complexity of the swept wing geometry and the multiple measurement techniques used to characterise the developing 3D boundary layer, various reference systems are defined throughout this work. These are sketched in figure 2.1(a), and are briefly outlined hereafter.

Two main reference systems can be defined starting from the wing geometry. One is integral to the wind tunnel floor (i.e. tunnel-attached) with spatial components given by (X, Y, Z) and velocity components U, V, W. The second one, (x, y, z), is aligned to the wing sweep (i.e. wing-attached reference system), having its x-axis and z-axis respectively orthogonal and aligned to the wing leading edge and y-axis coinciding with the tunnel-attached Y. The respective velocity components are (u, v, w). The origins of both the XYZ and xyz systems lay at the wing leading edge in correspondence with the mid-span (i.e. b/2) location. The wing-attached reference system xyz is mostly used for PIV and HWA acquisitions, while the tunnel-attached reference XYZ is the basis for IR thermography measurements and processing. In the schematic of figure 2.1(a), the airfoil chord in the XYZ is denoted as c_X (solid white line), defining the non-dimensional streamwise location as X/c_X. In the wing-attached reference frame, the wing chord c is aligned with the x-axis (white dashed line in figure 2.1(a)), defining the non-dimensional chordwise location as x/c. Given the semi-infinite swept wing flow assumption, the two definitions of the chordwise location are equivalent.

Another coordinate system employed during the data post-processing is obtained by rotating the wing-attached system around y, aligning the x-axis with the CF vortex axis. This reference system provides a suitable framework for the identification of 3D coherent structures dominating the boundary layer flow in the roughness vicinity, performed by applying a vortex identification criterion (Q-criterion) in Chapter 5. Such reference frame has spatial components ($x_R y_R z_R$) and is obtained by rotating the wing-attached system of 6.5° around the y-axis. The resulting frame has x_R aligned with the CF vortex axis, y_R coincident with y and z_R to complete the triad. The corresponding velocity components are named u_R, v_R, and w_R.

2.2. Surface Roughness Configurations

During this study, the effect of distributed roughness patches (DRP), isolated discrete roughness elements (IDRE) and discrete roughness elements (DRE) arrays on the swept wing BL development and transition is investigated. The manufacturing of the applied roughness elements is performed in-house, following the procedures described hereafter.

2.2.1. Distributed Roughness Patches (DRP)

By design, the employed wing model has an extremely smooth surface finishing [153], therefore to extend the applicability of the investigated flow features to more realistic transitional scenarios it is desirable to characterize the BL instability and evolution under conditions of elevated background roughness. To enable this DRP mimicking the effect of a rough wing surface finishing are applied. These patches are obtained by positioning a rectangular PVC mask on the wing surface, parallel to the wing span and extending for x/c=0.03 along the wing chord. The corresponding portion of the model is sprayed with a layer of spray adhesive[1], enhancing the wing surface roughness through the random deposition of adhesive particles.

When measuring the flow features incurred by such DRP, it emerged their peak amplitude is likely excessive (Chapter 6). Hence, to obtain thinner patches a second technique is employed in the last part of this research. Namely, a stripe of double-sided tape[2] is applied at a selected chordwise location on the wing surface. On the free adhesive surface of the tape, silicon carbide are dispersed in a random and saturated distribution. This provided DRP with comparable average height and smoother height distribution.

Both types of DRP are manually applied at various chord locations distributed between the leading edge (i.e. $x_{DRP}/c=0$) and $x_{DRP}/c=0.125$. As each patch contains a random distribution of local roughness peaks, multiple DRP configurations are measured during this campaign. To characterise the DRP geometrical features, a subset of the applied DRP is scanned with a scanCONTROL 30xx profilometer[3].

[1] 3M SprayMount™Adhesive, using petroleum distillates as solvent sprayed in a particle pattern. Technical sheet at `https://docs.rs-online.com/aed2/0900766b813665dd.pdf`

[2] 3M re-positionable tape, model 9425HT. Technical sheet at `https://multimedia.3m.com/mws/media/1429300/repositionable-tapes-665-666-9415pc-9416-9425-9425ht-9449s.pdf`

[3] The laser scanner operates with a semiconductor laser having a 405nm wavelength and 1.5μm

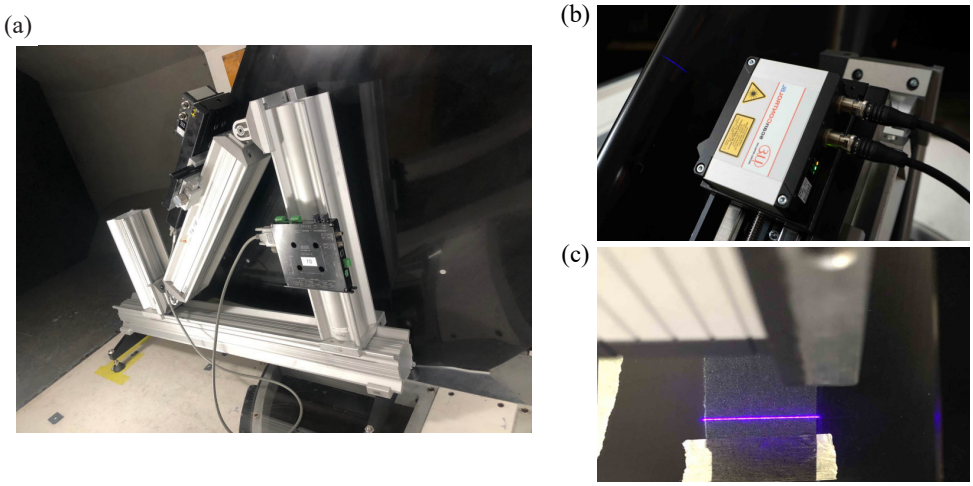

Figure 2.2: (a) Image of wind tunnel set-up for DRP characterization with scanCONTROL 30xx profilometer. (b) Image of scanCONTROL laser beam measuring the DRP in the wing leading edge vicinity. (c) Zoomed-in image of scanCONTROL used for at-bench preliminary measurements of silicon carbide DRP.

During the measurements, the laser scanner is mounted on a Zaber traversing axis[4] with step accuracy of 15μm. The scanned domain extends for x/c=0.02, acquiring the chordwise DRP amplitude signal (i.e. the local DRP height k_{DRP}) at various spanwise locations with a step of 30μm. With this procedure, the average and peak k_{DRP}, the DRP spanwise spectral (i.e. wavelength) content and its geometrical features repeatability are estimated. The patch characterization is conducted directly in the wind tunnel, measuring various DRP (indicated as D_n) while applied on the wing surface, as well as at bench. Figure 2.2 collects three images showing the overall experimental set-up employed for the scanCONTROL acquisitions.

The DRP amplitude signals (i.e. the k_{DRP} values) are then processed, delivering a 3D reconstruction of the measured patch (figure 2.3(c)) and characterizing the geometrical and spectral features of each DRP. Specifically, figure 2.3(a) indicates that the average height of an adhesive-glue roughness patch (averaged in the spanwise and streamwise directions) is $k_{DRP} \simeq 0.012 \pm 0.005$mm. However, the local roughness height can reach isolated peak values of $\simeq$0.18mm, comparable to the amplitude of the applied DRE elements (table 2.3). The DRP obtained by applying silicon carbide on the double-sided tape layer provide an average height still close to $k_{DRP} \simeq 0.01 \pm 0.001$mm, however the local peak heights are significantly lower reaching maximum values of 0.04mm. This provides a more uniform DRP amplitude distribution, still accompanied by a broadband spanwise spatial content.

The spanwise spectral content of the DRP is investigated by applying a spatial

reference resolution. Technical sheet at `https://www.micro-epsilon.com/download/manuals/man--scanCONTROL-30xx--en.pdf`

[4]Zaber LRQ-E series, model LRQ150-HL. Technical sheet at `https://www.zaber.com/products/linear-stages/LRQ-E/specs?travel=75-150`

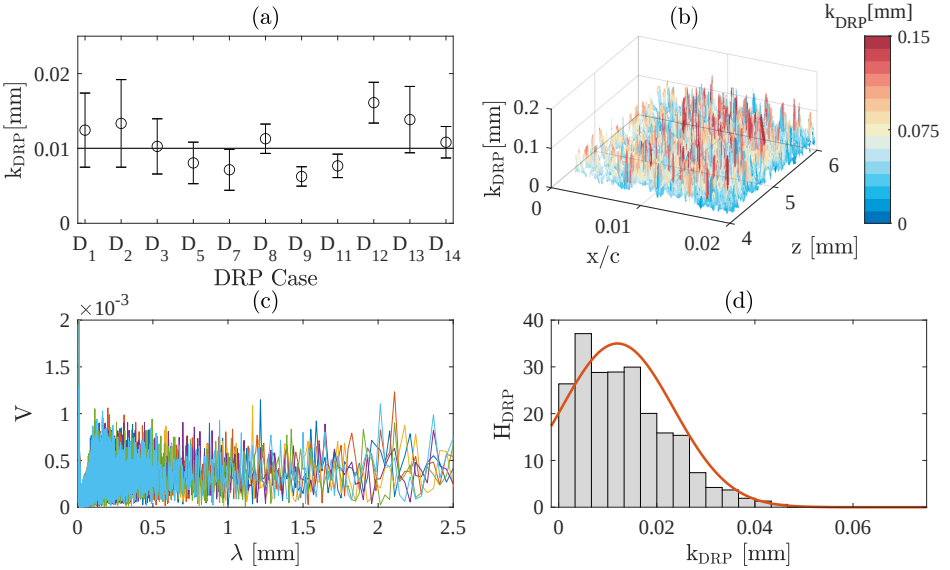

Figure 2.3: (a) Height of various DRP patches (outlined in table 6.1). Reconstruction of a region of a silicon carbide roughness patch (b) from the acquired profilometer data and (d) from the local heights histogram H_{DRP}. Probability density function plot for a normal distribution with a mean of 0.012 and a standard deviation of 0.0114 (red line). Spanwise spatial Fourier analysis of the DRE height distribution (c) at sample chordwise locations. V stands for $FFT_z(k_{DRP})$.

Fast Fourier Transform (FFT) to the acquired spanwise amplitude signal. The spectra extracted at the x/c location corresponding to half of the DRP extent, are reported in figure 2.3(b). The DRP geometrical features are described by a set of spanwise wavelengths distributed within the 0-2λ_1 range, all developing with comparable spectral energy. As such, the DRP patches are expected to excite a set of CFI modes with various spanwise wavelengths distributed within the same range, leading to the development of a BL containing a set of simultaneously developing small wavelengths CFI without resulting in the monochromatic forcing of a single stationary mode [135] . Finally, figure 2.3(d) represents the DRP patch as reconstructed from the local heights histogram. A sample patch applied on the wing surface is also visible in figure 2.4(b). Given the overall repeatability of the DRP geometrical features, the flow field induced by individual patches is mostly independent of the local patch geometry and is further investigated in Chapter 6.

2.2.2. Isolated Discrete Roughness Element (IDRE)

As a first step toward the characterization of the near-element flow topology, an isolated discrete roughness element (IDRE) is investigated. Balancing previous investigations [110, 154] and the desire of ensuring good experimental access to the near-element flow features, an isolated cylindrical element with height k≃0.5mm and nominal diameter d=6mm is positioned at x_{IDRE}/c=0.15. The IDRE is machined

Case	x_{IDRE}/c	k[mm]	D[mm]	D/k	Re_{c_X} ($\times 10^6$)	Re_k	k/δ^*
1	0.15	0.5	6	12	1.27	198	0.83
2	0.15	0.5	6	12	1.35	219	0.85
3	0.15	0.5	6	12	1.45	251	0.90

Table 2.2: Geometric parameters of the measured isolated roughness configurations.

from copper rods having the same diameter d, then polishing the upper and lower circular surfaces to remove imperfections [110]. The IDRE is applied to the wing by using a thin layer of double-sided tape[2] with nominal thickness $\simeq$0.01mm.

The geometry of the chosen IDRE can be related to the BL evolution by Re_k [58, 123], preliminary estimating its influence on the BL transition. Specifically, the critical value of Re_k is found to scale with $(k/d)^{2/5}$, starting from values in the range $Re_{k,crit}$ = 600-900 for an element with k/d=1 [52, 76]. Based on the element k/d ratio, the $Re_{k,crit}$ for the present application ranges between 225 and 335. Hence, three values of Re_k are considered, i.e. Re_{k_1}=251, Re_{k_2}=219 and Re_{k_3}=198, obtained by leaving the element geometry unaltered and decreasing Re_{c_X} (table 2.2). The considered Re_k span super-critical and critical transitional behaviour, as further discussed in Chapter 4.

In addition to Re_k, a second geometrical parameter can be used to orient the different regimes governing the instability growth and breakdown in the considered cases. This is the shear ratio k/δ^*, with δ^* being the local BL displacement thickness at x_{IDRE}/c. This parameter is representative of the characteristic magnitude of the shear of the laminar BL flow impinging on the roughness element. In particular, the shear ratio was found to successfully identify and distinguish the type of instability (i.e. sinuous or varicose [93]) developing in the wake of a cylindrical IDRE in 2D boundary layers [24]. For the configurations considered throughout this work, the k/δ^* is estimated to be 0.9, 0.85 and 0.83 for decreasing Re_k. These values all fall underneath the k/δ^* range at which varicose modes are found to dominate the boundary layer evolution aft of the IDREs in 2D cases (i.e. $k/\delta^* \simeq$1.5-2) [24]. Nonetheless, it must be noted here that the aforementioned critical parameters are widely established for isolated elements in 2D boundary layers. Their applicability in 3D boundary layers, such as the one considered in the present investigation, is not equally established and they are taken here only as preliminary estimates of the governing dynamics.

2.2.3. Discrete Roughness Elements (DRE) Arrays

DRE arrays are the form of roughness of major interest to this work as they are a validated and widespread technique employed to condition CFI. In this investigation, DRE arrays are initially employed to parametrically investigate the BL receptivity to their amplitude and chord location. Successive investigations are instead dedicated to detailing the DRE near-wake evolution and the receptivity process for a chosen subset of configurations. Therefore, throughout the conducted investigations numerous arrays with different amplitude, locations and inter-spacing have been produced and investigated. Hence, an efficient in-house manufacturing procedure has been

developed.

In experimental investigations on CFI, the DRE array is typically chosen to be located in the vicinity of the leading edge [16, 117, 154]. Specifically, for the presently used swept wing model and freestream conditions, past investigations made use of a DRE array with amplitude k≃0.1mm located at $x_{DRE}/c \simeq 0.02$. These forcing conditions establish a nominal downstream development of stationary CFI exhibiting both linear and non-linear growth, saturation, the emergence of secondary high-frequency instabilities and finally laminar breakdown [154]. As such, these forcing conditions are used as a nominal reference case for the present study.

To parametrically investigate the BL receptivity to DRE amplitude and chordwise locations, a suitable parameter range needs to be defined. Specifically, the range of amplitudes (k) and locations (x_{DRE}/c) to be measured, is estimated by using two purely geometrical scaling parameters: the shear ratio k/δ^*, accounting for element amplitude and chordwise location and Re_k, also accounting for the local BL momentum. Nonetheless, the aforementioned characteristic lengths are only used as a first approximation of the relative DRE amplitude as many research studies have clearly shown that the receptivity to roughness is linear only for very small DRE amplitudes, [e.g. 70, 145, 166]. To achieve a comparable DRE-BL scaling up to x/c=0.4 while keeping k/δ^* and Re_k similar to the nominal case, DRE arrays of cylindrical elements with fixed diameter d≃2mm and variable inter-spacing λ and nominal heights between 0.1mm-0.4mm are considered.

The DRE elements are manufactured in-house by CNC laser cutting of a 100μm thickness self-adhesive black PVC foil[5] (figure 2.4(a)). The desired element shape, inter-spacing and number (determining the array length) are designed in a CAD system. For the current application, the overall array length is 60cm, sufficient to guarantee the development of a spanwise invariant BL flow, unaffected by the array end-effects. The final array geometry is then imported in a dedicated software developed by Toolbotics[6], converting it into a GLRS coordinate file. Such file is used to operate the CNC laser cutting machine[7], importing the geometrical coordinates and locally cutting the PVC foil accordingly. The higher elements are obtained by pasting multiple layers of PVC foil on top of each other prior to starting the cutting procedure. At the two ends of the DRE array, two cuts in the shape of a curly bracket are added, allowing for the proper alignment and positioning of the array during its application to the wing surface.

An alternative way of cutting DRE elements is to employ a knife cutter. DRE arrays applied in the last part of this thesis have been obtained by knife cutting a 75μm[8] or 100μm[9] thickness self-adhesive PVC foil using a GCC Jaguar V 61 LX[10]

[5] d-c-fix deco foil. Technical sheet at https://www.plakfolie.nl/a-53045956/decofolie/velours-folie-zwart-45cm-x-p-m/$#$description

[6] Art2gcode: http://www.art2gcode.com/Art2GcodeV1/v1.html

[7] Tooli machine: http://www.art2gcode.com/help.toolbotics.com/Home.html

[8] Kemica self-adhesive vinyl foil. Technical sheet at https://graphic-vinyl.eu/en/3-5years-monomer-matt/71-3101-black-3-5years-old-plotter-vinyl-matt-kemica.html

[9] emica self-adhesive vinyl foil. Technical sheet at https://graphic-vinyl.eu/en/3-5years-monomer-matt/1082-stencil-self-adhesive-plotter-vinyl-white-kemica.html

[10] Jaguar knife cutter: https://www.gccworld.com/download.php?act=view&id=20

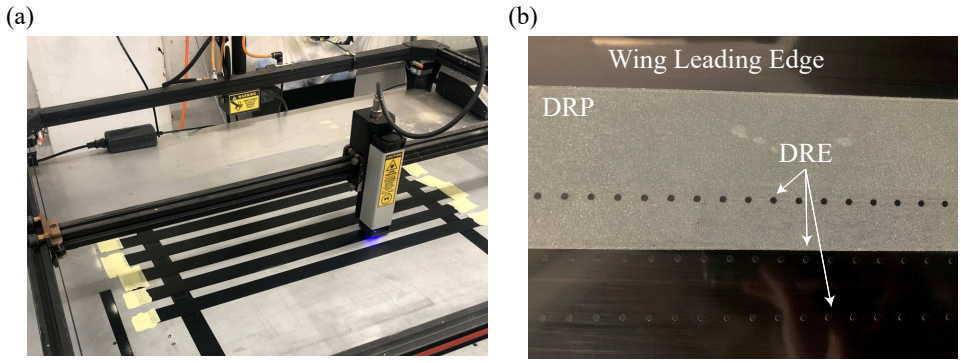

Figure 2.4: (a) Production of multiple DRE arrays by laser cutting black PVC foil using the Toolie machine. (b) Detail of the wing leading edge with spray adhesive DRP and DRE array applied.

knife cutter. The element shape and the array geometry (i.e. wavelength, diameter and number) can be imported into dedicated software, transferring the geometrical coordinates to the cutter. The cutting procedure in this second case is more precise than for the laser-cutting procedure, as it occurs without abrasion of the PVC material along the DRE edges. This provides a smoother cylindrical final shape (as visible in figure 2.5(d) and (e)) while supplying thinner DRE arrays thanks to the reduced foil thickness employed.

Once the cutting procedure is completed, a layer of transfer tape[11] is applied on top of the cut array, to avoid the detachment of the elements, and to preserve them from damage or material deposition. The chosen PVC foils are matt black and feature an adhesive back side covered by a backing throughout the whole cutting procedure. During the application procedure, the array is at first aligned with the desired x/c location (marked on the wing surface), then the backing side of the PVC foil is removed and the elements are gently pressed to adhere to the wing surface (figure 2.4(b)). The adhesive glue of the PVC foil is sufficiently strong to adhere to the wing, yet weak enough to guarantee a simple and fast removal procedure which does not damage the wing surface finishing.

Each DRE is designed to be cylindrical, however, practical limits of the manufacturing process entail slight deviations in their actual shape. This is particularly true for laser-cut DREs. Hence, to fully characterize the investigated roughness elements and ensure the comparability of the two employed manufacturing techniques, a statistical study is performed. A sub-set of 2 arrays of 70 elements per tested height is scanned through a scanCONTROL 30xx precision profilometer[3]. Measurements are both performed in the wind tunnel (with a set-up comparable to that presented in figure 2.2(a, b)) and at bench, as shown by figure 2.2(c). The acquired amplitude signals are processed to characterize the elements' wavelengths, diameters and heights, as shown in figure 2.5. Specifically, the dominant wavelength is established by performing a

[11] Tesa® masking tape, model 4308. Technical sheet at `https://www.tesa.com/nl-be/industrie/tesa-4308.html`

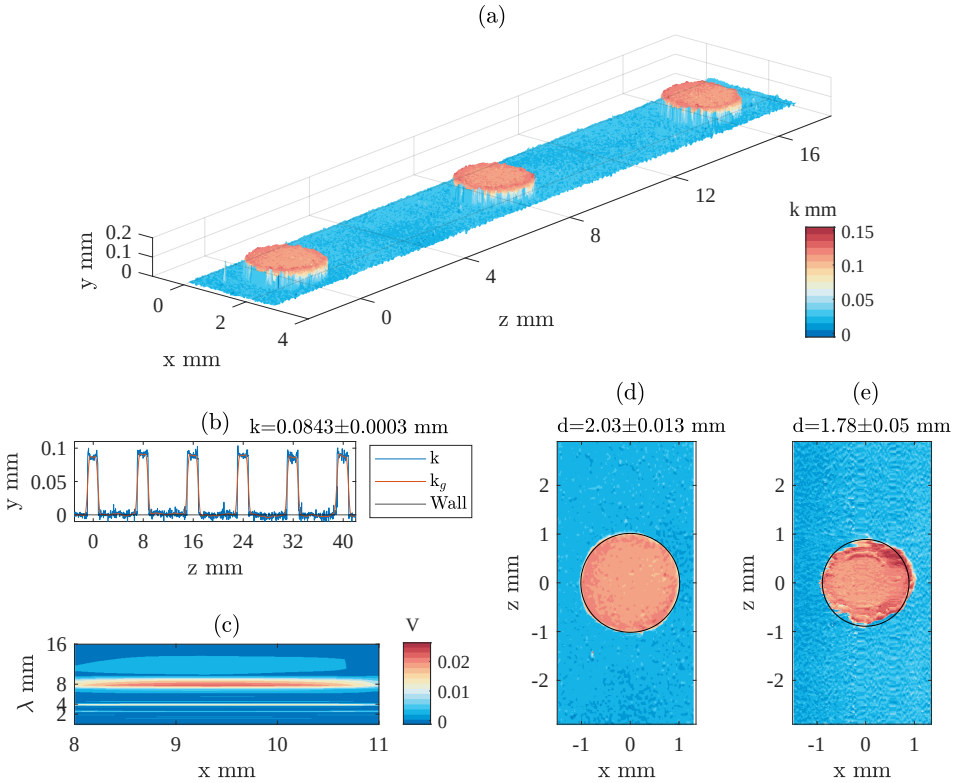

Figure 2.5: (a) Reconstruction of a region of a knife-cut DRE array with nominal height 75μm and diameter 2mm from the acquired profilometer data. (b) Spanwise height signal extracted in correspondence of the array middle point and the corresponding wall extraction. (c) Spanwise Fourier spectra of the DRE array are presented in the x-λ plane. V stands for FFT(k)$_z$. (d) Reconstruction of a single knife-cut DRE in the xz plane and comparison with a 2.03mm diameter circle. (e) Reconstruction of a single laser-cut DRE in the xz plane and comparison with a 1.78mm diameter circle.

spatial fast Fourier transform (FFT) analysis in the spanwise direction. The elements' height is characterized by performing a linear fit of their top surface height and computing its distance from the floor (i.e. the wing surface). Finally, the average diameter and corresponding variations, are computed by fitting a circular shape to the region corresponding to the top surface individual elements, identified given their height excess with respect to the floor. The diameter minimizing the difference between the corresponding circular shape and the considered element surface is chosen as the representative value. The resulting estimations are reported in table 2.3. In the remainder of this work, the four DRE heights obtained by CNC laser cutting are referenced simply as k_1, k_2, k_3 and k_4.

Case	λ [mm]	λ/λ_1	d [mm]	k [mm]	k/d
k_1	8	1	1.772 ± 0.017	0.1147 ± 0.0023	0.083
k_2	8	1	1.732 ± 0.008	0.2179 ± 0.0031	0.126
k_3	8	1	1.767 ± 0.004	0.3292 ± 0.0009	0.186
k_4	8	1	1.721 ± 0.009	0.4374 ± 0.0035	0.261
kk_1	8	1	2.03 ± 0.0013	0.0843 ± 0.0003	0.041
kk_2	8	1	2.07 ± 0.002	0.102 ± 0.0014	0.049

Table 2.3: Geometric parameters of DRE arrays. Laser-cut DRE indicated as k_n, knife-cut DRE indicated as kk_n.

2.3. Measurement Techniques

Throughout this research multiple measurement techniques are employed to acquire the flow features of interest. These are briefly described hereafter, while more complete reviews can be found, for example, in Tropea *et al.* [171].

2.3.1. Infrared (IR) thermography

Infrared (IR) thermographic imaging is a non-intrusive measurement technique capable of acquiring wall surface temperatures by using radiometric sensors, sensitive to the IR radiation emitted by a body. The fundamental aspects of heat radiation theory, technical features of IR cameras and applications in fluid mechanics are reviewed by Astarita & Carlomagno [8].

In low-speed applications as in the present study, the aerodynamic body is actively heated by an external radiation source (i.e. halogen lamps) and simultaneously cooled down by the flow through convection [41, 137, 152]. The M3J wing model is made of polymeric materials, therefore, heat conduction through the model is considered negligible [153]. Moreover, thanks to the M3J thermal inertia with respect to the low speeds involved, the model surface reaches an equilibrium temperature which allows for performing stationary thermography experiments. Specifically, several independent snapshots of wall temperature are averaged in order to lower the uncorrelated sensor noise.

Under equilibrium conditions, the convective heat flux from the wing surface to the flow largely defines the surface temperature distribution detected by the IR imager. Capitalizing on the Reynolds analogy [127], the correspondence between the convective heat flux and flow shear at the wall is ensured. Therefore, the turbulent BL, characterized by higher kinetic energy and wall-shear stress, enhances the surface heat transfer, lowering the surface temperature when compared to laminar BLs at similar conditions. Accordingly, the measured temperature differences allow for the distinction between regions of laminar and turbulent flow, consequently identifying the location of the transition front as well as the modulation of the transitional BL due to the primary stationary CFI development.

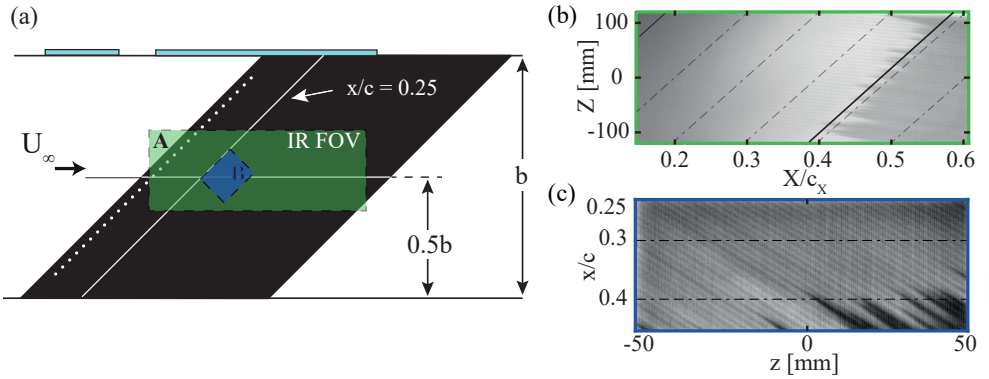

Figure 2.6: (a) Schematic of IR acquisition set-up for the experimental campaigns performed in the present work. A and B rectangles represent the global and zoomed-in fields of view (FOV) of the IR cameras. (b) Sample IR images acquired by global camera view (i.e. A) and (c) zoomed-in camera view (i.e. B). colourscale given by temperature values.

IR Thermography Configuration

During most of the conducted wind tunnel measurements, two Optris PI640 IR cameras[12] are mounted outside of the test section to image the model pressure side through two small openings on the vertical side wall. The cameras acquire the wing surface temperatures at chosen Reynolds numbers (with reference configuration Re_{cX}=2.17 $\times 10^6$) and fixed angle of attack (α=-3.36°) for different forcing configurations. The camera can be equipped with tele-lenses featuring various focal lengths, i.e. f=41.5mm, 18.7mm or 10.5mm, either providing a global overview of the developing flow features or a zoomed-in view in the region of interest, as sketched in figure 2.6(a).

Throughout the experimental measurements described in this work, the camera acquires 80 images at a frequency of 4Hz to perform stationary thermography. Five halogen lamps (3×400W and 2×500W) located outside of the test section are used during IR measurements to irradiate the model and establish sufficient thermal contrast between the warmer laminar BL region and the colder turbulent region. Throughout the presented measurement, the influence of the external model heating on the transition location is considered to be negligible. In fact, the model temperature modifications (T_m) compared to the reference flow temperature (T_f) are described by T_m/T_f, and always lays within the 1-1.04 range that Lemarechal *et al.* [88] identified as non-influential on the BL transition location.

After the acquisition, the IR images are spatially transformed into a wing-fitted domain. The spatial transformation is constructed by imaging a target of fiducial markers aligned to the model surface, introducing the necessary corrections for image distortion and airfoil curvature. Detailed description of the spatial calibration procedure can be found in Rius Vidales [section §2.2.1, 129].

The post-processing of the global IR images is performed through an in-house

[12]The camera has a thermal sensitivity (noise equivalent temperature difference, NETD) of 75 mK, a 640px×480px un-cooled focal plane array (FPA) sensor, sensitive in the 7.5-13μm spectral emission range. Technical sheet at `https://www.optris.global/thermal-imager-optris-pi-640`

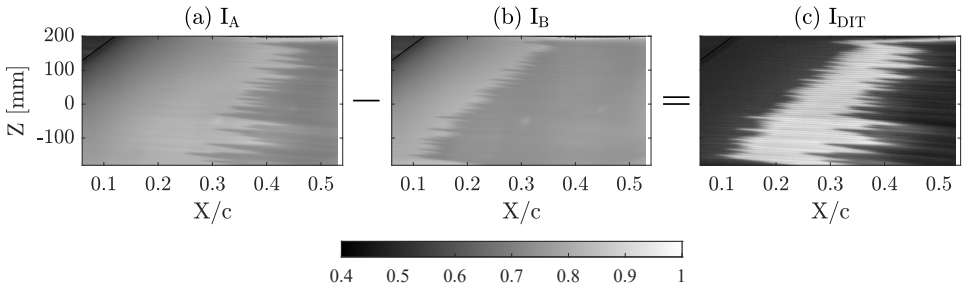

Figure 2.7: Schematic of Differential Infrared Thermography procedure: sample IR image of M3J model acquired in the LTT by global camera view at (a) Re_{c_X}=2.17 $\times 10^6$ (I_A); (a) Re_{c_X}=2.7$\times 10^6$ (I_B). (c) DIT image obtained as I_{DIT}=I_A- I_B.

developed routine based on the Differential Infrared Thermography (DIT, figure 2.7) approach [118, 129, 187]. During acquisition, two IR images are collected for each forcing case: one at the measurement Reynolds number (Re_{c_X}=2.17 $\times 10^6$or other) and the second one at a higher one, Re_{c_X}=2.7$\times 10^6$. Each pair of corresponding time-averaged images I_A and I_B is mutually subtracted to define the differential image, i.e. I_{DIT}=I_A-I_B. This technique minimizes the background noise, improving the image quality and reducing the possibility of identifying spurious transition fronts. Based on the temperature difference between the laminar and turbulent boundary layer flows, a transition front location is detected by identifying the maximum gradient location of the binarized I_{DIT} [129, 130]. A linear fit of the identified spanwise transition locations, controlled through suitable confidence bands (corresponding to 95% in this case), is then performed. A sample global IR image is reported in figure 2.6(b), showing the extracted transition front location as a black line.

Furthermore, capitalizing on the sensitivity of the IR imagers and the stationary nature of the forced primary CFI, a quantification of the spatial and spectral arrangement of the BL can be achieved. Specifically, individual pixel intensities in the zoomed-in IR images (figure 2.6(c)) are sampled and analysed along constant chord lines [129, 130]. The spanwise spatial power spectral density (PSD) analysis of the temperature is performed using Welch's algorithm [129, 152, 179]. Dominant spatial frequencies in the z-direction are then recovered with a resolution of 1.7mm/pixel from the zoomed-in field of view. Associating the PSD values to the corresponding physical wavelengths, the stationary CFI modes dominating the flow can be identified based on their thermal footprint at the model surface. This procedure provides a qualitative representation of the CFI evolution along the wing chord. Nevertheless, due to the non-uniform heating of the surface as well as varying absorption and emission coefficients, quantification of instability amplitudes from wall temperature measurements can be heavily influenced by uncertainties and is not followed.

2.3.2. Hotwire Anemometry (HWA)

HWA is a point-wise measurement technique making use of a hotwire probe of micron size capable of accessing thin BL regions, such as those of interest in this work. The

reduced sensor dimensions minimize the thermal inertia of the wire, improving the spatial measurement resolution if the sensor is coupled with a suitable traversing system. Hence, HWA allows the detection of velocity fluctuations significantly smaller than the mean flow, providing excellent temporal resolution. In this work, the probe is operated by a constant temperature anemometer (CTA) bridge, providing a high amplitude response to very high frequencies, as desirable for the measurement of unstable transitional BL. The CTA operations are based on a Wheatstone bridge with one of the four resistances represented by the hotwire probe. When exposed to the oncoming flow, the hotwire temperature is modified by heat convection fluxes, affecting its resistance and unbalancing the bridge. A feedback mechanism restores the bridge balance, by supplying a different voltage to the circuit, which represents an indirect measurement of the flow velocity. A complete introduction to the HWA measurement technique and its application in different fluids is reported by Bruun [21] and Lomas [94].

To correctly associate the voltage modifications to physical velocity measurements, a calibration procedure matching bridge voltages to known flow velocities is required. Multiple calibration points are acquired and are then fitted by a fourth-order polynomial approximating King's law [21]. Despite the overall stability of the tunnel flow conditions, during the measurements performed in this work the flow temperature and pressure are continuously monitored through dedicated sensors. In this way, the small changes occurring during the calibration/acquisition run are accounted for, suitably correcting the acquired HWA signal [68].

HWA is a single-point measurement technique, hence multiple acquisitions are required to characterize the flow features in a complete 2D plane. Accordingly, from sole HWA measurements, it is not possible to infer the spatio/temporal correlation of the measured flow structures or to discern the different velocity components and their direction, which can be problematic when flow reversal occurs.

HWA Configuration

HWA is employed in this work to collect local and temporal information on the near-element flow fields of a near-critical IDRE. Measurements are performed by operating a single-wire Dantec Dynamics 55P15 boundary layer probe[13] through a TSI IFA-300 CTA bridge[14] featuring automatic overheat ratio adjustment. An automated traverse system mounted in the wind tunnel diffuser holds the sensor (sketched in figure 2.8), granting the motion in the three XYZ directions with a nominal step resolution of 2.5μm in all axes.

The hotwire acquisitions are performed in the yz plane at different chord locations, mostly concentrated in the vicinity of the IDRE (as indicated by the red spanwise lines of figure 2.8(a)). An ensemble of HWA scans collected in the spanwise and wall-normal directions (i.e. in the yz plane) build up each x/c plane. Every wall-normal velocity profile is measured by acquiring 30 equally-spaced point-wise measurements along y. At each point, the CTA bridge signals are sampled for 2s at a frequency

[13]Technical sheet at `https://www.dantecdynamics.com/product/miniature-wire-probe-boundary-layer/`

[14]Technical sheet at `https://tsi.com/product-components/ifa-300-constant-temperature-anemometer-183151/`

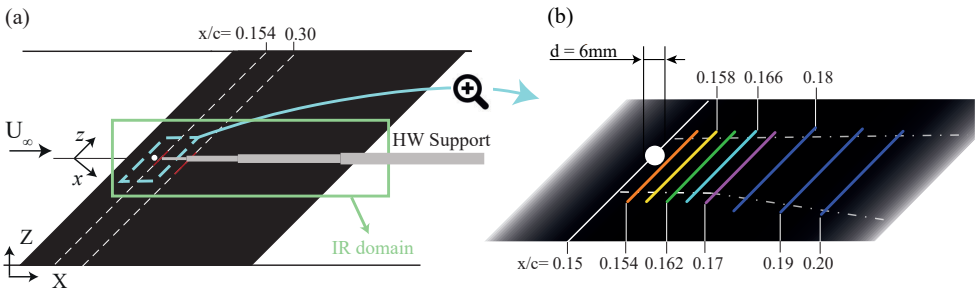

Figure 2.8: (a) Sketch of HWA experimental set-up and coordinate reference systems (not to scale). Y-axis and y-axis are directed towards the reader, HWA measurement domain (light blue rectangle), IR measurement domain (green rectangle). (b) Zoomed-in sketch of HWA acquisition yz planes in the element vicinity (dashed blue region in (a)).

of f_s ≃51.2kHz and filtered through an analog lowpass filter (cutoff frequency of 20kHz) before amplification. To account for the BL growth along the wing chord, the wall-normal spacing of the point-wise measurements is adjusted to capture the whole boundary layer evolution from the near-wall region (≃20%$\mathbf{U}_\infty$) to the local freestream. Accordingly, for the near-element planes (i.e. x/c=0.158, 0.162, 0.166, 0.170, figure 2.8(b)) the final y-spacing is set to 0.1mm, while for the more downstream planes (i.e. x/c=0.18, 0.19, 0.20, 0.25, 0.3, figure 2.8(b)) it is changed to 0.15mm. Once the acquisition of a BL profile is completed, the probe moves to the following spanwise location, repeating the measurement procedure until the set number of BL scans is acquired for the considered yz plane. Figure 2.9(a, b) show the hotwire in the vicinity of the wing surface as seen from a telescope imaging the XZ plane (figure 2.9(a)) or imaging the zy plane (figure 2.9(b) showing an equivalent set-up for measurements of the near-DRE flow fields).

The preliminary analysis of the acquired IR images provides an estimation of the relevant flow features and their spatial location and chordwise development with respect to the freestream direction. Consequently, the origin and span-wise extent of the HWA acquisition in the yz plane can be adjusted at each x/c of interest to follow the evolution of specific flow features along the chord. Specifically, in the current investigation for the near-element planes, the span-wise spatial resolution is kept constant at 0.5mm providing a 30mm spanwise extent, while for the downstream chord locations considered it is doubled in order to accommodate the spreading of the developing turbulent wedge. A Xz HWA plane is also acquired at a fixed wall distance of y=1mm. In this case, the velocity scans are composed of single-point acquisitions collected along the spanwise direction (z) with a spacing of 1mm. Successive spanwise scans are measured at a chordwise distance (i.e. in the X direction) of 1.2mm.

For the entirety of the performed measurements, the hotwire probe is aligned to the Z direction, therefore at each point, the velocity signal acquired by the sensor is a projection of the instantaneous wing-attached velocity components which can be reconstructed as

$$U(y,z) = \sqrt{(u \times cos(45°)^2 + (w \times sin(45°))^2 + (v)^2}. \tag{2.1}$$

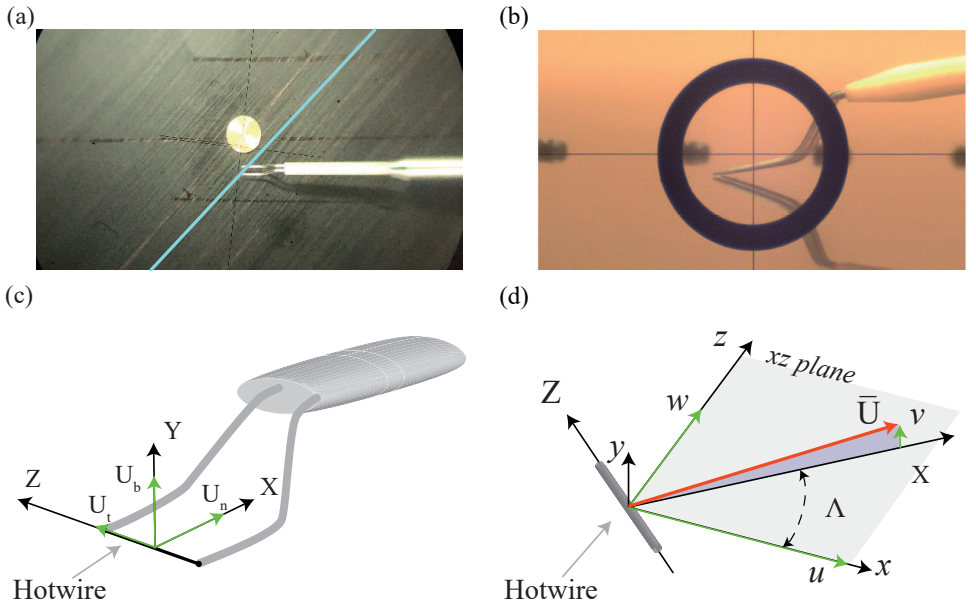

Figure 2.9: (a, b) Zoomed-in image of hotwire sensor in the wing surface vicinity as measuring the IDRE near-wake in a yz plane (light blue line). Image capturing the hotwire in (a) the XZ plane for near-IDRE acquisitions, and (b) the yz plane for acquisitions in the vicinity of a DRE array (not reported in this thesis). (c, d) Schematic of hotwire probe orientation (adapted from [129]): (c) Probe velocity decomposition into tangential (U_t), normal (U_n) and binormal (U_B) to the wire sensor. (b) Orientation of the measured velocity component $\overline{U}$ with respect to the wing-fixed reference system xyz.

The arrangement of the measured velocity components with respect to the known reference systems is sketched in figure 2.9(c, d). The main parameters of the performed HWA acquisitions are summarized in table 2.4, while the obtained results are thoroughly discussed in Chapter 4.

2.3.3. Planar Particle Image and Particle Tracking Velocimetry (PIV and PTV)

Particle Image Velocimetry (PIV, Raffel *et al.* [119]) and Particle Tracking Velocimetry (PTV, Dabiri & Pecora [40]) are non-intrusive optical techniques based on flow imaging. Both techniques measure the displacement of small tracer particles introduced and carried by the investigated fluid during a short time interval. In planar applications, the region of interest of the flow field is illuminated through a thin light sheet (usually $\simeq$1mm) typically generated by a green pulsed laser system. At each representative time instant, the light scattered by the tracer particles is captured as high-intensity pixels (figure 2.10(c)). In *double frame* measurements the laser system emits two successive pulses separated by a time difference Δt, chosen to be smaller than the relevant flow time scales. Accordingly, two subsequent image frames are acquired by a digital imaging device, providing information over a relatively wide flow domain thanks

Parameter	Near-IDRE	Far-IDRE	Wall-parallel
Acquired domain	yz Plane	yz Plane	Xz Plane
Acquired x/c range	0.152-0.17	0.18-0.3	0.152-0.22
Field of view [mm]	3×30	4.5×60	60×80
y vector pitch [mm]	0.1	0.15	-
x vector pitch [mm]	0.5	1	1.2
Sampling rate (f_s) [kHz]	51.2	51.2	51.2
Measured interval (Δt) [s]	2	2	2
Uncertainty [% local speed]	0.1	0.13	0.11

Table 2.4: Parameters of experimental HWA acquisitions

to the high light intensity available. Throughout this thesis, PIV/PTV acquisitions are performed with low-sampling frequency, acquiring image pairs that are not temporally correlated but provide time-averaged flow fields.

Spatial calibration of the acquired domain is performed by imaging a planar template bearing markers of pre-defined shape and size (figure 2.10(b)). These are mapped on a Cartesian grid, providing spatial mapping functions that associate the particle location within the image space to the corresponding positions in the physical space.

Within the PIV framework, to extract the corresponding velocity vector field, coupled image frames are divided into sub-domains called interrogation windows (IW). The light intensity signal of the corresponding IW in coupled frames is processed through a sliding cross-correlation algorithm. The average displacement of the tracer particles within the considered IW corresponds to the in-plane displacement (Δx, Δy) maximizing the cross-correlation coefficient. Given the knowledge of the time interval between the two frames (i.e. the chosen Δt) and the optical parameters (retrieved through the spatial calibration and mapping of the imaged field), the velocity vector corresponding to the obtained average displacement is computed. Repeating this process for the remaining IW, a complete 2D velocity vector field within the plane illuminated by the light sheet is obtained. Multi-pass, multi-size cross-correlation algorithms can be employed to enhance the PIV cross-correlation procedure spatial resolution [139].

An alternative way to improve the measurements' spatial resolution, especially in the wall vicinity, is to employ dual-pulse PTV for the velocity field reconstruction. Typically, PTV performs better for the reconstruction of flows featuring strong velocity gradients (such as BL flows, shear flows or wake flows [85]), as it is not based on spatial averaging but on the identification and the tracking of individual tracer particles. Specifically, PTV reconstruction capitalizes on three main steps: identification of the tracer particles in the acquired image, their localization within the physical domain, and tracking of their displacement in successive image frames. Particle identification is performed by determining which group of pixels constitutes a particle based on the intensity levels of the image [111]. To avoid excessive particle overlapping, when performing PTV acquisitions the tracer particle density can be reduced almost by

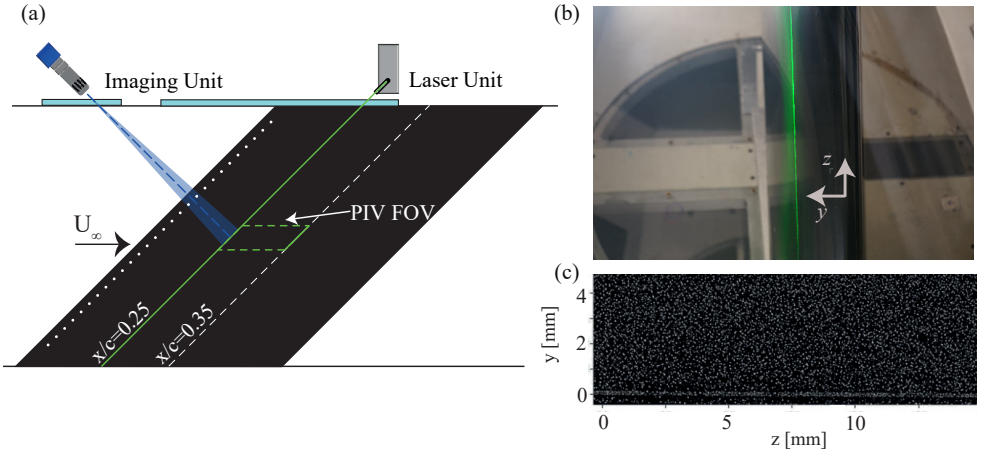

Figure 2.10: (a) Schematic of the planar PIV/PTV experimental set-up. (b) Image of the laser sheet wall-normal extension in the wind tunnel. (c) Sample images acquired through PIV, colourscale based on scattered light intensity: high-intensity pixels are given by the light scattering of tracer particles, horizontal higher intensity region at y=0 represents the wing surface (i.e. the domain wall).

a factor of 10 if compared to PIV acquisitions [37, 40]. Particle localization is then based on triangulation, building upon the spatial mapping functions provided by the geometrical calibration. Finally, a relaxation method [113, 134, 189] is employed to identify paired particles in the coupled frames and to compute the corresponding particle displacement. Given that the time interval between frames is known (i.e. Δt), the velocity vectors associated with each particle can be defined. The obtained velocity values are then converted to a traditional Cartesian grid by applying a *binning* procedure.

Planar PIV Configuration

Throughout this work, planar PIV is used to locally acquire the flow features in the yz plane, i.e. extending along the wall-normal and spanwise direction. The acquired BL flow is described by $\overline{w}$ and $\overline{v}$, time-averaged velocity components in the spanwise and wall-normal direction respectively. The planar PIV set-up is sketched in figure 2.10(a, b), also showing the laser sheet illuminating the yz plane. The main parameters of the PIV set-up are instead reported in table 2.5.

The laser and cameras are mounted on an automated traversing system[4] located on top of the test section (sketched in figure 2.10(a)), granting unison shifts with a step accuracy of 15μm. Optical access to the model is gained through a plexiglass window cut in the upper wall of the wind tunnel test section. The laser unit is a Quantel Evergreen Nd:YAG dual cavity laser[15], whose beam is manipulated through spherical and cylindrical lenses in a sheet aligned to the yz plane, thus inclined at 45° to the freestream direction. To capture a statistically significant number of stationary CFI

[15]The laser provides 200 mJ pulse energy at λ=532 nm. Technical sheet at `https://www.quantel-laser.com/en/products/item/evergreen-70-200-mj-.html`

Parameter	Planar PIV	Planar PTV	Tomo PTV
Acquired domain	yz Plane	yz Plane	xyz Volume
Field of view [mm]	3.8×40	2.7×32	30×3.8×30
Vector pitch [mm]	0.05	0.11	0.25×0.04×0.25
Magnification factor	0.45	0.47	0.41
Focal length [mm]	800	400	400
Numerical aperture ($f_\#$)	8	8	11
Spatial resolution [px/mm]	126	73	67
Sampling rate (f_s) [Hz]	15	10	10
Frame separation (Δt) [μs]	5	15	8
Freestream displacement [px]	12	18	10
Number of samples	1000	2000	4000
Acquired x/c range	0.25-0.36	0.15-0.35	0.15-0.176
Uncertainty [% local speed]	1	1.5	1.8
Seeding	$\simeq$0.5μm droplets of water-glycol mixture		

Table 2.5: Parameters of experimental PIV and PTV acquisitions

vortices, two LaVision Imager cameras[16] are arranged in a side-by-side orientation. To compensate for the large working distance between the cameras and the imaging plane ($\simeq$ 1.4m), the cameras are equipped with a 200mm lens and two 2× teleconverters. The optical arrangement results in an 800mm focal lens and numerical aperture $f_\#$=8, leading to a magnification ratio of 0.49 and a spatial resolution of 126px/mm. The boundary layer flow is resolved up to the wall vicinity, where $\overline{w}/W_\infty$=3.5% with W_∞ being the spanwise freestream velocity.

The traversing system allows for shifting the imaging plane to different chord locations while maintaining the alignment and focus of the cameras and the laser. With this configuration, planes between 25 and 36% of the chord are collected with an inter-spacing of 1% of the chord and a laser thickness of approximately 1mm. Flow seeding is obtained by dispersing $\simeq$0.5μm droplets of a water-glycol mixture in the wind tunnel through a SAFEX fog generator.

For each plane, 1000 image pairs are acquired at a frequency of 15Hz and time interval of 5μs, corresponding to a freestream particle displacement of almost 11 pixels. Each image pair is processed in LaVision Davis 10 through a multi-pass cross-correlation algorithm with a final interrogation window of 12px×12px and 50% overlap, resulting in a final vector spacing of approximately 47μm. The correlated velocity fields are then averaged and stitched through a Matlab routine delivering the time-averaged velocity components and identifying the wall location as the maximum light reflection region in the raw particle images (i.e. figure 2.10(c)). The results of planar PIV acquisitions are thoroughly discussed in Chapter 3.

[16] LaVision sCMOS camera, 2560×2160px, 16-bit, 6.5μm pixel pitch. Technical sheet at `https://www.lavision.de/en/products/cameras/cameras-for-piv/`

Planar Dual-pulse PTV Configuration

In this research, planar PTV flow fields are acquired with a set-up comparable to that of the previously described PIV acquisitions (figure 2.10(a, b)). In this configuration, however, only one LaVision Imager camera[16] equipped with a 200mm lens and a single 2× teleconverter images the flow field. This optical arrangement (summarised in table 2.5) results in a 400mm focal lens with numerical aperture $f_{\#}$=8, corresponding to a magnification ratio of 0.47 and a resolution of ≃73px/mm. The BL is resolved up to the wall vicinity, where $\overline{w}/\mathrm{W}_{\infty}$=0.1%.

Velocity fields are acquired between 15% and 35% of the chord. For each plane, 2000 image pairs are acquired at a frequency of 10Hz and time interval between pairs of 15μs, corresponding to a freestream particle displacement of ≃18 pixels. This higher freestream displacement allows for the detailed characterization of the velocity fields within the slow-moving BL flow region. Each image pair is processed in LaVision Davis 10 through a double-frame PTV algorithm, also performing binning and conversion to a Cartesian grid of the obtained velocity vectors. The final window size is 8×8pixels corresponding to a vector spacing of approximately 0.11mm along the y and z directions. The wall location is again identified through an in-house developed MATLAB routine as the maximum light reflection region in the raw particle images. The results of planar PTV acquisitions are thoroughly discussed in Chapter 6.

2.3.4. Tomographic Dual-pulse PTV (3D-PTV)

Tomographic PIV (Elsinga *et al.* [51]) or PTV (Dabiri & Pecora [40]) techniques represent an extension of the previously discussed PIV/PTV framework, providing a complete 3D vector field within a volumetric flow region. Tomographic configurations require volumetric illumination, typically provided by a green laser light source expanding its laser beam using spherical lenses. For the correct identification of the tracer particles' location within the acquired physical volume (i.e. triangulation), a minimum of three imaging cameras is necessary. These all image the same field of view albeit from different (non-orthogonal) angles. Scheimpflug adapters [31, 142] are employed to ensure that all camera lenses are focused on the desired plane.

In the current investigation tomographic dual-pulse, time-averaged PTV is employed [101, 140, 174], given its higher spatial resolution in the wall vicinity and shorter processing time than a corresponding tomographic PIV. As for the planar configuration, tomographic PTV is based on the identification, localization and tracking of individual tracer particles, performed by using dual-pulse shake-the-box (STB, [140]) algorithms.

An accurate volumetric calibration procedure is a fundamental starting point to minimize error sources and properly reconstruct particles and velocity vectors. This is based on a geometrical calibration, performed by imaging a dual layer calibration target (figure 2.11(b)) and combining the views of each camera to define the spatial mapping functions. A volumetric self-calibration procedure (VSC, [185]) is then initiated, acquiring a set of sample images representative of the tracer particles' light scattering (figure 2.11(c)). Using iterative particle reconstruction methods (IPR, [174]), individual tracer particles are iteratively identified and triangulated, progressively correcting the spatial mapping functions. The final calibration step

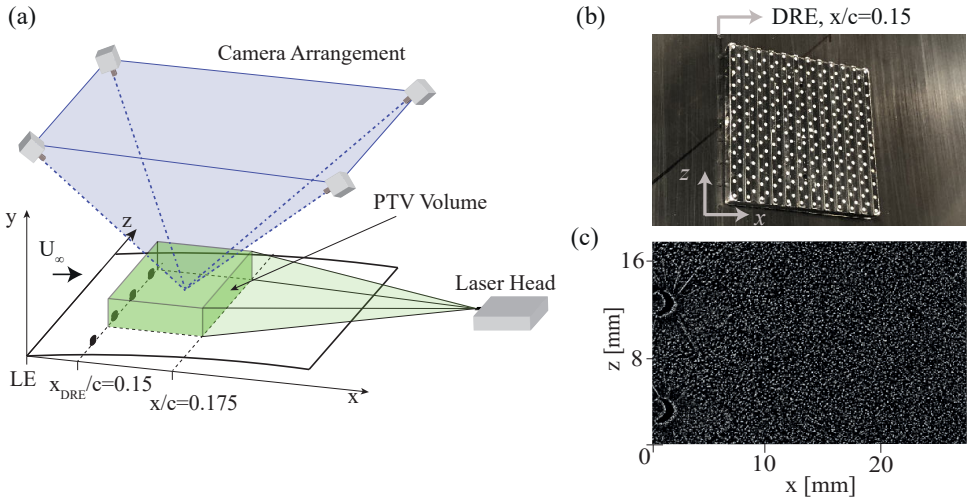

Figure 2.11: (a) Sketch of tomographic PTV experimental set-up and acquired volumetric domain (thin green volume at the wing surface). (b) Image of geometrical calibration dual layer target. (c) Sample image acquired through tomographic set-up, colourscale based on scattered light intensity, DRE visible in the leftmost part of the image as high scatter regions.

defines non-uniform (i.e. local) optical transfer functions (OTF, [141]). These describe a localized correction for distorted particle shapes in the acquired images, improving the particle identification and reconstruction capabilities.

Once the calibration procedure is completed, coupled frames can be processed based on the dual-pulse STB method [140]. This is an iterative process identifying and triangulating individual particles in each camera acquisition based on IPR, then iteratively performing particle paring through the *shaking* procedure. Specifically, each identified particle is shifted from the known triangulated location (x,y,z) to a new (x′,y′,z′) position, defining a projected image. This projected image is subtracted from the actual camera image, delivering a residual image. Particles are iteratively shaken within the acquired space to identify the best matching position, i.e. the one minimizing the residual image intensities. Hence, the result of STB procedures is a series of particle locations within the spatial 3D volume, defined over the time interval separating the two acquired frames. Given that the time interval between frames is known (i.e. Δt), the velocity vector associated with each particle can be computed. The obtained velocity vectors are then projected to the calibrated spatial geometrical volume by applying a *binning* procedure [2].

Tomographic Dual-pulse 3D-PTV Configuration

In the application discussed in Chapter 5 of this thesis, 3D dual-pulse PTV is used to measure the tomographic velocity field in the vicinity of a DRE array. The measured 3D domain extends in the xyz volume, as sketched in figure 2.11(a). The 3D measurement volume is illuminated with the Quantel Evergreen laser[15], optically accessing the test section through a plexiglass window cut on the test section floor

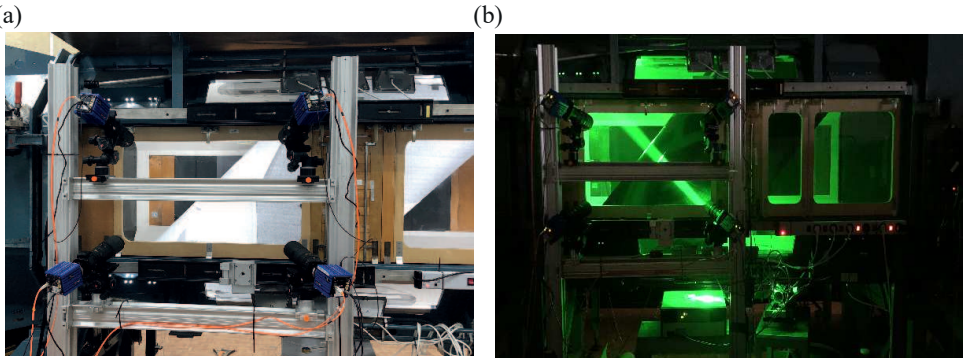

Figure 2.12: Image of tomographic PTV wind tunnel set-up (a) for the 4 LaVision cameras and (b) for a laser pulse.

(figure 2.12(b)). Through a suitable optical arrangement, the laser beam is shaped in a 40mm wide sheet and is expanded to a thickness of almost 4mm, illuminating a flow region parallel to the wing surface in the volume of interest (figure 2.11(a)). The flow is imaged through 4 LaVision Imager cameras[16], installed on the outer side of the test section with a tomographic aperture of approximately 45° (figure 2.12(a)). Each camera is equipped with a 200mm lens, a 2× teleconverter and a lens-tilt mechanism adjusted to comply with the Scheimpflug condition. The resulting focal length is 400mm for each camera, featuring an aperture of $f_{\#}$=11 to keep the particles in focus throughout the entire volume depth. The distance between the model surface and the optical plane is ≃1m, resulting in a magnification factor of ≃0.41 and spatial resolution of 67px/mm. The flow is seeded by dispersing 0.5μm droplets of a water-glycol mixture in the wind tunnel circuit.

For each investigated configuration, 4000 image pairs are acquired at a frequency of 10Hz. The time interval between paired images is set to 8μs, corresponding to a freestream particle displacement of almost 10px. The presented calibration procedure is applied, resulting in a calibration uncertainty of ≃0.04 px. The image pairs are processed in LaVision DaVis 10 using dual-pulse STB, while an in-house developed Matlab routine is employed to perform trajectory binning and conversion to a Cartesian grid. The final vector spacing results in approximately 0.25mm in the xz plane, and 0.04mm along the y-direction. The results of tomographic PTV acquisitions are thoroughly discussed in Chapter 5.

2.3.5. Measurements Uncertainty Quantification

Measurement uncertainty affects both HWA and PIV/PTV experiments performed in this work. Uncertainties in the acquired dataset derive from the combination of systematic and random errors. Systematic errors are typically corrected through calibration procedures, while random errors are unknown in magnitude and sign. In the case of HWA random errors can be related to probe disturbances, velocity calibration, signal interpretation in high-turbulence intensity regions, and reversed flow ambiguity. In PIV or PTV measurements, random errors can be caused by

misalignment and erroneous synchronization of the camera-light system, camera noise, out-of-plane motion of tracer particles or uneven illumination of the domain of interest. Additionally, the main source of random errors for PTV acquisitions is associated with a low signal-to-noise ratio of the images and overlapping particle images. The basis of the uncertainty quantification methods employed in this work are briefly described hereafter, while Bruun [21], Raffel *et al.* [119], Dabiri & Pecora [40] offer thorough reviews for HWA, PIV and PTV uncertainty estimation respectively.

The uncertainty of HWA measurements is estimated following the methods proposed by Sciacchitano [149]. Specifically, considering an acquisition composed of N_s uncorrelated samples, the measurement uncertainty is defined both for the signal (i.e. velocity) mean value ($\overline{U}$, equation 2.2) and for the signal (i.e. velocity) standard deviation (σ_u, equation 2.3) respectively as:

$$u_{\overline{U}} = \frac{\sigma_u}{\sqrt{N_s}}, \tag{2.2}$$

$$u_{\sigma_u} = \frac{\sigma_u}{\sqrt{2(N_s - 1)}} \tag{2.3}$$

The acquisition frequency for HWA data is f_s=51.2kHz, hence the high sample frequency leads to measurement which can be correlated in time. Therefore, the number of uncorrelated samples can be defined based on the integral time scale T_I, that following Smith *et al.* [158] is obtained from the autocorrelation of the measurement series. N_s is then computed as $N_s = N_T/(2T_I/\Delta\mathrm{t})$ where Δt is the sampling interval. For the HWA measurements presented in this work, the uncertainty estimation results in an averaged BL value of $u_{\overline{U}}$=0.1% and u_{σ_u}=0.07% of the local speed.

In PIV acquisitions the measurement uncertainty can be locally computed, defining an uncertainty value within each interrogation window. Among the variety of methods available for PIV uncertainty quantification [150] this work applies the correlation statistics method [186], based on the definition of residual intensity differences between each pair of interrogation windows. Specifically, given the mild differences in the intensity of each frame, the correlation of corresponding IW delivers an asymmetric peak shape. The contribution of individual pixels to the peak asymmetry is estimated and associated with a standard deviation value representative of the local uncertainty. For the planar PIV measurements reported in this booklet, this estimate results in an average uncertainty of 1% of the local velocity in the BL region.

The local estimate of PTV measurements uncertainty is, instead, computed along each extracted particle track by applying linear regression analysis tools and an adaptive filtering approach [71]. For the present case, in the BL region, $u_{\overline{U}}$ averages 1.5% of the local velocity for the planar configuration and 1.8% of the local velocity for the tomographic configuration.

Further discussion regarding the propagation of the uncertainty errors is reported by Sciacchitano *et al.* [150], and is applied to acquisitions performed in this work as described in Chapter 3 (section §3.3.3).

2.4. Boundary Layer Stability Solutions

The experimental measurements presented in this work are complemented by a numerical BL flow and the corresponding stability solution computed through in-house developed routines [152, 180]. BL stability is computed for a reference base flow which is a steady and incompressible solution of the 2.5D boundary layer equations (i.e. applying spanwise invariance assumptions). The followed procedure is fully described by Serpieri [152], and is based on the experimentally acquired freestream flow characteristics and pressure distribution. Specifically, these allow for the estimation of the Re_{c_X}, angle of attack, freestream and external BL velocities. The assumption of spanwise invariance of the flow allows for decoupling the z-momentum equation [100, 154, 166]. Hence the BL solution is computed in the leading-edge orthogonal reference system (x,y,z), discretizing the differential equations with second-order finite differences along x and with spectral elements (Chebyshev collocation method [178]) along the wall-normal direction.

2.4.1. Linear and Non-Linear Parabolized Stability Equations

The stability of the numerically computed BL is then solved both within a linear [61, 156] and non-linear PSE (parabolised stability equations) framework [15, 66]. PSE has been widely applied to analyse the stability of 3D boundary layers developing on swept wings [14, 62, 166]. The main principles of the in-house stability solver are briefly described hereafter, while a complete treatment is reported in Westerbeek [180].

The LPSE analysis is used to facilitate the experiment design, by identifying the wavelength of the most unstable stationary CFI modes and their spatial region of growth. The stability solution is initialized by using a local eigenvalue solution of the perturbation equations (given by local stability theory ILST, [98]), and is then computed for a series of stationary modes with given spanwise wavelengths λ and angular frequency ω=0. The streamwise wavenumber α is complex with the imaginary part describing the mode growth, while the spanwise wavenumber $\beta = 2\pi/\lambda$ is real. The spatial growth rate (i.e imaginary part of α) is corrected for the residual growth in the spanwise component of the PSE shape function, to enable reliable comparison to the experimental measurements [62, 65].

The amplification N-factor of a mode is defined by integrating the corrected spatial growth rate α_i along the wing surface not accounting for curvature effects. The N-factor evolution computed for a set of wavelengths (figure 2.13(a)), shows that the λ=λ_1=8mm mode corresponds to the most amplified mode, as also observed by previous experiments at similar conditions [131, 154]. Additionally, the variations of Re_{c_X} investigated in this work lay within the range of 1.35-2.17$\times 10^6$, only mildly affecting the spanwise wavelength associated with the most critical CFI mode. Specifically, the most unstable wavelength varies between 10mm and 7mm for the lower and higher Re_{c_X} investigated respectively (figure 2.13(a)). Hence, in all configurations considered in this thesis the λ_1=8mm is either the most unstable mode or among the most unstable modes, especially in the chordwise region where DRE arrays are applied. Based on these preliminary predictions, the critical array elements' inter-spacing is

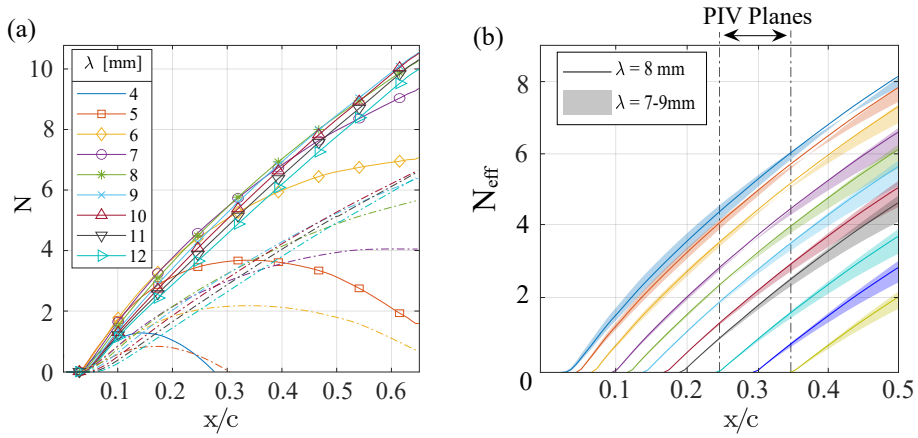

Figure 2.13: (a) N-factor curves evolution in the chordwise direction for a set of stationary modes with wavelengths λ=4-12mm from LPSE solution for the experimental reference flow α=-3.36° and Re_{c_X}=2.17 $\times 10^6$ (solid lines) and for α=-3.36° and Re_{c_X}=1.35$\times 10^6$ (dash-dot lines). (c) N_{eff} curves for λ=8mm mode from LPSE solution initialized at different chordwise stations. Shaded regions describe λ interval between 7 and 9mm.

chosen to coincide with the most unstable wavelength λ_1. Moreover, within the linear approximation this mode continuously grows between its onset at x/c≃0.03 and x/c=0.65 providing a first estimate for the range of DRE locations investigated in this study (as further discussed in Chapter 3).

An additional important parameter in receptivity studies is the local pressure gradient at the forcing (i.e. receptivity) location. While it is unrealistic to fully control the value of the pressure gradient on a wing geometry, during this study as little chordwise variations as possible are desired. Moreover, by conducting PSE simulations initialized at the various DRE locations used in the experiments, the effect of the local pressure gradient can be accounted for in the predicted growth curves. In each solution, the individual mode amplitude can be described as $A_w(\overline{x}) = A_0\ e^{N(\overline{x})}$ with A_0 being a representative initial disturbance amplitude. In the remainder of this work, the N-factor is computed relative to an initial amplitude A_0 estimated at the DRE array location, following the effective N-factor (N_{eff}) definition by Saric *et al.* [138]. The results reported in figure 2.13(b) confirm that the λ_1=8mm mode is either the dominant one or among the most unstable ones in all considered cases. Furthermore, the overall trend and value of the N-factor curves suggest that the local pressure gradient is only mildly influencing the stability of the boundary layer, justifying the direct comparison among the measured configurations. Nonetheless, the more relevant variations of the pressure gradient observed in the vicinity of the leading edge (i.e. x/c<0.15, figure 2.1(b)) may affect the near-DRE wake development, which is not modelled by the numerical solver.

While the LPSE serves as an efficient tool for the prediction of the most unstable mode, the limitations of linear theory prevent the estimation of the later stages of instability growth. This is particularly evident in the case of stationary CFI,

which produce strong non-linear effects through their inductive action on the laminar base flow. To account for these effects, a full NPSE solution for the stationary CFI is computed for a subset of the measured forcing configuration, estimating the instability amplitudes and shape functions from the DRE location to x/c=0.36. Each solution computes the development of the dominant mode λ_1, 6 stationary harmonics (λ_i=λ_1/i), and the mean flow distortion. The solution is initialized with the base flow and λ_1 mode only, while higher harmonics are automatically generated via non-linear forcing as their expected normalised amplitude exceeds the threshold of 10^{-9}. Additionally, preliminary tests have shown that both phase and amplitude of initialization of higher harmonics at the DRE location have a negligible effect on the overall stability solution. The comparison between NPSE results and experimental measurements is detailed in Chapter 3.

3

Receptivity of Stationary CFI to DRE Amplitude and Location

The effect of DRE arrays on the development and breakdown of stationary CFI on a swept wing is explored. Receptivity to various forcing configurations, designed based on linear stability predictions, is investigated using a combination of experimental and numerical tools. The scalability of the flow dynamics to DRE amplitude and chord location is analysed, offering preliminary insights in the near-DRE flow dynamics.

ZOPPINI, G., WESTERBEK S., RAGNI, D., & KOTSONIS, M. 2022. Receptivity of crossflow instability to discrete roughness amplitude and location. *Journal of Fluid Mechanics.* [199]

ZOPPINI, G., RAGNI, D., & KOTSONIS, M. 2022. Experimental investigation on receptivity of crossflow instabilities to discrete roughness amplitude and location. *AIAA SCITECH 2021 Forum.* [195]

3.1. Introduction

One of the most challenging aspects in the investigation of stationary CFI is the characterization of their receptivity process [107]. Despite the large body of experimental receptivity studies conducted to date, an estimation of the CFI initial amplitudes ensuing from receptivity to T_u and roughness is still missing. This aspect is treated in the literature background reported in Chapter 1, indicating that the investigation of the near-DRE flow development is necessary to gain further insights regarding the very initial phases of receptivity. As discussed in section §1.5, up to date only a few DNS investigations detail the near-DRE flow features and their dominant instability mechanisms in a 3D boundary layer scenario [23, 84]. These provide a significant breakthrough in the investigation of near-DRE flow, however, they do not yet define a clear correlation between the external disturbances and the initial amplitude of the ensuing CFI.

The survey of past experimental and numerical works on the receptivity of CFI reveals two unresolved challenges which have motivated and shaped the investigation presented in this Chapter. The first is an incomplete understanding of the relation between roughness amplitude and location and the development of CFI and BL transition. Past investigations focused either on global transition location correlations or localized measurements, typically using HWA under limited parameter ranges. Additionally, past studies made use of simplified metrics for the representation of the initial forcing amplitude such as the height-based Reynolds number ($\mathrm{Re_k}$) or the shear ratio (k/δ^*). However, these metrics are often used only as an indication of the super-critical behaviour (i.e. flow tripping) of a forcing configuration, while it is still unclear whether they can correctly represent the initial forcing amplitude of DRE [82, 84, 123]. The present study aims to combine local and global transition and flow measurements to better understand the main flow mechanisms dominating the receptivity of stationary CFI to DRE arrays. In addition, this investigation aims at establishing whether height-based metrics can be used to predict the initial forcing disturbance amplitude of a given roughness array configuration. In particular, despite the minimal attention received throughout the literature, the location of the forcing arrays is one of the main parameters considered in this study as it inherently governs the complex relationships between relative disturbances amplitude, local BL scales, pressure gradient and overall flow stability.

The second challenge is of a more practical nature and stems from the disparate scales governing the receptivity problem. More specifically, the detailed analysis of the evolving instabilities in relation to the amplitude and location of DRE can provide effective scaling principles. Such scaling can give the possibility of reproducing the swept wing leading-edge flow features through up-scaled forcing configurations more tractable in terms of experimental observability. In particular, the investigation of an up-scaled configuration would improve the experimental resolution of the near-element flow field, essential to clarify the relation between roughness and CFI onset along with the receptivity process and the conflicting outcomes in using DRE as a transition control technique (as discussed in section §1.4.3).

3.2. Experimental Set-up and Methodology

The measurements discussed in this Chapter are performed in the LTT, and characterize the flow features developing on the pressure side of the M3J model. More details regarding these aspects can be found in section §2.1.1.

Acquisitions are performed at a constant freestream Reynolds number Re_{c_X}=2.17 $\times 10^6$ and angle of attack α=-3.36°. Global flow features are acquired through IR thermography, while local BL analysis is performed using planar PIV acquisitions. Throughout this Chapter, the tunnel-attached reference system (i.e. XYZ) is employed to discuss the IR acquisitions, while the wing-attached system (i.e. xyz) is used to analyse the planar PIV flow fields (section §2.1.2). A detailed description of the set-up and roughness configuration employed can be found in section §2.3 and §2.2.3 respectively. The main aspects are summarized hereafter, including the procedures implemented for the velocity field reconstruction and processing.

3.2.1. Numerical Stability Solution

The experimental acquisitions are complemented by corresponding numerical BL and stability solution computed using linear and non-linear PSE as described in section §2.4. Specifically, LPSE analysis is used to facilitate the experiment design, however, the limitations of linear theory prevent the estimation of the later stages of instability growth. Thus, a full NPSE solution for the stationary CFI is computed for a subset of the measured forcing configuration, estimating the instability amplitudes and shape functions from the DRE location to the downstream end of the PIV domain (i.e. x/c=0.36).

For the present study, the NPSE results have been matched to the experimental measurements in the following manner. A dataset is generated for all considered DRE locations in the form of families of NPSE solutions computed within a range of initial amplitudes (A_0). The matched NPSE solution is chosen as the one that minimizes the squared differences between numerical and experimental amplitudes and shape functions of the λ_1 mode over the entire PIV domain (i.e. along the chord range x/c=0.25-0.36). Individual planes are given equal weight in the least mean squares minimisation. The initial CFI amplitude is then computed by tracing its upstream development, following the NPSE amplitude curve up to the DRE location. A_0 is defined as the equivalent amplitude at x_{DRE}/c that, within the frame of modal instability evolution, gives a downstream development of CFI comparable to the experimentally measured flow field. The comparison between NPSE results and experimental measurements is further discussed in section §3.3.3.

3.2.2. DRE Arrays Configurations

To investigate the influence of both DRE location and amplitude on the evolution of stationary CFI and ensuing transition a specific range for the DRE geometrical parameters is defined as described in section §2.2. Specifically, the amplitude and chord location range to be measured is identified by using a simple geometrical scaling, expressed by Re_k and k/δ^*, combined with the LPSE solution. As a result, in-house manufactured arrays of amplitudes k_1, k_2, k_3 and k_4 and geometrical parameters summarised in table 2.3 are applied at chord locations between x/c=0.02-0.3.

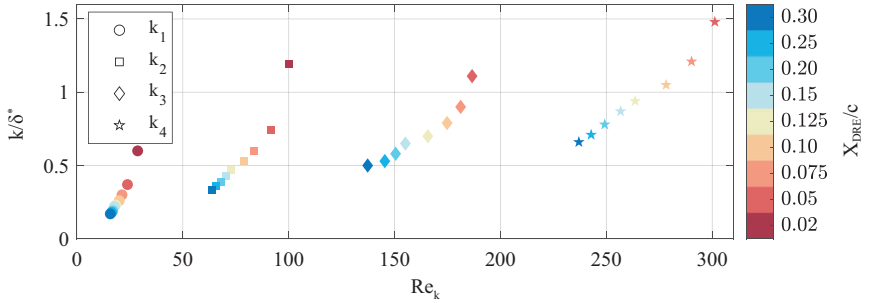

Figure 3.1: Geometrical parameters computed from numerical BL solutions at Re_{c_X}=2.17 $\times 10^6$ and α=-3.36° for all measured forcing configurations. Colourmap based on x_{DRE}/c, symbols based on element height.

The measured configurations and the corresponding values for the geometrical scaling Re_k and k/δ^* are reported in figure 3.1.

3.2.3. IR Thermography

IR acquisitions (section §2.3.1) are performed using one radiometric camera[12] imaging a portion of the model pressure side centred at x/c=0.23 and midspan with spatial resolution ≃0.85mm/px.

After the acquisition, the IR images are spatially transformed to the tunnel-attached reference frame (XYZ) and post-processed with Differential Infrared Thermography (DIT) [118, 131] to extract the transition front location. In addition, a spatial power spectral density (PSD) analysis of the temperature signal is performed along constant chord lines using Welch's algorithm [179] with 1.7mm/px resolution. Hence, the dominant spanwise spatial frequencies are identified based on their thermal footprint at the model surface.

3.2.4. Planar PIV Configuration

Planar PIV acquisitions provide a local description of the flow chordwise evolution, highlighting the effects of forcing amplitude and location on the developing CFI. The experimental set-up employed for PIV acquisitions is reported in section §2.3.3, while the main optical and acquisition parameters are reported in table 2.5.

For the application presented in this Chapter, PIV acquisitions are performed in the yz plane at various chord locations. The wall-normal direction is non-dimensionalized as $y/\overline{\delta}^*$ with $\overline{\delta}^* \simeq 0.64$mm being the experimental displacement thickness of the natural BL (i.e. no DRE) at x/c=0.25. The PIV domain, centred at the wing midspan extending for z/λ_1=5 and $y/\overline{\delta}^* \simeq 6$, describes the BL development in the yz plane through $\overline{w}$ and $\overline{v}$, time-averaged velocity components in the spanwise and wall-normal directions respectively. The velocity components are non-dimensionalized using the freestream velocity in the spanwise direction (i.e. W_∞).

Velocity Fields Reconstruction and Processing
With further processing of the velocity fields, the boundary layer mean velocity profiles ($\overline{w}_z$) are obtained by averaging the $\overline{w}$ velocity signal along the z direction. The disturbance evolution profile in the wall-normal direction ($\langle\overline{w}\rangle_z$) is instead computed as the root mean square (rms) of the velocity signal along z at each fixed y-coordinate [70, 123, 166]. Information on the dominant mode and its harmonics can be retrieved through a spatial Fast Fourier Transform (FFT) analysis: at each y-coordinate the spanwise velocity signal is transformed in the spatial frequency domain ($\mathrm{FFT}_z(\overline{w})$), providing the spectra and the dominant mode's chordwise development. Moreover, the CFI amplitude can be estimated for each acquired plane by integrating the disturbance profiles along y up to the local δ_{99} [47, 123], providing an estimation of the chordwise growth of individual modes (§ 3.3.3).

Finally, to better access the unsteady part of the flow disturbances, the velocity standard deviation fields (std, $\langle w'\rangle$) are computed by applying a proper orthogonal decomposition filter (POD, [97]) to the instantaneous velocity fields. A snapshot formulation [157] is applied to reconstruct the instantaneous velocity fields including a reduced ensemble of modes accounting for 60% of the flow kinetic energy. Following this procedure, the majority of the noise or measurement-related errors can be filtered out of the velocity fields, delivering $\langle w'\rangle$ fields closely describing the velocity fluctuations pertinent to flow physics. Subsequent processing, allows for the identification of the different structures contributing to the flow unsteadiness and their amplitudes, as further discussed in section §3.4.

3.3. Steady Perturbations Characteristics

In this section the onset and evolution of stationary CFI as identified by IR and PIV measurements is discussed. An overview of the flow receptivity to DRE arrays is reported, analysing the extracted transition fronts and the CFI growth.

3.3.1. Transition Behavior as Function of Forcing Amplitude and Location

The acquired IR thermography data provide a representation of the overall flow stability and transition under the effect of the various boundary layer forcing configurations tested. The IR visualization for the natural transition case, namely with no DRE forcing applied, is reported in figure 3.2(a). The imaged portion of the wing, extending up to x/c$\simeq$0.45, is characterized by a laminar boundary layer as no significant surface temperature change can be observed. Transition to turbulent flow is therefore expected to occur more downstream, likely around x/c$\simeq$0.6 as measured in comparable studies [131, 152]. Moreover, the characteristic light-dark streaks approximately aligned to the streamwise direction typical of IR acquisition of CFI-dominated boundary layers, are largely absent in this visualization [i.e 41]. Their presence is considered as the footprint of stationary CF vortices on the wing surface and is only mildly visible towards the end of the domain in this scenario, suggesting relatively low instabilities amplitudes. Further quantification of the spatial and spectral arrangement of the boundary layer can be performed through the power spectral density (PSD) analysis

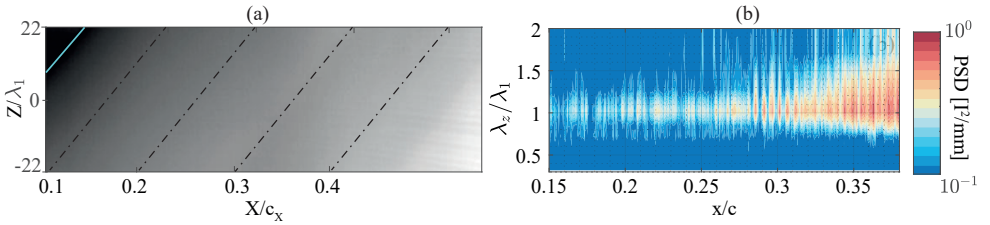

FIGURE 3.2: Natural transition flow case (i.e. no DRE) at α=-3.36° and Re_{c_X}=2.17 $\times 10^6$. (a) IR thermography fields: flow comes from the left, leading edge (blue line), x_{DRE}/c (yellow line), constant chord lines (-.). (b) Spatial power spectral density of the IR images in the spanwise direction. The analysis is performed between x/c=0.15 and x/c=0.38.

of images, computed in the spanwise wavelength domain following the procedure described in section §2.3.1. The results for the clean case are reported in figure 3.2(b), indicating that for such natural transition scenario a wide group of modes is excited, with considerable energy in the band of wavelengths between $0.5\lambda_1$ and $1.5\lambda_1$. Nonetheless, as a result of the randomly distributed micro-metric surface roughness of the polished wing, the λ_1 mode already appears among the most amplified modes, corresponding well to the linear PSE predictions (figure 2.13).

These observations, confirm the need and utility of applying DRE arrays to obtain a more uniform base flow and a deterministic flow scenario, focused on the single monochromatic λ_1 mode. Three representative fields are reported in figure 3.3, collecting the post-processed IR visualization (left column) of three different forcing cases: a reference upstream forcing Re_k=24, Re_k=18 representative for a downstream shift of the k_1 DRE array from x_{DRE}/c=0.05 to 0.15; and Re_k=155 representative for a height increase of the elements to k_3. The three cases feature a conditioned BL characterized by clearly developed stationary CFI also visible in the IR fields as a streak alternation. Moreover, figure 3.3(a) and (c) display an evident temperature difference between the upstream and downstream portion of the domain, which highlights the sawtooth pattern of the transition front, characteristic of CFI-dominated flows [41, 136].

The right column of figure 3.3 reports the PSD contours for the considered cases. Their spectral content is largely concentrated at the forced λ_1 wavelength, confirming the efficacy of the DRE array in conditioning the CFI development. Furthermore, the reported PSD contours also identify an evident growth in the fundamental mode energy along the chord. This corresponds to spanwise temperature profiles displaying higher contrast between regions of high and low shear at the wall, in turn corresponding to high and low-velocity streaks due to the presence of stationary CFI [130]. Nevertheless, caution is needed in the interpretation of the perceived growth in the spectral maps. This is due to the variable deposition of thermal energy as well as the non-uniform emission characteristics of the wing, which do not allow for quantitative assessment of surface heat flux without proper calibration. For the remainder of this booklet, the spectral analysis of the thermal maps will be used exclusively to extract dominant wavelengths.

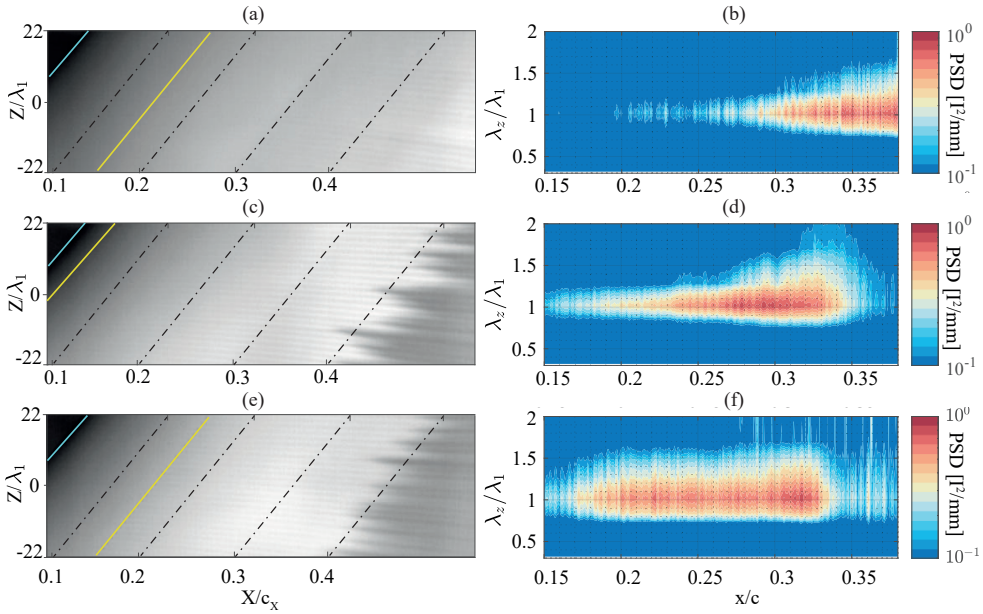

Figure 3.3: Forced transition flow cases: (a-b)Re_k=18; (c-d) Re_k=24; (e-f) Re_k=155 at α=-3.36° and Re_{c_X}=2.17 $\times 10^6$. (a, c, e) IR thermography fields: flow comes from the left, leading edge (blue line), x_{DRE}/c (yellow line), constant chord lines (-.). (b, d, f) Spatial power spectral density of the IR images in the spanwise direction. The analysis is performed between x/c=0.15 and x/c=0.38.

Extending the IR analysis to the full body of acquisitions allows for the extraction of the transition front location for all forced configurations considered. This provides the transition map reported in figure 3.4. Transition location x_{TR}/c is plotted against the DRE array chord location, x_{DRE}/c, for different DRE heights, k. The set of collected data identifies two main functional relations governing transition location: an increase (decrease) in element height and/or a decrease (increase) in streamwise location leads to an advancement (postponement) of laminar to turbulent transition. The employed metrics are not sufficient to deterministically predict the transition location. Nonetheless, despite the pronounced scatter observed in figure 3.4, Re_k qualitatively correlates to transition location. In particular, a critical behaviour is identified for forcing configurations with $Re_k \leq 190$, while arrays with higher Re_k demonstrate a super-critical behaviour, causing transition shortly after the array location [$0 \leq x_{TR}/c - x_{DRE}/c \leq 0.07$, 84, 123]. These tripping configurations are neglected in the remainder of this Chapter.

Considering these observations, it becomes evident that modifications of CFI-induced transition location due to DRE location and amplitude can not be simply approximated based on the local BL and geometrical scaling parameters of the roughness. Several factors can influence this behaviour, such as local pressure gradient, local boundary layer stability and near-DRE flow development. These effects can

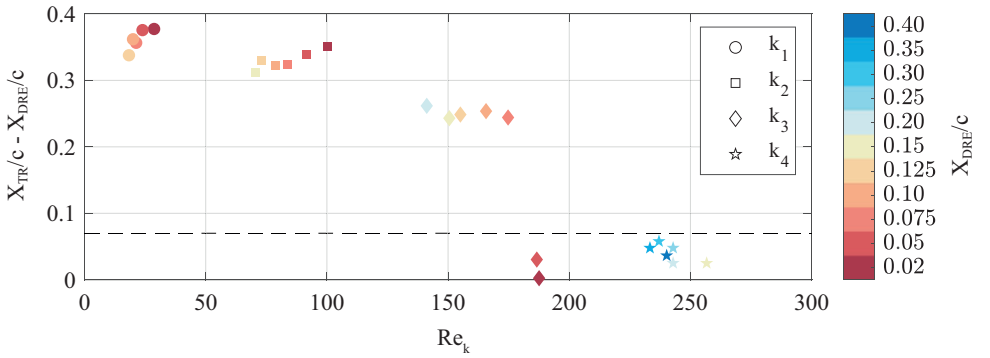

Figure 3.4: Transition locations x_{TR}/c - x_{DRE}/c vs. Re_k. Colourmap based on x_{DRE}/c, symbols based on element height. Cases with transition laying below the horizontal dashed line are supercritical (i.e. causing flow tripping).

be responsible for modifying the effective initial disturbance amplitude introduced by the DRE and thus produce the observed spread in the transition location. These amplitude modifications can then be associated with complex alterations of the flow and of the instabilities development induced by the specific forcing configuration applied, as can be further assessed considering the collected PIV data and performed stability analysis.

3.3.2. Mean Flow Development

Prior to the description of steady CFI evolution, the development of the time- and spanwise-averaged velocity fields within the PIV measurement domain is outlined. In particular, the present study investigates a wide range of chord locations for the DRE arrays application, namely from x/c=0.02 to 0.35 for which an LPSE solution accounting for the local pressure gradient is computed (figure 2.13(b)). To confirm that comparable stability conditions pertain to the experimental BL, the naturally growing BL (i.e. no forcing applied) measured through PIV is compared to the numerical solution for which stability is solved. Figure 3.5(b) collects the numerical and experimental BL velocity profiles estimated at x/c=0.35, ensuring a good match is achieved as further shown by the chordwise evolution of the BL geometrical parameters (figure 3.5(c)). Finally, to assess that the natural BL features are repeatable throughout the different forcing cases considered, the $\overline{w}_z$ velocity profiles for the natural transition case and the forcing case featuring arrays placed at x_{DRE}/c=0.30 (Re_k=64) are compared (figure 3.5(a)). Upstream of the array location, the BL development for this downstream forcing (for which no DRE is applied at the leading edge) compares well with the natural BL. The observed base flow repeatability allows for a systematic comparison of the flow modifications introduced by the different forcing configurations.

The mean boundary layer velocity distribution $\overline{w}_z$ for the Re_k=24 case is also reported in 3.5(b). The $\overline{w}$ velocity contours acquired at x/c =0.25, 0.30 and 0.35, for three representative forcing cases with Re_k in the critical range are reported in

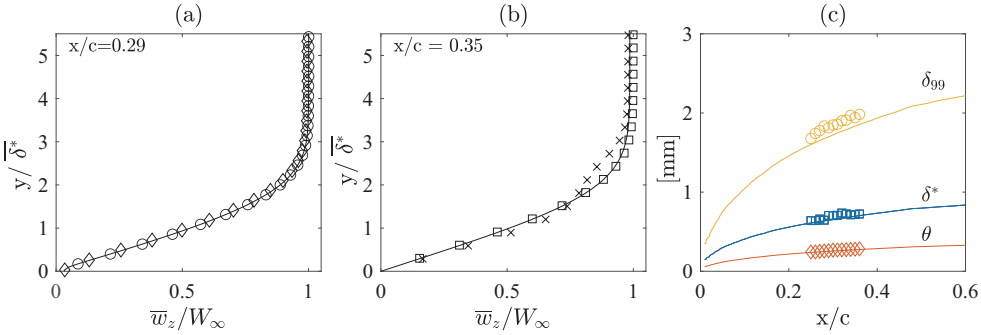

Figure 3.5: (a) $\overline{w}_z$ from numerical solution (solid line), from PIV for natural transition (-o) and PIV for $\mathrm{Re_k}$=64 ($\diamond$). (b) $\overline{w}_z$ from numerical solution (solid line), from PIV for natural transition ($\square$) and PIV for $\mathrm{Re_k}$=24 ($\times$). Only 1 in 3 marks are shown in the y direction. (c) BL integral parameters from numerical $\overline{w}$ (full lines) and PIV (symbols).

figure 3.6. In contrast to the clean case, the forced BL velocity profiles feature an inflection point (already present at x/c=0.25) and undergo further distortion moving downstream, indicating non-linearities are strongly affecting the forced scenario. This poses a limit for linear approaches to stability theory, warranting non-linear extensions computed through NPSE solutions, as further discussed in section §3.3.3. Moreover, the forced BL is thicker than the corresponding clean case and achieves a higher slope close to the wall, corresponding to an increased local skin friction coefficient. These modifications can be related to the onset of turbulent motions introduced by the strong instabilities and non-linearities characterizing the flow. These features also reflect in the development of the PIV disturbance profiles, as supported by the modes' growth and evolution analysed in the next section.

3.3.3. Stationary Crossflow Instabilities Growth

As described in section §3.2.4, a spanwise spatial FFT is applied to all collected PIV planes, to characterize the modes' evolution along the chord for each forcing case. The resulting spatial spectra are reported in figure 3.7(a) for the representative forcing configuration $\mathrm{Re_k}$=24. As expected, the dominant peaks correspond to mode λ_1 and its harmonics (λ_2 and λ_3), all growing along the wing chord.

Within the spatial FFT domain, each mode can be independently extracted and analysed. Hence, through an inverse FFT the time-averaged velocity fields $\overline{w}_{R_i}$ can be reconstructed as only composed by a chosen truncated ensemble of modes of interest i. Figure 3.7(b-c) shows the rms disturbance profiles $\langle\overline{w}\rangle_z$ computed for the reference forcing case from the $\overline{w}$ PIV fields. This is compared with the disturbance profiles extracted from two FFT reconstructed fields: $\overline{w}_{R_1}$ including only the λ_1 mode and $\overline{w}_{R_{1,2,3}}$ additionally accounting for λ_2 and λ_3 harmonics. Despite small discrepancies in their maximum amplitude, the three disturbance profiles have a similar shape, growing along the chord and featuring a secondary local maximum related to non-linear interactions. The mild amplitude differences reduce as more modes are included in the FFT flow reconstruction, even if the λ_1 mode is already

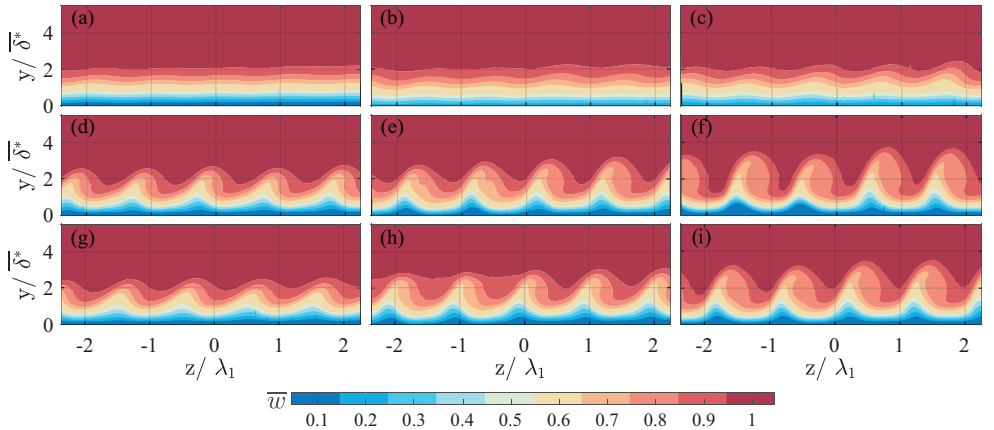

Figure 3.6: Contours of $\overline{w}$ velocity fields acquired for (a-c) Re_k=18; (d-f) Re_k=24; (g-i) Re_k=155 at α=-3.36° and Re_{c_X}=2.17 $\times 10^6$. PIV plane location: (a, d, g) x/c=0.25; (b, e, h) x/c=0.30; (c, f, i) x/c=0.35.

capturing all of the main flow features. The λ_1 mode shape function extracted from the NPSE solution at the corresponding chord locations shows a satisfactory matching behaviour, despite mild over-prediction of mode growth by the numerical solution. Similar discrepancies are also observed by Haynes & Reed [62] and can be attributed to the small differences between the experimental and numerical base flow and the actual wing curvature.

To quantify the CFI amplitude and growth, two different approaches have been proposed in past studies. By extracting the maximum value of the $\langle\overline{w}\rangle_z$ disturbance profile at each chord location [123, 166] a maximum amplitude value can be estimated, further indicated as A_{max} and non-dimensionalized by the freestream speed W_∞. An integral amplitude can be instead defined following the procedure presented in Downs & White [47], i.e. integrating the $\langle\overline{w}\rangle_z$ profiles in the wall-normal direction up to y=δ_{99} for each acquired plane to obtain $A_{int} = \frac{1}{\delta_{99} * W_\infty} \int_0^{\delta_{99}} \langle\overline{w}\rangle_z(y)dy$. Both approaches can either be applied to the original PIV fields or their FFT reconstruction only including the mean flow and the λ_1 mode. The latter procedure isolates the λ_1 mode growth while reproducing all the relevant disturbance characteristics. Figure 3.8(a-b) offers a comparison of the 4 resulting curves computed for the Re_k= 24, k_1 forcing case. The differences between the PIV and FFT estimations are minimal, confirming the λ_1 mode gives the main contribution to the disturbance amplitude and its development. However, significant differences appear between the two estimation procedures, with the A_{max} curves showing lower growth. This is confirmed by the growth curves reported in figure 3.8(b), estimated using a local definition of the N-factor, namely $\overline{N}$=ln($\frac{A}{A_{25\%}}$), where $A_{25\%}$ represents the disturbance amplitudes at x/c=0.25 for each measured configuration.

The relevant differences between the growth curves are in contradiction with the report of Reibert *et al.* [123], who observed a collapsing of the N-factor values independently of the amplitude estimation procedure. Nonetheless, in the present

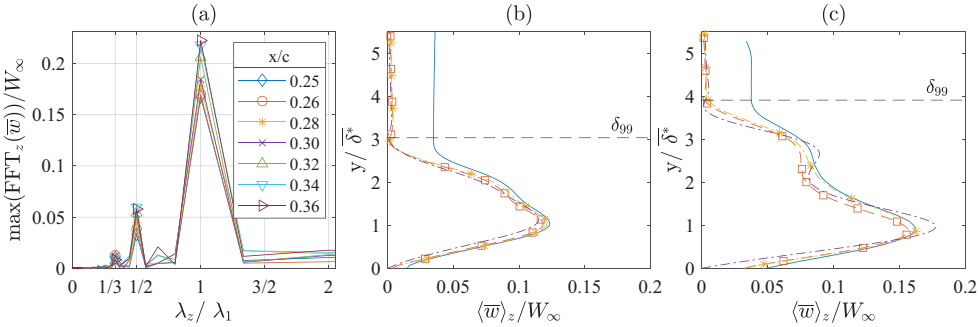

Figure 3.7: (a) Spanwise spatial FFT spectra and experimental $\langle\overline{w}\rangle_z$at (b) x/c=0.25; (c) x/c=0.35 for $\mathrm{Re_k}$=24 at α=-3.36° and Re_{c_X}=2.17 $\times 10^6$. $\langle\overline{w}\rangle_z$ from PIV (–), from two FFT reconstructed fields $\langle\overline{w}_{R_1}\rangle_z$ (□) and $\langle\overline{w}_{R_{1,2,3}}\rangle_z$ (∗) and from NPSE result (-.). Only 1 in 3 marks are shown along y. Experimental δ_{99} (- -).

forcing case, the flow is characterized by well-developed CFI from the very beginning of the experimental domain, see also figure 3.6(a-c). Additionally, figure 3.7(a) shows a secondary lobe develops in the disturbance profile starting from x/c=0.25, justifying the mild growth or even the saturation of the main peak amplitude along the considered portion of the chord. Correspondingly, the $\mathrm{A_{max}}$ undergoes small changes and mild growth throughout the domain. The second lobe, however, is also subject to growth along the chord and these modifications are captured by the $\mathrm{A_{int}}$ estimation since it considers the whole rms profile. Moreover, the reference case presented by Reibert *et al.* [123] refers to a much smaller element (k=0.006mm against the $\mathrm{k_1}$ of the present investigation) and corresponding amplitude forcing, which leads to comparable dominant mode and non-linearities development at more downstream chord locations. A comparison between amplitude and $\overline{N}$-factor values performed on a case with lower forcing amplitude and so weaker instabilities developing, such as the forcing case with $\mathrm{Re_k}$=18 and $\mathrm{k_1}$, leads to a better matching of the maximum and integral amplitudes growth rates (figures 3.8(c-d)).

Finally, an estimation of the PIV error propagation in the amplitude curves is performed starting from the calculation of the instantaneous uncertainty fields in the PIV measurements, and their respective average [186]. Two additional flow fields are built by adding or subtracting the uncertainties from the time-averaged PIV fields. They are then processed through the FFT reconstruction and amplitude extraction routine to estimate both the $\mathrm{A_{max}}$ and $\mathrm{A_{int}}$ curves. Their differences provide an error range for the amplitude calculation which has a mean value of ±1.2% for the maximum amplitude approach and of ±1% for the integral amplitudes. The lower error value in the latter approach is attributed to the inherent integration of the rms profile and associated uncertainties rather than extracting their single-point maximum value. Based on the comparable acquisition and processing configurations, these estimations are considered representative of the PIV errors affecting all tested configurations.

Hence, for more quantitative analysis, the CFI amplitude and growth are estimated

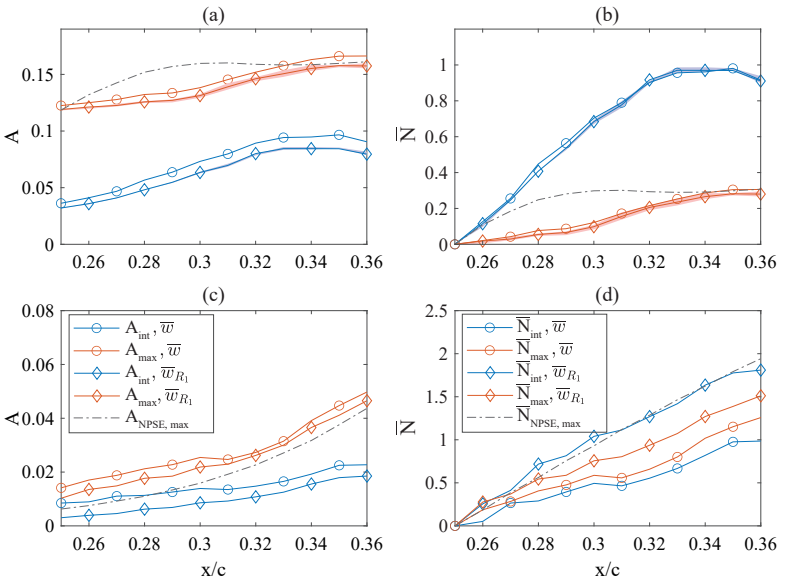

FIGURE 3.8: Amplitude (A) and N-factor ($\overline{N}$) along the wing chord, computed from PIV acquisitions at α=-3.36° and Re_{c_X}=2.17 $\times 10^6$ for forcing at (a-b) Re_k= 24 and (c-d) Re_k= 18. Comparison between integral amplitudes A_{int} (blue) and maximum amplitudes A_{max} (red) extracted from $\overline{w}$ (○) and from $\overline{w}_{R_1}$ (◇) fields. Markers each 2% chord staggered for clarity. (a,b) PIV error propagation in the amplitude calculation (shadowed areas, only reported for the $\overline{w}_{R_1}$ fields); NPSE amplitudes estimation (-.).

following the integral amplitude approach proposed by Downs & White [47]. Having confirmed the λ_1 mode gives the main contribution to the disturbance amplitude and its development, for the remainder of this Chapter the amplitudes estimations presented are extracted from the $\overline{w}_{R_1}$ and $\overline{w}_{R_2}$ reconstructed flow fields unless otherwise specified. This procedure is akin to the amplitude estimation from the computed NPSE solutions, allowing for a direct comparison of the numerical and experimental results. Repeating the amplitude estimation procedure for the acquired cases the A_{int} curves reported in figure 3.9 are obtained, showing the effect of different forcing configurations on the generated disturbances evolution.

In the most upstream forcing configurations, the instabilities grow throughout the domain up to a saturation amplitude level. In agreement with previous studies [62, 123, 181] for this subset of cases the forced primary structures reach saturation at comparable amplitude values ($A_{int,saturation} \simeq 0.06 W_\infty$), independent of the forcing amplitude and location. These cases are accompanied by the growth of the λ_2 mode, which also saturates for the more upstream configurations. However, forcing at more downstream chord locations as well as with higher DRE arrays leads to lower saturation amplitudes. This different behaviour can be attributed to several reasons, among which the breadth of the parameter range involved may lead to variations in the receptivity process. Moreover, cases with $Re_k \geq 24$, 90, 160 respectively for the three different heights considered, are as well affected by the early amplitude

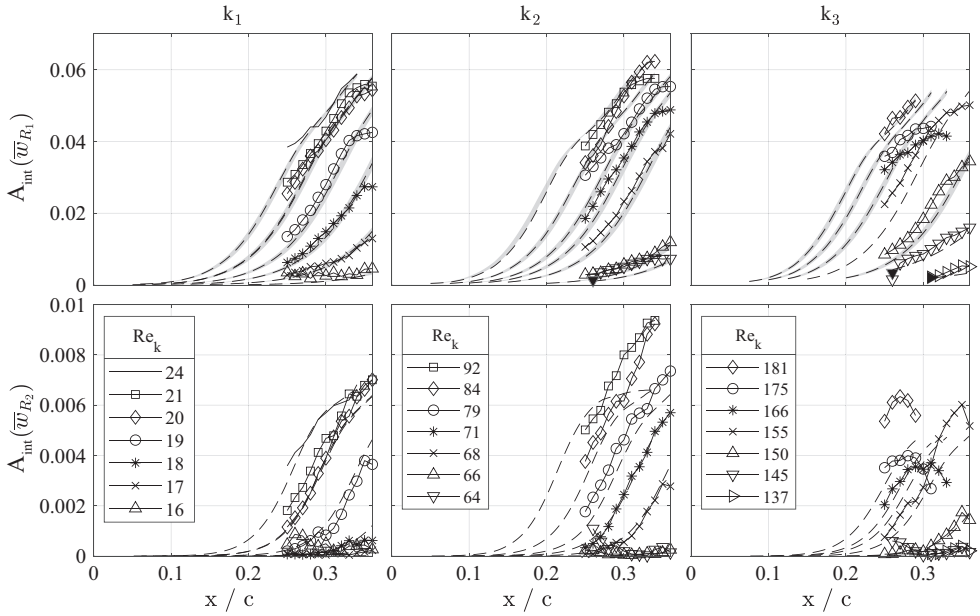

Figure 3.9: Chordwise A_{int} evolution from (*Top*) $\overline{w}_{R_1}$ fields and (*Bottom*) $\overline{w}_{R_2}$ fields. Columns refer to a fixed k, matching NPSE solution (- -), NPSE solution sensitivity (shaded regions), and NPSE initial amplitude estimations (full markers). Data relative to x/c locations downstream of the transition point are excluded from the plot.

saturation and subsequent decay. Such behaviour is indicative of the later stages of transition and onset of turbulence, which essentially breaks the spanwise coherence of the structures. Instead, with a further downstream shift (i.e. $Re_k \leq 18$, 70, 150) arrays of all considered heights induce instabilities that grow along the whole PIV domain without reaching saturation, accompanied by a negligible or absent development of the λ_2 mode.

Most of the measured upstream forcing configurations are characterized by well-developed λ_2 modes, indicating the BL flow is affected by non-linearities. Therefore, for each of these cases, an NPSE stability solution is computed (§3.2.1). The numerical amplitudes computed from NPSE solutions are reported for all the tested cases in figure 3.9. Figure 3.10 instead, shows the specific comparison between NPSE, LPSE and PIV computed amplitudes, N-factor and shape functions evolution for an upstream (Re_k=24) and a downstream (Re_k=18) forcing configuration. Overall, mild amplitude differences are observed in figures 3.9 and 3.10, mostly attributed to mild base flow discrepancies, possibly enhanced downstream of the roughness element due to the complex physics of the near-DRE flow region (as discussed in section §1.8). Additionally, the actual wing curvature as well as the experimental uncertainty on the roughness height and exact chord location can also contribute to the observed differences. More significant discrepancies characterise the $Re_k \geq 160$ cases. The pronounced discrepancies between experimental and numerical results at

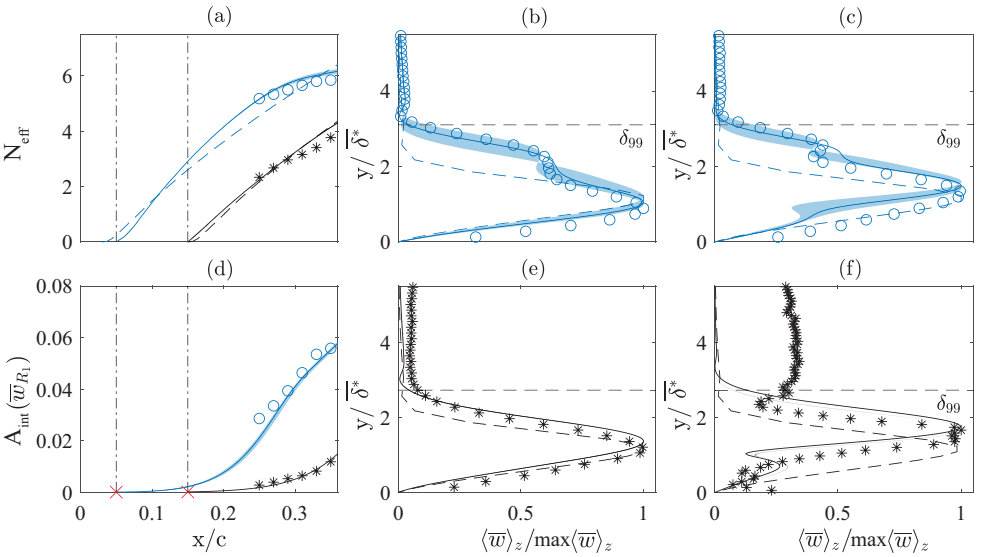

Figure 3.10: PIV and NPSE λ_1 mode (a) N_{eff} and (d) A_{int} for Re_k=18 (∗) and Re_k=24 (∘) with x_{DRE}/c (-.), A_0 (×). (b-e) Shape functions of the λ_1 and (c-f) λ_2 mode at x/c=0.30 for the NPSE (full line), LPSE (- -) and FFT shape functions from PIV (symbols). Experimental δ_{99} (- -), NPSE matching sensitivity (shadowed areas).

higher Re_kreveal possible effects near the DRE which are not modelled by the NPSE approach. Among others, these can include unsteadiness in the wake (e.g. vortex shedding) and non-modal effects in the stationary vortex system, as further discussed in section §1.8.

Notwithstanding mild topological differences, the NPSE correctly predicts the CFI saturation amplitude ($A_{int,saturation} \simeq 0.057 W_\infty$, $A_{max,saturation} \simeq 0.157 W_\infty$ in agreement with Reibert *et al.* [123]). The λ_2 harmonic and its evolution are also properly described, despite enhanced amplitude differences for the more upstream configurations considered, related to the primary amplitude discrepancies. To verify the sensitivity of the NPSE matching to the initial amplitude estimate, the area between the matching NPSE solution and two equivalent solutions initiated with $A_0 \times (1 \pm 0.1)$ is shown as a shaded region in figure 3.9. In addition, the experimental amplitude uncertainties given by the PIV correlation are smaller, thus contained also in the shaded region.

The overall CFI behaviour is well modelled by the NPSE, as already shown by Haynes & Reed [62]. Therefore, the upstream portion of the numerical solution can be exploited to extract an estimation of the perturbation initial amplitude A_0. This is computed as the equivalent amplitude a modal CFI should possess at the x_{DRE}/c location to give a downstream development of the flow field comparable to the experimental measurement. This is particularly instructive given the inability of experimental measurement techniques to resolve such mild effects. It must be noted that all NPSE simulations are initiated only with the λ_1 mode and as such A_0 refers

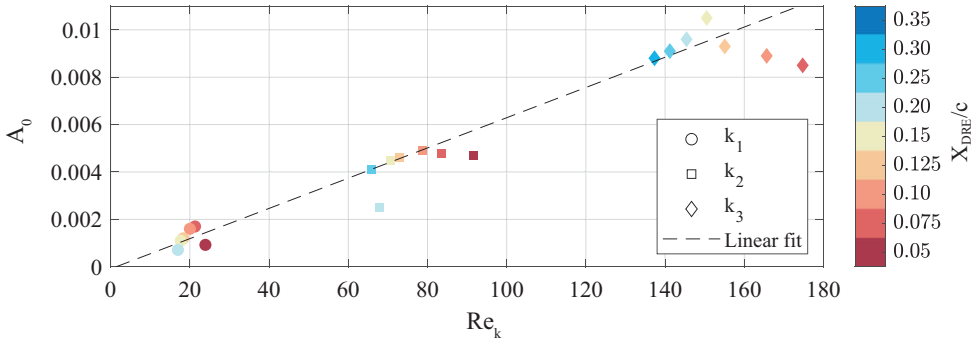

Figure 3.11: Initial CFI amplitude (A_0) from NPSE against Re_k. Linear fit of the A_0 data ($A_{0,fit}$, - -), colormap based on x_{DRE}/c, symbols based on element height.

to the latter. The A_0 extracted for the two cases of figure 3.10(d) are represented by the red $\times$ markers, while the ensemble estimates for the various tested heights and chord locations are reported in figure 3.11.

The observed A_0 curves immediately confirm that the receptivity process is not linearly dependent on the considered parameters. Nonetheless, Re_k appears to correlate surprisingly well to the estimated initial amplitude, possibly due to the inherent information used by this metric which includes the local velocity or momentum of the incoming flow. Despite not giving a complete description of the single forcing cases behaviour, the simple least-squares linear data fit ($A_{0,fit}=6.2\times10^{-5}Re_k$) reported in figure 3.11 appears to capture the main A_0 differences given by modifications of the DRE amplitude. A global estimation of the fit accuracy is described by the coefficient of determination ($R^2=0.97$), indicating the fit is capturing up to 97% of the data variance. More detailed considerations can be carried out considering the A_0-linear fit local residuals ($\Delta A_0=A_0-A_{0,fit}$), which appear to be relatively higher for the smaller elements. In particular, for k_1 the estimation of the residual reaches a maximum of $\Delta A_0 \simeq 0.5A_0$ in contrast to the $\Delta A_0 \leq 0.25A_0$ for $Re_k>70$. Additionally, for each of the three considered element amplitudes, higher deviations from the linear fit pertain to the more upstream configurations reported, which experience stronger local pressure gradient variations and possible local effects not properly modelled by the NPSE approach. This behaviour is in agreement with previous investigations stating that in the vicinity of the dominant mode neutral point, linear receptivity is only expected for DRE amplitudes much smaller than the ones of the present study [82, 145, 166]. The more downstream cases, however, are less affected by the local flow field characteristics (i.e. pressure gradient and local effects), falling closer to the linear fit approximation for the Re_k-A_0 relation. This behaviour validates the possibility of up-scaling the upstream configurations to further investigate the near-DRE flow phenomena and reflects the monotonic behaviour of transition location with Re_k observed from the IR measurements (figure 3.4).

Notwithstanding geometrical parameters, the direct solution of non-linear stability theory appears to capture best the overall increase of initial amplitude corresponding

to the three considered heights simply based on downstream measurements. Yet, the initial amplitude values are not linearly dependent on k, as the relative increase between estimated amplitudes is not representative of the proportional increase in DRE height [166, table 2.3]. In addition, the DRE location also appears to affect the initial amplitude estimation, showing an initial increase in A_0 followed by a slow decrease when considering more downstream application locations. However, DRE of higher amplitude placed at identical x_{DRE}/c (thus identical pressure gradient) lead to stronger differences between the NPSE and experimental amplitudes evolution (figure 3.9). The observed trends significantly differ from the results obtained by Tempelmann *et al.* [166] for smaller roughness heights (i.e. $\leq$10% of the local δ^*) that led to a linear receptivity process. This different correlation between A_0 and the elements' location, further suggests that the DRE amplitude is the dominant parameter for the receptivity of the cases considered in this investigation. Multiple error sources can be affecting the A_0 behaviour, including measurement uncertainties and modelling errors in the NPSE approach which, for example, does not account for the effect of the local pressure gradient on the near flow dynamics and consequently on A_0. In fact, a good match between numerical and experimental amplitude is obtained 1% of chord downstream of the array location, as shown by the full marks of figures 3.9. However, by comparing the amplitude values closer to the element (i.e. 0.3% downstream of the element, figure 3.16) differences between the experimental and the NPSE values can be observed, confirming modal stability theory does not accurately model the CFI growth immediately aft of the roughness array. These observations further justify the identified A_0 behaviour, stressing the importance of the near-DRE flow dynamics for the onset and later evolution of stationary CFI.

In conclusion, the investigation of the stationary CFI led to the description of the downstream development of the primary CFI mode and its harmonics. Moreover, complementing NPSE simulations allow for the estimation of the initial CFI amplitude represented by A_0. As expected, the reported values show a strong dependency of the CFI onset on the forcing amplitude being, however, only mildly affected by the forcing location. Yet, the defined geometrical parameters are not capable of completely describing the underlying receptivity relations. This can be traced back to the flow field dynamics in the immediate vicinity of the DRE, which can be affected by the local pressure gradient and potentially include non-modal and transient growth features similar to what is identified in two-dimensional flows by White *et al.* [183] or Reshotko [124]. The A_0 estimation directly from NPSE appears to support this hypothesis, therefore, a further step towards the analysis of the relation between the DRE element and the initial CFI amplitude can be guided by the near-DRE flow investigation reported in section §1.8.

3.4. Unsteady Perturbations Characteristics

The previous discussion, outlines a consistent dependence of the stationary CFI evolution, amplitudes saturation and laminar transition on the DRE forcing amplitude and location. Nevertheless, no universal relation between the DRE characteristics and the developing stationary CFI could be identified. Hence, the need of analysing the unsteady part of the developing perturbations emerges.

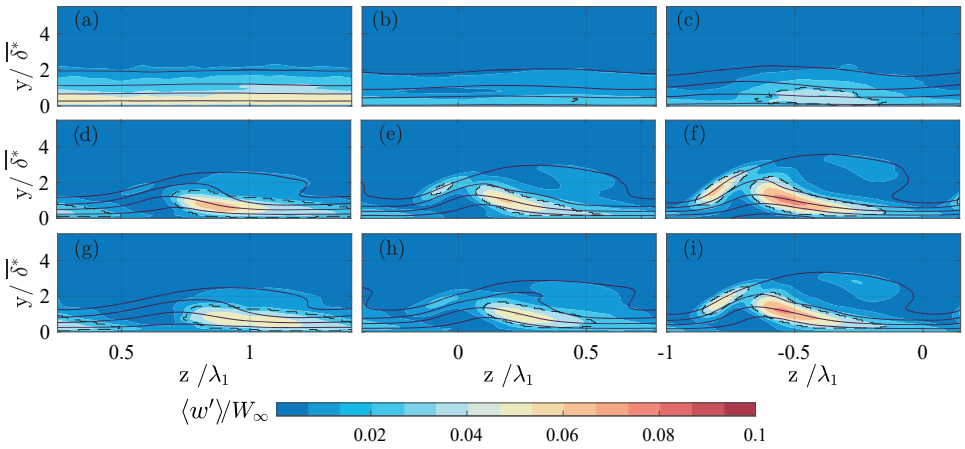

Figure 3.12: POD reconstructed $\langle w' \rangle$ contours at α=-3.36° and Re_{c_X}=2.17 $\times 10^6$ for forcing (a-c) Re_k=18; (d-f) Re_k=24; (g-i) Re_k=155. PIV plane location: (a, d, g) x/c=0.25; (b, e, h) x/c=0.30; (c, f, i) x/c=0.35. Superimposed contours of $\overline{w}$ (full lines, 5 levels from 0 to 1); masks isolating type I and type III structures (- -).

From the acquired PIV data, the standard deviation of the instantaneous velocity fields can be computed. As discussed in section §3.2.4, a good estimate of the $\langle w' \rangle$ fields can be obtained by first decomposing and then reconstructing the instantaneous velocity fields through POD. This procedure allows for isolating the background level of $\langle w' \rangle$ due to noise and other disturbances and is applied to all the considered configurations including the natural transition case. However, as discussed in section §3.3.2, the clean wing boundary layer develops stationary CFI only in the form of a weak spanwise modulation. Their amplitudes, identified from the time-averaged PIV fields, are already weak, therefore the unsteady perturbations are expected to be even smaller. Their analysis carries little insight into the BL characteristics, hence this case is not further treated hereafter.

The forced BL configurations developing strong stationary CFI, provide instead some interesting features. In particular, the reference forcing cases Re_k=18 and Re_k=24 with k_1 and Re_k=155 with k_3 can be again considered. To better grasp the unsteady structures characterizing the flow and their evolution, only a zoomed-in portion of the PIV domain containing a single reconstructed primary CF vortex is reported. To continuously follow the chosen structure, as moving towards downstream chord locations the fields are progressively shifted along the z-axis. The resulting contours of $\langle w' \rangle$ are collected in figure 3.12.

The upstream forcing (figures 3.12(d-f)) and the higher DRE amplitude cases (figures 3.12(g-i)) are characterized by higher unsteady disturbances. In particular, two regions of intense fluctuations can be identified at all considered chord locations, each one corresponding to a local maximum of $\langle w' \rangle$. The stronger peak lays close to the wall, in a region of velocity minimum on the inboard side of the vortex. Being located at the inner side of the upwelling region of the primary stationary CF

vortex, the corresponding structure can be associated with instabilities classified as type III [19, 100, 154, 175]. This mode refers to the interactions between primary stationary and primary travelling waves, therefore its relevance in the transition pattern strongly depends on the free stream turbulence level, which is kept constant in the present study. The second local peak of $\langle w' \rangle$ appears on the outboard side of the upwelling region of the primary CF vortex, an area characterized by a high streamwise flow velocity gradient along z, namely $\frac{\partial \overline{w}}{\partial z}$. This location is usually associated with secondary instabilities of type I mode, developing at a significantly higher frequency than the type III instabilities (in the order of kHz instead of Hz for comparable conditions [154]). Both the identified instabilities are observed to grow along the chord. Moreover, a third region of strong unsteadiness is developing on the top of the primary CF vortices, where the streamwise velocity wall-normal (i.e. y) gradients are larger. This is most likely related to instabilities of type II, although only visible in cases with strong primary CFI. On the other hand, the Re_k=18 forcing (figures 3.12(a-c)) displays a significantly different scenario. The time-averaged velocity fields show it is only developing weak flow modulation, therefore the unsteady fluctuations reach very low amplitudes. At the first two chord locations considered, no structure is clearly visible, but a widespread BL fluctuation typical of the development of travelling waves is registered [47]. More downstream, the fluctuations progressively reduce and are modulated by the stationary vortices: a peak in correspondence of the type III region is present at x/c=0.35.

As outlined from the presented fluctuation fields, pertinent modes develop at distinct locations in the yz plane depending on the velocity gradient peaks [100, 154]. Therefore the two structures associated with the type I and type III regions can be isolated and independently investigated, purely based on their spatial localization. In particular, for each field a mask is built (represented by the dashed lines in figure 3.12) by selecting only the points with $\langle w' \rangle$ values higher than a threshold fixed at 2.5 times the averaged velocity for each flow field considered. This procedure is capable of separating the two types of structures. Both the type I and type III amplitudes, respectively A_I and A_{III}, can then be computed by integrating the $\langle w' \rangle$ values in the yz domain and non-dimensionalised by W_∞. In this way, both an increase in the structure intensity and a growth in size can be accounted for. The same mask is also applied to the $\frac{\partial \overline{w}}{\partial z}$ gradient fields so that the gradient maximum in correspondence with the type I structures can be extracted. The cases with $\langle w' \rangle$ values lower than the selected threshold in the type I or type III structures regions display initially null amplitude values. The computed amplitude curves and the cumulative integral of the maximum $\frac{\partial \overline{w}}{\partial z}$ gradient in correspondence of the type I structures are collected in figure 3.13.

Overall, the reported configurations are characterized by similar values of the type III disturbance amplitudes, especially for the k_1 and k_2 arrays, confirming the dominance of the stationary CFI conditioned by the DREs. Further validating their strong dependence on freestream turbulence (kept constant in this study) [16], the type III structure amplitudes do not display a clear dependence on the forcing location and amplitude. Moreover, figure 3.5 shows the clean wing BL characteristics are repeatable up to the array location for downstream forcing cases, allowing the natural

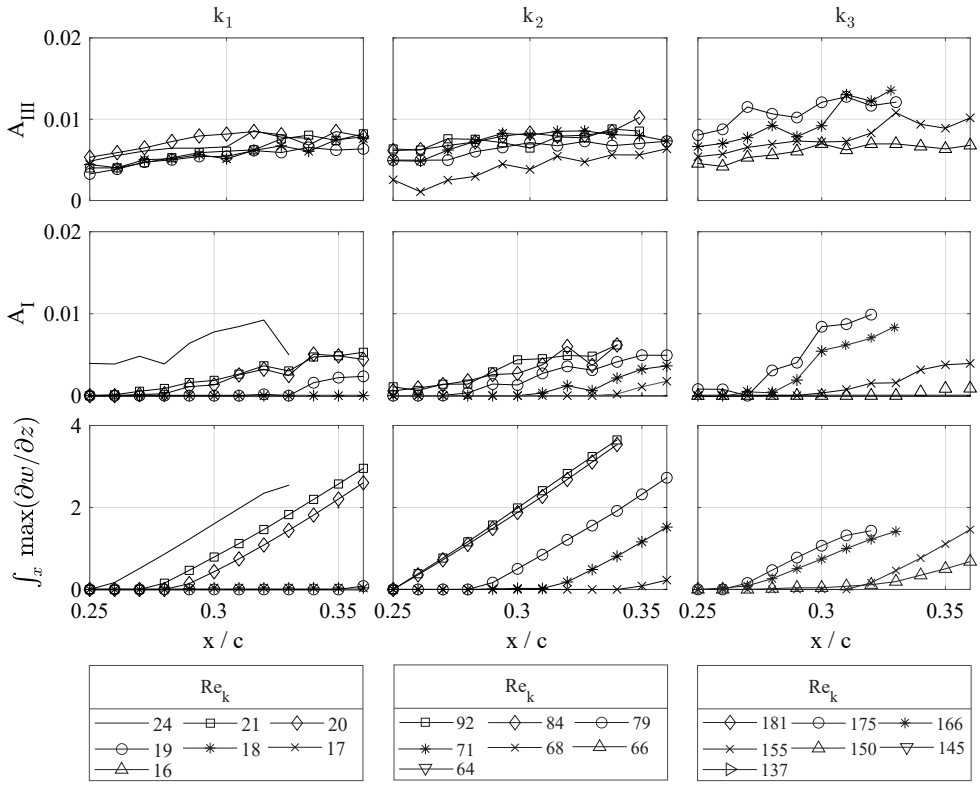

Figure 3.13: Chordwise (*Top*) A_{III} and (*Center*) A_I evolution from POD reconstructed $\langle w' \rangle$ fields. (*Bottom*) cumulative $\frac{\partial \overline{w}}{\partial z}$ integral at type I structures location. Columns refer to a fixed k.

and largely undistorted boundary layer to develop for a longer portion of the chord. In this scenario travelling modes appear along with the stationary ones, possibly leading to the development of more intense unsteady fluctuations of type III. However, the A_{III} estimate for the forced case Re_k=155 appear to be largely unaffected, as they are well-developed since x/c=0.25 and achieve weaker amplitudes than upstream cases. This can be related to the extremely low level of freestream turbulence achieved in the testing environment (approximately $T_u/\mathbf{U}_\infty \simeq 0.025\%$) and the relatively high amplitude of the applied forcing, generating stationary CFI which rapidly modulate the travelling waves developing on the wing. Finally, arrays placed more downstream (i.e. Re_k= 17 for k_1 or Re_k=70 for k_2) achieve negligible amplitudes for the unsteady modes corresponding to the type I, but they still reach significant A_{III}. In fact, for these cases stationary instabilities are too weak to give origin to secondary modes, while their interaction with the developing travelling waves still leads to significant type III unsteady disturbances. At further downstream locations, also the type III amplitudes reach values comparable with the background noise, rendering them too weak to be properly detected.

The type I structure amplitude is instead more sensitive to the forcing configuration. In particular, for the three considered heights, figure 3.13 shows the more upstream forcing cases are always characterized by stronger A_I. Type I mode amplitude and growth can be related to the $\frac{\partial \overline{w}}{\partial z}$ gradient, reported in the bottom row of figure 3.13. Both the amplitude and maximum gradient curves show a monotonic growth throughout the PIV domain, accompanied by a saturation effect for those cases characterized by early turbulence onset. Therefore, the type I evolution can be related to the transition front location and its modifications induced by the forcing. Moreover, stronger type I structures characterize cases with upstream transition front, reflecting the fact that the higher frequency secondary instabilities are ultimately the ones leading to transition [15, 100, 154, 175]. This is visible for the more upstream k_3 cases featuring transition within the PIV domain. The corresponding A_I amplitudes and $\frac{\partial \overline{w}}{\partial z}$ gradient undergo rapid growth and saturation as the identified transition location is approached.

Concluding, the forcing configuration appears to be affecting the transition location through the development of type I secondary instabilities, which are inherently rising due to the flow distortion the DRE array introduces. The type III mode is instead developing almost independently from the forcing applied, which is mainly linked to the environmental parameters, which remain constant in this study. Therefore, the relation between the forcing, the instabilities development and their breakdown and transition to turbulence appears with a certain clarity. However, the beginning of this chain of effects, namely the relation between the roughness element amplitude and location and the CFI onset, assumes an important role and is the subject of the following section.

3.5. Near-DRE Flow Topology

Of the results reported so far, only the A_0 estimation brings interesting insights on the initial phases of receptivity. However, despite observing a dependency on the forcing amplitude and location, the A_0 modifications appear to be mostly affected by the near-DRE flow dynamics, characterized by flow phenomena that can hardly be parametrized. Nonetheless, to better understand the initial receptivity phases, the last part of this Chapter is dedicated to a more in-depth investigation of the flow evolution in the DRE vicinity. For arrays applied between x/c=0.25-0.30 additional PIV planes are collected with a step $\simeq$0.16% chord starting 0.3% downstream of the DRE location to avoid light reflections.

The time-averaged spanwise $\overline{w}$ velocity contours for forcing at Re_k=145 (i.e. x_{DRE}/c=0.25, k_3) are reported in figure 3.14 along with the corresponding perturbation fields (estimated as $\overline{w}(y,z) - \overline{w}_z(y)$). This forcing case is chosen as the representative configuration throughout this section as it features the larger element considered (i.e. k_3), thus the developing flow features are most observable and less subject to noise issues. The average velocity fields reveal a boundary layer almost unaffected by CFI, as no flow modulation is yet present in the base flow. However, a momentum deficit region is developing directly in the wake of the element surrounded by higher speed flow possibly due to a momentum redistribution effect induced by the roughness element itself [84]. Already visible in the plane closest to the DRE (at x/c=0.253)

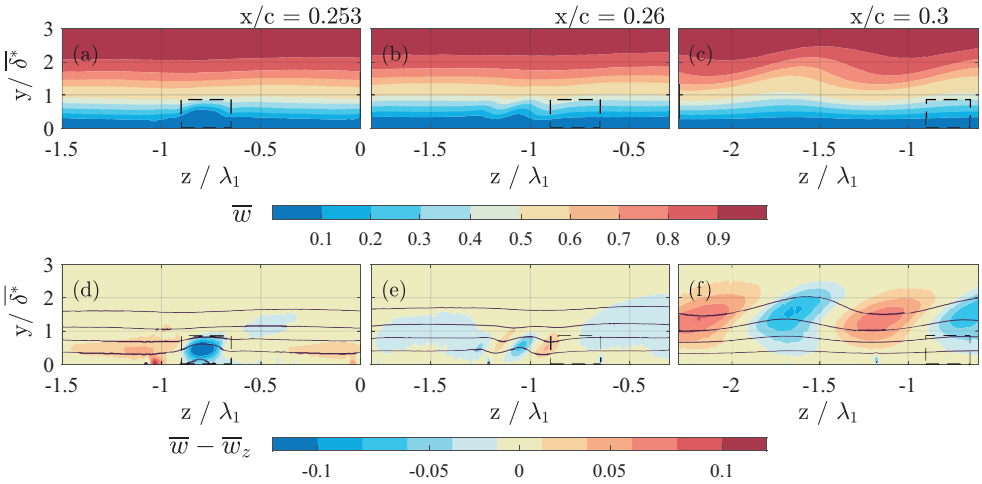

Figure 3.14: Contours of (a-c) $\overline{w}$ velocity and (d-f) perturbation velocity field ($\overline{w} - \overline{w}_z$acquired for Re_k=145 in the array vicinity. Superimposed contours of $\overline{w}$ (full lines, 5 levels from 0 to 1). Dashed rectangle represents the roughness shape and location.

this low-speed hump forms immediately downstream of each element present in the PIV domain and rapidly decays between x/c=0.253-0.26. Downstream (x/c=0.27), the disturbance field evolves into a weak but uniform high-speed low-speed region alternation typical of stationary CFI [16]. The topology of the flow modulation is very similar to corresponding cases of weak upstream forcing such as Re_k=18 shown in figure 3.6. These observations reconcile well with the DNS results by Kurz & Kloker [84], discussed in section §1.5. More specifically, they identified two pairs of horseshoe vortices developing around the roughness elements: an outer pair propagating from the element sides, most likely due to the element-induced spanwise shear, and an inner pair originating aft of the element due to wall-normal ejection of flow. In a 3D boundary layer, for both pairs only the leg co-rotating with the baseflow CF velocity component is sustained and develops along the chord, while the counter-rotating legs are suppressed shortly after the elements. The emergence of these vortices drives a momentum redistribution process which results in the formation of a low-speed hump in the wake of the elements due to low-momentum flow upwelling. Despite the different flow features characterizing a 2D or 3D boundary layer, Kurz & Kloker [84] observed that the near-DRE flow characteristics are comparable for the two cases. Flow features and evolution comparable to what is observed in the presented results, are reported in the work by Ergin & White [52], an experimental investigation on the flow past a roughness element in a two-dimensional boundary layer.

A spanwise FFT decomposition is applied to these near-DRE fields and the corresponding spectra are reported in figure 3.15 for case Re_k=145. Differently from the upstream forcing case (figure 3.7(a)), the spectra of the present case identify a high energy spectral content involving the dominant mode λ_1 and numerous harmonics. This is mainly attributed to the highly concentrated region of velocity deficit in the

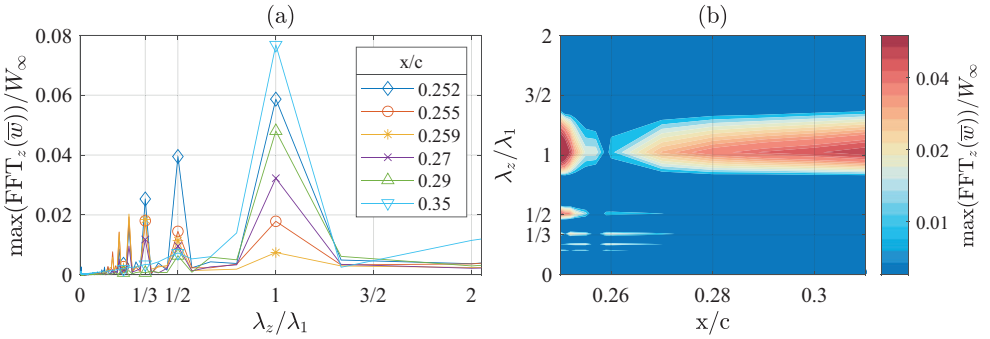

Figure 3.15: (a) Spatial spanwise FFT spectra and (b) spectra amplitudes in the x-λ plane for $\mathrm{Re_k}$=145.

wake of the elements, which are otherwise located in an undisturbed spanwise invariant flow. In terms of spatial spectra, the DRE wake essentially acts as a pseudo-pulse, effectively containing all spatial frequencies. The diameter of the DRE ($\simeq$1.7mm) is nevertheless finite and only four times less than the elements' inter-spacing. As such, the spectral energy is not equally distributed and decays with higher harmonics. For the results presented in figure 3.15, more than 35% of the spectral energy is contained in the first 5 harmonics. However, it must be noted that the identified spectral components do not necessarily correspond to natural modal instabilities in the flow, rather they can be seen as modal representations of the near-DRE wake in the FFT space. As such, the perturbation amplitude computed following the integral approach includes all the complex flow features corresponding to the near-DRE flow development. Integral amplitudes extracted from the $\overline{w}$ velocity fields and from the $\overline{w}_{R_1}$ field are reported in figure 3.16.

The amplitude development extracted from the time-averaged PIV fields displays a very mild total disturbance growth followed by a significant decay associated with the velocity deficit evolution and a subsequent growth due to the flow modulation development, figure 3.16(a). As also confirmed by the reported spectra, the downstream flow modulation is dominated by the λ_1 mode and despite overall smaller amplitudes, it reflects the CFI characteristics and growth process previously discussed for cases of more upstream located arrays (figure 3.6). Interestingly, the amplitude curves of the presented cases are characterized by comparable trends and amplitudes in the element vicinity. The change of height or chord locations of these arrays leaves the initial decay and subsequent growth almost unaltered, suggesting that the near-DRE flow region is mostly influenced by the flow blockage caused by the element itself rather than the overall flow stability. Unfortunately, the current set-up does not permit direct computation of experimental instability amplitudes for arrays located in regions affected by stronger variations of the pressure gradient as these are located closer to the leading edge, where the boundary layer is extremely thin. However, the observed near-DRE flow similarity is in agreement with the results of the numerical computations conducted by Kurz & Kloker [83] on a more upstream forcing configuration and sets an important starting point for the scalability of the

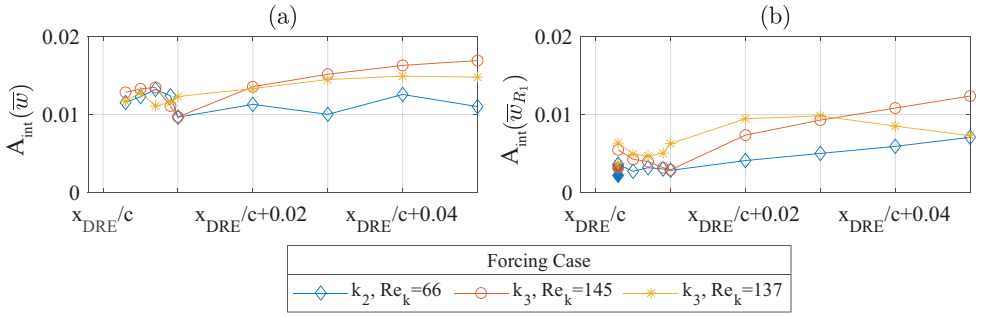

Figure 3.16: Chordwise A_{int}evolution in DRE vicinity from (a) $\overline{w}$ and (b) $\overline{w}_{R_1}$. NPSE integral amplitude at x/c=0.253 (full markers).

examined configurations.

The similarity among forcing cases is additionally evident on the amplitude curves extracted from the $\overline{w}_{R_1}$ fields (figure 3.16(b)). It must be emphasised that the identified FFT modes do not necessarily represent the naturally developing wake instabilities. Nonetheless, they provide a valid modal description of the wake flow field which delivers interesting insights into the relative flow dynamics. In particular, for the three presented configurations, the λ_1 mode shows a continuous decay from the DRE location to 1% of chord downstream, indicating that the initial amplitude growth observed in figure 3.16(a) may be linked to the behaviour of higher harmonics. To further address this consideration, hereafter we present a more detailed analysis of the individual Fourier modes' behaviour for case Re_k=145. Figure 3.17 includes the estimation of the total perturbation integral amplitude $A_{int}(\overline{w})$, as well as the integral amplitude of the first six harmonics of the dominant mode λ_1 extracted from the Fourier spectra. Additionally, $A_{int}(\overline{w}_{R_{1-6}})$ is the integral amplitude computed from a truncated FFT reconstructed flow field including only the six reported modes. Despite the mild amplitude differences between $A_{int}(\overline{w})$ and $A_{int}(\overline{w}_{R_{1-6}})$, both amplitude trends show a mild growth followed by a rapid decay in the element vicinity. However, both the λ_1 and λ_2 modes are decaying aft of the roughness element, and only start to grow downstream of x/c=0.26, where the NPSE-experimental amplitude match indicates that the CFI growth is following an exponential trend. On the other hand, in the element vicinity (i.e. x/c<0.26) Fourier modes λ_3, λ_4, λ_5 and λ_6 all show mild growth followed by a rapid decay. These flow features match well with the results presented by White *et al.* [183], who identified non-modal mechanisms and in particular transient growth as a fundamental feature of the near-DRE wake development for a non-swept flow. The individual modes behaviour described in figure 3.17 as well as the observed mild $A_{int}(\overline{w})$ growth, appear to reflect the characteristics of a transient growth process [87, 144] possibly driven by the behaviour of individual Fourier components comparable to those identified by White *et al.* [183].

Previous works by Corbett & Bottaro [39] and Breuer & Kuraishi [20], show that flow fields developing aft of a cylindrical element can produce a transient growth mechanism that can lead to the rapid initial growth of CFI, enhancing

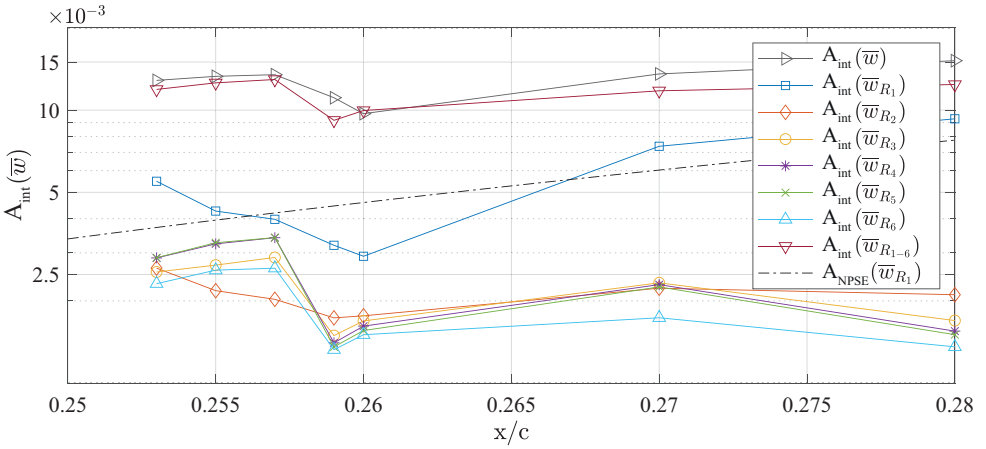

Figure 3.17: Chordwise A_{int}evolution in DRE vicinity for forcing case k_3, Re_k=145 from $\overline{w}$, $\overline{w}_{R_1}$, $\overline{w}_{R_2}$, $\overline{w}_{R_3}$, $\overline{w}_{R_4}$, $\overline{w}_{R_5}$, $\overline{w}_{R_6}$ flow fields and from the FFT reconstructed flow field $\overline{w}_{R_{1-6}}$. Matching NPSE integral amplitude (-.); y-axis plotted with logarithmic scale to ease visualization.

their downstream development which then follows an exponential growth process. This transient growth process is typically governing the linear superposition of the individually decaying non-orthogonal solutions to the stability problem [39, 90, 95, 144]. However, these eigensolutions appear at the same spanwise wavelength and frequency. As such, the decoupling of modal (i.e. exponential) and non-modal (i.e. algebraic) growth effects is not possible by means of an FFT decomposition.

Non-modal interactions are not accounted for in the NPSE solver, however together with the local pressure gradient, they could significantly affect the near-DRE wake development, further justifying the A_0 behaviour observed in figure 3.11. Additionally, the initial boost in the amplitude of higher harmonics of the primary stationary CFI mode given by a transient growth mechanism can lead to the formation of strong shear layers in the DRE wake. These can in turn induce unsteady wake instabilities (such as vortex shedding or shear layer instabilities of sinuous or varicose nature), that can affect the CFI initial amplitude, growth rate and transition location [20, 93, 95]. In particular, in the Re_k=145 forcing case presented in figure 3.17 the effect of the transient mechanism on the primary wavelength (i.e. λ_1) is visible in the initial decay. The latter cannot be modelled by NPSE, as is evident from the different evolution of $A_{int}(\overline{w}_{R_1})$ and the integral amplitude computed from the NPSE solution, i.e. $A_{NPSE}(\overline{w}_{R_1})$. The NPSE amplitude evolution is in fact purely exponential, thus resulting in an underestimation of the λ_1 mode A_0 . This consideration explains the observed numerical and experimental amplitude differences registered in figure 3.16(b), where the NPSE initial amplitude is underestimated for all the reported cases if compared with the experimental values. The result in figure 3.17 is possibly the first experimental observation of transient growth in a swept wing boundary layer. Nevertheless, the region in which the perturbation amplitude initially grows while individual modes are decaying is extremely short (less than 1% chord). This spans merely three PIV measurement planes rendering the spatial resolution insufficient to

identify one of the signature features of transient growth which is algebraic amplitude evolution. The elucidation of such mechanisms is the main subject of the investigations presented in Chapter 5.

In conclusion, for the limited number of cases investigated in this study, the application of DRE in a region affected by linearly developing natural CFI is still successfully conditioning the downstream CFI development. Moreover, the pre-existing CFI modulation appears to have negligible effects on the near-DRE flow features which present comparable amplitude and behaviour independently of the forcing chord location, as also observed by Kurz & Kloker [83]. Therefore, the withstanding relation between external DRE forcing and CFI onset may be more complex than a simple two elements interaction, involving a chain of effects moving from the elements to the near-DRE flow and consequently to the onset of the CFI. The identified near-DRE behaviour can potentially be linked to a transient growth process which affects the BL flow providing the proper initial conditions to the modal CFI development [39]. Considering the narrow parameter range examined and the insufficient spatial resolution for the current investigation this remains a hypothesis. However, its potentially pertinent role in the complete definition of the receptivity process justifies further detailed investigations dedicated to the near-DRE flow field, which are thoroughly discussed in Chapters 4 and 5 of this thesis. These investigations can be simplified by the observed repeatability of the near-DRE wake characteristics demonstrated beforehand, allowing for performing near-DRE measurements at more downstream and experimentally more accessible chord locations.

3.6. Concluding Remarks

The presented experimental investigations explore the overall effect of discrete roughness elements amplitude and chord location on the development and breakdown of stationary CFI. Roughness arrays are manufactured with a fixed element inter-spacing corresponding to the wavelength of the dominant CFI mode (λ_1 according to LPSE), to force a deterministic flow scenario focussed on a single monochromatic mode. The forcing arrays are applied on the wing surface at various chord locations, while four different element heights are considered, spanning a broad range of $k/\delta^* \simeq 0.15\text{-}2.4$ and $Re_k \simeq 15\text{-}280$.

The global inspection of transition performed through IR thermography relates the forcing configuration to the observed transition modifications. An increase (decrease) in element height and/or a decrease (increase) in DRE streamwise location lead to an advancement (postponement) of laminar to turbulent transition. Reflecting the transition front modifications, configurations characterized by higher Re_k introduce instabilities with higher amplitudes which rapidly grow along the chord up to saturation and turbulence onset.

The non-linear development of primary CFI is numerically modelled by solving NPSE through an in-house developed solver. A good match is found between the experimental and numerical development of the instabilities as they progress in the boundary layer, including the extracted instabilities' amplitude and saturation amplitudes. As such, the upstream initialisation of the numerical solution provides an estimation of the equivalent CFI initial amplitude (A_0) at the DRE array location

leading to comparable downstream development of CFI. The collected A_0 values indicate the forcing amplitude is the main parameter influencing the initial CFI amplitudes. The direct estimation of A_0 using NPSE appears to capture the overall influence of the forcing elements sufficiently well, while still revealing pertinent differences from a universal scaling law. In particular, the inherent relations between forcing configuration and the initial CFI amplitudes as well as the transition locations, are not following a simply linear trend. Nonetheless, Re_k performs relatively well in capturing both transition modifications and estimation of the initial perturbation amplitude stemming from a given DRE configuration. However, the residual data scatter suggests more complex and possibly non-modal mechanisms, likely influenced by the local pressure gradient and not captured by the NPSE, are active in the element vicinity.

The final part of this Chapter presents an investigation of the near-DRE flow development for a limited set of cases. In the velocity fields, a momentum deficit region is identified behind the element and is observed to decay further downstream, where a boundary layer modulation corresponding to a stationary CFI mode (with λ_1 wavelength) emerges [84]. These flow features are reflected by the reported amplitude estimations. Additionally, DRE arrays are applied in a region affected by the development of weak (i.e. still linear) natural CFI disturbances, conditioning the CFI evolution also in this configuration. This confirms the near-DRE flow is mostly influenced by the blockage effect of the element rather than the local flow stability, further reconciling the inability of NPSE back-projections to fully capture the initial amplitude (A_0). Furthermore, this observation opens new possibilities for up-scaling of the considered forcing configurations, which would simplify the experimental investigation of the near-DRE flow features. Moreover, preliminary evidence of transient growth behaviour can be identified in the DRE wake, based on spanwise spectral analysis. However, the few cases considered and the low spatial resolution achieved, require further dedicated investigations to confirm this hypothesis.

From the reported results it appears that the inherent relation between roughness elements and CFI onset is more complex than a simple two elements interaction. A chain of effects relating the physical elements to their near-DRE flow features and consequently to the onset of the CFI is revealed, effectively making the near-DRE flow development an intermediate and important receptivity step. This step is eventually responsible for setting the initial conditions for the modal CFI development. Considering their pertinent role in the complete definition of the receptivity process, near-DRE dynamics is the subject of the next Chapters of this booklet.

4

The Near-element Flow of a Near-Critical IDRE

In this Chapter the effect of a near-critical isolated discrete roughness element in a swept wing boundary layer is investigated. Steady and unsteady velocity modifications induced in the near-wake of a cylindrical element are measured, identifying and describing the nature of the introduced instabilities, their development in the near- and far-wake region, and their role in the transitional process.

ZOPPINI, G., RAGNI, D., & KOTSONIS, M. 2022. Transition due to isolated roughness in a swept wing boundary layer. *Physics of Fluids.* [197]

ZOPPINI, G., RAGNI, D., & KOTSONIS, M. 2022. Experimental investigation of isolated roughness induced transition in a swept wing boundary layer. *AIAA SCITECH 2022 Forum.* [196]

4.1. Introduction

The literature background regarding 2D and 3D boundary layers receptivity to IDREs has been presented in section §1.4.2. Within the proposed framework, numerous experimental and numerical works are dedicated to the characterization of IDREs applied in 2D boundary layers, while only few numerical simulations investigate the near-wake flow topology of IDREs applied in swept wings scenarios. However, a notable lack of experimental measurements detailing these flow configuration is identified, particularly for near-critical regimes (i.e. configurations featuring $Re_k \approx 200$ for the considered set-up) which are representative of large real-life roughness features such as rivets or debris deposition.

Hence, in this Chapter the IDRE near-element flow (i.e. the flow region including near-wake and far-wake flow) in a 3D boundary layer is experimentally investigated, characterizing the dominant stationary and unsteady flow features. The near-wake flow topology and its downstream development are outlined, posing particular focus on the characterization of the nature of the induced instabilities. The chosen IDRE amplitude is intentionally set to near-critical levels, thus ensuring a strong BL forcing resulting in boundary layer transition within the acquired domain. Furthermore, such configurations effectively bypass classical modal CFI inherent to micron-sized roughness elements. Hence, the role of the near-wake instability onset and downstream development in the transitional process is as well investigated. This allows for the identification of similarities and discrepancies between the 3D boundary layer scenario considered in the present investigation and the well-known 2D transitional scenario described in the literature.

Throughout the presented experimental campaign, a cylindrical IDRE is placed in the otherwise undisturbed laminar BL developing on the swept wing surface. Measurements are performed at three Re_{c_X} obtained by varying the freestream velocity. This grants the possibility of studying the flow behaviour in presence of a super-critical and a near-critical forcing configuration without changing the geometrical characteristics of the considered element. Infrared thermography (IR) imaging is employed to investigate the base flow topology, including a quantification of the onset location and chordwise development of the turbulent wedge. Additionally, local hotwire anemometry (HWA) scans are performed allowing for detailed characterization of the flow features dominating the element near-wake, as well as of the development of stationary and unsteady structures. In particular, the time-dependent velocity signal is analysed to investigate the spectral characteristics of the identified velocity fluctuations, which provide fundamental information regarding the nature and evolution of the developing instabilities.

4.2. Experimental Set-up and Methodology

The presented measurements are performed in the LTT, and acquire the flow features developing on the pressure side of the M3J swept wing model (section §2.1.1). Acquisitions are performed at a fixed angle of attack α=-3.36° for three freestream Reynolds numbers Re_{c_X}=1.45, 1.35 and 1.27×10^6 (see table 2.2, replicated hereafter). To inform the scaling of the problem, a numerical BL solution is

Case	x_{IDRE}/c	k[mm]	D[mm]	D/k	$Re_{c_X}(\times 10^6)$	Re_k	k/δ^*
1	0.15	0.5	6	12	1.27	198	0.83
2	0.15	0.5	6	12	1.35	219	0.85
3	0.15	0.5	6	12	1.45	251	0.90

Table 4.1: Geometric parameters of the measured isolated roughness configurations.

computed for each of the three tested Re_{c_X} as described in section §2.4. The global flow features are experimentally monitored through IR thermography, while local quantitative acquisition of the near-element flow is performed through HWA measurements. Throughout this Chapter the *near-wake region* comprehends structures and instability developing immediately aft of the element location, while the *far-wake region* is characterized by the flow features evolution into modal instabilities or their breakdown and turbulence onset process.

Throughout this Chapter, the tunnel-attached reference system (i.e. XYZ) is employed to discuss IR acquisitions, while the wing-attached system (i.e. x,y,z) is employed to analyse the HWA flow fields (section §2.1.2). A detailed description of the employed set-up and roughness configurations can be found in section §2.3.2 and §2.2.2 respectively. The main aspects are summarized hereafter, including the procedures implemented for the velocity field reconstruction and processing.

4.2.1. IDRE Configurations

As preliminary discussed in section §2.2, throughout this investigation a cylindrical IDRE with nominal height k≃0.5mm and diameter d=6mm is applied at x_{IDRE}/c=0.15. In the three considered Re_{c_X} configurations, the element geometry corresponds to Re_kvalues of Re_{k_1}=251, Re_{k_2}=219 and Re_{k_3}=198, spanning super-critical and near-critical transitional behavior for decreasing Re_{c_X} (table 4.1). Furthermore, the roughness configurations considered correspond to k/δ^* values of 0.9, 0.85 and 0.83 for decreasing Re_k (table 4.1). These values all fall underneath the k/δ^* range at which varicose modes are found to dominate the boundary layer evolution aft of IDREs applied in 2D boundary layers (i.e. k/δ^*≃1.5-2) [24].

4.2.2. IR Thermography

One radiometric camera[12] images a portion of the model pressure side centred at the wing midspan and extending for all the chord length with a spatial resolution of 0.85mm/px (section §2.3.1, figure 2.8(a)). After the acquisition, the IR images are spatially transformed to the tunnel-attached reference frame (XYZ) and post-processed to extract the relevant flow features.

4.2.3. HWA Configuration

Hotwire anemometry (HWA, section §2.3.2) is employed to collect local temporal information on the near-element velocity fields, aiming at characterizing both steady and unsteady flow disturbances. A sketch of the employed set-up is reported in figure 2.8(b), while the main experimental parameters summarized in table 2.4.

HWA acquisitions are performed in the yz plane at various chord locations, mostly distributed in the element vicinity. The wall-normal and the spanwise location are both non-dimensionalised as $y/\overline{\delta}^*$ and $z/\overline{\delta}^*$, with $\overline{\delta}^*$ being the BL thickness of the numerical BL solution for Re_{k_1} at x/c=0.15 (namely $\overline{\delta}^*$=0.595mm). At each point, the velocity signal acquired by the hotwire sensor is a projection of the instantaneous velocity components ($\overline{U}$), reconstructed as in equation 2.1. During data analysis, the velocity fields are normalized by the experimentally measured time-averaged freestream velocity $\overline{U}_\infty$.

4

Velocity Fields Reconstruction and Processing

The time average of the acquired HWA velocity signal is indicated as $\overline{U}(y,z)$, and allows for the investigation of the stationary flow features. The spanwise extension of the acquired velocity fields accommodates the flow region corresponding to the instabilities development at each considered chord location. Additionally, each field also includes a portion of the undisturbed laminar BL developing on both sides of the perturbed flow region. This is visible in figure 4.1(a), where the unperturbed BL flow develops on the left and right respectively of the two vertical dash-dotted lines. Therefore, the spanwise average of the velocity signal of the unperturbed flow region at each chord location provides an estimation of the laminar BL baseline development $\overline{U}_b(y)$. Moreover, each of the laminar $\overline{U}_b$ profiles acquired outside of the perturbed flow region, allows for the identification of the wall location at the corresponding spanwise coordinate ($\overline{z}$). In particular, each $\overline{U}(y,\overline{z})$ profile is assumed to evolve linearly in the wall vicinity, in agreement with the typical form of the laminar BL velocity profile. Therefore, the BL velocity values are linearly extrapolated up to the y-location corresponding to the local $\overline{U}(y,\overline{z})$=0. This procedure can be repeated on both sides of the perturbed flow region, such that a linear interpolation along the z-direction defines the wall location also in the perturbed portion of the flow. The acquired velocity field is then locally shifted at each z such that the y=0 location corresponds to the wing surface. The steady BL disturbance fields are then computed as $\overline{U}_d(\mathrm{y},\mathrm{z}) = \overline{U}(\mathrm{y},\mathrm{z})$- $\overline{U}_b(\mathrm{y})$, and allow for characterization of the high-speed and low-speed regions developing in the flow, as well as for the investigation of their downstream evolution.

Additionally, HWA time-dependent velocity signal is considered to investigate the unsteady disturbances. The velocity fluctuation fields (U'), allow for the identification of the highest fluctuation regions. The frequency spectra extracted at the corresponding locations, outline the frequencies pertaining to the dominant fluctuation and their harmonics. Furthermore, the energy associated with the considered frequency range is computed by integrating the spectral power in the yz planes. The main results and conclusions are presented in section §4.4.

4.3. Stationary Flow Topology

In this section the stationary flow topology and the dominant stationary near-wake disturbances are identified and discussed.

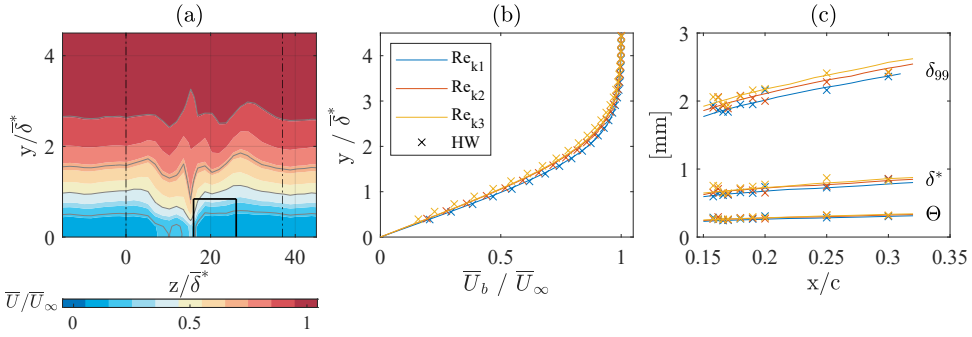

Figure 4.1: (a) $\overline{U}$ contours for Re_{k_2} at x/c=0.2. Velocity isolines plotted every 20% of $\overline{U}_\infty$ (grey lines); element location (black rectangle); limits of the perturbed flow region (vertical -. lines). Comparison of (b) HWA (×) and numerical (-) BL evolution along y extracted at x/c=0.2; (c) chordwise evolution of BL parameters computed from HWA (×) and numerical BL profiles (-).

4.3.1. Base Flow Evolution

To fully characterize the unperturbed BL (i.e. base flow) development, the numerical boundary layer solution is considered (section §2.4.1, [152]). The laminar BL velocity profile ($\overline{U}_b$) is then estimated both from the numerical and experimental data at each Re_k at a fixed chord location. To facilitate direct comparison with the experimental BL profiles, the numerical BL is projected to the HWA measurement system through equation 2.1. The resulting comparison is reported in figure 4.1(b), while integral BL parameters are shown for the three Re_k in figure 4.1(c). The obtained $\overline{U}_b$ velocity profiles confirm that the unperturbed (i.e. no roughness element applied) incoming BL flow is fully laminar and no significant CFI is developing upstream of the IDRE.

Further base flow analysis can be performed by considering the acquired IR thermography data, allowing for preliminary characterization of the wedge evolution as shown in figure 4.2. The IDRE appears as a low-temperature circle at x_{IDRE}/c=0.15 in the reported IR images. For all three Re_k considered, the flow past the IDRE evolves into a turbulent wedge similar to what was observed for 2D boundary layers [10]. The turbulent region is deflected inboard (i.e. towards negative Z) as evolving downstream, inducing an asymmetric flow features development typical of the 3D boundary layers configurations [22, 84]. Moreover, the wedge evolution shows a monotonic behaviour as the Re_k is modified. Its origin is located further away from the element for Re_{k_3}, suggesting weaker disturbances are introduced in the flow.

The extraction of individual surface temperature profiles along z-parallel lines, delivers a quantitative estimation of the turbulent wedge development in terms of origin ($\Delta x_0/c$), width (W) and opening angle. Specifically, within each extracted temperature profile, the wedge is identified as a region of temperature drop with respect to the corresponding local laminar flow temperature (T_{lam}). The latter is locally extracted as the averaged temperature value of the unperturbed flow regions and is subtracted from the temperature profile to facilitate the temperature drop identifications. Flow regions corresponding to temperature values lower than $0.9T_{lam}$ are associated with turbulent flow. This analysis is performed between x/c=0.158-0.35,

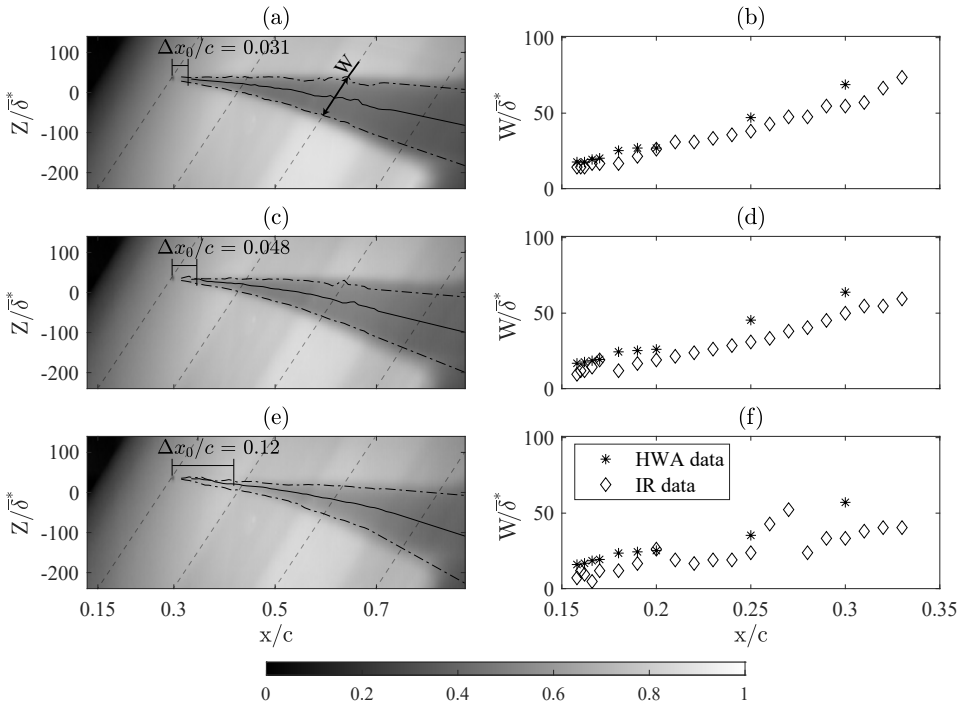

Figure 4.2: (a, c, e) IR thermography fields and (b, d, f) estimation of wedge width (W) evolution along wing chord for x_{IDRE}/c=0.15 and (a-b) Re_{k_1}, (c-d) Re_{k_2}, (e-f) Re_{k_3}. (a, c, e) Flow comes from the left, wedge middle point (- line); linear interpolation of the wedge limits (-. lines); wedge origin distance from the element ($\Delta x_0/c$). (b, d, f) Values collected from post-processing of HWA ($*$) and IR ($\diamond$) data.

and the resulting wedge width (W) evolution is shown in figures 4.2(b, d, f). The origin of the turbulent wedge is identified as the first chord location for which W is larger than 1.5D. This representative value is chosen in similarity to the wedge geometry analysis proposed in previous works [13] investigating the flow field incurred by an IDRE in a 2D boundary layer. The proposed procedure is based on the symmetric flow features of the developing turbulent wedge, and as such would not apply to the present case. However, the choice of 1.5D as a threshold allows for the initial development of the ensuing disturbances in the element vicinity, in agreement with the observation of a finite distance between the wedge origin and the element location reported in literature [76]. Moreover, such a threshold is also consistent with the anticipation of unsteady disturbances and turbulent structures development due to the increase of Re_k [1, 76]. In fact, the resulting wedge origin distance from the element location is $\Delta x_0/c = 0.03$ and 0.05 for Re_{k_1} and Re_{k_2} respectively, while it reflects the milder disturbance effects introduced in the Re_{k_3} case, evolving for almost 12% chord before laminar breakdown occurs. These results agree well with previous works dedicated to IDREs in 2D BL flows, indicating that also in the present case the instabilities driving the transitional process are initiated in the recirculation region

developing aft of the IDRE [13, 22, 76].

Overall, cases Re_{k_1} and Re_{k_2} show strong similarities, featuring wedge opening angle of approximately 8° and 9° respectively, while Re_{k_3} features a higher opening angle of about 12°. The obtained values compare well with previous 2D boundary layers investigations [147]. However, for the current configurations, the traditional wedge spreading half angle definition [76] cannot be applied since the typical symmetry of wedges in 2D boundary layers is lost. Consequently, by computing the spanwise location of the wedge centre along the chord (full black lines in figures 4.2), the angle between the wedge development axis and the X-direction (hereafter called α_{skew}) is estimated, representing a measure of the overall skewness. Its values for the considered cases lay between 6° and 8°, which are angles comparable to the ones developing between the X-direction and classical crossflow vortices observed in a similar experimental set-up, but at higher Re_{c_X} numbers [22, 117, 152]. The sensitivity of α_{skew} to the temperature threshold chosen for the wedge edges identification is considered as well. Few representative threshold values are selected, associating turbulent flow regions to temperature values lower than 0.85, 0.90, or 0.95 T_{lam}. Absolute modifications of α_{skew} in the order of 1 to 0.5° (i.e. $\simeq$10 to 5%) are registered respectively for the lower and higher threshold chosen, leaving the identified α_{skew} values in a range comparable to the CFI orientation.

A comparable procedure is applied to estimate the width of the wedge from the collected HWA velocity fields. In particular, the wedge evolution can be estimated at each x/c location from a spanwise velocity profile extracted at a fixed y-location close to the wall. The region of velocity drop with respect to the BL velocity values at the same y is identified, giving an estimate of the wedge width also reported in figures 4.2(b, d, f). Despite the different measurement and processing techniques, the wedge evolution is comparable at all tested Re_k confirming the ability of IR thermography to properly describe the developing changes in the BL. The HWA-estimated wedge width appears to be overestimated at downstream locations (i.e. x/c=0.25, 0.3), possibly due to the lower spanwise resolution when compared to the IR acquisitions. Confirming previous observations, Re_{k_3} features a wider chordwise region characterized by a slowly varying wedge width.

4.3.2. Steady Disturbances

The base flow analysis corroborates that the base flow features in the present investigation compare well with those of previous studies [e.g 10, 24, 80, 93, 115]. Based on these similarities, the stationary disturbances introduced by the IDRE are further analysed, considering the HWA time-averaged velocity fields.

Figure 4.3 shows the disturbance velocity fields (computed as $\overline{U}(X,z) - \overline{U}_b(y/\overline{\delta}^* = 1.7)$) collected for the three Re_k at a constant $y/\overline{\delta}^*$=1.7 distance from the wing surface. As suggested by the IR fields, an asymmetric wake is identifiable downstream of the IDRE, accompanied by the development of high- and low-speed structures, approximately aligned to the X-direction. For all three Re_k cases, a low momentum region forms aft of the element [80], with a couple of alternating high- and low-speed streaks developing on both sides adjacent to the IDRE wake [55, 56, 80, 93, 102]. The low momentum region persists in the wake core, up to the merging of the outer

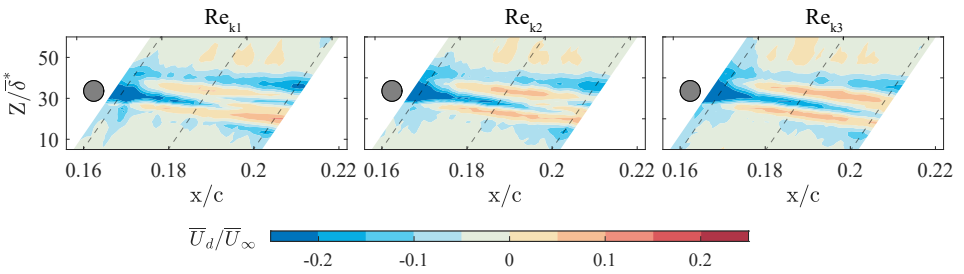

4

Figure 4.3: $\overline{U}$ contours at constant wall-normal distance $y/\overline{\delta}^*$=1.7 for Re_{k_1}=251, Re_{k_2}=222 and Re_{k_3}=198.

high-speed streaks. This occurs earlier for the higher Re_k considered, rapidly leading to the development of the turbulent wedge, as previously identified in the IR images (figure 4.2). The asymmetric development of the turbulent flow region is evident in the largely differing behaviour of the streaks located on the inboard (i.e. towards lower $Z/\overline{\delta}^*$ values) and outboard (i.e. towards higher $Z/\overline{\delta}^*$ values) side of the wake region in the Xz plane. Specifically, the inboard high-speed streak forms shortly downstream of the element location, as shown in figure 4.3, and develops along the wake's inboard side. Once initiated, such streak structure is sustained along the downstream direction, and is most likely induced by a vortex that is co-rotating with the baseflow crossflow. In contrast, the high-speed streak on the outboard side of the wake is attenuated and substituted by a large and intense low-speed streak similar to what was described in previous works [34].

These considerations are confirmed and detailed by the disturbance flow fields extracted from the HWA scans acquired in the yz plane, reported in figure 4.4. The low momentum region (L_1) is visible in correspondence of the IDRE wake [13, 80, 102, 190], as are the two weaker low-speed streaks developing on the element sides. The inboard low-speed region is quickly decaying and is substituted by a strong high-speed streak (H_1). The outboard low-speed streak (L_2), instead grows while moving downstream, accompanied by the dampening of the outboard high-speed structures (H_2), as observed in figure 4.3. Two high-speed regions are identified on the side of the low-momentum wake region shortly downstream of the element location. They initially grow individually in the element vicinity, while they merge further downstream (forming the high-speed region named *HM*) replacing the low momentum region developing in the IDRE wake, comparably to the behaviour observed in 2D boundary layers configurations [75].

To further characterize the dominant stationary structures and their corresponding amplitudes, the disturbance velocity fields are masked based on a threshold disturbance value. This allows for isolating the two dominant low-speed regions (L_1 and L_2) and two high-speed regions (H_1 and H_2) developing downstream of the element (figure 4.4). The local absolute amplitude is estimated as the maximum and minimum disturbance velocity within the high-speed and low-speed masked regions respectively (figure 4.5), and reflects the flow features described beforehand. The amplitude of the

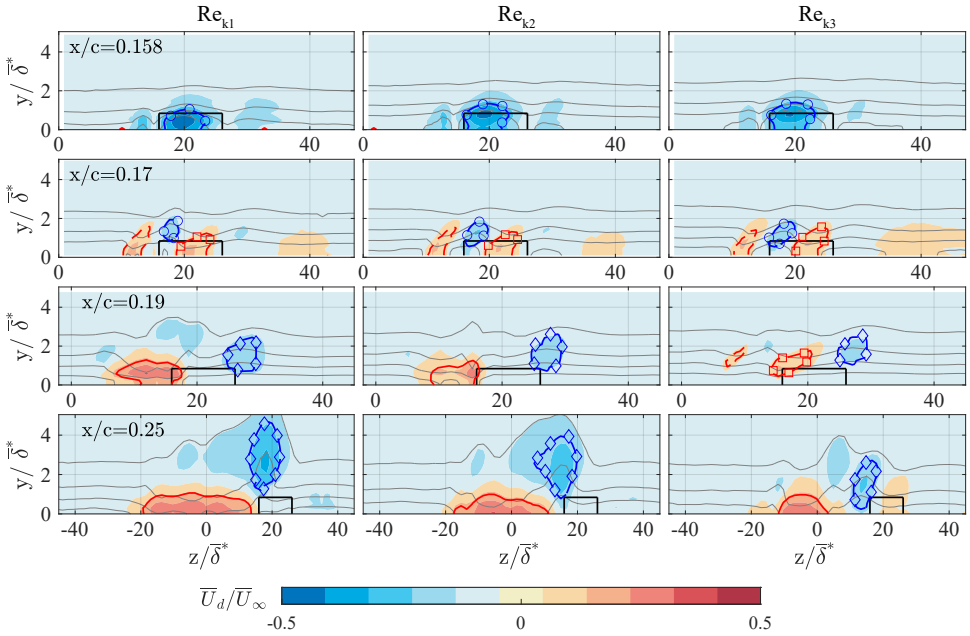

Figure 4.4: $\overline{U}$ contours in yz plane for the three $\mathrm{Re_k}$ at different x/c locations. Low-speed region in the IDRE wake ($L_1, \circ$), outboard low-speed region ($L_2, \diamond$), inboard high-speed region (H_1, - - line), outboard high-speed region ($H_2, \square$), merged high-speed region (*HM*, full red line). Velocity isolines plotted every 20% of $\overline{U}_\infty$ (gray lines); element location (black rectangle).

low-speed regions in the wake and on the inboard side of the element rapidly drops to 0, while the high-speed structures' amplitude grows prior to their merging. Further downstream, the merged high-speed region grows up to a saturation amplitude level indicative of turbulence onset [43, 55, 75, 93, 102].

In addition to localised absolute amplitude estimations, Andersson *et al.* [5] proposed a relative streak amplitude metric, i.e. $\mathrm{A_{And}(x)}$=0.5* [max($\overline{U} - \overline{U}_b$) - min($\overline{U} - \overline{U}_b$)]. Based on this criterion, for the present investigation, the maximum disturbance amplitude in the element vicinity is estimated to be $0.29\overline{U}_\infty$, $0.28\overline{U}_\infty$ and $0.25\overline{U}_\infty$ respectively for decaying $\mathrm{Re_k}$. For 2D boundary layers, a critical streak amplitude of $0.2\overline{U}_\infty$ is identified as a sufficient condition for the laminar breakdown of the developing velocity streaks. Hence, the streak amplitude values resulting from the present study, indicate a similar transitional process is dominating the considered 3D set-up. This indicates that the IDRE is introducing flow perturbations that rapidly develop in the element's wake and initiate a transitional process guided by the breakdown of the high-/low-speed streaks structures. However, based on the observations reported so far in this scenario, classical CFI is largely absent, as the IDRE wake is dominated by the developing system of low- and high-speed streaks. The role of the crossflow velocity component present in the baseflow appears to be limited to the introduction of asymmetry observed in the topology of the turbulent

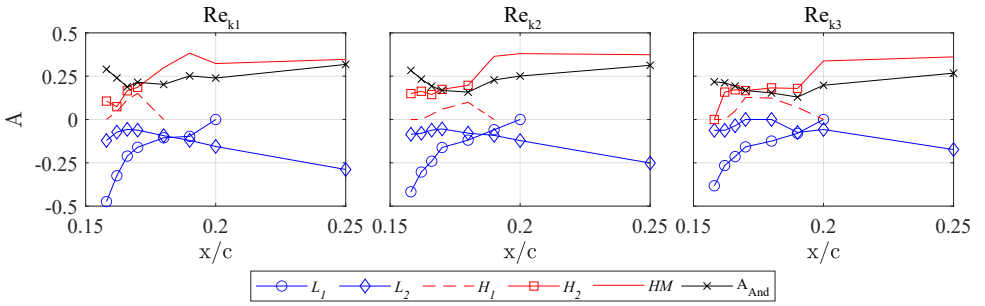

Figure 4.5: Amplitude estimation of near-element flow structures for Re_{k_1}=251, Re_{k_2}=222 and Re_{k_3}=198. Colours and symbols identify structures as in figure 4.4. Andersson *et al.* [5] amplitude definition (A_{And}, X).

wedge.

4.4. Unsteady Perturbations Characteristics

Despite giving relevant insights on the dominant flow structures developing in the downstream vicinity of the element, the stationary disturbance analysis does not fully characterize the transitional process. To identify the path towards turbulence onset and to further clarify the nature of the developing instabilities, the unsteady disturbance fields are considered hereafter.

Andersson *et al.* [5] identify two main types of unsteady structures supported by the developing stationary streaks in the downstream vicinity of an IDRE in 2D flow. Based on the aforementioned relative amplitude metric (A_{And}), they determine streak amplitudes higher than $0.26\overline{U}_\infty$ as sufficient to develop streak breakdown due to so-called sinuous modes, associated with the stationary spanwise shear in the element wake. Instead, for a streak amplitude larger than $0.37\overline{U}_\infty$, the varicose mode resulting from a 3D shear layer instability is dominating the disturbance field. Instabilities dominated by varicose symmetry, are found to be amplified in the wake flow of IDREs in many 2D configurations, even when, according to linear stability theory, the dominant flow instability mode is of a sinuous nature [24, 25]. However, the roughness configurations considered by Bucci *et al.* [24, 25], all feature a shear ratio of approximately 1.5-2, which is much higher than the cases presented in this investigation (i.e. $k/\delta^* \simeq 0.85$-0.9). The single-point HWA measurements performed in the current investigation prevent the extraction of information regarding the relative phase of developing unsteady disturbances. As a consequence, the collected set of data cannot provide a conclusive characterization of the nature of the vortex shedding occurring aft of the IDRE. Nonetheless, based on the works discussed beforehand by Andersson *et al.* [5], Loiseau *et al.* [93] and Bucci *et al.* [25], and considering the streak amplitude thresholds [5], the element aspect ratio ($k/d \simeq 0.08$) [93] and the element shear ratio ($k/\delta^* \simeq 0.85$-0.9) [25] of the current set-up, sinuous type of instabilities could dominate the shedding in the element's wake. Nevertheless, the aforementioned works are DNS computations performed on Blasius BLs, hence they do not take into account

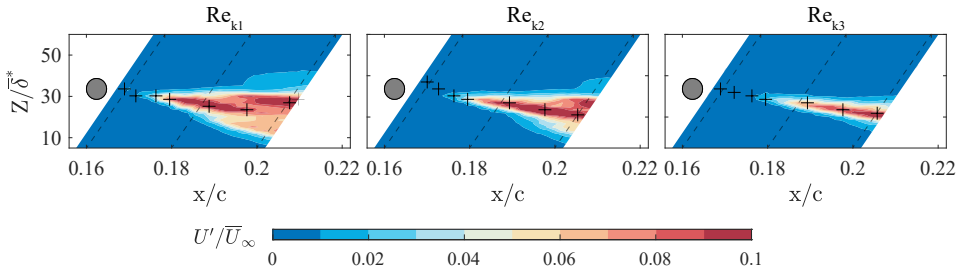

Figure 4.6: U' contours at constant wall-normal distance y/$\overline{\delta}^*$=1.7 for Re$_{k_1}$=251, Re$_{k_2}$=222, Re$_{k_3}$=198. Highest U' locii (+) computed at the same chord location of the acquired yz planes; IDRE top view (grey circle).

the combined effect of the wing sweep angle and the chordwise variation of the pressure gradient, both affecting the local boundary layer flow stability, possibly modifying the nature and growth process of the developing instabilities. In the following section, an examination of the stationary velocity gradients and related shear layers is provided, to incur a more reliable estimation of the developing instabilities' nature.

4.4.1. Unsteady Perturbation Fields

To localize the flow field regions characterized by high fluctuations, the standard deviation of the point-wise time-dependent hotwire velocity signal (U') is considered. The U' fields computed from the HWA measurements in the Xz plane are reported in figure 4.6. For all three Re$_k$ cases, the velocity fluctuations are concentrated in the flow region corresponding to the IDRE direct wake and the later development of turbulent flow, in agreement with the orientation and configuration of the steady flow structures previously observed (figure 4.3). Similar to what was reported by previous works [13, 80, 93], the areas of higher fluctuations develop in correspondence to the low-speed streaks, hosting the turbulent portion of the flow. Moving downstream, the opening of the wedge region is accompanied by a corresponding spatial (spanwise) spreading and an overall increased level of unsteady fluctuations. This effect is less visible in the Re$_{k_3}$ case, for which the developing instabilities are relatively weaker and the laminar breakdown occurs at more downstream chordwise locations.

Comparable flow features can be identified in the yz planes reported in figure 4.7 for the near-wake flow and figure 4.8 further downstream. From the near-wake flow fields, a region of intense velocity fluctuations on top of the IDRE can be recognized. In previous investigations [1, 22, 76], this flow region is identified as responsible for the origin of the cylinder eddy shedding, which induces an increased level of unsteadiness in correspondence to the IDRE wake. A region of weaker unsteadiness is located on the inboard side of the IDRE, while almost no significant fluctuations are present in the rest of the flow field. As evolving downstream, the unsteady region located on the IDRE top side expands along its flanks, possibly guided by the horseshoe vortex legs development [10, 93]. On the other hand, the fluctuations region located on the inboard element side rapidly decays. Further downstream, for the Re$_{k_1}$ and Re$_{k_2}$ cases, the stationary high- and low-speed streaks alternation develops and the

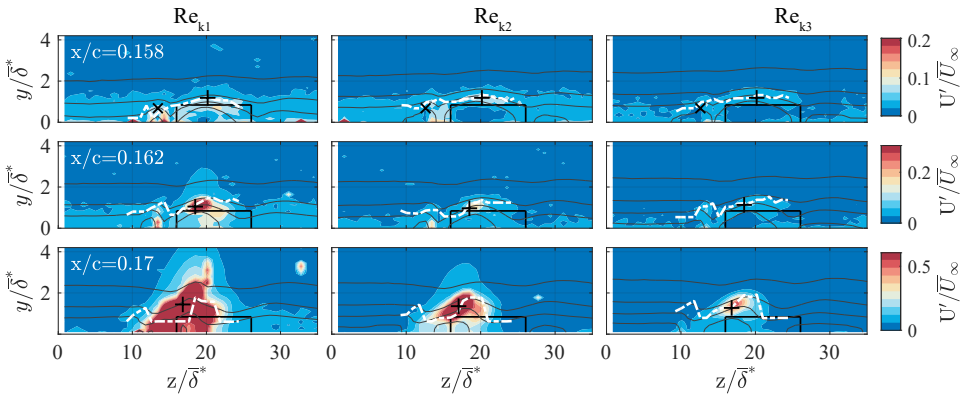

FIGURE 4.7: U' contours in yz plane for the three Re_k at different x/c location. Velocity isolines plotted every 20% of $\overline{U}_\infty$ (full lines); $\frac{\partial \overline{U}}{\partial y}$ gradient maximum (i.e. inflection point) (white - - line); maximum fluctuation locii on IDRE top side at which spectra (figure 4.10) are extracted (+); maximum fluctuation locii on the IDRE side (X) at x/c=0.158.

unsteady core broadens and covers a wider portion of the BL both in the z and y directions. The Re_{k_3} case is characterized by comparable flow evolution, even if the overall fluctuations are weaker and the broadening due to turbulence onset is visible at relatively more downstream chord locations.

Similar to previous analysis [52], the wall-normal and spanwise gradients of the stationary velocity field are investigated, providing interesting insights regarding the nature of the dominant unsteady instability. For the considered configuration, the wall-normal mean velocity gradients (acting on the local BL velocity profile and the small length scale of the element height) are considered to have a stronger effect on the flow with respect to their spanwise counterparts (acting on a larger length scale associated to the wedge width). Therefore, the wall-normal gradient $\frac{\partial \overline{U}}{\partial y}$ is first considered and computed at each spanwise location.

An inflection point in the BL velocity profile is a typical source of inviscid instabilities. Inflection points are weakly identifiable on the $\overline{U}$ profiles, however, they correspond to a local maximum or minimum of the wall-normal gradient of the mean velocity profile, as well as to a null value of the mean velocity profile secondary derivative in y. Therefore, figure 4.9(a-c) reports the $\overline{U}$, $\frac{\partial \overline{U}}{\partial y}$ and $\frac{\partial^2 \overline{U}}{\partial y^2}$ profiles extracted for the three Re_k cases at a fixed chord location of x/c=0.162 and spanwise position located inside the wake of the element (i.e. $z/\overline{\delta}^*$=19.5). The corresponding U' profiles are also reported in these graphs and multiplied by a factor of 10 to ease visualization. It is evident that for the considered chord location the $\frac{\partial \overline{U}}{\partial y}$ maximum coincides with the U' maximum. Accordingly, the same y-location corresponds to the null value of the second derivative profile, i.e. $\frac{\partial^2 \overline{U}}{\partial y^2}$, thus identifying an inflection point of the $\overline{U}$ profiles. Similar behaviour is observed at most spanwise locations where inflectional points appear within the wake. Such inflection points are not directly visible in the BL velocity profiles reported in figure 4.9, however, their wall-normal location is

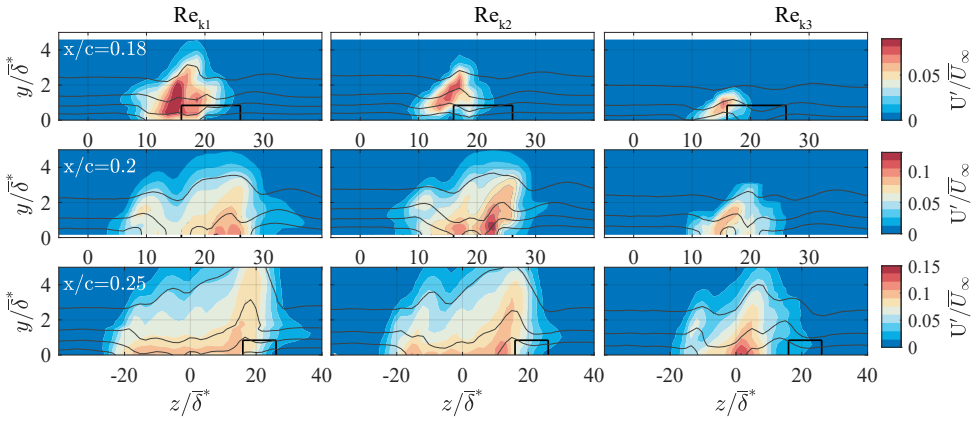

Figure 4.8: U' contours in yz plane for the three $\mathrm{Re_k}$ at different x/c location. Velocity isolines plotted every 20% of $\overline{U}_\infty$ (full lines).

shown by the white dashed line reported in the contours of figure 4.7. The observed correspondence suggests that the development of the dominant instabilities strongly relates to the wall-normal shear layer evolution [52]. The extracted fluctuation spectra at these locations (figure 4.10) further confirm this connection, showing the presence of a main high-amplitude peak and increasingly amplified harmonics as $\mathrm{Re_k}$ is increased. Hence, the inflectional BL profile inherently contributes to the instabilities sustainment and growth process, however, in the considered near-critical amplitude range, a different mechanism is responsible for initiating the unsteady disturbances (as further discussed in §4.4.2). The correspondence between the fluctuation amplitude local maxima and the gradient maxima is lost at more downstream locations as the flow becomes turbulent. This is already visible at x/c=0.17 for case $\mathrm{Re_{k_1}}$ (figure 4.7), therefore, the maximum gradient location is not reported in the flow fields of figure 4.8 for the sake of clarity.

A similar analysis can be performed for the spanwise gradients of the mean velocity field. The standard deviation fields, along with the already discussed $\frac{\partial \overline{U}}{\partial y}$, show that the region of higher fluctuations lies at a wall-normal location of $y/\overline{\delta}^* \simeq 1$ in the element vicinity. Therefore, to visualize the $\frac{\partial \overline{U}}{\partial z}$ gradient profile, the spanwise mean velocity and fluctuation standard deviation profiles are extracted at the same y-location. The $\frac{\partial \overline{U}}{\partial z}$ is then computed for these velocity profiles. The results are reported in figure 4.9(d-f) for x/c=0.162 at all three $\mathrm{Re_k}$ numbers measured. The spanwise gradient behaviour confirms that the low-speed streaks are the regions containing higher unsteady fluctuations. As stated previously and in agreement with previous works [13, 80, 93], the minimum of the velocity appears to be aligned with the maximum of the fluctuation amplitude.

Considering the reported results, the developing instabilities strongly relate to the region of inflectional velocity fields in the element wake and the related shear layers, similar to the results of numerical and experimental investigations dedicated

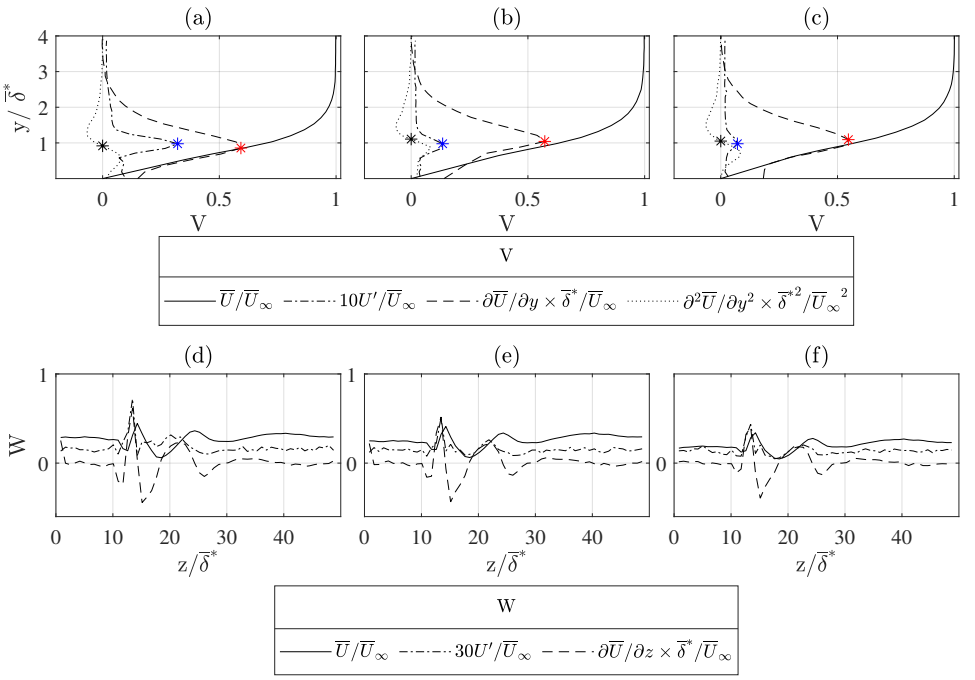

Figure 4.9: (a, b, c) $\overline{U}$ wall-normal profile, $\frac{\partial\overline{U}}{\partial y}$ gradient profile, $\frac{\partial^2\overline{U}}{\partial y^2}$ profile and U' wall-normal profile extracted at $z/\overline{\delta}^*$=19.5, x/c=0.162 for (a) Re_{k_1}=251, (b) Re_{k_2}=222, (c) Re_{k_3}=198. Maximum of $\frac{\partial\overline{U}}{\partial y}$ gradient profile (red $*$) and maximum of fluctuation amplitude profile (blue $*$); inflection point of $\frac{\partial^2\overline{U}}{\partial y^2}$ profile (black $*$). (d, e, f) $\overline{U}$ spanwise profile, $\frac{\partial\overline{U}}{\partial z}$ gradient profile and U' spanwise profile extracted at $y/\overline{\delta}^* \simeq 1$, x/c=0.162 for (d) Re_{k_1}=251, (e) Re_{k_2}=222, (f) Re_{k_3}=198.

to IDREs in 2D BL. This behaviour suggests that, in analogy with the 2D cases, shedding phenomena near occurring in the IDRE vicinity play a dominant role. Additional information to further ascertain these dominant instabilities' nature, can be inferred by analysing the features of the frequency spectra extracted from the time-resolved velocity signals. Further confirming the observations from the analysis of the stationary disturbance fields, locally-generated CFI do not appear to manifest or influence the near-element flow development [22, 84].

4.4.2. Spectral and Intermittency Analysis

The time-dependent velocity signal is analysed to extract the frequency spectra in correspondence to the maximum velocity fluctuation locii, indicated with the black cross in figure 4.7. The velocity signal power spectral density (PSD) is computed through a Welch [179] periodogram procedure implemented in Matlab, resulting in a final frequency resolution of 25Hz. The extracted spectra are collected in figure 4.10, and clearly show the higher amplitude of fluctuations present in the IDRE

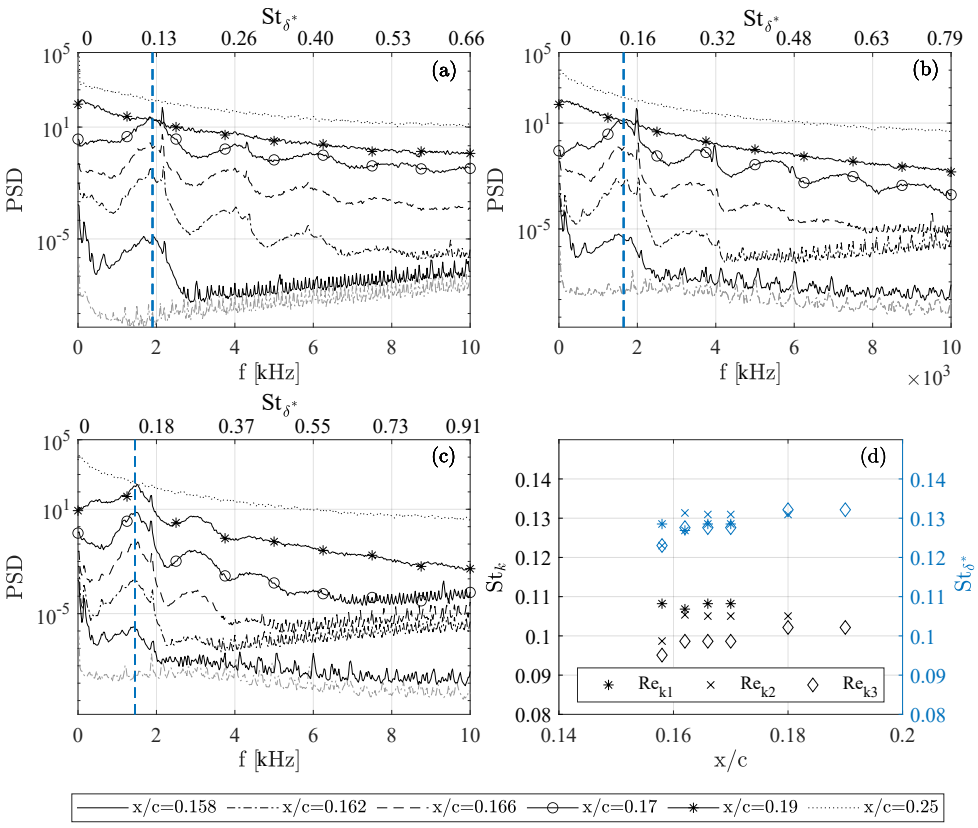

Figure 4.10: (a, b, c) Frequency spectra extracted for different Re_k in correspondence to the maximum fluctuation amplitude region for each chord location acquired. For visualization purposes, the spectra pertaining to each chord location are offset by a decade. Freestream flow frequency spectra extracted at x/c=0.158 (grey -. line); spectral peak (blue - - line). (a) Re_{k_1}=251, (b) Re_{k_2}=222, (c) Re_{k_3}=198. (d) St_k and St_{δ^*} extracted for different Re_k and chord locations at the location of maximum std.

wake with respect to the freestream flow regions (grey lines in the plots) [13, 79]. The near-wake flow is characterized by a strongly tonal behaviour, with PSD peaks identifying dominant frequencies in the 1.4-1.9kHz bandwidth. Specifically, the peak frequency (f_1) monotonically decreases with Re_k , corresponding to 1.85kHz, 1.65kHz and 1.45kHz for the three Re_k cases. Moreover, harmonics of f_1 are also well defined between x/c=0.162 and x/c=0.17 for Re_{k_1} and Re_{k_2}, while they persist even more downstream for Re_{k_3}. The flow region characterised by tonal behaviour can be associated with the near-wake region. At more downstream locations (x/c>0.17, identifiable with the far-wake region), the spectra are characterized by overall higher fluctuations level, which is spread over a broader frequency range without identifying a clear spectral peak. This behaviour is indicative of the breakdown of the laminar structures and is observed with a $\simeq$3% chord delay for Re_{k_3}, in agreement with the

results discussed beforehand and confirming that the instabilities developing in this lower Re_k case are milder. The observed spectral behaviour bears a strong similarity to 2D boundary layer transition cases, thus indicating that the crossflow velocity component has a limited effect on the onset of the unsteady disturbance. This agrees well with the comparable 2D and 3D boundary layers flow topology observed by Kurz & Kloker [84] and is firstly confirmed experimentally by the presented investigation.

In particular, the comparability between the two BL scenarios lends some useful observations for the present cases. In a typical 2D boundary layer configuration, the tonal behaviour observed in the element vicinity can either be driven by the amplification of a local instability mode [24] or by the quasi-resonance of a marginally stable mode, originating from background noise or external disturbances and enhanced by the IDRE [25]. Past investigations highlighted that the occurring behaviour is strongly related to multiple geometrical and freestream parameters, among which Re_k, k/d, k/δ^* and T_u [24]. In 3D boundary layers, the pressure gradient and sweep angle may also play an additional and relevant role, as they significantly affect the local BL stability and evolution. In this investigation, a direct comparison between the experimentally identified dominant instabilities and the dominant modes identified by a numerical stability solution is not available. Therefore, it is not possible to provide conclusive proof regarding the nature of the IDRE behaviour. Nonetheless, the extremely low level of freestream turbulence characterizing the wind tunnel flow in the present investigation ($T_u/\mathbf{U}_\infty$=0.025 [152]), much lower than that considered in 2D investigations [24]) tend to limit the role of the resonating behaviour of the IDRE. This, in turn, would point towards the amplification of instability modes as the main mechanism responsible for the unsteadiness development. Such behaviour would agree with the fact that the transitional flow scenario of the current set-up is dominated by the rapid amplification of convective instabilities, which are typically enhanced by the IDRE [115]. Additionally, as visible from the spectra reported in figure 4.10, the dominant frequency peak is relatively broad. Accordingly, in the element vicinity, a small range of frequencies can be excited, inducing a range of instability modes initially growing due to non-modal interactions and transient phenomena [24, 165, 166, 183]. Further sustaining this hypothesis, recent investigations [199] showed that transient phenomena can be relevant in the initial phases of the receptivity process of a DRE array applied in a 3D boundary layer. These observations do not exclude the possibility of exciting weaker modes by means of the roughness resonant behaviour, nonetheless, this mechanism would play a less relevant role in the transitional process.

Towards confirming that the identified tonal behaviour can be associated with the amplification of BL instabilities, the extracted dominant frequencies are compared to those pertaining to the element shedding [76, 80], by estimating the local Strouhal number. For this analysis, the Strouhal number is defined as $St_{\delta^*}=f_1 \times \delta^*/|\mathbf{u}_k|$, or as $St_k=f_1 \times k/|\mathbf{u}_k|$, where k is the element height and $|\mathbf{u}_k|$ is the unperturbed boundary layer velocity at height k extracted from the BL numerical solution for the three considered Re_k [1, 76, 102]. The former definition (St_{δ^*}) proved helpful in comparing the spectral characteristics within a universal frame [76], while the St_k is strongly dependent on the Re_k as it also accounts for the local BL development and its relation to the element geometry. Both St number definitions are based on the reference

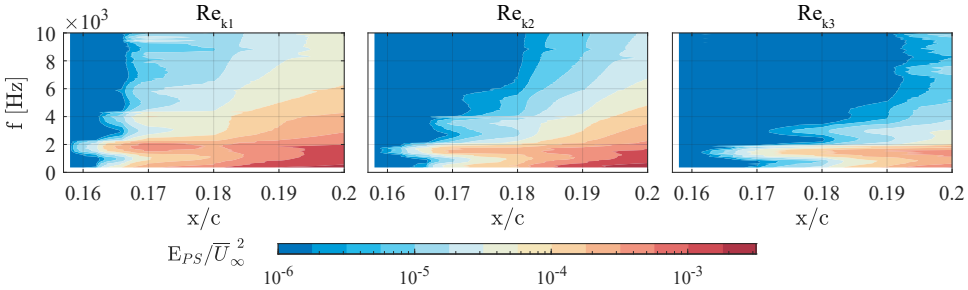

Figure 4.11: $E_{PS}/\overline{U}_{\infty}^{2}$ contours extracted from the integration of the spectral power computed through the Welch periodogram.

frequency corresponding to the maximum of the PSD spectra at each chord location considered and are collected in figure 4.10. The tonal behaviour outlined by the reported spectra reflects in the St_{δ^*} values, which retain an almost constant value in the range of 0.12-0.13 throughout all the cases considered. On the other hand, the St_k values are weakly scaling with the Re_k. A direct comparison between the St numbers extracted in this investigation with cases presented in literature is difficult to achieve, as due to the 3D nature of the considered BL, the Re_k and k/d considered herein lay outside of the typical parameter range explored in 2D boundary layer investigations [76, 80, 102]. Nonetheless, in the element vicinity, the St_k values fall within the range of values generally associated with cylinder shedding [76, 80], namely $St_k \simeq 0.09\text{-}0.12$. This further suggests that the instability onset process is initiated and dominated by the IDRE shedding. Nonetheless, the St number definition loses its relevance once turbulence begins to play an important role in the BL, as the tonal behaviour and shedding are overcome by the increased level of broadband fluctuations. As such, St values are only reported for the chord locations characterized by spectra with a clearly identified frequency peak (i.e. upstream of x/c=0.2).

The performed Welch's periodogram analysis additionally provides the spectral power of the acquired point-wise velocity signal. Hence, the spectral power values corresponding to each frequency can be integrated into the yz plane to obtain an estimate of the associated integral energy (hereafter named E_{PS} and non-dimensionalized by $\overline{U}_{\infty}^{2}$) and its location in the frequency space. The contours of the resulting integrated energy are reported in figure 4.11, using a logarithmic colour scale for visualization purposes. The strong tonal behaviour is confirmed for all three Re_k in the element vicinity. In particular, local energy peaks corresponding to the dominant frequency and its harmonics can be identified. The chordwise instability growth is initially accompanied by an energy growth of the sole dominant frequencies, while a global energy increase spread over the whole considered frequency bandwidth occurs with the turbulence onset. The spreading of spectral energy occurs more downstream for the lower Re_k cases, in agreement with the results previously reported.

Finally, the velocity signal intermittency (γ) is estimated [80, 120]. The resulting contours are reported in figure 4.12 for a set of chord locations between x/c=0.17-0.25. More upstream chord locations are not reported as they show no or little relevant

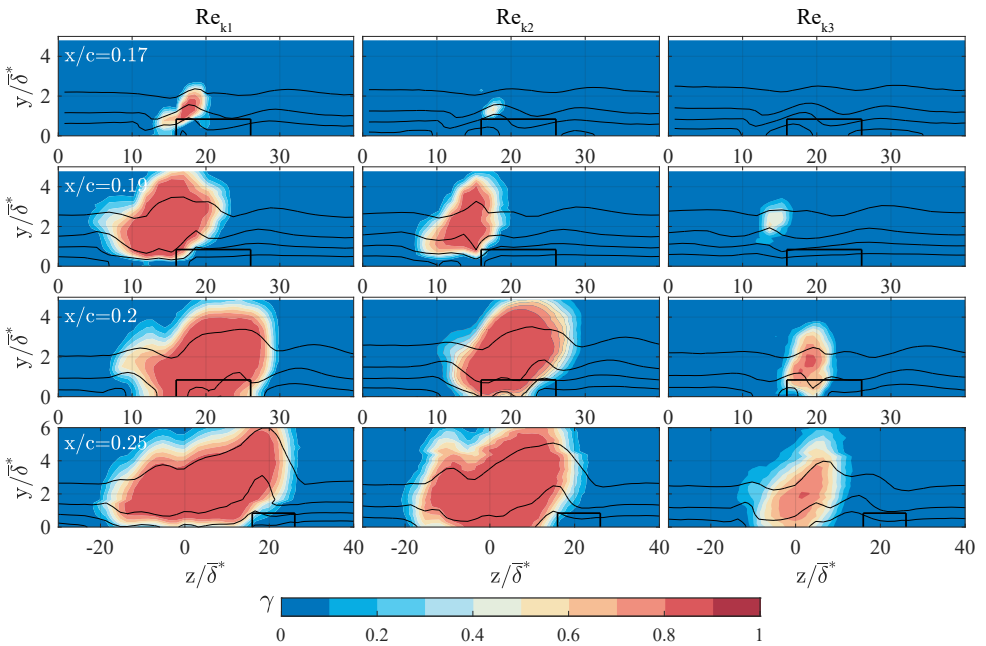

Figure 4.12: Intermittency contours for the three Re_k at the indicated x/c locations.

region of intermittency, i.e. γ is approximately zero in the whole domain. Nonetheless, the well-developed $\gamma \simeq 1$ regions characterizing the Re_{k_1} case are indicative of the early development of the turbulent wedge observed for this super-critical case. The Re_{k_2} case closely follows this behaviour, displaying a highly turbulent region quickly extending both in the spanwise and wall-normal directions as moving downstream. Minor turbulence spreading is observed for the Re_{k_3} case, in agreement with all other observations reported for this case. The analysis of the intermittency highlights the asymmetric development of the turbulent flow region. Especially considering the Re_{k_3} case, thanks to the slower turbulence spreading, the turbulent structure is observed to shift towards negative z coordinates while moving downstream, in agreement with the asymmetrical wedge opening observed in figure 4.2. Moreover, it is also possible to identify the overhang effect of the turbulent region, i.e. the sides of the $\gamma > 0$ region always appear to be separated from the wall by a thin laminar layer. Overall, the γ evolution confirms how the higher fluctuation region is initially located in the element wake, while all three Re_k show a turbulent region spreading in the spanwise and wall-normal directions at x/c=0.25, with high γ values characterizing a wider portion of the domain.

In conclusion, the collected results indicate that the developing near-wake instabilities are strongly related to the wall-normal shear layer evolution, and are effectively sustained by the inflectional nature of the BL velocity profile. The analysis of the standard deviation and gradient peaks allows for the identification of an inflection point that coincides with the y-location of maximum fluctuations developing on top

of the element. Based also on the observed dominant frequency, the developing instabilities are initiated by the shedding process occurring on the element top. The introduced instabilities persist and grow in the IDRE wake, influencing a wider region of the acquired domain and leading to the formation of a turbulent wedge. Overall, the near-element flow development and the instability onset process are considered to be qualitatively comparable to the one observed in 2D boundary layer studies, confirming that classical modal CFI are not dominating the present transitional scenario. Nonetheless, the presence of the crossflow velocity component in the BL baseflow, fundamentally conditions the downstream flow development in the 3D boundary layer scenario, introducing a flow asymmetry affecting the evolution of both steady and unsteady flow features.

4.5. Concluding Remarks

The measurements presented in this Chapter investigate the transitional process of a 3D boundary layer forced by an isolated cylindrical roughness element. By varying the freestream velocity, the flow is investigated at super-critical (i.e. Re_{k_1}, causing flow tripping aft of the element location) and two critical (i.e. Re_{k_2}, Re_{k_3}) conditions through IR thermography and HWA. Detailed geometrical parameters of the measured configurations are reported in table 4.1.

The current set-up develops a base flow topology comparable to the dominant flow features identified in 2D boundary layers, suggesting that IDRE-induced CFI are not dominant in the considered 3D boundary layer. This can be traced back to the relatively high amplitude of the applied IDRE, which introduces steady and unsteady disturbances that rapidly develop and cause flow tripping. Nonetheless, notable differences between IDRE-induced transition in 2D and 3D boundary layers are identified. These mostly derive from the presence of the crossflow velocity component in the BL base flow, which induces asymmetric downstream development of the identified near-element flow features.

Specifically, the turbulent flow region forms at a finite distance from the element location (i.e. $\Delta x_0/c$=0.03-0.12 for decreasing Re_k [76]), and evolves following an inboard-tilted trajectory. This is described by the parameter α_{skew}, which is found to correspond to the trajectory of classical modal crossflow vortices developing in the same geometry at higher Re (i.e. a 6-8° angle with respect to the X direction, [154]).

Additionally, the stationary near-element flow topology features one main low-speed flow region developing aft of the element in correspondence to its wake. This is accompanied by the alternation of two high-/low-speed streaks on its inboard and outboard sides. The high-speed structures evolve individually in the IDRE vicinity, however, they merge further downstream and substitute the low-speed wake streak. This high-speed region localizes in correspondence to the turbulent wedge region, growing asymmetrically up to saturation.

On the other hand, the crossflow velocity component has a limited effect on the unsteady instabilities onset and dominant frequencies. Detailed analysis of the unsteady velocity signal, suggests that the unsteady instabilities are initiated by the shedding process occurring on top of the IDRE. This compares well with previously investigated 2D boundary layer scenarios and is firstly confirmed for a 3D boundary

layer configuration in the present investigation. Additionally, the y-location of the maximum fluctuation region corresponds to the wall-normal gradient maximum, indicating that the inflectional BL profile inherently contributes to the unsteady instabilities sustainment and growth process. Furthermore, the spectral analysis of the time-dependent velocity signal, shows a tonal behaviour dominating the near-element flow development (upstream of the onset of turbulence), with dominant frequency monotonically varying with $\mathrm{Re_k}$. The definition of the Strouhal number based on the identified frequency peak provides values that lay within the shedding range identified in the literature (namely $\mathrm{St}_{\delta^*} \simeq$ 0.12-0.13 and $\mathrm{St_k} \simeq$0.09-0.12) [1, 76, 102]. However, despite the similarities observed in the near-element flow region, the baseflow crossflow component actively conditions the instabilities downstream development and the entire transition topology. This is confirmed by the asymmetric spanwise and wall-normal broadening of the high-fluctuations region and the area of elevated intermittency (representative of the turbulent flow region).

5

The Near-element Flow Topology of a DRE Array

This Chapter experimentally investigates the dominant flow features developing in the vicinity of a DRE array applied in a swept wing boundary layer. High-resolution tomographic flow diagnostics are employed to acquire all three velocity components in the array vicinity. The BL receptivity and the near-wake stationary flow topology are investigated for a critical and a super-critical DRE amplitude. In addition, transient growth and decay processes are identified in the near-wake flow region, fundamentally conditioning the modal CFI onset.

ZOPPINI, G., MICHELIS, T., RAGNI, D., & KOTSONIS, M. 2022.The near-wake of discrete roughness elements on swept wings: tomographic PTV measurements. *12th International Symposium on Turbulence and Shear Flow Phenomena (TSFP12).* [193]

ZOPPINI, G., MICHELIS, T., RAGNI, D., & KOTSONIS, M. 2023. The near-wake of discrete roughness elements on swept wings. *Journal of Fluid Mechanics.* [194]

ZOPPINI, G., SEQUEIRA, A.D., MICHELIS, T., RAGNI, D., & KOTSONIS, M. 2023. The Near-Wake of Super-Critical Discrete Roughness Elements on Swept Wings. *AIAA, SciTech 2023 Forum.* [198]

5.1. Introduction

Important insights on the near-element flow topology and instability development are offered by the numerical and experimental investigations summarized in Chapter 1, section §1.5. In particular, DNS investigations by Kurz & Kloker [84] and Brynjell-Rahkola *et al.* [23] provide detailed description of the near-element flow topology for DRE arrays located in both 2D and 3D boundary layers. Additionally, White *et al.* [183] observed transient growth phenomena occurring in the near-wake region of DRE arrays applied in a 2D boundary layer. These transient phenomena are considered to be fundamental for the development of the near-wake flow, and play a fundamental role in the onset of modal instabilities or boundary layer transition [20, 39]. Nonetheless, a correlation between the forcing geometry and the CFI onset is still missing in the considered works. This remains an open subject which requires further understanding and insights on the near-wake flow development in order to determine its role on the initial phases of the receptivity process.

Towards this objective, the last part of Chapter 3 is dedicated to the characterization of the DRE near-wake in a 3D boundary layer. The obtained results, extend the possible presence of transient and non-modal mechanisms to the near-wake of DRE arrays located in swept wing boundary layers. However, the proposed experimental measurements provide an insufficient spatial resolution to identify the algebraic growth of the instabilities, which is a fundamental trait of the transient growth process. Accordingly, the role of the transient growth mechanism in conditioning the modal CFI onset, as well as their dependence on the external forcing configuration, could not be clearly outlined. The available literature framework, shows that forcing cases with sub-critical amplitude can be approximated by a *k-dependent* receptivity process [e.g. 83, 166], as they are represented through a direct relation with k and without depending on the effective DRE shape. Higher amplitude elements follow a receptivity process with no clearly outlined dependence on the external forcing geometry. Therefore, a clear receptivity model for the characterization of the critical amplitude cases considered in the present investigation is still missing. Additionally, in the super-critical amplitude forcing the near-wake flow receptivity is likely dominated by mechanisms leading to bypass transition processes [4, 52, 84, 151].

Overall, the near-wake mechanics is considered to substantially contribute to the receptivity process of stationary CFI. Nevertheless, a systematic experimental flow field exploration in 3D boundary layers (i.e. swept wings) is currently not available. As such, this Chapter aims at deepening the near-wake flow analysis confirming the presence of transient growth mechanisms and characterizing their role in the initial conditioning of the modal CFI. In particular, the BL receptivity to DRE arrays of various amplitudes is characterized, delivering a conceptual model that details the 3D boundary layer receptivity to critical and super-critical DRE thus extending the transitional paths model proposed by Morkovin [108]. A first-of-its-kind experimental investigation of the near-element flow field is provided, accessing the 3D time-averaged velocity fields in the element vicinity through specialized high-resolution dual-pulse tomographic Particle Tracking Velocimetry (PTV) and the shake-the-box algorithm. The presented experimental data detail the near-element stationary flow topology and identify the dominant flow structures and their spatial organization both for

critical and super-critical DRE amplitudes. The modal composition of the flow field is investigated by means of a spanwise spatial spectral analysis. Additionally, the high spatial resolution of the acquired data details the total perturbation as well as the amplitude and energy growth associated with individual modes in the element near-wake region. Finally, the flow development is monitored under varying DRE configurations, investigating the receptivity of instabilities to the forcing amplitude and wavelength.

5.2. Experimental Set-up and Methodology

The experimental acquisitions presented in this Chapter are performed in the LTT measuring the M3J wing model pressure side. More details regarding the wind tunnel facility and the employed wing model can be found in section §2.1.1.

The developing flow fields are measured for various roughness configurations with fixed angle of attack α=-3.36° and various Re_{c_X} (i.e. Re_{c_X}=1.35×10^6, 1.85×10^6, 2.17×10^6). Global flow features are acquired using IR thermography (section §2.3.1), however this in only employed as a visualization technique ensuring proper development of the dominant flow features. Consequently, the IR acquisitions are not discussed throughout this Chapter for the sake of brevity. Dual-pulse tomographic PTV is instead employed to acquire volumetric time-averaged velocity fields as described in section §2.3.4. The wing-attached reference system (i.e. xyz) is employed to analyse the PTV velocity fields. The experimental acquisitions of this Chapter are complemented by stability solutions computed for the three measured Re_{c_X} each based on the LPSE routine described in section §2.4.

5.2.1. DRE Arrays Configuration

DRE arrays are employed in this investigation to detail the near-element flow topology and its role in the receptivity process. The results reported in Chapter 3 outline that a downstream shift of the forcing array location induces CFI with smaller initial amplitude while keeping the near-element flow topology almost unaltered. Hence, the configurations considered in this Chapter feature DRE arrays placed at $\mathrm{x_{DRE}/c}$=0.15, where the unperturbed (i.e. no DRE applied) experimental BL displacement thickness is $\overline{\delta}^*$=0.44mm (corresponding to δ_{99}=1.4mm). In comparison, the boundary layer thickness at x/c=0.02 is estimated to be $\overline{\delta}^*$=0.14mm (corresponding to δ_{99}=0.6mm). While still extremely thin, the boundary layer at x/c=0.15 is sufficiently thick to be measured by the high spatial resolution optical velocimetry technique used in this Chapter. Additionally, the local growth rate of the modal CFI is described by $\partial N/\partial x$, where N is the N-factor evolution provided by the LST solution at Re_{c_X}=2.17 ×10^6. The $\partial N/\partial x$ value at x/c=0.15 is comparable with the value obtained in the vicinity of the dominant mode neutral point (i.e. within a 10% difference), validating the possibility of investigating the near-wake flow development for the downstream applied DRE array. The applied DRE arrays are manufactured as described in section §2.2, with main geometrical characteristics summarized in table 2.3.

Various forcing configurations are investigated to characterize the receptivity of the near-element flow features to the DRE amplitude (k) and forcing wavelength

(λ_{f1}). Specifically, DRE of heights k_1, k_2, k_3 and k_4, as well as three different forcing wavelengths are considered. Following the definition of $\lambda_i=\lambda_1/i$, forcing wavelengths $\lambda_{3/2}\simeq$5mm, $\lambda_1\simeq$8mm and $\lambda_{2/3}\simeq$11mm are measured. LST solutions computed at the lower and higher Re_{c_X} investigated, indicate that the most unstable CFI mode corresponds to wavelengths of 10mm to 8mm respectively (section §2.4). Hence, within the range of Re_{c_X} investigated in this Chapter, the λ_1=8mm mode is either the most unstable mode or among the most unstable modes the vicinity of x_{DRE}/cat all considered Reynolds number cases.

Throughout this Chapter, the distinction between the DRE near-wake and far-wake region is based on the near-element flow topology of the critical DRE forcing case. Specifically, the near-wake is considered to extend up to the chord location at which the primary stationary disturbance recovers a normal modal behavior (i.e. x/c=0.164), thus growing exponentially further downstream (i.e. in the far-wake). This aspect is further discussed in section §5.3 and illustrated in figure 5.7.

The measured forcing configurations can be described through a purely geometrical scaling offered by k/δ^* [145] and Re_k [58, 123]. Numerous investigations showed that the receptivity to roughness is *k-dependent* only for very small DRE amplitudes [83, 166]. However, previous investigations by White *et al.* [183] showed that for a 2D boundary layer, Re_k^2 offers a partial but valuable scaling of the near-element flow evolution. Additionally, Re_k proves successful in predicting the criticality of the considered forcing configurations. In particular, for the current set-up configurations featuring $Re_k\geq$200 behave super-critically (as shown in Chapter 3, [199]), therefore they are only considered in section §5.4 dedicated to the characterization of the near-element features of super-critical amplitude DREs.

The geometrical parameters corresponding to the investigated forcing configurations are reported in figure 5.1. A correlation of the considered cases to previous investigations can be obtained using the Von Doenhoff & Braslow [173] diagram, relating the critical Re_k to the inverse aspect ratio of the forcing elements (i.e. d/k) in 2D base flows. For the sake of conciseness a direct graphical comparison is omitted, however, the reference critical and super-critical cases (i.e. $Re_{c_X}=2.17\times10^6$ with DRE amplitude k_3 or k_4) respectively correspond to d/k=6.7, 5 and $\sqrt{Re_k}$=13.8, 18.1. Hence, the critical case falls on the lower bound of the transitional region identified by Von Doenhoff & Braslow [173], while the super-critical case falls well inside it.

5.2.2. Tomographic Dual-Pulse PTV

Volumetric dual-pulse PTV acquisitions provide a local description of the BL flow chordwise evolution, outlining the effects of the considered forcing configuration on all three velocity components. The experimental set-up is illustrated in section §2.3.4, with the main optical parameters summarized in table 2.5. Throughout this Chapter, the wall-normal direction (y) is non-dimensionalised by the experimentally measured unperturbed (i.e. no DRE applied) BL displacement thickness at x/c=0.165 for $Re_{c_X}=2.17\times10^6$, hereafter defined $\overline{\delta}^*$=0.46mm. The acquired xyz volumetric domain is centred at x/c=0.165 and extends for almost x/c=0.027, $y/\overline{\delta}^*\simeq6$ and z/λ_1=3.5 in the streamwise, wall-normal and spanwise directions respectively.

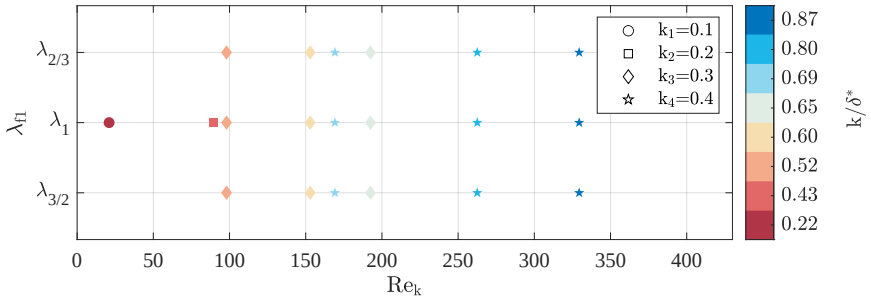

Figure 5.1: Geometrical parameters of the measured forcing configurations computed from numerical BL solutions. Colormap based on k/δ^*, symbols based on DRE height, legend indicating nominal element height [mm].

5

Velocity Fields Reconstruction and Processing

The time-averaged $(\overline{u}, \overline{v}, \overline{w})$ and standard deviation (u', v', w') velocity fields are obtained for all three velocity components in the xyz domain. For the sake of conciseness, the main data processing techniques adopted throughout this Chapter are hereafter briefly described as applied to $\overline{u}$, while the treatment of $\overline{v}$ and $\overline{w}$ follows a similar procedure. The wall-normal BL velocity profile $(\overline{u}_b)$ is estimated by averaging the $\overline{u}$ velocity signal along z for each fixed xy location. At each chordwise location, the freestream velocity U_∞ is estimated as the average of $\overline{u}_b$ for y> δ_{99}, and its value at x/c=0.165 is used to non-dimensionalize the three velocity components. The disturbance velocity field $(\overline{u}_d)$ is computed at each (x,y_*,z) as $\overline{u}_d = \overline{u}$(x,$y_*$,z) - $\overline{u}_b$(x, y_*), with y_* representing a fixed wall-normal location. The analysis of such velocity fields allows for the extraction of the amplitudes of the high- and low-speed streaks [5]. The wall-normal disturbance velocity profile $(\langle\overline{u}\rangle_z)$ is computed as the root mean square (rms) of the $\overline{u}_d$ velocity signal along z [123, 166]. Furthermore, a spatial Fast Fourier Transform (FFT) analysis is performed on the spanwise velocity signal at each xy location ($FFT_z(\overline{u})$), characterizing the BL spectral composition, as well as the development of the dominant spanwise mode and its harmonics. This allows for the computation of the total and the modal (i.e. per individual FFT mode) instability amplitude by integrating respectively $\langle\overline{u}\rangle_z$ or the individual FFT modes shape functions along y up to the local BL δ_{99} [47, 123]. This provides an estimation of the velocity disturbances growth and evolution along the airfoil chord. Following White *et al.* [183], the CFI energy is instead computed as $E(\overline{u})=\int_0^{\delta_{99}}(\langle\overline{u}\rangle_z)^2 dy$. The summation of the disturbance energy associated to each of the three velocity components, provides the total disturbance energy $E(\overline{\mathbf{u}})$. Similar processing is applied to the individual FFT shape functions in order to compute the modal energy evolution.

By considering all three velocity components available through the tomographic PTV measurement, the 3D coherent structures dominating the near-wake flow are identified by applying a vortex identification criterion, namely the Q-criterion [69]. The flow field is first decomposed into its spectral components and is reconstructed

accounting for a truncated set of Fourier modes to improve the data signal-to-noise ratio. The reconstructed domain includes the statistically represented flow field incurred by one DRE element, and is rotated to obtain a reference frame (x_R, y_R, z_R) with x_R aligned with the CF vortex axis, y_R coincident with y and z_R normal to the x_R-y_R plane. The corresponding time-averaged velocity components are named $\overline{u}_R$, $\overline{v}_R$, $\overline{w}_R$.

5.3. Critical Near-Element Flow

In this section the near-element flow topology of a critical amplitude DRE is investigated, clarifying the mechanisms dominating the receptivity process for varying amplitudes and forcing wavelengths.

5.3.1. Stationary Disturbance Topology

Direct characterization of the near-element flow topology and dominant stationary disturbances is obtained through the time-averaged and standard deviation velocity fields. The critical wavelength forcing configuration (i.e. $\lambda_{f1}=\lambda_1$) at $Re_k=192$ is considered hereafter as the baseline case for the stationary flow topology investigation. The corresponding disturbance velocity field ($\overline{u}_d$) is reported in figure 5.2(a-c), while figure 5.2(d-f) presents the temporal standard deviation contours (u').

Owing to the volumetric measurement, the stationary flow features dominating the near-element flow evolution can be identified in both the xz and yz planes. Specifically, the velocity contours in figure 5.2(a-c) reveal a low-speed streak developing aft of each DRE in correspondence to the element's wake. This low-speed region is accompanied by two high-speed streaks developing on its flanks. The resulting streak alternation corresponds well to the horseshoe vortex legs wrapping around and extending aft of the element, identified by previous investigations [10, 84]. In between neighbouring roughness elements the incoming BL maintains a laminar behaviour as the velocity disturbances introduced by each DRE are highly localized in correspondence to the individual element's wake. The identified stationary flow topology closely resembles the near-element flow of isolated DRE in 2D or 3D boundary layers [e.g. 10, 24, 93, 197]. This is also in agreement with the findings of Von Doenhoff & Braslow [173], in which the near-element behaviour of the individual elements of a DRE array was found to be comparable to that of an isolated DRE if they are arranged at a wavelength $\lambda_{f1} > 3d$. Nonetheless, due to the presence of the crossflow velocity component in the baseflow, the stationary structures identified in the near-element flow region follow an asymmetric downstream development [23, 84, 197]. In particular, in figure 5.2(a) the outboard high-speed streak (denoted by a solid line) is decaying in the downstream direction and is substituted by the development of an outboard low-speed streak (denoted by a dash-dot line). Instead, the inboard high-speed streak (indicated by a dashed line) persists until the end of the acquired domain albeit decreasing in amplitude. This results in a far-wake flow dominated by an almost periodic alternation of high- and low-speed regions, respectively induced by the evolution of the inboard high-speed streak and the merging of the outboard low-speed streak and the low-speed wake. The ensuing BL velocity modulation is a typical feature of a modal stationary

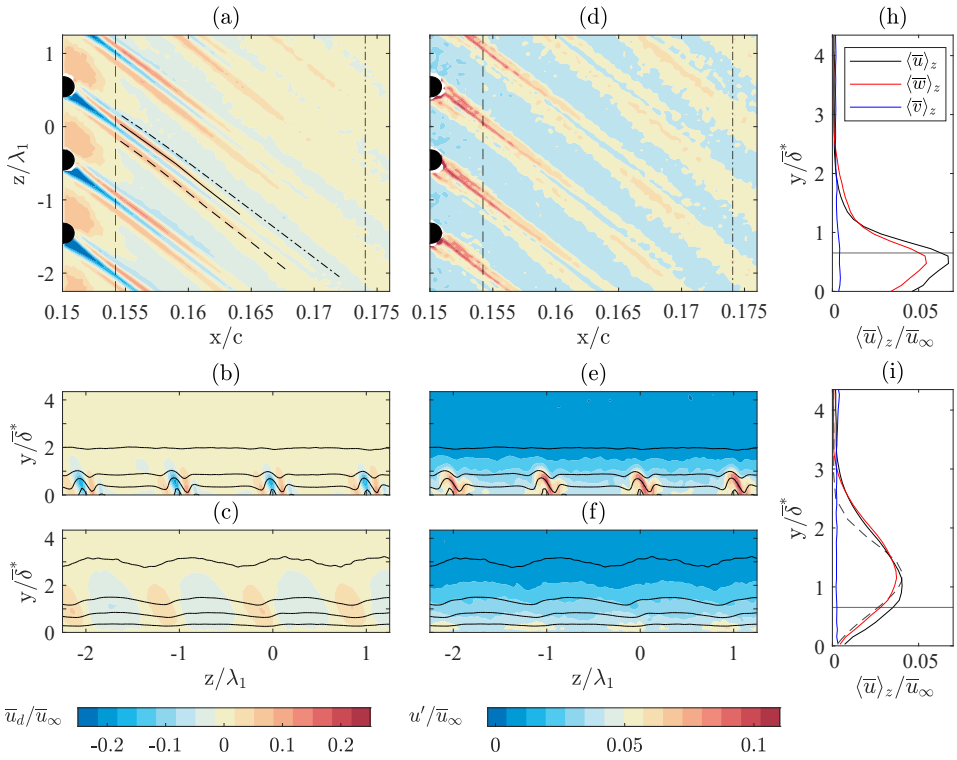

Figure 5.2: (a-c) $\overline{u}_d$ and (d-f) u' for forcing case $\lambda_{f1}=\lambda_1$, $Re_k=192$ (for k_3) in (a, d) the xz plane at $y=0.55\overline{\delta}^*$; (b, e) the yz plane at $x_1=0.154c$ (vertical dashed line in (a,d)) and (c, f) at $x_2=0.174c$ (vertical dash-dot line in (a,d)). Disturbance profiles at (h) x_1 and (i) x_2 for all three velocity components; element height (solid horizontal black line); LST λ_1 shape function (dashed grey line) scaled to match $\langle\overline{u}\rangle_z$ maximum; element height (horizontal full line).

CFI, resulting from the momentum redistribution across the BL induced by the crossflow vortices [figure 5.2(c), 16, 137]. Based on the observed development, a near-wake flow region can be defined (i.e. x/c<0.164) which is mostly affected by the stationary streak structures development, while the far-wake flow region (i.e. x/c>0.164) is mostly dominated by modal CFI development (as further discussed in figure 5.7). Furthermore, the identified streak structures develop by following a constant phase trajectory which is oriented at an angle of $\simeq 6°$ towards the inboard direction with respect to the freestream flow (i.e. the X direction). This mild tilting compares well to the angle forming between developing stationary crossflow vortices and the freestream velocity in the same set-up at more downstream chord locations, as experimentally measured and predicted by LST [152].

The standard deviation fields reported in figure 5.2(d-f) indicate that in the element vicinity the regions of higher unsteadiness are mostly located in correspondence to the identified streak structures. In particular, stronger unsteady velocity fluctuations appear at the interface between the outboard low-speed and high-speed streak,

representing a local high (mostly spanwise) shear region [13, 76, 79]. This suggests that the near-wake disturbances onset and downstream evolution are strongly related to the wall-normal and spanwise shear layers induced by the recirculation region developing in the element's wake [figure 5.2(e), 23, 197]. The overall level of unsteady fluctuations reduces further downstream accompanied by the progressive weakening of the streaks structures. Additionally, as the flow structures evolve downstream the higher fluctuation regions locally shift in correspondence to the inboard high-speed streak. Despite the observed early rise of strong unsteady disturbances, the overall transition scenario occurring in the present case appears to be driven by a typical modal CFI breakdown, as revealed by global thermography-based imaging (not shown here for brevity). Hence, it can be expected that the unsteady fluctuations detected at the end of the imaged domain further decay downstream.

Stationary disturbance velocity profiles ($\langle\overline{u}\rangle_z$) are extracted at two representative chord locations x_1/c=0.154 and x_2/c=0.174 (figures 5.2(h-i)). The reduction of the disturbance profile amplitude at x_2 reflects the weakening of the streak structures at more downstream locations. In addition, the developing flow disturbances are observed to grow in size along the wall-normal direction, as their maximum value moves from y=0.55$\overline{\delta}^*$ to y=1.05$\overline{\delta}^*$. This effect is evident in the yz plane $\overline{u}_d$ and u' contours, and can be related to the natural thickening of the BL as well as to the development of the modal CFI downstream of x/c=0.164 [137]. Specifically, at x_1 (figures 5.2(b, e, h)) the velocity streaks developing in the element vicinity only affect the near-wall BL region, reaching the amplitude peak value at a wall-normal distance comparable to the element height. On the contrary, the downstream evolution of the developing structures (figures 5.2(c, f, i)) affects the whole BL wall-normal extent through the well-known momentum modulation associated with the CFI development [16, 137]. Nonetheless, the absence of a secondary lobe in the disturbance velocity profiles and the relatively low maximum amplitude of the stationary disturbances ($\langle\overline{u}\rangle_z$ <0.05$\overline{u}_\infty$) indicate a largely linear evolution of CFI within the investigated domain. This is reflected by the close match between $\langle\overline{u}\rangle_z$ and the numerically computed local LST shape function for the λ_1 mode evolution (figure 5.2(i)).

Overall both the $\overline{u}_d$ contours and $\langle\overline{u}\rangle_z$ profiles in figure 5.2 show that the streak structures developing in the near-wake region undergo an initial growth phase while decaying shortly downstream. The behaviour of the individual streaks can be quantified by extracting the streak amplitude (A_{str}), estimated as the maximum (minimum) $\overline{u}_d$ value for the high- (low-)speed streaks respectively. The resulting A_{str} is reported in figure 5.3(a) for three Re_k configurations obtained by modifying the DRE array amplitude. Both in Re_k=192 and Re_k=90 cases the high-speed streaks feature an initial growth phase followed by subsequent decay which is more evident for the higher amplitude forcing. The low-speed streak is instead showing a monotonic decay of the absolute amplitude value. Similar behaviour is seen for the lowest forcing amplitude considered (i.e. Re_k=21). However, the measurement accuracy in this case is hindered by the overall weaker amplitude values, therefore this configuration is disregarded in the remainder of this Chapter.

In addition to the localised amplitude estimations, a relative streak amplitude metric is defined as A_{And}=0.5×(max($\overline{u}_d$) - min($\overline{u}_d$)) based on the criterium introduced

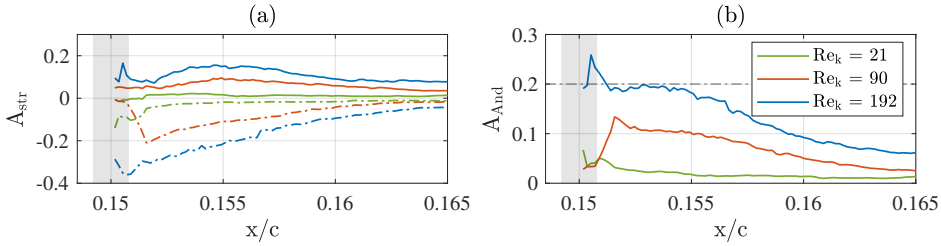

Figure 5.3: Streak amplitude analysis for varying Re_k: (a) A_{str} for high-speed (full line) and low-speed (-.) streaks; (b) A_{And} and amplitude limit for laminar streak breakdown (-., [5]). Element location (shaded grey region).

by Andersson *et al.* [5]. The resulting estimation is reported in figure 5.3(b) and shows that the initial growth phase and subsequent decay concentrate within comparable chordwise extent for the two higher Re_k considered. Additionally, based on the A_{And} definition Andersson *et al.* [5] identified a critical streak amplitude value of approximately $0.2\overline{u}_\infty$ as a sufficient onset condition for laminar breakdown of the developing velocity streaks in 2D boundary layers. This value is not reached in the presented cases, in agreement with the laminar evolution of the flow structures observed in figure 5.2 and confirming the Re_k predictions. Nonetheless, the relatively high initial amplitude of the induced near-wake disturbances (especially in case Re_k=192) can lead to increased unsteadiness and enhanced shear layer development in the element near-wake flow as shown in figure 5.2(e).

Capitalising on the volumetric information, the application of vortex identification criteria to the measured flow field allows for the characterization of the 3D coherent structures dominating the near-element flow evolution. Specifically, in the current analysis the Q-criterion [69] is applied to the time-averaged velocity field as described in section §5.2.2. The identified coherent structures are projected on the vortex-aligned coordinate frame (x_R, y_R, z_R) and presented in figure 5.4 by a positive (i.e. Q=0.005, red) and a negative (i.e. Q=-0.01, blue) Q-criterion iso-surface. As outlined beforehand the near-wake flow development of each DRE is dominated by strong spanwise and wall-normal shear layers initiated by the recirculating flow region located aft of the element, identified by the green $\overline{u}_R$=0 iso-surface in figure 5.4(a). Accordingly, the flow region corresponding to the low-speed element wake is characterized by negative values of the Q-criteria in figure 5.4(a). Conversely, the positive iso-surface identifies two coherent flow structures developing on the high-shear sides of the low-speed element's wake. These structures develop in correspondence to the positive streamwise vorticity regions and correlate well with the development of the vortical systems wrapping around and developing aft of each DRE as well as with the formation of the high-/low-speed streaks alternation.

Specifically, Kurz & Kloker [84] describe two vortical systems forming in the element vicinity: an HSV originating from the element's sides and an inner vortex pair (IV) arising in correspondence to the element's low-speed wake. In both vortex systems, only the leg conforming to the crossflow direction of rotation (i.e. co-crossflow leg) is supported by the baseflow, the other leg decaying shortly downstream.

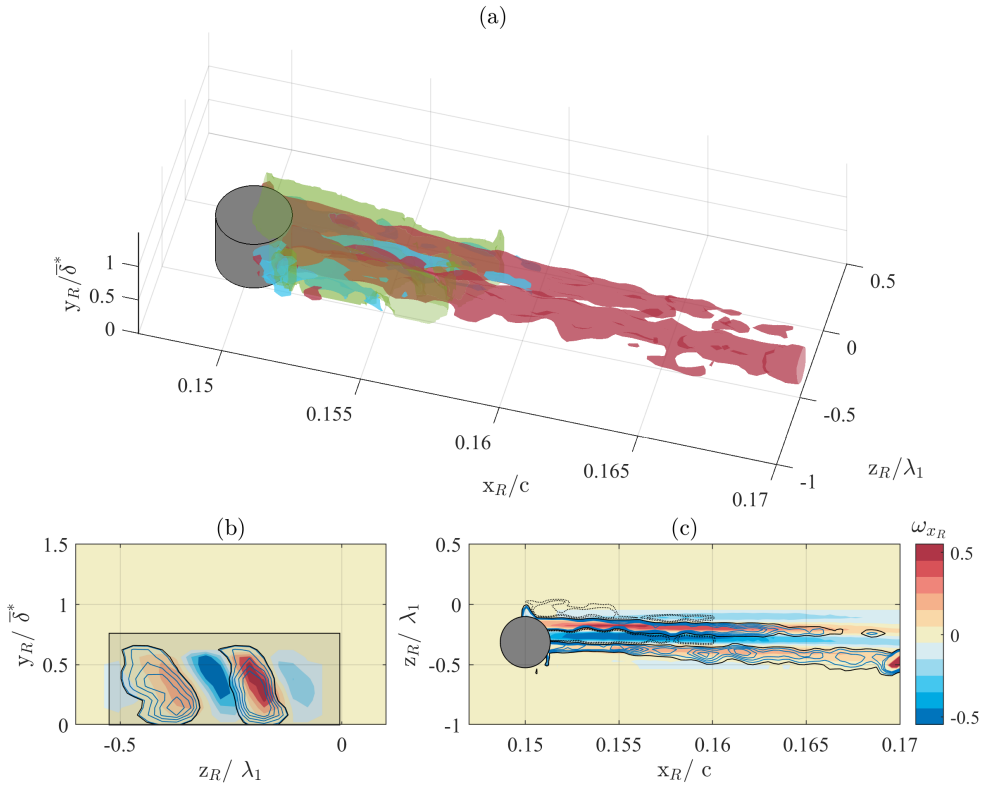

Figure 5.4: (a) Q-criterion iso-surface Q=0.005 (red) and Q=-0.01 (blue) for Re_k=192 case; $\overline{u}_R$=0 isosurface (green). Streamwise vorticity contours and Q-criterion iso-lines in (b) $y_R z_R$ plane at x/c=0.16 and (c) $x_R z_R$ plane at $y/\overline{\delta}^*$=0.55. Full blue lines Q>0 levels (5 between 0.005, 0.01), full black line Q=0.005 level, grey dash-dot lines Q<0 levels (5 between -0.001, -0.01).

Accordingly, the two coherent structures identified by the presented Q-criterion iso-surface correspond well to the sustained co-crossflow HSV and IV legs. Further downstream the inboard leg likely develops into a crossflow vortex, while the outboard structure appears to decay towards the downstream end of the imaged domain. The counter-crossflow HSV and IV legs described by Kurz & Kloker [84] are not identified by the current Q-criterion application possibly due to their lower intensity and rapid decay.

Towards confirming the observed flow features, iso-lines of the Q-criterion in the $y_R z_R$ and $x_R z_R$ plane are reported in figure 5.4(b, c) extracted at x/c=0.16 and $y/\overline{\delta}^*$=0.55 respectively. The flow region surrounding the low-speed wake of the DRE is characterized by the development of the identified co-crossflow HSV and IV legs, as shown by the spatial organization of the Q>0 isolines. Additionally, the streamwise vorticity contours reported in figures 5.4(b, c) confirm that the two iso-surfaces describe co-rotating structures corresponding well to the co-crossflow HSV and IV

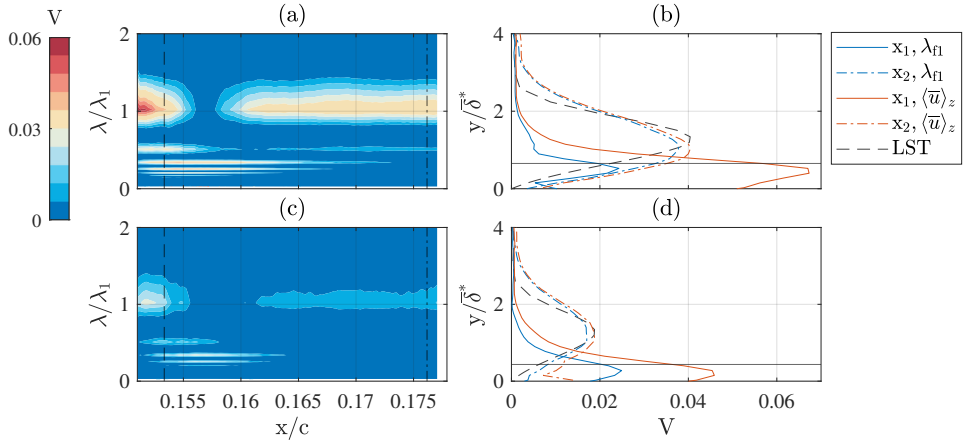

Figure 5.5: Spanwise FFT analysis for (a, b) Re_k=192 and (c, d) Re_k=90. (a, c) FFT spectra in the x-λ plane; (b, d) $\langle\overline{u}\rangle_z$ profiles and λ_{f1} FFT shape function at x_1 (dashed vertical line in (a) and (c)) and x_2 (dash-dot vertical line in (a) and (c)). LST λ_1 shape function (- -) scaled to match $\langle\overline{u}\rangle_z$ maximum; element height (horizontal full line). V stands for $FFT_z(\overline{u})/\overline{u}_\infty$.

legs. Finally, the Q>0 iso-lines as well as the streamwise vorticity contours chordwise evolution confirm that the outboard structure decays while the inboard leg persists up to the domain end.

The results discussed so far characterize the near-wake stationary flow topology, however they offer little insight regarding the observed growth and subsequent decay of the identified streak structures. To further investigate this aspect a spatial spectral analysis of the time-averaged spanwise velocity signal is presented hereafter, outlining the chordwise evolution of the individual Fourier modes.

5.3.2. Spectral Analysis and Transient Growth

To investigate the spectral composition of the near-element flow development and to identify the dominant instability modes and their evolution, a spatial FFT in the spanwise direction (i.e. z, section §5.2.2) is applied to the time-averaged velocity components. The spatial spectra development in the x-λ plane extracted at the wall-normal location of the disturbance maximum in the near-wake region (namely the maximum of $\langle\overline{u}\rangle_z$ at x_1, i.e. $y/\overline{\delta}^*$=0.55) for Re_k=192 and Re_k=90, are reported in figure 5.5(a, c).

In both considered cases, high spectral energy is contained in the forced mode $\lambda_{f1}=\lambda_1$ both in the near-wake and in the far-wake flow region. However, in the near-wake region (i.e at x_1) the spectral energy appears to be distributed among a wide range of higher harmonics (i.e. smaller wavelengths defined as $\lambda_{fi}=\lambda_{f1}/i$). This effect can be related to the highly localized velocity deficit region developing in the element's wake, which acts as a pseudo-pulse containing all spatial frequencies. Thus the geometrical constraints given by the finite diameter of the DRE and their inter-spacing (i.e. d and λ_{f1}) drive the spectral energy distribution among a wide set of

harmonic modes to properly describe the near-wake flow features [199]. The identified spectral components do not necessarily correspond to natural modal instabilities (i.e. eigensolutions to the disturbance equations), nonetheless, they are fundamental to represent the near-wake development in the modal FFT space. Accordingly, the harmonics of the dominant stationary mode achieve comparable or even higher spectral peaks in the element vicinity (figure 5.5(a, c)). As an example, for Re_k=192 up to 56% of the total disturbance energy is contained by the dominant mode and its first four harmonics. Further downstream at x_2, the λ_{f1} mode is dominating the far-wake development, only accompanied by a weak λ_{f2} and λ_{f3} mode reflecting the typical traits of linear CFI modal evolution.

The behaviour of individual FFT modes is further outlined by considering the dominant features of the λ_{f1} mode shape function compared to the disturbance velocity profile $\langle\overline{u}\rangle_z$ (figure 5.5(b, d)). At x_1, the $\langle\overline{u}\rangle_z$ profile reaches significantly higher peak amplitude values than the λ_{f1} shape function, confirming the significant contribution of the higher harmonics to the near-wake flow development. However, as previously observed the disturbances' evolution is confined within the BL region closer to the wall. Accordingly, the $\langle\overline{u}\rangle_z$ and λ_{f1} shape function peak is reached at a wall-normal distance comparable to the DRE height. This location corresponds well to the maximum fluctuation locii typically identified in the wake of isolated DRE [13, 76, 197]. Nonetheless, further downstream (i.e. at x_2) the boundary layer development is satisfactorily approximated by the λ_{f1} mode, as shown by the amplitude and shape match of the two profiles. Such behaviour is indicative of the onset and growth of modal CFI, as is confirmed by the similarities between $\langle\overline{u}\rangle_z$ and the λ_1 mode shape function extracted from the local LST solution [figure 5.5(b, d), 98, 152]. This agreement further suggests that non-linear interactions have a limited effect on the modal CFI development within the acquired domain.

The total disturbance amplitude ($A_{int}(\overline{u})$) and disturbance energy ($E(\overline{\mathbf{u}})$) as well as the amplitude ($A_{int,\lambda_{fi}}(\overline{u})$) and disturbance energy ($E_{\lambda_{fi}}(\overline{\mathbf{u}})$) of individual FFT modes are estimated as described in section §5.2.2. The chordwise evolution of the extracted amplitude and energy is reported in figure 5.6 for cases Re_k=192 and Re_k=90. Overall, the amplitude and energy evolution is similar, however, both quantities are presented at this stage as they will be the subject of independent analysis in the remainder of the Chapter. After the initial peak and decay due to the presence of the low-momentum region in the element's wake, the total disturbance evolution undergoes mild amplitude (energy) variations in the element vicinity. However, the amplitude of the dominant λ_{f1} mode rapidly decays in the near-wake region, recovering values comparable to $A_{int}(\overline{u})$ further downstream. The observed energy recovery can be traced back to the inherently unstable nature of the primary stationary mode, which in this 3D boundary layer scenario should be continuously growing up to and beyond the downstream domain end according to LST [98, 152]. In the near-wake the harmonic λ_{f2} mode follows the primary stationary mode trend albeit retaining lower amplitude values up to the domain end. On the contrary, the higher harmonics reported (i.e. λ_{f3}, λ_{f4}, λ_{f5} and λ_{f6}) all show a mild amplitude growth between x/c=0.151-0.16 before decaying further downstream. The behaviour of the individual FFT modes combined with the almost invariant total disturbance amplitude evolution indicates the presence of

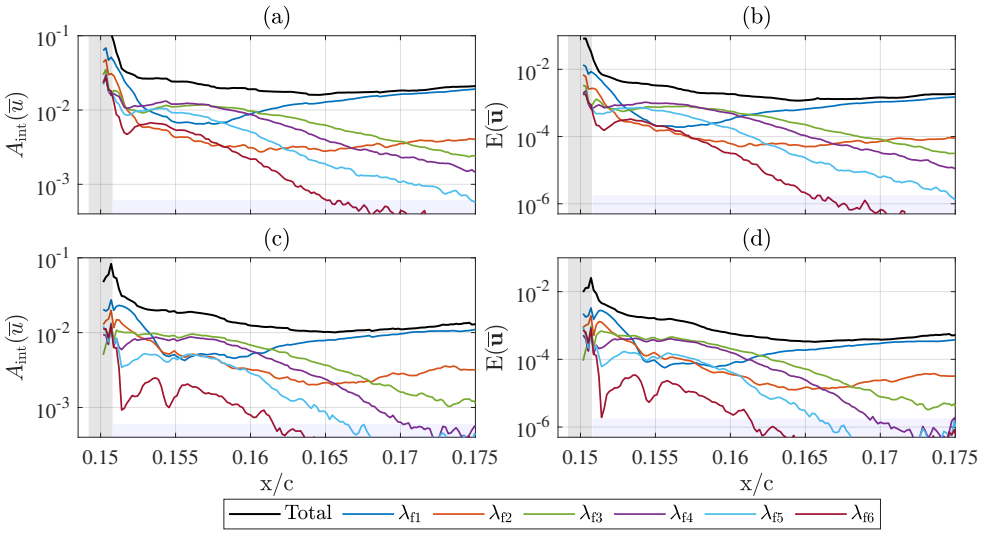

Figure 5.6: (a, c) $A_{int}(\overline{u})$ and (b, d) $E(\overline{\mathbf{u}})$ for the total disturbance field and for the λ_{f1}-λ_{f6} FFT harmonics for forcing cases (a, b) Re_k=192; (c, d) Re_k=90. Element location (grey shaded region); PTV uncertainty (blue shaded region).

stationary transient mechanisms which, despite the mild amplitude variations they induce, actively condition the near-wake flow development [87, 165, 183, 199]. In fact, as discussed later the occurrence of transient growth mechanisms can lead to rapid initial growth of the near-wake instabilities, enhancing the CFI onset amplitude and initiating them in the far-wake region. In turn, the onset conditions impact the downstream evolution and eventual breakdown of CFI, as widely discussed in Saric *et al.* [137]. Additionally, these aspects can further explain the inability of simply linear and modal solvers to accurately describe the BL receptivity to DRE, possibly providing the necessary insights to improve these predictions. In their investigation dedicated to a non-swept BL, White *et al.* [183] already outlined that non-modal mechanisms, and in particular transient growth, are fundamental features of the near-wake flow development. Despite the reduced chordwise extent of the development of the transient mechanisms in the present set-up, namely 1.5% chord (i.e. $\simeq$9.5d), the evolution of the individual FFT modes is strongly comparable with the results of White *et al.* [183]. The λ_{f1} and λ_{f2} modes rapidly decay while the growth of modes λ_{f3} and λ_{f4} appear to sustain the total disturbance amplitude, thus driving the transient process.

Past theoretical works [20, 39, 87] showed that BL dominated by instabilities in the form of streak structures can be subject to transient growth mechanisms. These can lead to rapid initial growth of the near-wake instabilities, enhancing the CFI onset amplitude and downstream development that then follows an exponential growth process. In the present case, the occurring transient growth mechanisms are not sufficiently strong to induce the $A_{int}(\overline{u})$ growth. Nonetheless, the stationary transient disturbances appear to actively dominate and condition the near-wake flow, while

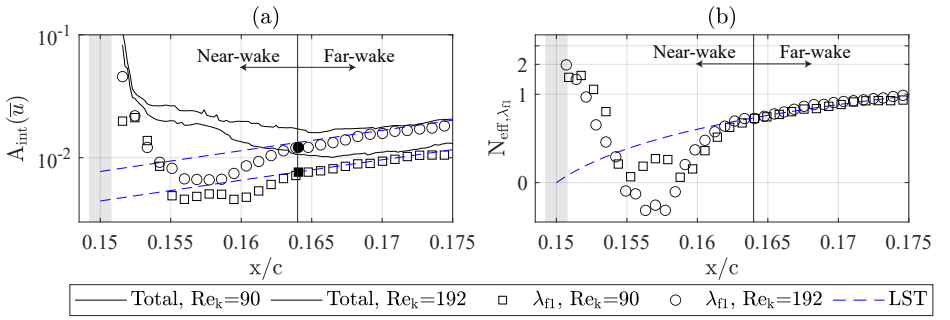

Figure 5.7: A_{int} and N_{eff} estimation for the experimental FFT λ_{f1} mode (symbols) and for the LST solution λ_1 mode (solid lines). A_0 shown by filled black markers.

5

the modal CFI onset occurs at a finite distance from the element. Hence, a modal framework such as that provided by the LST method is not sufficient to thoroughly characterize the near-wake evolution.

Based on these considerations, the disturbance amplitude downstream of the initial transient growth phase can be considered as an approximation of the initial amplitude for the modal CFI growth (i.e. A_0). More specifically, the primary stationary mode amplitude ($A_{int,\lambda_{f1}}$) compared to the total disturbance amplitude evolution (figures 5.6 and 5.7(a)) indicates that the effect of the transient growth is limited to the near-wake flow region. In particular, aft of x/c$\simeq$0.164 the primary stationary CFI (i.e. λ_{f1}) contains more than 80% of the total disturbance energy, thus being representative for the modal development of the total disturbance. Therefore, the $A_{int,\lambda_{f1}}$ value at x/c$\simeq$0.164 is considered to be representative for the λ_{f1} mode onset amplitude (A_0, black full marker in figure 5.7(a)), as confirmed by the exponential (i.e. modal) growth of the CFI further downstream. The resulting A_0 estimations for cases Re_k=192 and 90 are respectively $A_0 \simeq 0.024\overline{u}_\infty$ and $A_0 \simeq 0.012\overline{u}_\infty$.

Based on the extracted A_0 values, the experimental effective N-factor [138] can be defined as $N_{eff} = \ln(A_{int,\lambda_{f1}}/A_0)$. The classical N_{eff} definition proposed by Saric *et al.* [138] considers the amplitude of the disturbances at the DRE location as the reference amplitude. However, within this Chapter the N_{eff} is computed based on the A_0 extracted at the first location where the disturbances are found to grow exponentially (i.e. x/c=0.164). Figure 5.7(b) compares the experimental and LST [N_{LST}, 98, 152] effective N-factor evolution. For the purpose of this comparison all the obtained N_{eff} are offset such that the $N_{LST}(x_{DRE}/c)$=0. This procedure allows for the extraction of the N-factor values starting from the x_{DRE} location. In agreement with the observed $A_{int,\lambda_{f1}}$ trend, the experimental N_{eff} undergoes an initial decay followed by rapid growth. Further downstream, the experimental and numerical N_{eff} curves collapse, confirming the exponential growth of the CFI downstream of x/c=0.164. This behaviour suggests that linear stability solutions can provide a good approximation of the initial linear phases of development of CFI granted that the onset amplitude A_0 is known downstream of the near-wake transient growth region. Specifically, for the considered case the A_0 estimate 1.4% (i.e. 9d) downstream of the

element location provides a satisfactory prediction. The numerical amplitude evolution can then be computed as $A_{LST}=A_0\ e^{N_{LST}}$ and is reported in figure 5.7(a), collapsing well on the experimental amplitude trends downstream of the transient growth phase. The upstream extrapolation of the LST amplitude estimation to the DRE location in figure 5.7(a) reveals the inability of fully modal assumptions to accurately predict the CFI receptivity to surface roughness [199]. This further highlights the importance of non-modal/transient effects in the near-wake region development, as these effectively define the A_0 value based on both the forcing geometry (mostly represented by λ_f and d) and the local BL characteristics (i.e. Re_k).

In conclusion, the FFT analysis discussed beforehand suggests that transient and non-modal mechanisms are driving the near-wake flow evolution, conditioning the onset of the emerging modal CFI. A transient growth process can be described as the combination of two signature features, i.e. an initial algebraic growth followed by an exponential decay of the developing disturbances. Therefore, to confirm the nature of the identified transient mechanisms and how these condition the CFI onset, further efforts have been dedicated to the identification of these features in the experimental disturbance energy development.

5.3.3. Algebraic Growth in Disturbance Energy and Scalability

To further characterize the nature of the stationary transient growth identified in the near-element flow, the modal disturbance energy evolution is investigated. Throughout the following discussion various Re_k cases are considered, obtained by modifying the element amplitude (cases Re_k=90 and Re_k=192 considered beforehand) or varying the freestream Reynolds number for a fixed element height (cases Re_k=100, $Re_c=1.35\times10^6$ and Re_k=153, $Re_c=1.85\times10^6$ featuring k_3 elements). In all cases the forcing wavelength is kept constant to $\lambda_{f1}=\lambda_1$=8mm.

As shown in figure 5.6, the FFT dominant stationary mode undergoes a decay-growth pattern, while modes λ_{f3} -λ_{f6} follow an evident growth-decay pattern indicative of the transient mechanism occurring in the near-wake flow region. The modal disturbance energy (defined as the wall-normal integral of streamwise kinetic energy per individual FFT mode, section §5.2.2) is reported in figure 5.8(b-e) for modes λ_{f3}-λ_{f6} at the different Re_k considered. The observed energy development confirms that these modes initially grow in the element near-wake, each reaching a maximum value (indicated as the red marker) and decaying further downstream. Both the maximum energy value and its distance from the element (x_{max}) depend on Re_k, while the overall chordwise extent of the transient behaviour reduces for decreasing modal wavelengths.

To further describe the growth and decay of the λ_{f3} and λ_{f4} FFT modes, White *et al.* [183] proposed two transient growth model functions following the work by Böberg & Brösa [18]. Specifically, the two functions encompass the description of the initial algebraic growth and the exponential decay trends as follows:

$$E_{\lambda_{f3}} = a_3(x - x_{DRE})e^{-(x-x_{DRE})/b_3} \quad \text{with} \quad b_3 = (x_{max} - x_{DRE}) \quad \text{and} \quad (5.1)$$

$$E_{\lambda_{f4}} = a_4(x - x_{DRE})^2 e^{-(x-x_{DRE})/b_4} \quad \text{with} \quad b_4 = 0.5(x_{max} - x_{DRE}). \quad (5.2)$$

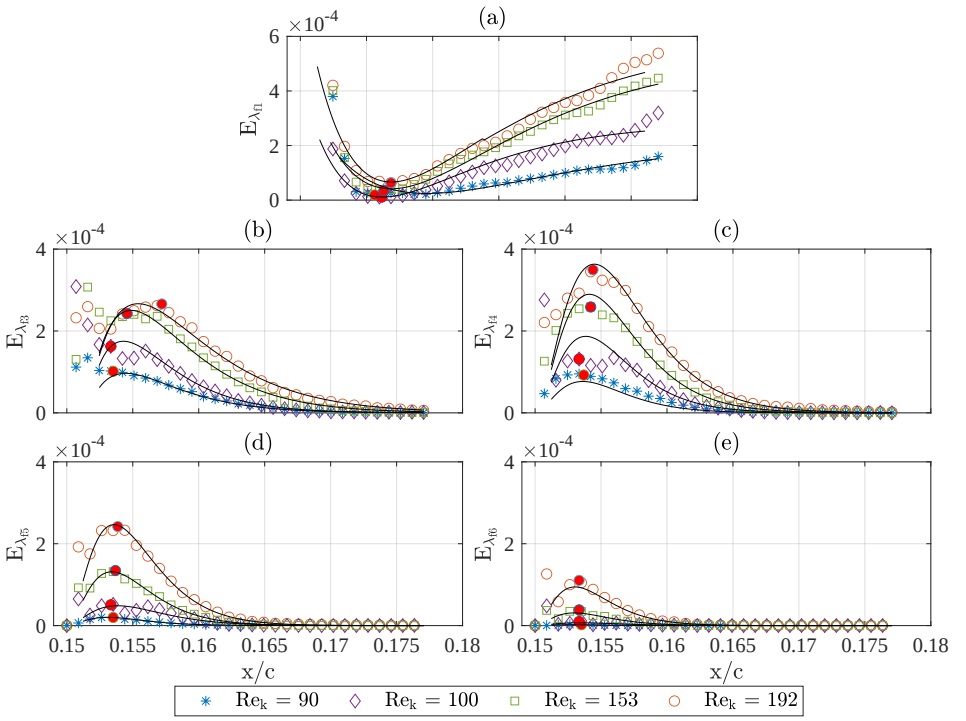

Figure 5.8: $E_{\lambda_{fi}}(\overline{\mathbf{u}})$ trends (symbols, 1 out of 5 shown) and maximum values (red circle), and transient growth modelling functions [black lines, 183] at various Re_k for individual FFT modes (a) λ_{f1}, (b) λ_{f3}, (c) λ_{f4}, (d) λ_{f5}, (e) λ_{f6}.

In these models, coefficients a_3 and a_4 account for the algebraic growth rate as well as for the disturbance energy scaling with Re_k. Coefficients b_3 and b_4 instead are representative of the exponential decay and directly relate to the chordwise extent of the transient region. In particular, the latter coefficients can be associated with the location of the corresponding mode energy maximum (x_{max}), as indicated in equations 5.1 and 5.2. The evolution of the disturbance energy pertaining to λ_{f3} follows a faster growth in the immediate vicinity of the element, while displaying a broader peak with respect to the λ_{f4} modal energy evolution. As such, the λ_{f3} energy is described by a linear dependence on the chordwise distance from the element (equation 5.1), while the λ_{f4} energy follows a quadratic dependence on x/c (equation 5.2). The latter model function is applied to describe the energy evolution of modes λ_{f5} and λ_{f6} as well. To fit the transient growth model functions to the experimental energy trends, only the data acquired downstream of x/c=0.151 are considered to exclude the initial steep amplitude decay observed immediately aft of the element. The resulting fitted curves for the modelling of the energy transient evolution are reported in figure 5.8(b-e) as full black lines.

Despite being designed to describe stationary transient disturbances in a 2D boundary layer, the proposed modelling functions satisfactorily represent the λ_{f3}

and λ_{f4} modal energy evolution in the considered 3D boundary layer case. The initial algebraic growth of λ_{f3} (figure 5.8(b)) is correctly captured by the linear model function, despite mild offset of the maximum location. The following exponential decay is also well-modelled and shows once more that the extent of the transient behaviour is comparable throughout the different Re_k considered. Satisfactory matching is obtained for the λ_{f4} modal energy evolution (figure 5.8(c)), even if the peak value is mildly overestimated for the higher Re_k cases. The model function confirms that the modal energy trend associated with modes λ_{f5} and λ_{f6} follows an initial algebraic growth and exponential decay as well (figure 5.8(d, e)). The solid match observed between the quadratic-exponential fit and the energy evolution of modes $\lambda_{f4} - \lambda_{f6}$ reflects the quadratic dependence of the energy on x/c, coming from its definition in section §5.2.2. The fact that the behaviour of the λ_{f3} modal energy is better approximated by the linear-exponential model outlines the importance of the receptivity process and its sensitivity to the external forcing geometry in conditioning the evolution of individual FFT modes [102, 183].

Differently from the 2D boundary layer scenario investigated by White *et al.* [183], in the 3D boundary layer considered in this Chapter the primary stationary mode λ_{f1} is inherently unstable [LST and experimental measurements, 152]. Therefore, this mode undergoes an initial energy decay in the near-wake region in correspondence to the harmonics energy growth region while it grows further downstream (figures 5.6 and 5.8(a)). Furthermore, the characterization of the CFI initial amplitude (figure 5.7) showed that the λ_{f1} mode rapidly recovers to exponential growth downstream of the transient growth region occurring in the element near-wake. Given these considerations, the initial decay and subsequent growth of λ_{f1} in the element vicinity can be regarded as composed of a linear algebraic decay followed by exponential growth. Figure 5.8(a) shows that the experimental disturbance energy development is well approximated by the transient growth model function of equation 5.1 also for the λ_{f1} mode if the sign of the a coefficient is inverted. As such, the energy evolution of the primary stationary mode describes a negative (i.e. opposite) transient growth process which conditions both the near-wake evolution and the receptivity of critical amplitude DRE. Within this work, this energy evolution is indicated as *transient decay* to express its direct opposition to the traditional transient growth process. This behavior correlates well with the *wake relaxation* process described by Ergin & White [52] in 2D boundary layer scenarios. Specifically, they identified the transient evolution of the steady instabilities to drive the near-wake towards a more stable state prior to the onset of modal instabilities. However, in the 3D boundary layer scenario considered in the present investigation, the baseflow is inherently unstable to CFI, hence the wake relaxation is rapidly followed by the onset and growth of modal CFI independently of the amplitude value reached by the decaying instabilities. Nonetheless, the λ_{f1} transient decay fundamentally conditions the onset amplitude of the modal CFI, influencing their modal growth further downstream, as also discussed in section §5.3.2 and figure 5.7 and observed in previous investigations [20, 39, 95].

In their investigation White *et al.* [183] identified that both a and x_{max} are well approximated by a linear dependence on Re_k. Given the mathematical composition of the considered transient growth model functions, the disturbance energy evolution is

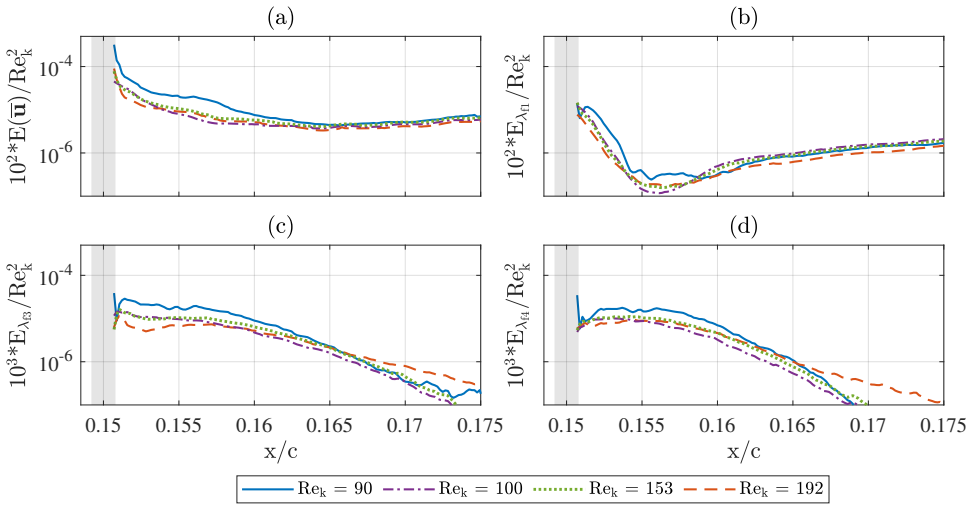

Figure 5.9: Variation of (a) E($\overline{\mathbf{u}}$), and E$_{\lambda_{fi}}$($\overline{\mathbf{u}}$) computed for FFT modes (b) λ_{f1}, (c) λ_{f2} and (d) λ_{f3} modes at varying Re$_k$. Energy is scaled by Re$_k^2$; element location (grey shaded region).

expected to scale with Re$_k^2$. The total disturbance energy and the energy of individual FFT modes scaled by Re$_k^2$ are reported in figure 5.9. Both the scaled total disturbance and modal energy curves almost collapse onto a single curve for the reported cases. The energy associated with the dominant mode evolution (figure 5.9(b)) is strongly scalable both in the transient decay region and in the far-wake flow field, where it recovers a modal behaviour and grows exponentially. Instead, the scaled energy of the harmonic FFT modes (figure 5.9(c, d)) shows comparable behaviour in the near-wake region where transient growth occurs, even if the lower Re$_k$ considered features a mildly different evolution of the algebraic growth process. Additionally, the energy associated with the harmonic modes rapidly decays in the element far-wake in agreement with the linear development of the primary stationary mode observed in the downstream flow region.

The results reported so far indicate that a transient growth mechanism driven by the primary stationary mode and its higher harmonics is dominating the near-wake evolution almost independently of the considered Re$_k$. Specifically, the λ_{f1} modal energy undergoes a transient decay, while the energy associated with the harmonic modes λ_{f3}-λ_{f6} undergo a transient growth process. Both processes are localized within the near-wake region and feature an initial algebraic decay (growth) phase followed by exponential growth (decay) respectively. It must be noted that, given the modal energy growth characterizing the harmonics evolution and the energy decay featured by the primary stationary mode, the identified transient processes can potentially co-exist with non-linear mechanisms. The acquired dataset, however, does not provide sufficient information to prove this hypothesis. Nonetheless, transient growth processes in 3D boundary layers receptive to critical DRE need to be accounted for to correctly estimate the modal instabilities' initial amplitude and growth despite their very mild

effect on the total disturbance amplitude evolution. This can be regarded as one of the main differences between the investigated 3D scenario and the more typical wake realxation or bypass transition configurations widely characterized for 2D boundary layers, in which the primary streak mode simply decays downstream if not strong enough to cause laminar breakdown.

Overall, the observed transient energy evolution scales well with Re_k^2. The current investigation only considers DRE of cylindrical shape, but modifications of the spanwise array wavelength (i.e. element inter-spacing) and DRE diameter appear to significantly affect the identified transient mechanisms by conditioning the modal energy distribution. In fact, the relation between the chosen element inter-spacing (i.e. λ_{f1}), setting the primary stationary mode wavelength, and the element diameter (d) conditions the range of wavelengths following an algebraic growth process (i.e. modelled by equation 5.2). Specifically, for the considered critical forcing case $\lambda_{f3} \simeq$1.3d, $\lambda_{f4} \simeq$1d, $\lambda_{f5} \simeq$0.8d and $\lambda_{f6} \simeq$0.7d. This can be related to the effect of the finite element diameter on the spatial arrangement and spacing of the HSV system [110], which further contributes to defining the strength of the near-wake transient growth process [102, 183]. Thus, the investigated parameter range has been expanded by modifying the DRE array forcing wavelength λ_{f1} to further investigate the steady transient disturbances receptivity to the forcing geometry.

5.3.4. Variations of Forcing Wavelength

The previous discussion outlined a significant dependence of the modal energy distribution and consequently of the occurring transient processes in the near-wake on the geometry of the considered problem (parametrized using λ_{f1} and d). Therefore, to further investigate the effects of the external forcing configuration the receptivity of the near-wake steady transient disturbances to a modification of the forcing wavelength is explored. At this point, it must be clarified that none of the forcing cases considered in this section leads to BL transition in the element vicinity, hence they fall in the critical amplitude forcing definition. Nonetheless, to distinguish between configurations forcing at wavelength $\lambda_{f1} < \lambda_1$ and $\lambda_{f1} > \lambda_1$ the definitions of sub-critical wavelength (SBW) and super-critical wavelength (SPW) forcing are respectively used throughout the following discussion. With reference to figure 5.1, in the previous sections cases Re_k=100, 153 and 192 have been inspected in a critical wavelength forcing configuration (i.e. forcing the most unstable mode λ_1). In the following analysis for each of the considered Re_k a sub-critical wavelength ($\lambda_{f1}=\lambda_{3/2}$, [136]) and a super-critical wavelength ($\lambda_{f1}=\lambda_{2/3}$) array are investigated. It should be noted that according to LST analysis the λ_1 wavelength corresponds to the most unstable mode in all considered configurations, however, modes $\lambda_{3/2}$ and $\lambda_{2/3}$ are both locally amplified at the DRE location of application.

Considering the sub-critical wavelength forcing case, the velocity contours reported in figure 5.10 show that the near-wake flow topology retains its main characteristics, albeit being dominated by a $\lambda_{3/2}$ flow periodicity. A low-speed streak develops in correspondence to each element's wake, while two high-speed streaks form on the wake's sides. The streaks evolution compares well with the critical wavelength case, as confirmed by the $\mathrm{A}_{\mathrm{And}}$ estimation (figure 5.10(d)). Moreover, the extracted FFT

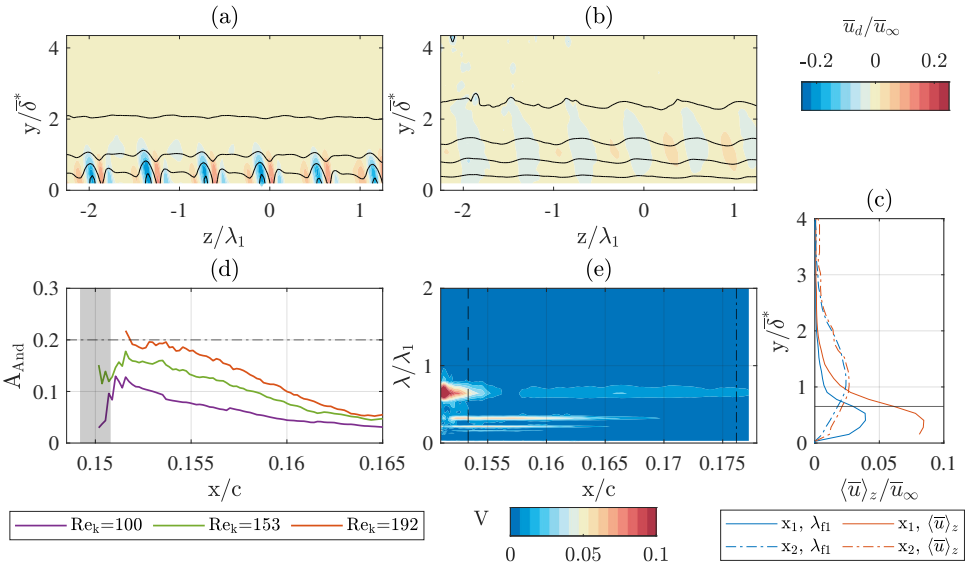

FIGURE 5.10: Stationary flow topology for forcing case $\lambda_{f1}=\lambda_{3/2}$, $Re_k=192$ (i.e. k_3). (a, b) $\overline{u}_d$ in the yz plane at(a) $x_1=0.154c$ and (b) at $x_2=0.174c$. (c) $\langle\overline{u}\rangle_z$ profiles and λ_{f1} FFT shape functions at x_1 and x_2; element height (horizontal full line). (d) A_{And} and amplitude limit for laminar streak breakdown (-. line) for various Re_k. (e) Spanwise FFT spectra in the x-λ plane at $y=0.55\overline{\delta}^*$. V stands for $FFT_z(\overline{u})/\overline{u}_\infty$.

spectra indicate that the near-wake features high spectral energy content for the forced $\lambda_{f1}=\lambda_{3/2}$ mode and its harmonics (figure 5.10(e)). The spectral energy associated with harmonic modes decays further downstream, leaving a BL modulated by the development of a sub-critical CFI [136]. The disturbance velocity profiles compare well to the λ_{f1} FFT shape function towards the downstream end of the acquired domain, while the amplitude differences observed in the near-wake are attributed to the harmonics contributions (figure 5.10(c)).

The near-element flow for the super-critical wavelength forcing case (not reported for the sake of brevity) is characterised by similar features as the so-far considered cases. Once more, the harmonics have an important role in the element's near-wake, while rapidly decaying shortly downstream. Additionally, the $Re_k=192$ forcing case reaches an A_{And} amplitude close to the laminar breakdown threshold identified by [5]. Nonetheless, the streak amplitude rapid decay prevents the onset of laminar breakdown in the near-element region.

Despite the variation of the dominant flow periodicity due to the modified forcing wavelength, the near-element stationary flow topology reflects all the dominant flow features discussed for the $\lambda_{f1}=\lambda_1$ forcing case. Accordingly, stationary transient growth disturbances drive the near-wake evolution also in the SBW and SPW configurations. In particular, figure 5.11 shows the chordwise evolution of the total disturbance amplitude and of the amplitude of individual FFT modes (where $\lambda_{fi}=\lambda_{f1}/i$) for the two forcing wavelengths considered. In both cases the decay of the dominant mode (i.e.

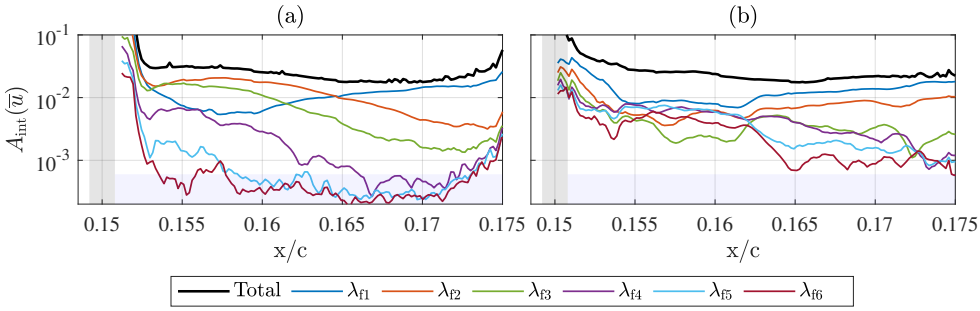

Figure 5.11: $A_{int}(\overline{u})$ for the total disturbance field and for the $\lambda_{f1} - \lambda_{f6}$ FFT harmonics for forcing cases Re_k=192 and (a) $\lambda_{f1}=\lambda_{3/2}$, (b) $\lambda_{f1}=\lambda_{2/3}$. Element location (grey shaded region); PTV uncertainty (blue shaded region).

5

the forced mode λ_{f1}) combined with the evolution of the total disturbance amplitude indicate that a transient growth mechanism is driving the near-wake evolution and relaxation. Figure 5.6 outlined that in the $\lambda_{f1}=\lambda_1$ forcing case the evolution of stationary transient disturbances is mostly represented by the transient decay of mode λ_{f1} and the transient growth of FFT modes λ_{f3}-λ_{f6} (i.e. 1.3d-0.7d). However, figure 5.11 shows that a change of λ_{f1} leads to a redistribution of the disturbance energy associated with the individual FFT modes. More specifically, in the SBW forcing (figure 5.11(a)) the harmonic modes λ_{f2} and λ_{f3} undergo a strong transient growth process. Additionally, the λ_{f4} mode is only giving a mild contribution, while the higher harmonics are rapidly decaying. The SPW forcing reported in figure 5.11(b) is characterized by the decay of the first three harmonic modes (i.e. λ_{f1}-λ_{f3}). In this case, the transient growth behaviour appears to be only weakly sustained by mode λ_{f4} with more significant contribution of modes λ_{f5} and λ_{f6}. In the latter case, the larger element spanwise inter-spacing leaves the possibility of stronger modal interactions [136], justifying the more irregular amplitude trends observed. These observations further highlight that besides affecting the overall modal CFI development, the geometry of the external forcing tends to drive the non-modal processes and the behaviour of the instabilities also in the near-wake flow region. In fact, the energy distribution within the FFT spectra appears to favour the modes corresponding to wavelengths close to the DRE diameter. This is the case for wavelengths λ_{f2}=1.25d and λ_{f3}=0.8d in the SBW case; or for wavelengths λ_{f5}=1.1d and λ_{f6}=0.9d in the SPW scenario.

Nonetheless, the primary stationary mode appears to undergo transient decay both in the SBW and SPW forcing scenarios, almost independently from the forcing wavelength modification. This is confirmed by comparing the experimental amplitude trends to the LST prediction as already outlined in the analysis presented in figure 5.7. The corresponding results are reported in figure 5.12 for Re_k=192 and varying λ_{f1}. This comparison outlines once more that the instability evolution differs from the modal LST solution in the element vicinity, however, the experimentally computed the experimentally computed amplitude trend follows a modal growth downstream of

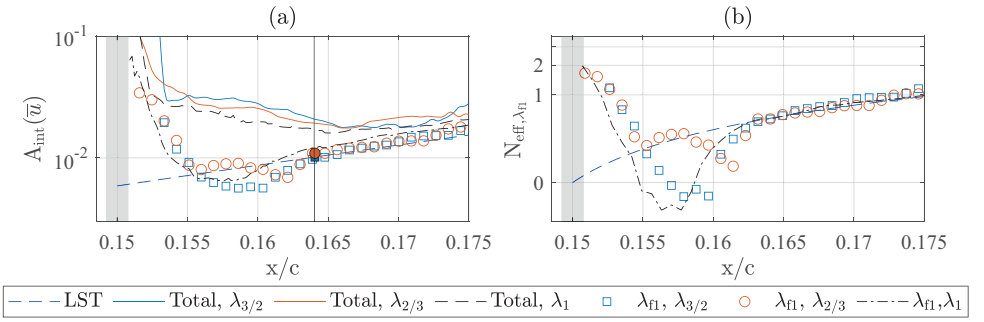

Figure 5.12: A_{int} and N_{eff} estimation for the experimental FFT λ_{f1} mode (symbols) for cases λ_{f1}=$\lambda_{3/2}$ and $\lambda_{2/3}$ at Re_k=192 and for the LST solution λ_1 mode (solid lines). A_0 shown by filled black-coloured markers.

5

x/c=0.164. Hence, the A_0 amplitude for the dominant (i.e. most unstable) CFI mode can be estimated at x/c=0.164 also for these cases, resulting in A_0=$0.010\overline{u}_\infty$ and $0.011\overline{u}_\infty$ for the SBW and SCW forcing respectively. These values are slightly lower than those found for the critical forcing at comparable Re_k, reflecting the variation of the forcing geometry (i.e. the diameter and λ_{f1} ratio, [117]). Nonetheless, the mild A_0 differences observed suggest that the transient growth process is mostly unaffected by the boundary layer stability characteristics [83].

Additionally, figure 5.13 compares the experimental energy trend associated with the forced wavelength λ_{f1} to the transient growth model function of equation 5.1. This analysis is presented for both SBW and SPW configurations at various Re_k. The modelled energy corresponding to the baseline case Re_k=192 and λ_{f1}=λ_1 is also reported (black dotted line). It is apparent that the primary stationary mode undergoes transient decay in all measured cases, as confirmed by the match between the experimental energy trend and the energy model function. This indicates that within the considered critical amplitude range, the transient decay experienced by the primary stationary mode occurs independently from the chosen forcing wavelength and can be satisfactorily modelled by using equation 5.1 and inverting the sign of the *a* coefficient. This provides a reliable approximation of the modal CFI onset amplitude and location as discussed for the critical forcing case (section §5.3.2). Furthermore, the forced mode (i.e. primary stationary mode) energy evolution obtained in the critical wavelength forcing case appears to undergo steeper decay and faster growth than for the non-critical cases considered. This agrees well with the idea that the λ_{f1} mode energy growth in this 3D boundary layer scenario is driven by the inherently unstable nature of the forced mode.

For each of the considered forcing wavelengths, the energy distribution among the individual FFT modes is robust to Re_k modifications. This is evident in figure 5.14, reporting the evolution of the total disturbance energy and the modal energy scaled by Re_k^2 for the various forcing wavelengths considered. The scaled total energy collapses on a single curve for the super-critical and critical forcing (black dash-dot line), while it follows a mildly different growth process in the near-wake region for the

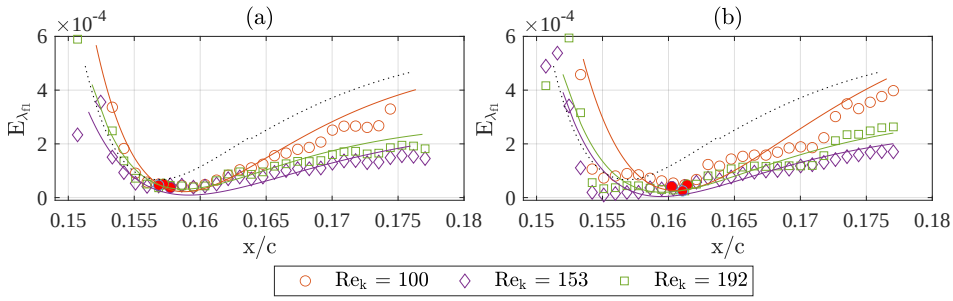

Figure 5.13: $E_{\lambda_{f1}}(\overline{\mathbf{u}})$ trends (symbols, 1 out of 5 shown) and minimum values (red circle), and transient growth modelling functions [full lines, 183] at various Re_k for (a) $\lambda_{f1}=\lambda_{3/2}$ and (b) $\lambda_{f1}=\lambda_{2/3}$. Energy modelling function for $Re_k=192$, $\lambda_{f1}=\lambda_1$ (black dotted line).

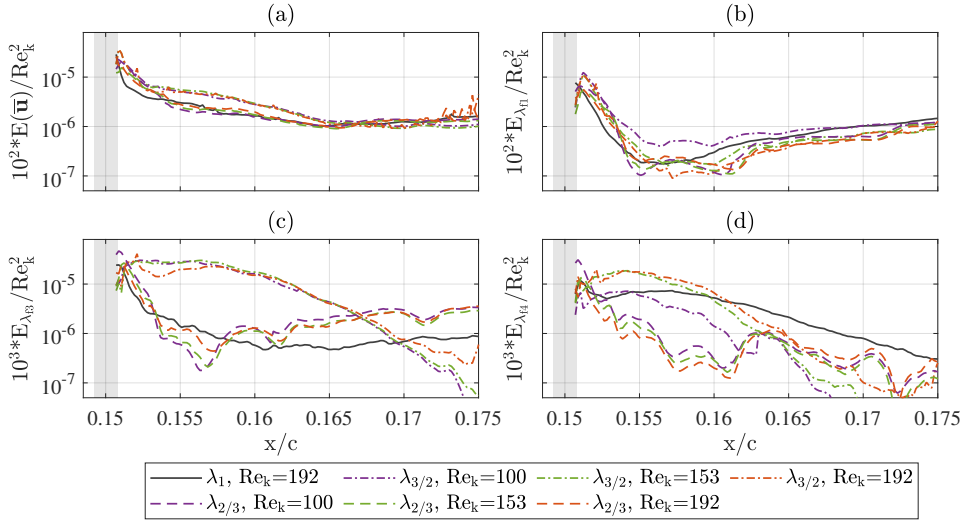

Figure 5.14: Variation $E(\overline{\mathbf{u}})$ for (a) total disturbance field, (b) FFT λ_{f1}, (c) λ_{f2} and (d) λ_{f3} modes at varying Re_k and λ_{f1}. Energy is scaled by Re_k^2; element location (grey shaded region).

sub-critical wavelength forcing case. The λ_{f1} mode chordwise evolution scales well with Re_k^2, confirming the dominant mode initial decay and downstream exponential growth are common traits to all of the considered forcing configurations. Given the dependence of the modal energy distribution on λ_{f1} and d, the scaling of the higher harmonics collapses on a different curve for each forcing wavelength considered.

The presented analysis indicates that, independently from the chosen λ_{f1}, the evolution of the primary stationary mode and its harmonics in the near-wake region is strongly affected by the presence of transient growth mechanisms, driving the near-wake relaxation through two different scenarios. On the one hand, the primary stationary mode appears to follow a transient decay process, recovering from an initial algebraic decay into exponential energy growth. This is in agreement with the

inherent instability of the primary stationary mode, which according to LST grows modally along the wing chord. On the other hand, a sub-set of the higher harmonic modes undergoes a more traditional transient growth process in the near-wake region. The external forcing geometry, mostly represented by the combination of the λ_f and d, significantly affects the modal energy distribution within the FFT spectra, thus selecting the set of harmonics and the strength of the transient growth process.

5.4. Super-critical Near-Element Flow

The analysis of the near-element stationary flow indicates that transient growth is a fundamental mechanism for the near-wake flow evolution. Nevertheless, none of the cases considered in the previous sections features forcing amplitudes leading to bypass transition (i.e. BL transition in the element vicinity). Therefore, the last part of the presented Chapter is dedicated to the investigation of forcing configurations associated with super-critical behaviour, i.e. flow tripping, outlining the corresponding near-element flow topology and the role of the near-wake stationary transient disturbances in the transitional process. With reference to figure 5.1, configurations featuring Re_k >200 are considered under Re_k and λ_{f1} modifications.

The critical DRE wavelength array (i.e. λ_{f1}=λ_{f1}) at Re_k=330 is initially considered as the representative forcing case. The corresponding time-averaged disturbance velocity field ($\overline{u}_d$) is reported in figures 5.15(a-c), while figures 5.15(d-f) show the temporal fluctuations standard deviation contours (u'). The $\overline{u}_d$ contours of figure 5.15(a) indicate that the near-wake flow is dominated by the alternation of high- and low-speed streaks spatially organized as described for the previously considered critical cases (i.e. figure 5.2). However, for the current super-critical amplitude forcing the high-speed streaks developing on the wake's flanks rapidly merge, substituting the low-speed wake at x/c$\simeq$0.158 (i.e. $\simeq$5d downstream of the element, solid vertical black line in figure 5.15(a)). This behaviour closely resembles the near-wake flow development of isolated DRE with super-critical amplitude in 2D and 3D boundary layer cases [75, 76, 84, 197]. Additionally, the inboard and outboard high-speed streaks forming in the near-wake flow region can be identified within the merged high-speed wake. As observed for the critical amplitude elements, the inboard high-speed streak undergoes a stronger growth process while evolving downstream if compared with its outboard counterpart.

The identified merging of high-speed streaks is usually associated with the onset of turbulent flow in spatial correspondence to the element's wake [75, 76]. This is confirmed by the increased velocity fluctuation level shown by the u' contours in figure 5.15(d). Specifically, the super-critical near-wake (x/c<0.155) is characterized by the development of a high-fluctuation region spatially overlapping to the low-speed streak [figure 5.15(d, e), 76, 93]. However, further downstream at the region of high-speed streak merging (x/c$\simeq$0.158), the intensity of the velocity fluctuation increases and its spatial distribution begins to spread along the spanwise and wall-normal directions, eventually occupying the whole element's wake. Accordingly, each individual DRE wake appears to initiate a turbulent wedge at the merging location of x/c$\simeq$0.158 [76].

The u' contours provide additional information regarding the wedge formation and development. Specifically, the spanwise spreading of the wedge can be associated with

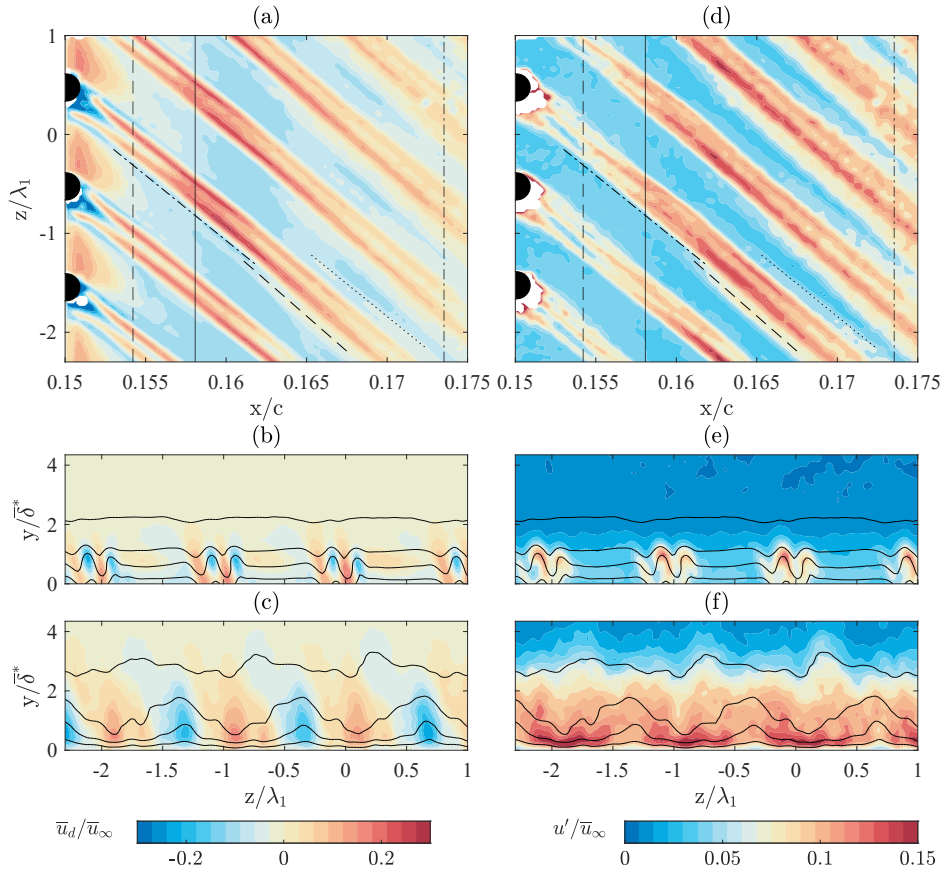

Figure 5.15: (a-c) $\overline{u}_d$ and (d-f) u' for forcing case λ_{f1}, Re_k=330 in (a, d) the xz plane at $y/\overline{\delta}^*$=0.55; (b, e) in the yz plane at x_1=0.154c (vertical dashed line in (a)), and (c, f) at x_2=0.174c (vertical dash-dot line). Vertical full line in (a) at x/c=0.158.

the formation of a cascade of low- and high-speed streaks on the sides of the high-speed wake [13]. An inboard low-speed streak (dash-dot line in figure 5.15(a)) is initiated in the immediate vicinity of the element and grows along the inboard side of the high-speed wake. More downstream, a high-speed streak becomes evident at x/c≃0.16 on the wake inboard side (dashed line in figure 5.15(a)), merging shortly downstream with the element's high-speed wake. A similar mechanism drives the spanwise wedge opening towards the outboard direction as shown by the high-speed streak development at x/c≃0.165 and its downstream merging with the high-speed wake region (dot-dot line in figure 5.15(a)). The development of the identified high-speed structures leads to a localized increase in the level of the velocity fluctuation, driving the spanwise expansion of the high-fluctuation region as shown by figure 5.15(d). However, the role of this wedge-opening mechanism in the current configuration is limited by the flow periodicity. Specifically, the DRE inter-spacing leads to the merging of the individual

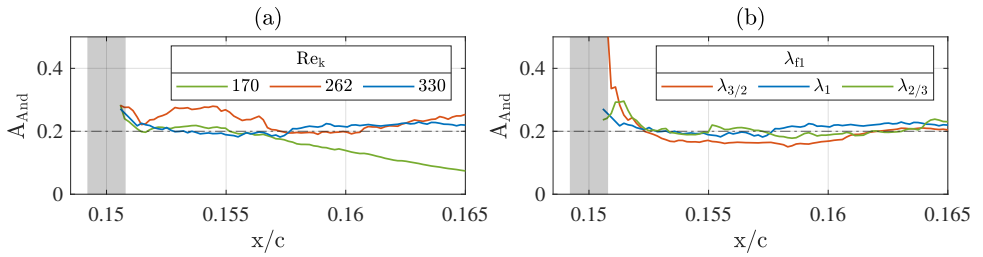

Figure 5.16: A_{And} and amplitude limit for laminar streak breakdown (-. line) for forcing (a) at $\lambda_{f1}=\lambda_1$ varying Re_k; (b) at $Re_k=330$ and varying λ_{f1}. Element location (grey shaded region).

turbulent wedges already towards the downstream end of the acquired domain (i.e. x/c≃0.174). While the extent of the PTV domain is not sufficiently long to confirm this, the newly formed turbulent BL is expected to be largely homogeneous in the spanwise direction shortly downstream.

The estimation of the relative streak amplitude A_{And} clearly shows that the amplitude limit for the laminar breakdown is reached in the element vicinity (figure 5.16). While evolving downstream, the A_{And} values corresponding to the Re_k=330 forcing case are still higher than $0.2\overline{u}_\infty$, differently than the Re_k=192 case previously investigated and in agreement with the observed breakdown of the streak structures and turbulence onset. Figure 5.16(a) indicates that comparable behaviour is achieved for the Re_k=262 forcing (obtained by reducing Re_c to 1.85×10^6), while the lower Re_k case (corresponding to $Re_c=1.35\times10^6$) features A_{And} behaves critically, leading to the development of modal CFI as discussed in section §5.3. Despite the higher DRE amplitude considered (i.e. k_4), this behaviour agrees well with the Re_k <200 threshold pertaining to critical amplitude forcing configurations. Figure 5.16(b) instead shows that a modification of λ_{f1} has an almost negligible effect on the A_{And} amplitude trends for Re_k=330.

The observed stationary flow topology is reflected by the analysis of the Q-criterion iso-surfaces reported in figure 5.17. Comparably to figure 5.4, the strong spanwise and wall-normal shear layers dominating the near-wake flow development are identified in figure 5.17(a) by a negative Q iso-surface (i.e. Q=-0.08, blue). The coherent structures organization is instead presented by means of a positive Q-criterion iso-surface (i.e. Q=0.01, red). In this super-critical scenario, three coherent flow structures are identified developing in correspondence to the low-speed element's wake and its high-shear sides. The two structures developing at the element's inboard side and in correspondence with its low-speed wake are initiated in the element vicinity, while the outboard structure originates shortly downstream of x/c≃0.155 (i.e. shortly downstream of the super-critical DRE near-wake region). The former two structures correlate well with the development of the co-crossflow HSV and IV legs wrapping around and developing aft of each DRE [84], comparably to what was observed for the critical DRE amplitude case of figure 5.4. On the other hand, the identified outboard structure possibly relates to the merging of the high-speed streaks, as it

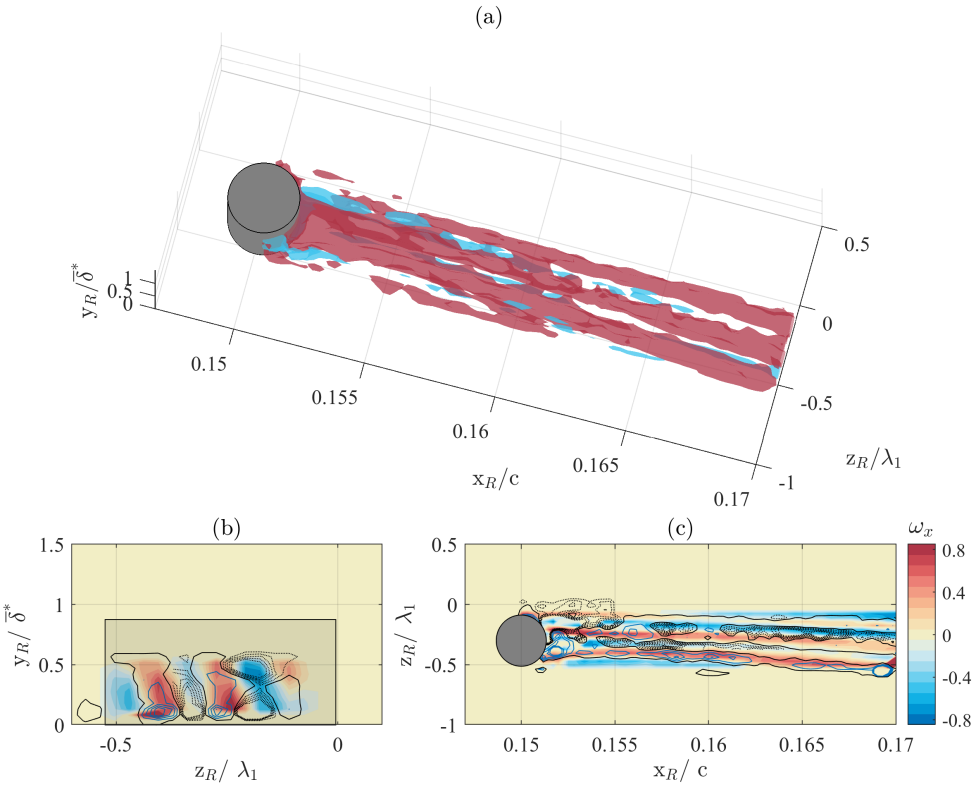

Figure 5.17: (a) Q-criterion iso-surface Q=0.01 (red) and Q=-0.08 (blue) for Re_k=330 case. Streamwise vorticity contours and Q-criterion iso-lines in (b) $y_R z_R$ plane at x/c=0.157 and (c) $x_R z_R$ plane at y/δ^*=0.55. Full blue lines Q>0 levels (5 between 0.01, 0.1), full black line Q=0.01 level, grey dash-dot lines Q<0 levels (5 between -0.008, -0.01).

can contribute to the observed increase in the overall flow unsteadiness. The three structures grow and persist up to the downstream domain end, possibly merging further downstream with assistance from the breakdown-enhanced mixing. Towards confirming the observed flow features, iso-lines of the Q-criterion in the $y_R z_R$ and $x_R z_R$ plane are reported in figure 5.17(b, c) in combination with the streamwise vorticity contours. The ω_x contours indicate that the three coherent structures are all co-rotating. Additionally, the spatial organization of the Q>0 isolines confirms that the inboard and wake structures form already in the element near-wake, while the outboard structure appears further downstream.

The spatial FFT performed for the super-critical near-wake flow region compares well to the previously considered lower Re_k cases (i.e. Re_k=90, 100, 153, 192), despite overall higher spectral amplitude levels (figure 5.18). For all the three λ_{f1} considered the forced wavelength strongly conditions the dominant flow periodicity, however, the λ_{f1} harmonics always retain high energy content in the near-wake region (figure

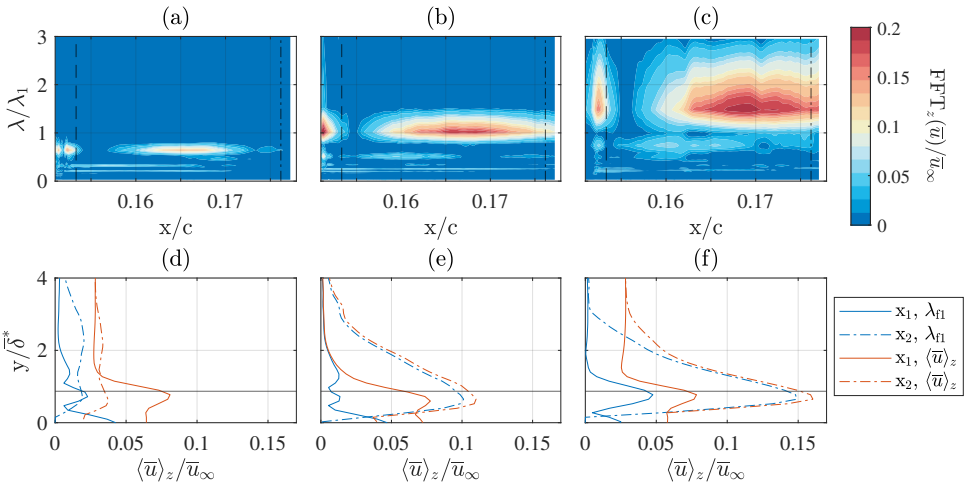

FIGURE 5.18: (a, c) Spanwise FFT spectra in the x-λ plane (vertical dashed line at x_1, verical dash-dot line at x_2) and (d-f) $\langle\overline{u}\rangle_z$ profiles and λ_{f1} FFT shape function at x_1 and x_2 for forcing at Re_k=330 and (a, d) $\lambda_{f1}=\lambda_{3/2}$; (b, e) $\lambda_{f1}=\lambda_1$; (c, f) $\lambda_{f1}=\lambda_{2/3}$; element height (horizontal full line).

5.18(a-c)). Additionally, dominant near-wake disturbances only affect the BL in the wall vicinity as confirmed by the peak of the corresponding FFT shape functions, located approximately at the same wall-normal location as the element's top (figure 5.18(d-f)). Interestingly, the amplitude peak location is almost unaltered at the downstream chord location considered (x_2). This suggests that the dominant BL disturbances develop in the form of velocity streaks even downstream of the near-wake region, without evolving into modal CFI. This effect is comparable to the flow field incurred by isolated super-critical DRE in 2D and 3D boundary layer [76, 93, 197].

To investigate the presence of transient growth mechanisms in the near-wake flow region, the evolution of the individual FFT modes is considered. The critical amplitude forcing configurations (section §5.3) proved that the FFT modes undergoing stronger transient growth are mostly sensitive to the ratio between the forcing wavelength and the diameter of the DRE. As such, the total disturbance amplitude evolution and the integral amplitude of the individual FFT modes are reported in figure 5.19 for the three λ_{f1} considered at Re_k=330. The observed amplitude evolution is indicative of the presence of stationary transient disturbances in the near-wake. However, for the three considered λ_{f1}, the primary stationary mode rapidly recovers to amplitude values comparable to the total disturbance amplitude (i.e. at x/c$\simeq$0.158), growing further downstream. The mild decay observed in both the total amplitude and the primary stationary mode amplitude towards the end of the domain, reflects the breakdown of the laminar structures developing in the BL and the onset of turbulence [16].

The energy distribution within individual FFT modes and their contribution to the transient process are consistent with the previously discussed cases for the $\lambda_{f1}=\lambda_{3/2}$ forcing (figures 5.19(a)). Redistribution of the modal energy towards mode λ_{f2} is instead observed for the $\lambda_{f1}=\lambda_1$ and $\lambda_{f1}=\lambda_{2/3}$ forcing (figure 5.19(b, c)). This suggests

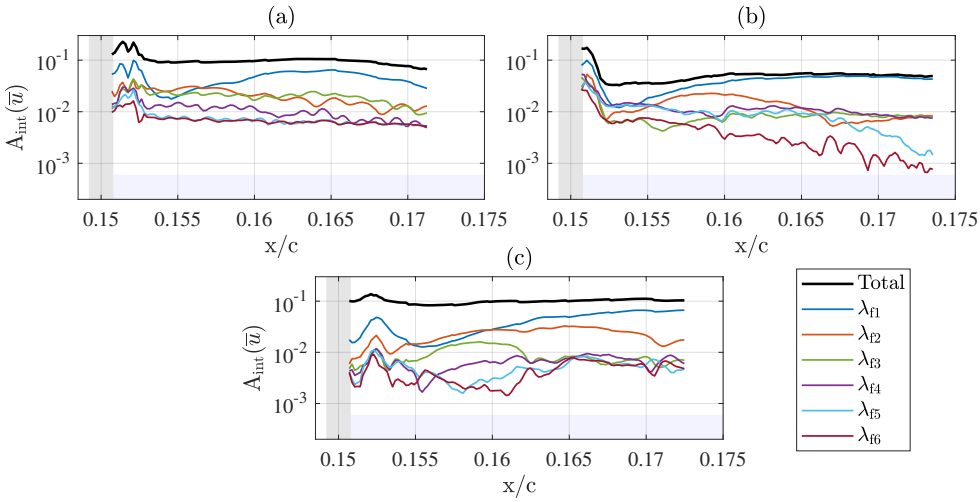

FIGURE 5.19: $A_{int}(\overline{u})$ for the total disturbance field and for the $\lambda_{f1} - \lambda_{f6}$ FFT harmonics for forcing at Re_k=330 and (a) $\lambda_{f1}=\lambda_{3/2}$, (b) $\lambda_{f1}=\lambda_1$, (c) $\lambda_{f1}=\lambda_{2/3}$. Element location (grey shaded region); PTV uncertainty (blue shaded region).

that more amplified transient disturbances develop in the considered super-critical forcing scenario, driven by the λ_{f2} mode evolution as well. Nonetheless, the growth of the stationary disturbances as described by the reported amplitude trends only gives a partial insight into the instabilities responsible for the observed laminar breakdown. More specifically, as indicated by the high and widespread unsteady fluctuations level, the unsteady disturbances developing in the element's wake appear to play a fundamental role in driving the turbulence onset [76]. In fact, figure 5.19 indicates that the rapid growth of the dominant mode occurs in the proximity of x/c$\simeq$0.158, namely the chord location corresponding to the initiation of the inboard high-speed streak driving the spanwise spreading of the high-fluctuations region. For this super-critical amplitude scenario, the role of the primary stationary mode transient decay (and of the wake relaxation) appears to be reduced, as the onset of modal CFI is bypassed by the breakdown of the laminar structures. On the contrary, the transient growth of the harmonic modes and the geometrical characteristics of the forcing element, i.e. the diameter and amplitude of the DRE, appear to play a more relevant role. Due to the increased forcing amplitude, the near-wake flow evolution is accompanied by an overall increase of unsteady fluctuations level, indicative of the growth of unsteady wake instabilities. The combination of higher shears and harmonics transient growth in the near-wake region rapidly drives the velocity streaks growth to super-critical levels according to the model proposed by [5], preventing the relaxation of the near-wake to a state stable to unsteady fluctuations [183]. Hence, in the super-critical flow scenario the receptivity process leads to the laminar breakdown of the near-wake structures and the onset of turbulence through bypass transition, as commonly identified in previous works [e.g. 4, 124]. The time-averaged nature of the conducted measurements does

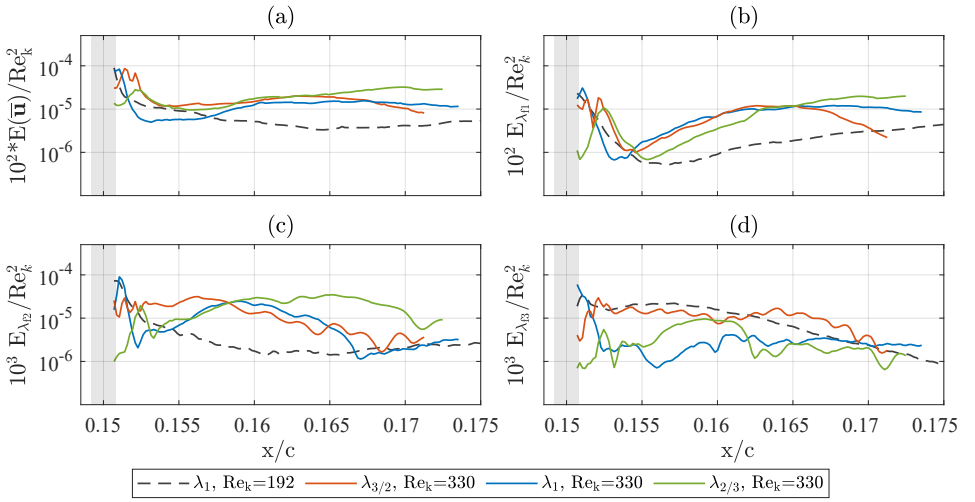

Figure 5.20: Variation of E($\overline{\mathbf{u}}$) for (a) total disturbance fields, (b) FFT λ_{f1}, (c) λ_{f2} and (d) λ_{f3} modes for varying Re_k and λ_{f1}. Energy is scaled by Re_k^2; Element location (grey shaded region).

not allow access to unsteady disturbance frequency information. Nonetheless, the stationary near-wake flow field of the super-critical DRE appears to be comparable to that of super-critical isolated roughness elements. This is largely expected as the locality of the near-wake and developing unsteady mechanisms allows for decoupling each element in a DRE array from its neighbours in the corresponding flow region. Hence, the available past studies on the unsteady near-wake of isolated elements can provide preliminary insights on the nature of the unsteady instabilities dominating the super-critical DRE near-wake [e.g. 52, 80, 93, 197].

The scalability of the stationary disturbance energy with Re_k^2 is reported in figure 5.20 for the considered super-critical configuration, in comparison with the reference critical forcing case (i.e. $\lambda_{f1}=\lambda_1$, Re_k=192). The total disturbance energy shows a larger decay in the element vicinity for the Re_k=330 cases. This can be attributed to the stronger recirculation region developing aft of the DRE, which is in turn related to the increased element height (k_4 for these cases). Nonetheless, the disturbance energy rapidly grows, reaching or overtaking the Re_k=192 values already at x/c=0.158. For all of the presented cases, the evolution of the modal energy associated with the forced wavelength rapidly decays in the element near-wake. However, for the super-critical amplitude cases the minimum energy is reached at more upstream chord locations (i.e. at x/c$\simeq$0.155) with respect to the critical amplitude case. Additionally, the disturbance energy associated with mode λ_{f2} in the Re_k=330 cases shows a substantially different trend when compared to the critical amplitude case, as it undergoes a rapid growth in the element vicinity decaying further downstream. However, the scalability of the energy trends with Re_k^2 is strongly reduced in the super-critical case, especially for the higher harmonics evolution. The lack of trend self-similarity in these super-critical cases is a further indication that

the transient growth process is affected by the high unsteadiness and the bypass transition mechanism initiated in the element wake.

Therefore, the receptivity process in critical and super-critical amplitude forcing cases is substantially different. Specifically, in the super-critical case the modal energy evolution shows that the primary stationary mode describes a rapid transient decay, while higher harmonics undergo a transient growth process. Given the increased forcing amplitude, the roughness elements induce a stronger recirculation region and shears that initiate enhanced unsteady disturbances. As such, the combination of the stationary harmonics transient growth, the excessive streak amplitude achieved in the near-wake region, and the enhanced flow unsteadiness are sufficient conditions to initiate the laminar breakdown of the streak structures in the near-wake region. This in turn induces the onset of turbulence, bypassing the development of modal CFI. This behaviour strongly differs from the previously discussed critical amplitude forcing, where the primary stationary mode transient decay is fundamental for the conditioning and onset of the modal instabilities.

5.5. Concluding Remarks

The near-element flow topology of critical and super-critical DRE in a swept wing BL is detailed, revealing the presence of transient growth in the DRE near-wake and characterizing its role in the onset of modal CFI. The 3D velocity fields in the vicinity of a DRE array are acquired by high-magnification tomographic PTV for a set of $\mathrm{Re_k}$ and λ_{f1} configurations. The proposed investigation represents a first effort towards experimentally validating the transient growth model in swept-wing boundary layer flows. Furthermore, it results in the production of a conceptual sketch that can be considered as an expansion of the transitional paths model proposed by [108], detailing the 3D boundary layer receptivity to DRE (figure 5.21).

For the sake of completeness, the conceptual model includes receptivity to sub-critical (not investigated in the present Chapter), critical, and super-critical DRE amplitudes. The investigation of sub-critical configurations lays outside the scope of the present investigation, however, these have been widely characterized in previous studies [e.g. 70, 83, 145, 166]. These works outlined that sub-critical roughness configurations are well-modelled by k-dependent receptivity relationships, which directly correlate the initial CFI amplitude to the roughness height (k/δ^*) or geometrical parameters depending on it (i.e. $\mathrm{Re_k}$). This is summarized by the leftmost branch of the proposed scheme. In the following discussion, the main findings of the present investigation on critical and super-critical receptivity are summarised.

The critical near-wake stationary flow topology is characterized by the alternation of low- and high-speed streaks, which are the locii of high-fluctuation regions. As evolving downstream, the amplitude of the streaks reduces, with a single high-speed streak persisting in the flow field and accompanied by the development of a low-speed region on its sides. These structures modulate the BL, resulting in the formation of localised spanwise and wall-normal shears. Spanwise spatial spectral analysis suggests that transient mechanisms dominate the near-wake flow evolution, affecting both the primary stationary mode and its higher harmonics (i.e. smaller wavelengths). Specifically, transient growth affects the chordwise evolution of FFT

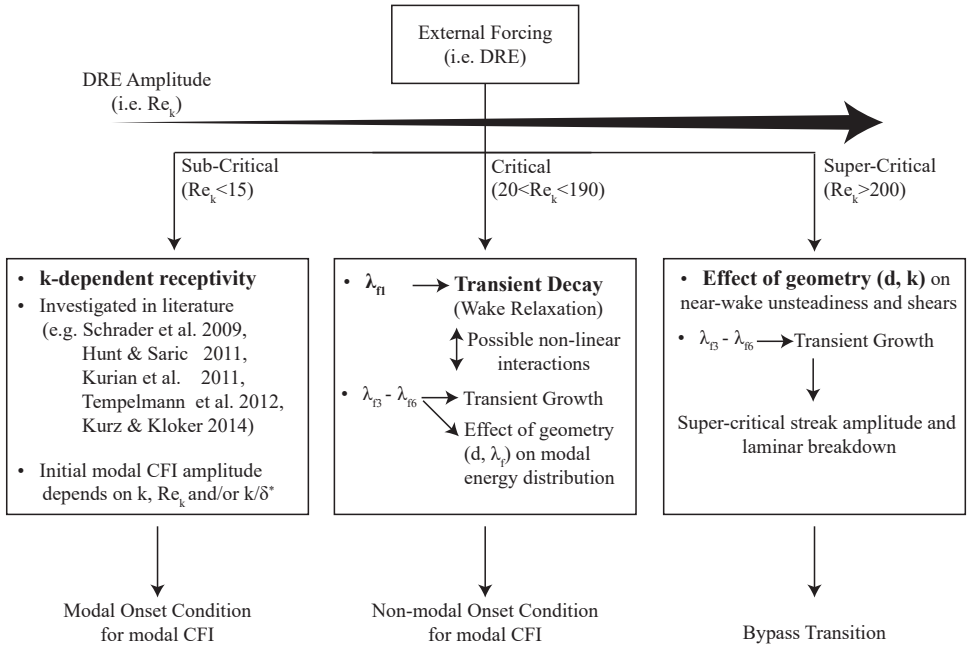

Figure 5.21: Conceptual sketch of 3D boundary layer receptivity to external DRE forcing, depending on the external forcing amplitude (i.e. $\mathrm{Re_k}$). Primary stationary disturbance indicated as λ_{f1}, higher harmonics indicated as $\lambda_i = \lambda_{f1}/i$. Main receptivity mechanism for each forcing amplitude range in bold characters.

modes $\lambda_{f3} - \lambda_{f6}$, comparably to what is observed by White *et al.* [183] in 2D boundary layers. Additionally, in this 3D boundary layer scenario the primary stationary mode (λ_{f1}) evolves following a *transient decay* process, which can be correlated to the wake relaxation concept proposed by Ergin & White [52]. The dominant mode evolution is well-modelled by an initial algebraic decay followed by an exponential growth driven by the inherently unstable nature of the λ_{f1} mode, which essentially evolves into a modal stationary CFI. The identified transient decay and growth processes are robust to $\mathrm{Re_k}$ modifications and the corresponding energy evolution is self-similar when scaled by $\mathrm{Re_k^2}$. Nonetheless, they appear to be sensitive to the DRE spacing λ_{f1} and diameter d. Specifically, the combination of λ_{f1} and d conditions the disturbance energy distribution within the FFT spectra. The wavelengths undergoing the most significant transient growth appear to always be included in the 0.7d-1.3d range. This suggests a correlation between the element geometry, the spatial arrangement of the developing HSV, and the observed transient growth in agreement with previous investigations [e.g. 117]. Notwithstanding this, all the considered cases show transient decay affecting the λ_{f1} mode.

The identified transient process comprises weak stationary transient disturbances, which allow for the rapid relaxation of the baseflow and the development of modal CFI further downstream. Nonetheless, the transient decay of the λ_{f1} mode is fundamental

to establish the onset conditions and downstream evolution of the modal instabilities. More specifically, the CFI onset amplitude estimation (A_0) can be related to the $A_{int,\lambda_{f1}}$ value achieved immediately aft of the near-wake flow region (i.e. the flow region affected by the transient decay mechanism). In this region, the integral amplitude and effective N-factor pertaining to the λ_{f1} CFI mode evolution are well approximated by LST results confirming that the instabilities follow an exponential (thus modal) growth process further downstream. The discussed receptivity scenario for critical DRE amplitudes is summarized by the central branch in figure 5.21.

To conclude, the near-element flow evolution of a super-critical amplitude DRE is investigated. The near-wake stationary flow topology is dominated by the alternation of high- and low-speed streaks, with the former merging shortly downstream of the element location, substituting the low-speed wake. This results in a stronger and more spread high-fluctuations region, which propagates into a turbulent wedge while evolving downstream. The formation of high- and low-speed streaks cascade on the wake's sides drives the spanwise opening of the turbulent region [13]. The spectral analysis once more highlights the relevant contribution of the stationary transient disturbances to the near-wake development. In the super-critical scenario, steeper decay and growth rates characterize the disturbances' evolution, thus reducing the chordwise extent of the transient process. In this flow scenario, the transient growth process occurs in conjunction with enhanced shears and excessive amplitude of the velocity streaks developing in the near-wake region. Thus, the breakdown of the laminar structures is initiated shortly downstream of the element, leading to increased flow unsteadiness and the onset of turbulence through bypass transition comparably to what has been previously observed in 2D BL [4, 124]. Accordingly, the role of the transient decay of the λ_{f1} mode becomes secondary in the super-critical scenario, as the onset and evolution of modal CFI is bypassed by the breakdown of the laminar structures. This is in agreement with the reduced scalability offered by Re_k^2 in the super-critical case. The receptivity mechanism identified for super-critical amplitude forcing cases is summarized by the rightmost branch of figure 5.21, completing the first conceptual map for 3D boundary layer receptivity to DRE.

6

Stationary CFI Suppression via Multiple DRE Forcing

This Chapter introduces a novel suppression technique for stationary CFI, building upon the linear superposition of the velocity disturbances introduced by a streamwise series of optimally arranged DRE arrays. The robustness of this technique is investigated for a smooth wing surface as well as in the presence of enhanced distributed surface roughness.

ZOPPINI, G., MICHELIS, T., RAGNI, D. & KOTSONIS, M. 2022 Cancellation of crossflow instabilities through multiple discrete roughness elements forcing. *Physical Review Fluids* 7 (12). [192]

6.1. Introduction

Numerous experimental and numerical investigations dedicated to stationary CFI control or suppression, manipulate the wing surface roughness to act as a LFC technique. In 2D boundary layers investigations, this resulted in the concept of roughness shielding [50, 79, 155] or in the implementation of destructive superposition of properly tuned velocity systems [57, 105, 176]. The latter technique has been extended to specific 3D boundary layers applications, however, passive control of stationary CFI in swept wing scenarios is typically attempted by using sub-critical roughness forcing [136, 138] or UFD techniques [175]. These techniques are all discussed in further detail in the literature framework presented in section §1.11.

The detailed knowledge of the near-element flow topology combined with the clarification of the dominant receptivity mechanisms identified in Chapter 5, sets the basis for the development of innovative LFC techniques dedicated to the suppression of CFI. Specifically, this Chapter introduces a technique based on the linear superposition of stationary CFI introduced by the application of a streamwise series of optimally positioned DRE arrays. Reduction of the amplitude of the developing CFI and a consequent BL transition delay are achieved thanks to the destructive interference of the velocity disturbances introduced by the streamwise successive arrays when these are appropriately adjusted in amplitude and spanwise phase shift. Such a forcing configuration is compatible with the suppression of CFI developing in a realistic free-flight scenario. Specifically, given the residual distributed surface roughness of common swept wings, the naturally developing BL is typically dominated by the simultaneous development of a set of CFI modes with a-priori unknown phase and wavelength. Therefore, the application of a *reference* DRE array is expected to condition the developing flow field by focussing the instabilities into a monochromatic CFI mode [117, 137], while damping the BL spectral content associated with the other excited wavelengths [175]. This results in a flow scenario comparable to what is obtained by UFD. Accordingly, successive DRE arrays (named *control* arrays), can be optimally arranged and applied at more downstream chord locations in order to dampen the introduced monochromatic CFI through linear destructive interference.

The main purpose of the presented investigation is to map the effect of multiple DRE arrays in suppressing CFI artificially introduced by a reference array. Comparably to previous investigations, the reference DRE array is applied to force the most unstable CFI mode [λ_1, 84, 137, 154]. The control arrays are then designed with different amplitude and suitable phase shift to introduce velocity disturbances that linearly superimpose and dampen the pre-existing CFI. Forcing the critical CFI mode differs from the traditional flow control applications, in which DRE arrays or UFD force a sub-critical wavelength (typically of $2/3\lambda_1$, [136, 175]). This design choice is based on the desire of investigating the suppression capabilities of the sole linear superposition of the reference critical CFI and the control velocity disturbance systems. Nevertheless, the proposed control method can be expected to work also for other than the critical forced wavelengths.

To extend the applicability of the proposed technique to more realistic transition scenarios, the present investigation additionally tackles the effect of multiple DRE arrays on the developing CFI in the presence of enhanced distributed surface roughness.

This is obtained by applying DRPs on the wing surface, as described in section §2.2. Patches obtained from spray adhesive are employed, and the incurred flow fields are assessed to ensure the repeatability of the forced BL dominant features. Multiple DRE configurations, comparable to the ones measured for the smooth wing surface, are then applied on the wing. In such a scenario, the reference array is expected to focus the set of CFI modes excited by the DRP into a single monochromatic instability, in a process similar to UFD. This results in a fixed CFI periodicity and phase, possibly damping the BL spectral content associated with the smaller wavelength induced by the DRP [175]. As such, the application of successive control arrays enables the suppression of the monochromatic CFI induced by the DRP-reference array combination.

6.2. Experimental Set-up and Methodology

The investigations presented in this Chapter are performed in the LTT, and measure the flow features developing on the pressure side of the M3J swept wing model (section §2.1.1).

Acquisitions are performed at a constant α=-3.36° while varying the freestream Reynolds number Re_{c_X} in a range of 1.9-2.9$\times 10^6$ to ensure the robustness of the investigated suppression technique. Global flow features are acquired through IR thermography, delivering an estimate of the transition front location and its modifications depending on the applied roughness configuration. Local BL analysis is instead performed using planar PTV. Throughout this investigation, the tunnel-attached reference system (i.e. XYZ) is employed to discuss the IR acquisitions, while the wing-attached system (i.e. xyz) is used to analyse the planar PTV flow fields. A detailed description of the employed set-up can be found in section §2.3.3, while the main aspects are summarized hereafter including the procedures implemented for the velocity fields reconstruction and processing.

6.2.1. DRE Arrays Configurations

The multiple array configurations explored in this Chapter are manufactured by CNC laser cutting (section §2.2), cutting he spanwise series of arrays from a unique PVC foil. Assuming the correct placement of the reference array, this procedure ensures that the relative chordwise and spanwise shifts imposed between consecutive arrays are accurately reproduced on the wing surface.

The design of the multiple DRE configurations considered in this Chapter, combine the insights on the dominant floe features gained in the previous Chapters with dedicated LPSE solutions. Specifically, LPSE solutions indicate that the λ_1 wavelength corresponds to the most amplified mode (or to one of the most amplified modes) throughout the whole Re_{c_X} range considered (section § 2.4). Additionally, the results reported in Chapter 3 outline that a downstream shift of the forcing array location (i.e. x_{DRE}/c=0.125) induces CFI with smaller initial amplitude while keeping the near-element flow topology almost unaltered. These downstream configurations, however, provide easier measurement access to the near-element flow field thanks to the naturally increased BL thickness. Finally, in Chapter 5 the main near-element flow structures and their orientation in the flow field are detailed. This provides

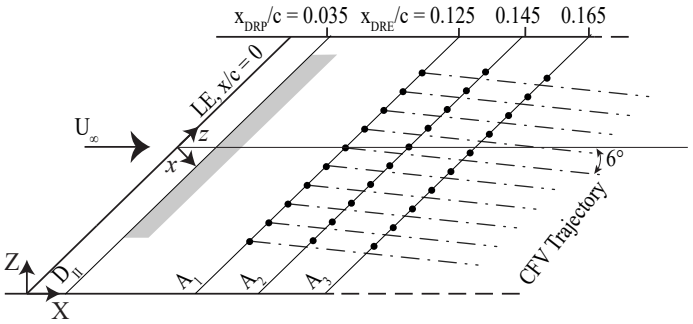

Figure 6.1: Scheme of multiple DRE array and DRP patch application on the wing surface for forcing case C10 (not to scale).

a measure of the existing constant phase angle between the near-wake structures and the freestream flow ($\simeq 6°$), which in turn allows for proper computation of the required shift between the reference (A_R) and the following control (A_C) array.

The chordwise shift between the two arrays is set to x/c=0.02, sufficiently extended for the damping of the initial transient and the emergence of modal stationary CFI (Chapter 5). As such, the velocity disturbances introduced by A_C, superpose to the CFI induced by A_R, without interacting with the complex flow structures dominating the DRE near-wake field [22, 84, 199]. The A_C application is designed with a spanwise shift such that its elements are located in correspondence to the evolving CF vortices induced by A_R. Moreover, an additional spanwise phase shift of $\lambda_1/2$ is introduced between the two DRE arrays, to superpose high (low) speed regions induced by A_R to low (high) speed regions induced by A_C. Further control arrays are added with the same chordwise spacing and no phase shift with respect to A_C, only accounting for the CF vortex tilt with respect to the freestream flow.

The main roughness configurations discussed within this Chapter are reported in table 6.1. The multiple array forcing cases are built by combining a reference array and one or more control arrays. Individual DRE arrays are indicated as A_n and feature specific characteristics collected in table 6.1. The sketch reported in figure 6.1, additionally shows the multiple arrays forcing geometrical arrangement for a representative case. Both the effect of individual arrays (i.e. case C1-A_1) and multiple arrays forcing (i.e. case C1-A_{1-3} given by the superposition of reference array A_1 and control arrays A_2 and A_3) are investigated and discussed in section § 6.3.

6.2.2. DRP Configurations

In order to extend the applicability of the introduced technique to more realistic transition scenarios, it is desirable to evaluate its suppression capabilities under conditions of elevated background roughness. To enable this, the wing surface roughness is enhanced by applying DRP patches, mimicking the effect of a rough wing surface finishing.

The manufacturing and characterization of these patches are detailed in section

Case	DRE/DRP	k [mm]	x_{DRE}/c	Re_k	k/δ^*	x_{DRP}/c
C1-	A_1	0.2	0.125	94	0.44	-
	A_2	0.2	0.145	89	0.40	-
	A_3	0.2	0.165	87	0.39	-
	A_4	0.2	0.185	85	0.37	-
C2-	A_1	0.2	0.1	101	0.49	-
	A_2	0.2	0.12	95	0.44	-
	A_3	0.2	0.14	90	0.41	-
	A_4	0.2	0.16	88	0.39	-
C3-	A_1	0.2	0.1	101	0.49	-
	A_2	0.1	0.12	22	0.22	-
C4-	A_1	0.1	0.1	23	0.24	-
	A_2	0.2	0.12	94	0.44	-
C5-	A_1	0.2	0.1	101	0.49	-
	A_2	0.2	0.13	93	0.42	-
	A_3	0.2	0.125	94	0.44	-
	A_4	0.2	0.155	88	0.39	-
C6-	A_1	0.2	0.075	113	0.29	-
	A_2	0.2	0.095	102	0.49	-
C7-	D_1-D_{11}	-	-	-	-	0
	D_{13}	-	-	-	-	0.035
C8-	A_1	0.1	0.02	42	0.57	-
	A_2	0.1	0.04	32	0.38	-
	A_3	0.1	0.05	30	0.35	-
	A_4	0.1	0.075	26	0.28	-
	A_5	0.1	0.095	23	0.25	-
	A_6	0.1	0.1	24	0.24	-
	A_7	0.1	0.125	22	0.21	-
	A_8	0.1	0.145	21	0.20	-
	D_I	-	-	-	-	0
	D_{II}	-	-	-	-	0.035
C9-	A_1	0.2	0.05	127	0.35	-
	A_2	0.2	0.07	113	0.29	-
	D_I	-	-	-	-	0
C10-	A_1	0.1	0.125	22	0.21	-
	A_2	0.2	0.145	89	0.41	-
	A_3	0.2	0.165	87	0.39	-
	D_{II}	-	-	-	-	0.035

Table 6.1: Geometrical parameters of measured forcing configurations. Individual DRE arrays (A_n, forcing mode λ_1) and DRP patches (D_n). IR acquisitions for all reported cases at α=-3.36° and Re_{c_X}=1.9-2.9×10^6. PTV acquisitions for selected cases at at α=-3.36° and Re_{c_X}=2.17 ×10^6.

§2.2, where the repeatability of the DRP geometrical features is outlined. The flow field induced by individual patches is instead investigated in section §6.4, confirming that the dominant BL flow features are mostly independent of the local patch geometry. As such, the investigation of the interaction between the velocity disturbance systems induced by the DRP and the DRE arrays is only performed accounting for two representative DRP patches: D_I located at the leading edge, and D_{II} located at x_{DRP}/c=0.035. The flow features resulting from the superposition of DRP and DRE arrays are discussed in section §6.5.

The DRP and DRP-DRE configurations discussed in the current Chapter are reported in table 6.1 (i.e. cases C7-C10). The measured DRP patches are indicated as D_n, while the configurations resulting from the superposition of DRP and DRE are, for example, indicated as C10-D_{II}-A_{1-3}. This case forces the BL flow with DRP patch D_{II}, reference array A_1 and control arrays A_2 and A_3. Figure 6.1 sketches the geometrical arrangement of the roughness elements of case C10, featuring the simultaneous application of a DRP patch and multiple DRE arrays.

6.2.3. IR Thermography

IR acquisitions (section §2.3.1) are performed using one radiometric camera[12] imaging a portion of the model pressure side for the chosen range of Re_{c_X} at α=-3.36°. The acquired domain covers the whole wing chord and is centred at the wing midspan with a spatial resolution of ≃1.7mm/px.

After averaging and calibration, the IR images are post-processed with Differential Infrared Thermography (DIT) [118, 131] to extract the transition front location. The resulting chordwise estimate is considered representative of the BL laminar-to-turbulent transition location (x_{TR}/c) and is compared among the various roughness forcing configurations considered.

6.2.4. Planar Dual-Pulse PTV

Planar PTV acquisitions provide a local quantification of the BL flow and its chordwise evolution, highlighting the effects of the considered forcing configurations on the developing CFI. The experimental set-up employed for PTV acquisitions is reported in section §2.3.3, while the main optical and acquisition parameters are reported in table 2.5.

Throughout this investigation, the PTV acquisitions are performed in the yz plane (i.e. the spanwise wall-normal plane). The wall-normal direction is non-dimensionalised as $y/\overline{\delta}^*$, where $\overline{\delta}^*$≃0.75mm is the experimental displacement thickness of the natural BL (i.e. no DRE applied) at x/c=0.25 and Re_{c_X}=2.17 ×10^6. The PTV domain is centred at the wing midspan and extends for z/λ_1 ≃4 and $y/\overline{\delta}^*$≃3.5. The BL development in the yz plane is described by the spanwise and wall-normal time-averaged velocity components, namely $\overline{w}$ and $\overline{v}$ respectively. PTV planes between 15% and 35% of the chord are measured to incur the CFI chordwise evolution.

Velocity Fields Reconstruction and Processing

Further processing of the time-averaged velocity fields is performed to extract the main flow features. The spanwise average of $\overline{w}$, performed at each y-location, provides

an estimate of the wall-normal BL mean velocity profiles ($\overline{w}_b$). By subtracting the $\overline{w}_b$ profile to $\overline{w}$, the disturbance velocity field is obtained ($\overline{w}_d$). The root mean square (rms) of the spanwise velocity signal, can instead provide an estimation of the disturbance profile along the y-direction ($\langle\overline{w}\rangle_z$) [e.g. 70, 123, 166]. Additionally, a spatial FFT is performed to infer the spectral organization of the flow field: at each y-coordinate the spanwise $\overline{w}$ signal is transformed in the spatial frequency domain ($\mathrm{FFT}_z(\overline{w})$), providing information on the modal composition of the developing BL and on the chordwise evolution of the individual Fourier modes, for different forcing configurations. Moreover, for each acquired PTV plane, the local CFI amplitude ($\mathrm{A_{int}}$) is estimated following the integral amplitude definition [47]. Namely, the disturbance profiles $\langle\overline{w}\rangle_z$, or the FFT shape functions corresponding to a single mode, are integrated along y up to y=δ_{99} to quantify the CFI chordwise evolution.

6.3. Effect of Multiple DRE Arrays Forcing

In this section the stationary BL developing in the presence of multiple DRE arrays is investigated. Modifications observed in the transition front location and the local CFI development are quantified and discussed for the various configurations considered.

6.3.1. Effect of Multiple DRE Arrays on Transition

The baseline configuration discussed in the following analysis is case C1-A_{1-4}, composed by 4 DRE arrays of height k_2 spaced at λ/λ_1=1 (table 6.1). The reference array C1-A_1 is located at $\mathrm{x_{DRE}/c}$=0.125, while the control arrays are placed at successive intervals of 2% chord downstream. As discussed in section §6.2.1, the first control array C1-A_2 is arranged to have a phase shift of $\lambda_1/2$ with respect to A_1, while control arrays C1-A_3 and C1-A_4 are in phase with C1-A_2.

IR images are acquired for the considered range of Re_{c_X} starting from the reference array configuration (C1-A_1) and progressively adding the control arrays. The resulting images for case C1 at Re_{c_X}=2.27×10^6 are reported on the top row of figure 6.2, while DIT images computed by subtracting the C1-A_1 data to the multiple array cases are reported in the bottom row. The brighter portion of the DIT images is indicative of the transition delay achieved through the multiple arrays forcing. Significant transition delay is already obtained by applying a single control array (i.e. C1-A_2). Nonetheless, the cumulative effect given by the addition of control arrays C1-A_3 and C1-A_4 shifts the BL laminar-to-turbulent transition further downstream.

The transition front chordwise location ($\mathrm{x_{TR}/c}$) and, therefore, the achieved transition delay, is quantified for each considered forcing configuration within the acquired Re_{c_X} range. The resulting transition locations are reported in figure 6.3(a), showing the achieved transition delay is robust to the mild modifications of Re_{c_X} considered in this investigation. Figure 6.3(a), indicates that the considered multiple array forcing case (C1-A_{1-4}) significantly affects the developing BL, delaying the transition front location up to 8% chord downstream. The first two control arrays applied (i.e. C1-A_2 and C1-A_3) play a major role towards this result, nonetheless, array C1-A_4 is contributing to a further downstream shift of the transition location, especially for

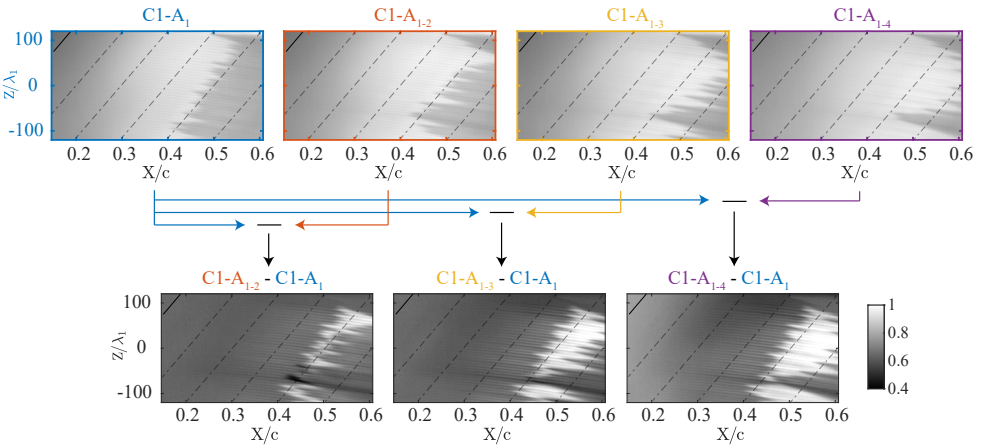

Figure 6.2: IR acquisitions at $Re_{c_X}=2.27\times10^6$ for forcing case C1. (*Top*), IR images for C1-A_1, C1-A_{1-2}, C1-A_{1-3} and C1-A_{1-4} configurations. (*Bottom*), DIT images are computed by subtracting the C1-A_1 case from the multiple array cases. Wing leading edge (full black line); flow comes from the left.

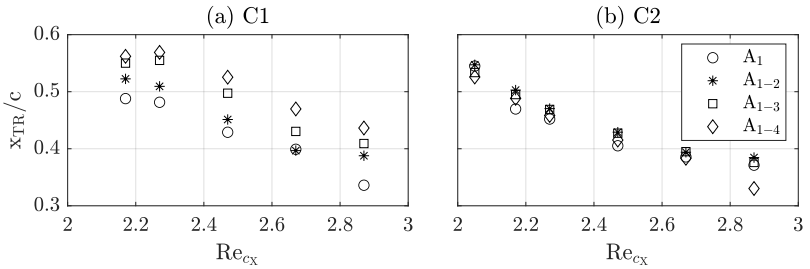

Figure 6.3: x_{TR}/c extracted at various Re_{c_X} for all configurations of cases (a) C1 and (b) C2.

the higher Re_{c_X} considered.

6.3.2. Linearity of the Disturbances Superposition

To better understand and characterize the underlying flow mechanisms, the flow field resulting from the superposition of arrays of case C1 is further investigated through the PTV acquisitions. Figure 6.4 reports the disturbance ($\overline{w}_d$) and time-averaged ($\overline{w}$) velocity contours for the reference array forcing (C1-A_1) and for the multiple array forcing (C1-A_{1-4}) at two representative chord locations. The BL resulting from forcing configuration C1-A_1 (figures 6.4(a,b)), is modulated by the development of a typical CFI, showing the periodic alternation of high- and low-speed regions along the spanwise direction [16, 137, 154]. Both the geometric size of the developing CF vortices, as well as the CFI intensity, are reduced by the application of multiple control arrays (C1-A_{1-4}, figure 6.4(d, e)), correlating well with the observed delay in transition. Furthermore, the $\langle\overline{w}\rangle_z$ wall-normal evolution (figure 6.4(c,f)), indicates

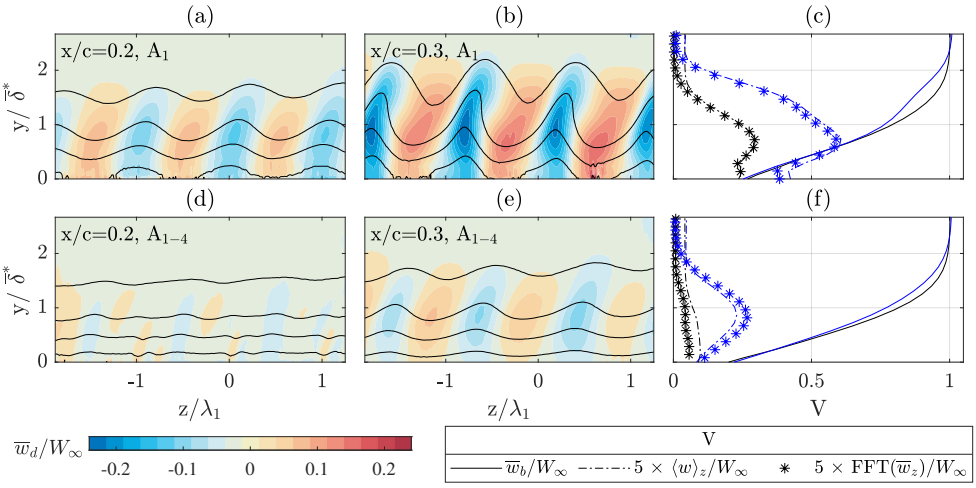

Figure 6.4: $\overline{w}_d$ contours at (a, d) x/c=0.2 and (b, e) x/c = 0.3 for configurations (a, b) C1-A$_1$ and (d, e) C1-A$_{1-4}$. Contours of $\overline{w}$ every 20%W$_\infty$ (black solid lines). (c, f) Comparison of $\overline{w}_b$ (solid line), $\langle\overline{w}\rangle_z$ (-. line) and λ_1 FFT shape function ($*$) at x/c=0.2 (black) and x/c=0.3 (blue).

that the significant CFI amplitude reduction obtained by applying the control arrays prevents the development of non-linearities. In fact, the weak secondary peak visible in the $\langle\overline{w}\rangle_z$ profile at x/c=0.3 for case C1-A$_1$, is absent in case C1-A$_{1-4}$. Additionally, by hindering the CFI evolution, the flow field resulting from the DRE arrays superposition is reducing the deformation of the mean flow. This is indicated by the absence of the inflection point in the $\overline{w}_b$ profile at x/c=0.3 for forcing case C1-A$_{1-4}$ (figure 6.4(f)).

The CFI amplitude reduction and the consequent transition front delay, are achieved thanks to the linear superposition of the velocity disturbance systems introduced by each of the applied arrays. This affects the CFI in their initially linear development phase, reducing their onset amplitude and downstream growth. To verify the assumption of linear superposition, the summation of the velocity disturbances induced by each of the individual arrays applied in case C1 is compared to the disturbances measured aft of the multiple arrays configuration. PTV acquisitions of the flow field incurred by individual arrays are performed for cases C1-A$_1$, C1-A$_2$, C1-A$_3$. For sake of simplicity, the spanwise disturbance velocity signal $\overline{w}_d$ is extracted at a single x- and y-location corresponding to x/c=0.25 and $y/\overline{\delta}^*$=0.5. The spanwise velocity signal extracted from the flow fields originated by each array is reported in figure 6.5(a). The spanwise phase shift imposed on the velocity signals corresponds to the geometrical spanwise shift imposed between subsequent arrays of case C1-A$_{1-4}$. Figures 6.5(b, c) respectively compare the summation of the velocity signals for the first two and three arrays, to the velocity disturbances measured in the multiple arrays flow fields (i.e. configurations C1-A$_{1-2}$ and C1-A$_{1-3}$). The reported velocity signals are comparable both in trend and amplitude, confirming the linearity of the superposition effect.

A spatial FFT is applied to the spanwise time-averaged PTV velocity signal to

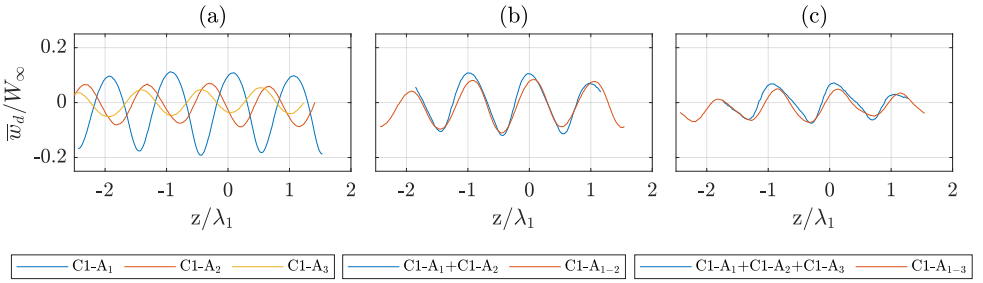

Figure 6.5: Spanwise $\overline{w}_d$ signal extracted at x/c=0.25 and y/$\overline{\delta}^*$=0.5 for: (a) C1-A$_1$, C1-A$_2$, C1-A$_3$; (b) the summation of C1-A$_1$, and C1-A$_2$ (blue) and C1-A$_{1-2}$ (red); (c) the summation of C1-A$_1$, C1-A$_2$ and C1-A$_3$ (blue) and C1-A$_{1-23}$ (red).

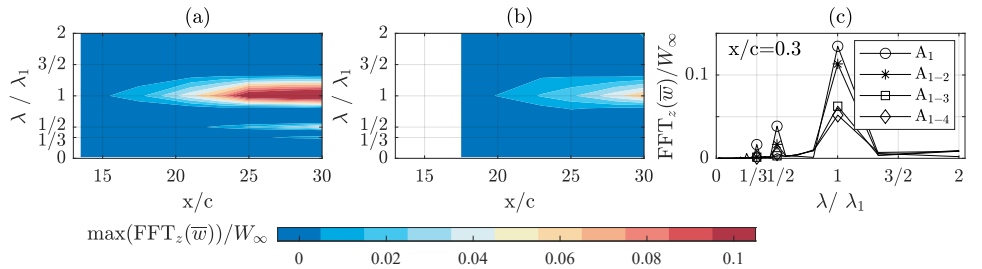

Figure 6.6: Spatial FFT analysis for case C1. FFT spectra contours in the x-λ plane for (a) C1-A$_1$ and (b) C1-A$_{1-4}$. (c) Fourier spectra at x/c=0.3 and y/$\overline{\delta}^*$=1 for C1 configurations.

investigate the BL spectral content and identify the dominant stationary CFI and their chordwise evolution. Considering the baseline forcing case C1, the spectral analysis of the reference array configuration (C1-A$_1$) and of the four array configuration (C1-A$_{1-4}$) is reported in figure 6.6(a-b). As expected, the application of the sole reference array results in a monochromatic flow field focussed on the λ_1 mode, figure 6.6(a). The excited CFI rapidly grows throughout the domain, accompanied by the second (λ_2=λ_1/2) and third (λ_3=λ_1/3) harmonics, which appear successively downstream. The development of higher harmonics, confirms the presence of non-linearities in the evolution of the BL forced by C1-A$_1$, in agreement with the weak secondary peak identified in $\langle\overline{w}\rangle_z$ (figure 6.4(c)). Figure 6.6(b) indicates that the BL incurred by the multiple arrays forcing configuration, is as well dominated by the development of the λ_1 mode. However, in case C1-A$_{1-4}$ the CFI spectral amplitude is significantly reduced, to the point that no harmonics are detected. This agrees well with the absence of measurable non-linear interactions and the reduced flow distortion observed for this forcing case (figure 6.4(f)). Additionally, the FFT shape functions are compared to the $\langle\overline{w}\rangle_z$ profiles in figure 6.4(c, f). A good match in both shape and maximum amplitude is observed, suggesting that the λ_1 FFT mode is sufficient to correctly describe the dominant CFI within the considered BL region. In fact, as also indicated by the spectra reported in figure 6.6(c), the λ_1 mode harmonics

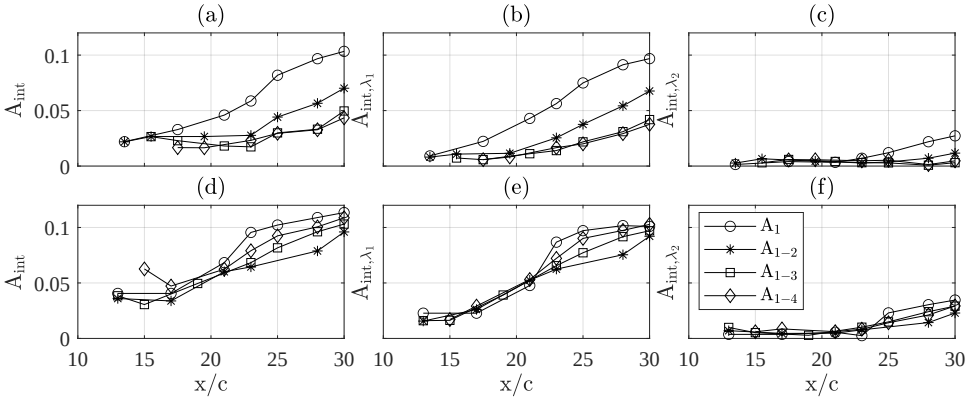

Figure 6.7: A_{int} chordwise evolution for cases (a-c) C1 and (d-f) C2. (a, d) A_{int}; (b, e) A_{int,λ_1}; (c, f) A_{int,λ_2}.

are still relatively weak (for case C1-A_1) or even below the measurement resolution threshold (for case C1-A_{1-4}) within the considered domain. It is noteworthy that the CFI dominant wavelength is left unaltered by the array superposition. This further confirms that the CFI suppression is the result of the linear superposition of the reference CFI and the velocity disturbances introduced by the applied control arrays, rather than being driven by the introduction of non-linear interactions as is the case for the UFD technique [136, 138, 175].

Further characterization of the BL flow field resulting from the array superposition, is given by the estimation of the amplitude of the developing CFI instabilities [47]. In particular, the integral amplitudes (A_{int}) are estimated by integrating the $\langle\overline{w}\rangle_z$ profile along the y-direction, up to y=δ_{99}. Comparable amplitude calculations can be obtained by integrating the FFT shape function corresponding to one specific mode (i.e. wavelength), estimating amplitudes of individual harmonics, such as λ_1 and λ_2 (i.e. A_{int,λ_1} and A_{int,λ_2} respectively), excluding all other flow disturbances. The resulting amplitude values are reported in figure 6.7(a-c) as extracted for the reference array configuration C1-A_1 and for the multiple arrays forcing C1-A_{1-2}, C1-A_{1-3} and C1-A_{1-4}. The A_{int} describing the CFI evolution for the flow field forced by the sole reference array C1-A_1, is almost double with respect to the amplitudes pertaining to the CFI developing in the multiple array forcing cases. Moreover, only mild differences can be observed between A_{int} and corresponding A_{int,λ_1}, confirming the prevalent role of the dominant λ_1 mode on the flow field development for all forcing configurations of case C1. With the single array forcing, amplitude saturation is reached at the end of the acquired domain, accompanied by the growth of the λ_2 harmonics, as shown by figure 6.7(c). The cumulative effect of the superposition of control arrays leads instead to significant amplitude reduction: amplitude saturation is no more reached for the multiple DRE forcing cases, and the λ_2 harmonics retain almost null values. Results presented in figure 6.7(d-f) are discussed in the following section §6.3.3.

Throughout the considered configurations, the unsteady disturbance development

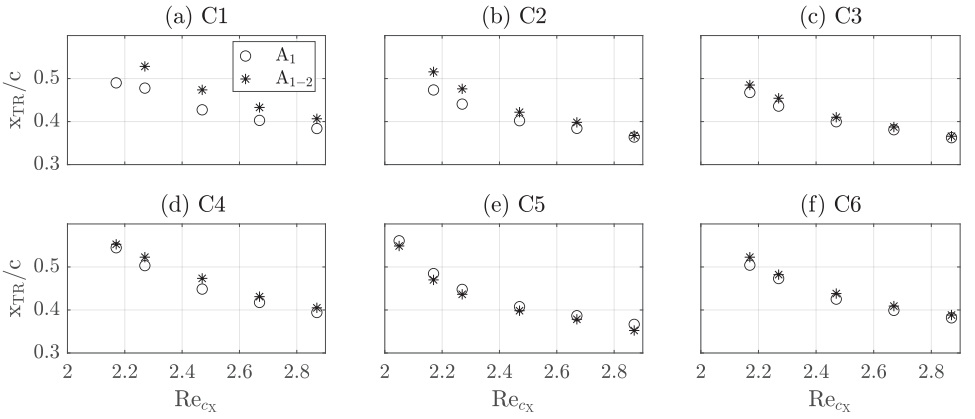

Figure 6.8: x_{TR}/c extracted at various Re_{c_X} for various forcing cases. Refer to table 6.1 for the specifics of each forcing case considered.

is left mainly unaltered by the DRE array superposition. Reduced primary CFI amplitudes, correspond to later development or weaker unsteady disturbances. Nonetheless, in all considered cases the BL transition occurs due to the development of secondary instabilities and their rapid breakdown, as previously observed by multiple investigations [154, 175]. Given that these considerations are well-established within the CFI investigation and development, no extended treatment of the unsteady disturbance development is included in the present Chapter.

6.3.3. Sensisitivity to DRE Arrays Parameters

To ensure the robustness of the DRE superposition technique in suppressing the CFI introduced by the reference array, a range of double arrays configurations (A_R and A_C) with different design and arrangement is measured. This parametric investigation is performed through IR acquisitions while modifying the x_{DRE}/clocation, the arrays chordwise spacing and the DRE height k. The analysis of these cases is limited to the extraction of the transition front location for the acquired Re_{c_X} range, reported in figure 6.8. The effects of the three considered parameters, namely the DREs amplitude, chordwise spacing and chord location, are discussed hereafter.

Effect of DRE amplitude

Forcing configurations composed by a reference array and a control array of height k_2, successfully delay BL transition when arranged with a 2% chordwise distance and a phase shift of $\lambda_1/2$ (i.e. C1-A_{1-2}, C2-A_{1-2}, figure 6.8(a, b)). However, comparable configurations built using DRE arrays of smaller amplitudes (i.e. k_1) reduce the effectiveness of the multiple DRE forcing technique. This can be associated with the excessively high or insufficiently low amplitude of the velocity disturbances introduced by the control array with respect to the reference CFI. As an example, case C3-A_{1-2} is presented in figure 6.8(c). For this forcing configuration, A_1 features DRE of the amplitude of k_2, while A_2 is designed with a nominal DRE amplitude of

k_1. Therefore, the control array induces velocity disturbances that are too weak to effectively suppress the existing reference CFI. This results in minor changes to the transition front location. Configuration C4-A_{1-2}, shows instead the opposite effect, as the control array induces velocity disturbances that are too strong, thus effectively "overshooting" the reference CFI. Also, this configuration results in a mild delay of the transition front location (figure 6.8(d)).

Effect of arrays chordwise spacing
Forcing configurations composed by a reference and a control array arranged at a chordwise spacing of x/c=0.03, provide reduced suppression capabilities with respect to case C1-A_{1-2}. This effect is possibly due to the superposition of the velocity disturbances introduced by A_C, to already too strong CFI forced by the A_R, resulting in a transition advancement (i.e. C5-A_{1-2} or C5-A_{3-4}, figure 6.8(e)). In fact, in their initial phases of development the modal CFI follow an exponential growth process, rapidly over-growing the control velocity disturbances introduced by A_C.

A shorter chordwise spacing between the reference and control array (i.e. x/c=0.01, not reported for the sake of brevity), is as well leading to an upstream shift of the transition location. This can be related to the application of A_C in a region affected by flow structures pertaining to the element near-wake evolution. Therefore, the velocity instabilities introduced by the control array, interact with complex flow structures that evolve into modal CFI only further downstream [84, 199].

Effect of arrays chord location
Reference DRE arrays located in the vicinity of the wing leading edge, are expected to introduce stronger CFI, advancing the BL transition [138, 199]. Nonetheless, case C2 shows that the multiple arrays forcing technique is capable of suppressing the CFI incurred by a reference array located at x_{DRE}/c=0.1. As indicated in table 6.1, the multiple array design of case C2 is identical to the design of case C1, except for the more upstream x_{DRE}/c. Figures 6.3(b) and 6.7(d-f), confirm that the application of control arrays (i.e. configuration C2-A_{1-4}) is capable of hindering the development of the CFI introduced by C2-A_1. The effect of the first applied control array significantly delays the BL transition and reduces the CFI amplitude. However, the more upstream location of the application is reducing the suppression capabilities of the multiple DRE arrays technique. Accordingly, the addition of further control arrays with the same design as case C1 appears to be detrimental to the transition location and CFI amplitude evolution.

If shifted towards more upstream chord locations, the combination of the reference and control arrays has the undesired effect of advancing the transition front (i.e. C6-A_{1-2}, figure 6.8(c)). This is attributed to the excessively high initial amplitude of the disturbances introduced by the reference array, as well as to the rapid exponential growth of the CFI at these chord locations, which may be affected by the stronger pressure gradient typical of the LE region, making the applied array design inefficient [199]. Ideally, arrays of smaller amplitudes and relative displacement placed at upstream chord locations (i.e. $x_{DRE}/c \leq 0.075$), may effectively delay the transition. Fabrication of repeatable and robust DREs of lower height than those used in the present study is deemed essential for the evaluation of such cases.

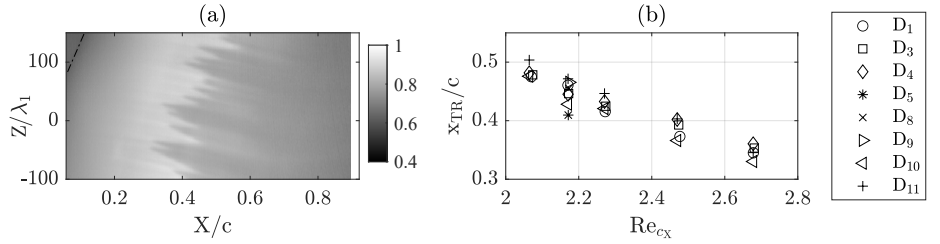

Figure 6.9: (a) IR acquisition at Re_{c_X}=2.17 $\times 10^6$ for forcing case C7-D_8. (b) x_{TR}/c extracted at various Re_{c_X} for DRP of case C7.

The considerations reported beforehand, indicate that the multiple arrays design parameters (i.e. DRE height, chordwise distance, $x_{DRE}/c$and arrays phase shift), are fundamental for the successful suppression of the CFI introduced by the reference array. However, the results presented so far, only consider the suppression of a monochromatic CFI introduced in the BL. As such, a further step is taken to investigate the robustness and capabilities of the proposed suppression technique by simulating the elevated surface roughness finishing of a realistic wing, which typically leads to the development of multiple randomly spaced and phased CFI modes in the BL. The resulting flow field and its interaction with the velocity disturbances introduced by multiple DRE configurations are discussed hereafter.

6.4. Effect of DRP Patches Forcing

Randomly distributed roughness is applied on the swept wing surface using patches of spray adhesive. Given the need to investigate several combinations of DRE and DRP forcing, these patches are applied in-situ, measured and then removed. The repeatability of the various DRP geometry has been assessed in section §6.2.2, nevertheless, the flow field forced by the DRP is hereafter investigated to ensure no considerable variations appear among the different measured cases.

6.4.1. Effect of DRP on Transition and CFI

Hereafter, the dominant flow topology is characterized for a representative DRP located at the wing leading edge (C7-D_8, table 6.1). A global overview of the flow field induced by C7-D_8 is acquired through IR measurements (figure 6.9(a)). The saw-tooth pattern of the transition front appears more irregular with respect to the DRE forced cases, in agreement with previous works [16, 117, 137]. This effect is related to the simultaneous development in the BL of multiple CFI wavelengths with varying initial amplitude, as well as to the spanwise local characteristics of the DRP patch which may induce locally stronger or weaker CFI. The transition front location of the BL flow incurred by a set of DRP measured throughout this investigation is presented in figure 6.9(b). Despite the local geometrical features of the applied DRP, the forced flow scenario is comparable among considered cases, as also confirmed by the repeatability of the transition front location at fixed Re_{c_X} and the outcome of

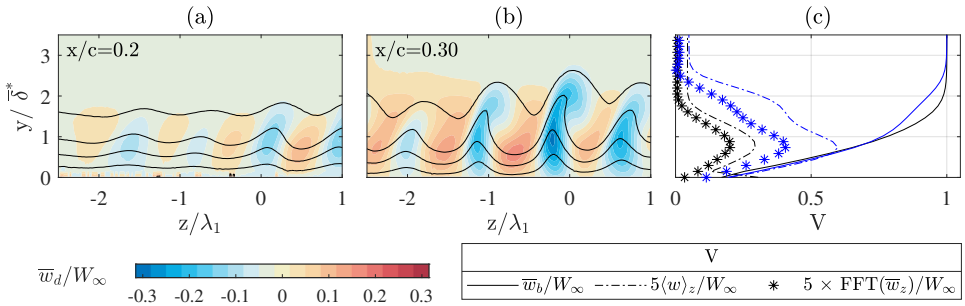

Figure 6.10: $\overline{w}_d$ contours at (a) x/c=0.2 and (b) x/c = 0.3 for C7-D$_8$ forcing. Contours of $\overline{w}$ every 20%W$_\infty$ (black solid lines). (c) Comparison of $\overline{w}_b$ (solid line), $\langle\overline{w}\rangle_z$ (dot-dashed line) and λ_1 FFT shape function ($*$) at x/c=0.2 (black) and x/c=0.3 (blue).

the DRP characterisation (figure 2.3). The mild residual data scatter observed in the extracted transition location, can be attributed to the specific geometrical variations among the collection of applied DRP (figure 2.3).

Local characteristics of the BL flow incurred by the C7-D$_8$ forcing, are investigated through the PTV acquisitions. Figures 6.10(a,b), presenting the $\overline{w}$ and $\overline{w}_d$ velocity contours, show that the resulting BL velocity is significantly modulated, indicating the presence of well-developed CFI [75, 125]. The early development of CFI in the considered case can be related to the vicinity of the C7-D$_8$ patch to the wing leading edge, which is the most receptive region to external flow disturbances [137, 138]. Accordingly, figure 6.10(c) shows that at x/c=0.3 the corresponding $\overline{w}_b$ profile features an inflection point indicative of the mean flow deformation. Moreover, due to the local geometrical characteristics of C7-D$_8$, each of the identified CF vortices mildly differs from its neighbours either in strength, size or stage of development. This can be related to the interaction of the multiple CFI modes excited by the DRP, as well as to the presence of individual peaks and valleys in the DRP patch. The latter induce CFI with higher or lower initial amplitudes, and consequently faster or slower development [48, 50, 117]. Furthermore, figure 6.10(c) exhibits the $\langle\overline{w}\rangle_z$ profile extracted from the displayed flow fields. Similarly to the reference DRE forcing of figure 6.4, $\langle\overline{w}\rangle_z$ is characterized by the presence of a secondary peak at x/c=0.3, suggesting non-linear interactions occur between the developing CFI modes.

The investigation of the BL spectral content is performed through the spanwise FFT, resulting in the spectra reported in figure 6.11(a) for the representative C7-D$_8$ case. The chordwise spectra evolution, confirms that the BL is still dominated by the λ_1 mode, as would be expected from stability theory predictions for similar conditions [98, 152]. Nonetheless, high spectral content is also associated with a wide range of wavelengths distributed between $\lambda_1/3$ and $3/2\lambda_1$. This further motivates the non-linear characteristics observed in the $\langle\overline{w}\rangle_z$ evolution (figure 6.10(c)). Comparable flow features are observed for other leading-edge DRP patches (i.e. C7-D$_9$), whose corresponding spectra are reported in figure 6.11(b). The lower CFI spectral amplitude measured in the latter case can be related to the mildly lower k$_{DRP}$ of configuration

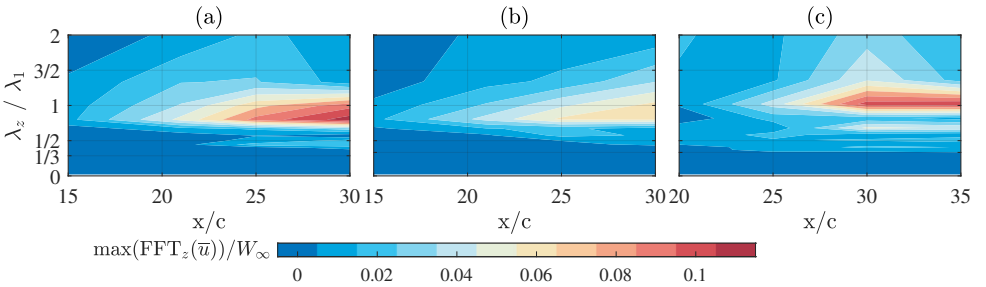

Figure 6.11: Spatial FFT spectra contours in the x-λ plane for case (a) C7-D_8, (b) C7-D_9 and (c) C7-D_{13}.

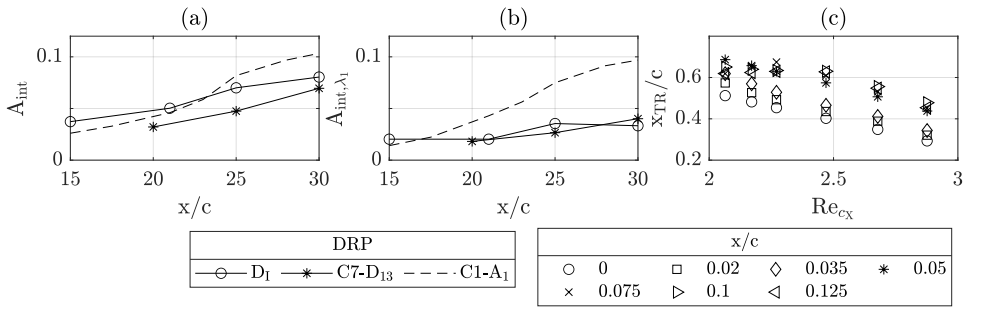

Figure 6.12: A_{int}chordwise evolution for cases D_I, C7-D_{13} and C1-A_1. (a) A_{int}; (b) A_{int,λ_1}. (c) Transition front chordwise location at various Re_{c_X} for DRP patches starting at various x_{DRP}/c.

C7-D_9 (figure 2.3(a)).

Having demonstrated the repeatability of the DRP patches geometry (section §6.2.2) and of BL flow features they induce, in the remainder of this Chapter, the DRP patch located at the leading edge is generically indicated as D_I. The CFI amplitudes induced by the representative D_I are reported in figure 6.12(a, b). In agreement with the spectral characteristics and the observed presence of non-linearities, for the D_I forcing case, the A_{int} (figure 6.12(a)) achieves significantly higher values than those computed for A_{int,λ_1} (figure 6.12(b)). In particular, the λ_1 mode accounts for almost half of the total disturbance amplitude, while the evolution of the initiated set of small wavelength modes contributes to the remaining CFI amplitude. The relevant contribution of the developing set of CFI wavelengths is as well evident in the amplitude differences between the λ_1 FFT shape function and the $\langle\overline{w}\rangle_z$ profile, enhanced at x/c=0.3 due to the increased strength of the excited CFI modes. This behaviour, as well as the overall amplitude values, are comparable between the various DRP patches measured (not reported for sake of conciseness), further confirming that the global flow features induced by the DRP are mostly independent of their local geometry.

6.4.2. Effect of DRP chord location

As a final step for the DRP characterization, the sensitivity of the BL transition and the developing CFI to x_{DRP}/cis investigated. In particular, DRP patches of 3% chord streamwise length are applied starting at various chord locations. The x_{TR}/cextraction for the considered cases shows that a downstream shift of the DRP starting location is accompanied by a downstream shift of transition (figure 6.12(c)). Furthermore, the FFT analysis of the $\overline{w}_d$ signal for a representative case C7-D_{13} (with x_{DRP}/c=0.035, indicated as D_{II} in the remainder of this Chapter) is reported in figure 6.11(c)). The spectral evolution, confirms that the BL contains CFI modes corresponding to a range of wavelengths between $\lambda_1/3$ and $3/2\lambda_1$, with significant peaks for the λ_1 mode and its harmonics. Both the spectral peaks and the corresponding CFI amplitudes (reported in figure 6.12 for D_{II}) achieve mildly lower values with the x_{DRP}/c downstream shift. This agrees well with the observed downstream shift of the transition location and reflects the results obtained by the authors in a previous investigation dedicated to the BL receptivity to DRE arrays location [199]. Nonetheless, also for the D_{II} case the λ_1 mode amplitude only accounts for part of the total disturbance amplitude (A_{int}), as multiple CFI modes are simultaneously developing and interacting in the BL.

Overall, the dominant flow features incurred by the DRP appear to be repeatable among the various considered cases. As such, DRP applied at the leading edge (i.e. D_I) or slightly downstream (i.e. D_{II}) is used as a baseline configuration to investigate the role and effectiveness of DRE arrays in BL forced by enhanced surface roughness.

6.5. Effect of DRE Arrays Forcing in the Presence of DRP

The characterization of the flow field induced by the sole DRP forcing, confirms that the induced dominant flow features are repeatable among the various measured cases. Hence, in the following section, DRE arrays are applied on the wing surface in combination with the DRP, towards investigating the flow field resulting from the interaction between the velocity disturbances induced by the two roughness systems.

6.5.1. Effect of a Reference DRE Array Superposition to a DRP

As a starting configuration, reference arrays forcing the dominant λ_1 mode are applied in combination with D_I. The DIT image obtained by subtracting the flow field induced by D_I to the C8-D_I-A_1 configuration is reported in figure 6.13(a). With the addition of C8-A_1, the saw-tooth pattern of the transition front appears more regular and uniform. However, both the DIT image as well as the extracted transition locations (figure 6.13(b)), indicate that the addition of a reference array forcing the dominant mode enhances the CFI development strongly advancing transition. This is the case for all forcing configurations reported in figure 6.13(b), in agreement with the results described by previous works for 2D boundary layers [50, 79].

Figure 6.13(c) reports a comparable investigation performed by adding the reference array to the BL forced by the more downstream DRP patch D_{II}. Despite the mildly

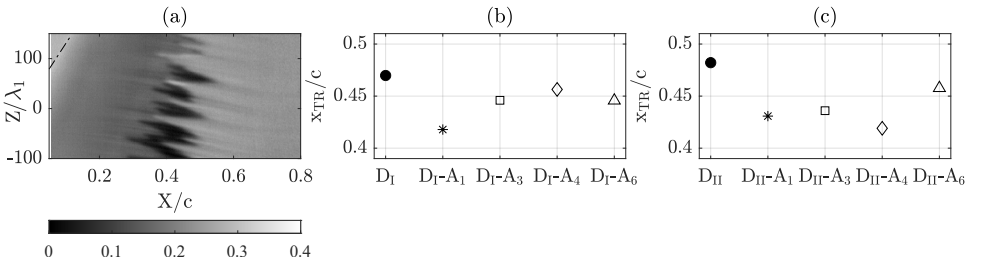

FIGURE 6.13: (a) DIT image at Re_{c_X}=2.17 $\times 10^6$ computed subtracting the D_I case to C8-D_I-A_1. (b, c) x_{TR}/c extracted at various Re_{c_X} for cases (b) D_I, C8-D_I-A_1, C8-D_I-A_3, C8-D_I-A_4 and C8-D_I-A_6; (c) C8-D_{II}, C8-D_{II}-A_1, C8-D_{II}-A_3, C8-D_{II}-A_4 and C8-D_{II}-A_6.

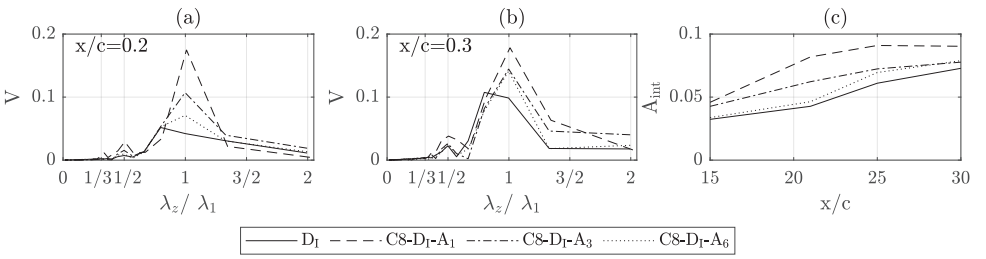

FIGURE 6.14: Spatial FFT spectra for $y/\overline{\delta}^*$=1 at (a) x/c=0.2 and (b) x/c=0.3 for cases D_I, C8-D_I-A_1, C8-D_{II}-A_3 and C8-D_{II}-A_6. V stands for $\max(\mathrm{FFT}_z(\overline{w}))/W_\infty$. (c) Integral amplitude A_{int}computed for all cases.

weaker CFI introduced by D_{II}, the application of the reference DRE array at any of the considered chord locations significantly advances the transition location. Case D_{II}-A_4 appears as an outlier in comparison to the general trend, possibly due to improper alignment of the DRE arrays.

This indicates once more, that the dominant flow topology and the CFI downstream evolution are consistent for the various DRP considered. However, the near-flow field induced by each DRP is expected to be locally affected by the patches' geometrical features, particularly in the presence of peaks in the DRP distribution [48, 49, 75, 125]. For the current investigation, this can lead to the formation of a near-DRP flow field that has a destructive interaction with the velocity disturbances introduced by the reference DRE array. Thus, the superposing velocity disturbance systems enhance the existing CFI instead of damping them, if the phase shift of the two disturbance systems is not suitably set.

Further quantification of the interaction between the flow structures induced by the DRP and DRE array, is given by the FFT and amplitude analysis. The spanwise FFT spectra are reported in figure 6.14 for cases forced by D_I and a reference DRE array. The addition of the reference array enhances the development of the forced λ_1 mode, which rapidly overtakes the smaller wavelength modes introduced by D_I (figure 6.14(a, b)). Consequently, the estimated A_{int} (figure 6.14(c)) rapidly reaches higher values in the presence of both DRP and DRE, motivating the recorded advancement

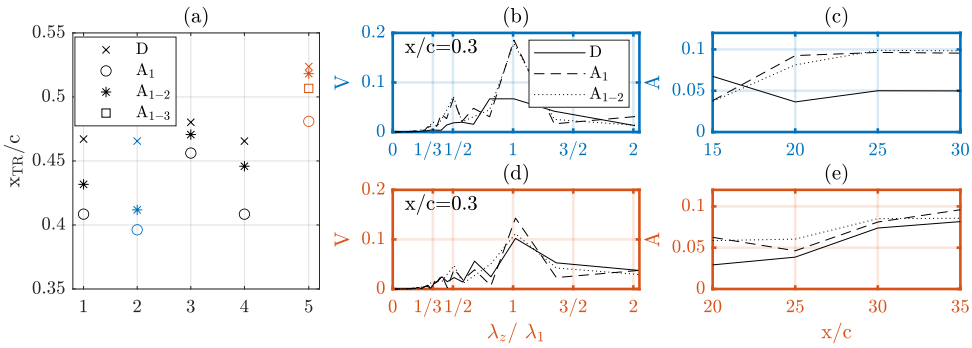

Figure 6.15: (a) x_{TR}/c extracted at Re_{c_X}=2.17 $\times 10^6$ for cases 1.C8-D_I-A_{1-2}, 2.C8-D_I-A_{4-5}, 3.C8-D_{II}-A_{7-8}, 4.C9-D_I-A_{1-2}, 5.C10-D_{II}-A_{1-3}. (b) FFT spatial spectra at x/c=0.3 and $y/\overline{\delta}^*$=1 for cases C8-D_I-A_{4-5} and (d) C10-D_{II}-A_{1-3}. V stands for $\max(FFT_z(\overline{w}))/W_\infty$. (c) A_{int} chordwise evolution for cases C8-D_I-A_{4-5} and (e) C10-D_{II}-A_{1-3}.

in transition. In particular, configuration C8-D_I-A_1 forces the λ_1 mode on top of the D_I patch, thus introducing high initial amplitude CFI close to the highly receptive leading edge region [137, 138, 199]. This results in the rapid growth of the dominant stationary CFI and its harmonics, with the dominant CFI reaching amplitude saturation shortly after x/c=0.2. Differently from what was observed for sub-critical UFD configurations [175], the reported spectra indicate that despite the critical mode forcing applied, some residual small-wavelength modes remain present in the BL. This can be related to the relatively high amplitude of the applied DRP, which excites a strong set of CFI (see also section §6.5.2). Additionally, the lack of control on the phase shift between the DRP-induced CFI and the superposing disturbance systems introduced by the reference array may also affect the spanwise invariance of the resulting flow field. Nonetheless, despite resulting in enhanced CFI, the application of a reference DRE array in combination with a DRP patch succeeds in focussing most of the BL spectral energy content on the forced CFI mode. The resulting CFI develops with fixed wavelength and phase, however, the reference array does not dampen the set of small-wavelength modes introduced by the DRP. This is attributed to the excessive amplitude of the DRP patches, which introduces CFI that are too strong to be effectively controlled by the reference DRE array.

6.5.2. Effect of Multiple DRE Arrays Superposition to DRP Patches

As the superposition of the reference DRE array to the DRP leads to the development of more uniform albeit stronger CFI, the effect on the developing CFI of the addition of control DRE arrays is hereafter investigated. Forcing configurations comparable to the ones presented in section §6.3 are measured in the presence of the DRP.

The BL transition location resulting from the superposition to a DRP patch of a set of 2 or more arrays (i.e. a reference and one or more control arrays), is shown in figure 6.15(a). Cases C8-D_I-A_{1-2}, C8-D_I-A_{4-5} and C9-D_I-A_{1-2} are applied in combination

to D_I, while cases C8-D_{II}-A_{7-8} and C10-D_{II}-A_{1-3} are applied in combination to D_{II} (with reference to table 6.1). Both of the considered upstream array forcing cases (C8-D_I-A_{1-2}, C9-D_I-A_{1-2}), feature a reference array with nominal height k_1 located on top of D_I. As previously observed, in such configurations the reference array induces the rapid development of a strong monochromatic λ_1 mode, enhancing the existing CFI (figure 6.15(b, c)). The application of a control array successfully delays transition with respect to the BL forced by the superposition of D_I and the reference array (figure 6.15(a)). The achieved transition delay is relatively mild for configuration C8-D_I-A_{1-2}, while it appears to be more significant for case C9-D_I-A_{1-2}, featuring a control array with higher nominal amplitude k_2. However, none of the three considered forcing configurations is strong enough to delay the transition location with respect to the sole D_I forcing. This can be related to the persistence in the BL of residual incoherent modes initiated by the DRP (figure 6.15(b)). These modes accompany the development of the dominant λ_1 mode, enhanced by the DRE forcing. Consequently, the multiple DRE arrays technique demonstrates reduced suppression capabilities in the presence of DRP.

The effect of the superposition of the more downstream patch and the multiple DRE arrays is also investigated. The C8-D_{II}-A_{7-8} configuration shows comparable behaviour to the previously described cases, while the C10-D_{II}-A_{1-3} configuration appears to be more effective (figure 6.15(a)). In particular, in the latter case the superposition of the velocity disturbance systems induced by D_{II}, the reference array C10-A_1 with nominal amplitude k_1 and the control array C10-A_2 with nominal amplitude k_2, leads to a BL transition location comparable with the one of the sole D_{II} forcing. Accordingly, the FFT (figure 6.15(d)) and amplitude (figure 6.15(e)) analysis of the incurred flow fields, show comparable CFI evolution and behaviour for the sole D_{II} and for the C10-D_{II}-A_{1-2} configuration. This effect can be related to the milder (possibly lower peak amplitude) patch applied in case C10-D_{II}, which results in the development of a weaker set of small-wavelength instabilities as confirmed by the more downstream transition location. Accordingly, the application of the reference DRE array focuses the CFI on the forced mode but is also more effective at damping the incoherent set of modes introduced by the DRP. This partially restores the suppression capabilities of the proposed linear superposition technique. However, the addition of a second control array (C10-A_3) to the forcing configuration leads again to transition advancement. This effect is observed also in the presence of different DRP patches and with changes in the amplitude and location of the DRE arrays (results not reported for the sake of conciseness).

Overall, the multiple DRE forcing configuration proves to be less effective at suppressing the CFI in the presence of enhanced surface roughness, at least within the investigated parameter space. This is mostly attributed to the residual non-uniformity of the developing BL, which prevents the effective suppression of the phase shift between the existing CFI (incurred by the DRP) and the velocity disturbances introduced by the applied DRE arrays. Consequently, the combined forcing given by the DRP and DRE roughness systems, can enhance the existing CFI instead of damping them. Nonetheless, the application of a control array effectively delays the transition location with respect to the reference array-DRP forcing configuration. This

indicates further investigation of the proposed technique can lead to the development of a more robust design for the multiple DRE forcing applied in combination with the DRP. A possible expansion of the investigated parameter space can be insightful towards identifying more efficient configurations. Furthermore, the exploration of multiple DRE forcing based on sub-critical arrays (i.e. UFD) can result in improved control capabilities, thanks to the combined effect of the non-linear conditioning and the linear superposition of velocity disturbances. Alternatively, the wing surface can be equipped with sensors to sense the incoming CFI actual phase and location on the wing, thus tuning the suppression technique to the proper antiphase. As an example, this could be achieved by employing smart morphing surfaces, protruding membranes or micro-plasma actuators [103, 168].

6.6. Concluding Remarks

This chapter presents a suppression technique aiming at damping the CFI introduced by a reference DRE array by applying a streamwise series of optimally designed control arrays. All the DRE arrays applied throughout this investigation, force the most unstable CFI mode and are arranged with suitable DRE amplitude and spanwise phase shifts. The presented flow fields are measured by IR thermography and planar PTV acquisitions, respectively allowing for the characterization of the BL laminar-to-turbulent transition location and the quantification of the local BL development.

The successive application of multiple control DRE arrays on a smooth wing surface leads to significant damping of the monochromatic CFI introduced by a reference array. Accordingly, the transition location shifts up to 8% chord more downstream with respect to the sole reference array forcing case. The observed transition delay appears to be robust to the mild changes of Re_{c_X} considered in this investigation, however, it proves sensitive to the multiple array configuration design parameters (i.e. DRE height, chordwise spacing and chord location). The spanwise spatial FFT analysis, confirms the forced λ_1 mode dominates the BL development both in the sole reference array forcing, as well as with the addition of successive control arrays. In the latter configuration, the amplitudes of the dominant stationary CFI and its harmonics are both significantly decreased, reducing the mean flow modulation and the non-linearities affecting the BL development. The fact that the dominant CFI wavelength is left unaltered by the array superposition, further confirms that the introduced technique is based on the linear superposition of the velocity disturbance systems introduced by each of the applied DRE arrays.

However, the suppression capabilities of the proposed method are reduced by the presence of enhanced distributed surface roughness, such as the effect of a rough wing surface finishing. During this investigation, randomized distributed surface roughness is simulated by applying multiple DRP patches obtained by spraying adhesive on the wing surface. These patches contain a random distribution of geometrical peaks, initiating a set of CFI with various wavelengths and phases. Accordingly, the resulting BL is still dominated by the most unstable stationary mode λ_1, but also contains a set of CFI modes with wavelengths between $\lambda_1/2$-$3/2\lambda_1$.

In such a scenario, the application of a reference DRE array succeeds in focusing

the developing CFI on the forced λ_1 mode, albeit resulting in a transition front advancement. However, the developing BL still suffers from residual spanwise non-uniformity due to the persistence of the weaker CFI modes induced by the DRP. Therefore, the application of successive DRE arrays in this configuration proves to be more challenging from a design perspective, as well as less effective in suppressing the pre-existing CFI. More specifically, the addition of control arrays successfully delays the transition location with respect to the flow field incurred by the DRP-reference array combination. Nonetheless, in all of the configurations measured throughout the current investigation, the superposition of multiple DRE arrays to the DRP patch results in a reduced (or unchanged) extent of the laminar flow region with respect to the sole DRP forcing. This can be related to the lack of control on the phase shift between the pre-existing CFI, introduced by the DRP-reference array combination, and the velocity disturbances induced by the applied control arrays. Therefore, further investigation will be necessary to fully understand and control the mechanisms dominating DRP and DRE superposition.

7

Conclusions and Recommendations

This Chapter summarises the most important findings discussed throughout this booklet, providing few recommendations and a preliminary outlook on future work.

7.1. Conclusions and Recommendations

The research discussed in this booklet characterizes the receptivity of stationary crossflow instabilities to surface roughness in a swept wing boundary layer, combining numerical stability solutions with advanced flow diagnostics.

Scaling of Roughness Configurations for Receptivity Analysis
The impact of amplitude and chord location of DRE arrays on CFI development and breakdown is explored in Chapter 3. The obtained results outline that an increase (decrease) in element height and/or a decrease (increase) in DRE streamwise location lead to an advancement (postponement) of laminar to turbulent transition, introducing instabilities with higher (lower) amplitudes. While Re_k partially captures these changes, a one-parameter correlation is insufficient to account for the complex receptivity mechanisms. The investigation of near-element flow features appears necessary for a more complete understanding of the receptivity process and a more accurate estimation of CFI initial amplitude.

As a step towards this, the conducted parametric investigation suggests that up-scaled roughness configurations at downstream chord locations provide comparable flow scenarios while ensuring easier experimental access to the near-element flow region. Hence, a subset of configurations is selected for further analyse the near-element flow features and their role in the receptivity process.

The Near-element flow and Receptivity to Roughness
As a first effort, in Chapter 4 the near-element flow topology and transitional scenario incurred by nearly-critical IDRE is investigated. The dominant instabilities in the near-wake of the element are introduced by the shedding process occurring on the top side of the IDRE, initiating strong, tonal unsteady fluctuations driving the onset and growth of the turbulent flow region. Therefore, IDRE-induced CFI provide a limited contribution to the onset of instabilities and their initial evolution, only appearing in the asymmetric downstream development of the identified flow features.

To properly investigate the stationary CFI receptivity to roughness, DRE forcing configurations closer to the CFI regime are considered. For critical amplitude forcing scenarios, the receptivity process results from the combination of the transient decay of the dominant CFI mode and the transient growth of a sub-set of its harmonics. The set of harmonic modes undergoing transient growth depends on the combined effect of the forcing wavelength and DRE diameter. Nonetheless, in all considered cases the transient processes are well-described by simple mathematical functions robust to modifications in Reynolds number and self-similar when scaled by Re_k^2. The identified transient processes substantially condition the onset of modal instabilities, with the proposed mathematical models providing an estimation of the CFI onset amplitude (A_0) corrected for the initial transient behavior. Downstream of the near-wake, the evolution of the instabilities is well-approximated by an exponential growth process described by an LST solution initiated with the experimentally estimated A_0. These considerations highlight the need and open the way to the development of more accurate and complete numerical solvers which account for the initial non-modal behavior of the instabilities, embedding it in the receptivity process.

At last, the CFI receptivity to super-critical DRE arrays is investigated. In this scenario, the transient decay/growth process identified in the near-wake combine with strong shears and excessive streaks amplitude. Unsteady near-wake instabilities are rapidly enhanced, initiating bypass transition in the element vicinity, thus limiting the effects of the transient processes. Hence, the receptivity mechanism identified for super-critical amplitude forcing cases mostly relates to the forcing geometry and the excessive near-wake unsteadiness and shears.

Overall, the investigations discussed throughout this booklet, led to substantial insights regarding the flow mechanisms dominating stationary CFI to various forcing amplitudes. In addition, the results presented in Chapter 5 demonstrate that the application of high-resolution tomographic flow diagnostics can correctly capture the stationary micron-scale flow mechanisms occurring in highly-convective flow regimes. Hence, this technique can be employed to expand the considered parameter range and investigate the receptivity of stationary CFI to various types of roughness (e.g. DRP or various DRE geometries) or other parameters (e.g. freestream turbulence, pressure gradient). In this way, the characterization of the receptivity process can be further expanded and consolidated, possibly providing a more robust estimation of the CFI onset amplitude depending on the external forcing configuration. In addition, the application of a time-resolved flow diagnostics, can provide further insights on the receptivity of super-critical DRE scenarios by characterizing the unsteady instability mechanisms. This can be coupled with a global instability analysis performed for a range of different forcing geometries and external parameters, to establish if it plays a role in the receptivity process.

Passive control of CFI

Building upon the insights gained on the near-element flow topology, Chapter 6 presents a novel suppression technique based on the linear superposition of the velocity disturbances introduced by a streamwise series of optimally designed DRE arrays. On a smooth wing surface, this technique demonstrates significant suppression capabilities, which are robust to Re_{c_X} modifications but sensitive to the design parameters of the control configuration applied. Nonetheless, the multiple DRE suppression capabilities are reduced in the presence of enhanced surface roughness, as the DRP-reference array combination induces a boundary layer characterized by residual spanwise non-uniformity of the developing CFI modes. This prevents the accurate control on the phase shift between the non-uniform pre-existing CFI and the velocity disturbances induced by the applied reference and control arrays.

Hence, further investigation of the interaction between the DRP-reference array is necessary to fully understand and control the mechanisms dominating their superposition. In particular, given the sensitivity of the velocity disturbances superposition to the design parameters of the applied DRE arrays, the expansion of the investigated parameter space may identify more robust roughness designs. To better control the phase shift between the pre-existing and the introduced velocity disturbances, the forcing of sub-critical CFI modes (both for the reference and control arrays) can prove effective. This would combine the effect of the sub-critical control (UFD) and the linear superposition of velocity disturbances, possibly resulting in improved control capabilities. Additionally, the implementation of active flow control techniques capable

of monitoring and actively actuating the spanwise location of the developing CFI disturbances and their phase content, can be investigated. Specifically, by knowing the location and phase of the CFI initiated by the DRP, the reference and control array location and spanwise phase shift can be suitably adjusted to achieve the desired destructive interference between the existing CFI and the superposing disturbance systems. Such techniques would improve the design and suppression capabilities of the multiple array forcing, possibly extending its applicability to more realistic flight scenarios.

7.2. Outlook: Spanwise Invariant Roughness Configurations

A possible way to overcome the limitations related to the multiple array forcing technique is to consider passive flow control methods based on spanwise-invariant roughness geometries. An example is represented by the application of a streamwise series of shallow roughness stripes extending parallel to the wing span. Such configuration is investigated in a proof-of-concept experimental campaign providing the preliminary results presented hereafter.

Methodology

An experimental investigation is conducted in the LTT (section §2.1.1) employing infrared thermography (section §2.3.1) to characterize the effects on the transition front location of roughness configurations composed of multiple stripes. Acquisitions are performed at a constant freestream Reynolds number Re_{c_X}=2.17 $\times 10^6$ and angle of attack α=-3.36°. After the acquisition, the IR images are spatially transformed to the tunnel-attached reference frame (XYZ) and post-processed with Differential Infrared Thermography (DIT) to extract the transition front location.

A reference DRE array (A_1) manufactured through the knife cutting procedure (section §2.2.3) with height kk_1 and critical inter-spacing λ_1=8mm, is applied at x_{DRE}/c=0.02. The applied array is left unaltered throughout the performed measurements, providing what is considered as the *baseline flow field*. A streamwise series of stripes is added to the baseline configuration in order to investigate the effect of the superposition between the pre-existing and introduced velocity disturbance fields. The design of the investigated roughness configurations follows from the analysis of the baseline flow field. Specifically, using the acquired IR images, the corresponding critical chordwise wavelength (λ_x) is estimated to be 9.2mm (i.e. 0.0072% of chord), and is chosen to correspond to the chordwise spacing of successive stripes in any multiple stripes *control configuration* considered.

In particular, the reference control configuration is represented by case C1 in table 7.1, and features a streamwise series of 20 stripes of nominal height k_{ST}= 0.170mm and width in the chordwise direction w_{ST}=2mm, with the first stripe located at a chord location of x_{ST}/c=0.125. A sketch of the resulting roughness configuration is reported in figure 7.1. This and all other control configurations employed are manufactured using the knife cutting procedure described in section §2.2.3, producing the multiple stripe series as a single piece to accurately control λ_x. A parametric

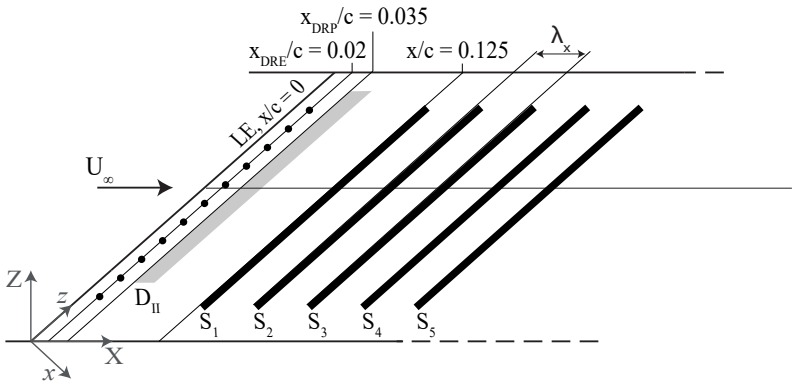

Figure 7.1: Schematic of DRE array, DRP and stripes application on the wing surface for the baseline forcing case (not to scale).

Case	DRE	DRP	Stripes				
			Number	k_{ST} [mm]	λ_x/λ_1	x_{ST}/c	w_{ST} [mm]
C1	A_1	-	20	0.17	1.15	0.125	2
C2	A_1	-	5	0.07-0.17	1.15	0.125	2
C3	A_1	-	5	0.07	1.15	0.1-0.2	2
C4	A_1	-	5	0.07	1.15	0.125	1-4
D1	A_1	D_I	5	0.14	1.15	0.125	2

Table 7.1: Geometrical parameters of measured forcing configurations. All configurations feature DRE array A_1, while the parameters characterizing the stripes geometry and application are modified as indicated. Case D1 also features DRP D_I.

investigation is then conducted, modifying the stripes number, height, chord location and width as indicated in table 7.1. Case names are built as C1-A_1-S5, indicating the superposition of array A_1 and five stripes with the geometrical characteristics listed under case C1.

To extend its applicability, also the multiple stripes technique is investigated in presence of enhanced distributed surface roughness. A DRP produced from carborundum grains is applied at a chord location of x_{DRP}/c=0.035, i.e. shortly downstream of the reference DRE array. Its characteristics are represented by DRP D_I described in section §2.2.1. The superposed control configuration features 5 stripes of k_{ST}=0.140mm applied at x_{ST}/c=0.125 as described by case D1 in table 7.1.

Results

Throughout this discussion, the baseline flow field is represented by C1-A_1, while the reference control configuration is C1-A_1-S5 (table 7.1). Representative IR images for the two considered cases are reported in figure 7.2, along with the differential thermography image obtained by subtracting the C1-A_1-S5 case to C1-A_1. In the DIT image the transition delay, i.e. the gained extension of laminar flow, is identified

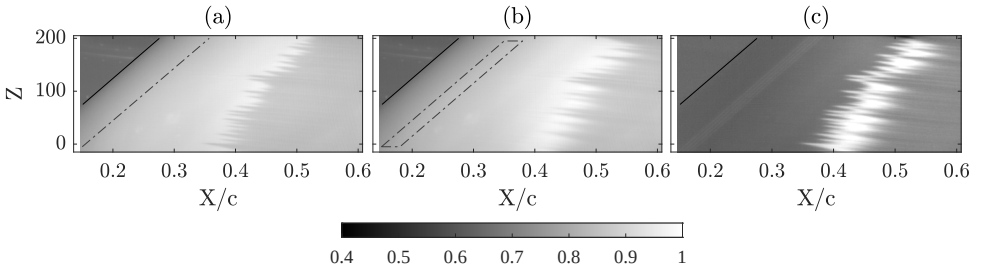

Figure 7.2: IR acquisitions at Re_{c_X}=2.17 $\times 10^6$ for forcing case C1. (a) IR images for C1-A_1 (b) C1-A_1-S5 (c) DIT image computed by subtracting the C1-A_1-S5 case to C1-A_1. Wing leading edge (full black line); stripes location (dash-dot rectangle); flow comes from the left.

as the brighter white region, and indicates that the application of multiple roughness stripes is capable of significantly delaying transition with respect to the baseline DRE-forced case. By extracting the location of the transition front corresponding to each roughness configuration, the observed transition delay is quantified to be 7% of the chord. This value is comparable to that obtained for the multiple DRE forcing case on a smooth wing. However, the CFI controlled by the application of multiple stripes are initiated more upstream than in the multiple DRE forcing case (at x_{DRE}/c=0.02 instead of x_{DRE}/c=0.125), suggesting that the former technique effectively controls strong and well-developed instabilities. In addition, the application of multiple roughness stripes does not pose requirements on the relative phase of the pre-existing and introduced velocity disturbances, possibly overcoming one of the main limits of the multiple DRE forcing technique.

To investigate the robustness and reliability of the observed transition delay a parametric study is conducted, starting from the investigation of the cumulative effect of the successive stripes. The transition location obtained by progressively adding 20 stripes to case C1-A_1, is reported in figure 7.3. The application of the first 5 stripes progressively extends the portion of laminar flow on the wing surface, with configuration C1-A_1-S5 providing the most downstream transition location achieved (i.e. x_{TR}/c=0.5). The addition of subsequent stripes, still leads to an overall transition delay up to configuration C1-A_1-S8. However, the control configuration capabilities are progressively reduced, suggesting that two competing mechanisms are active in the interaction between the pre-existing CFI (introduced by configuration C1-A_1) and the velocity disturbance systems introduced by the stripes. Nonetheless, the results presented here come from a preliminary investigation and are insufficient to provide insights on the nature and development of the underlying flow mechanisms and their interaction. Finally, flow tripping occurs in correspondence of the last stripe when a control configuration featuring more than 8 stripes is applied.

Figure 7.3 shows that the maximum transition delay in case C1 is achieved for the control configuration featuring 5 stripes. This result has been confirmed by multiple considered cases (not reported for the sake of brevity), hence, the effect of a change of the forcing amplitude, location and width is investigated for control configurations composed by 5 stripes. The transition front location is reported in figure 7.4(a) for

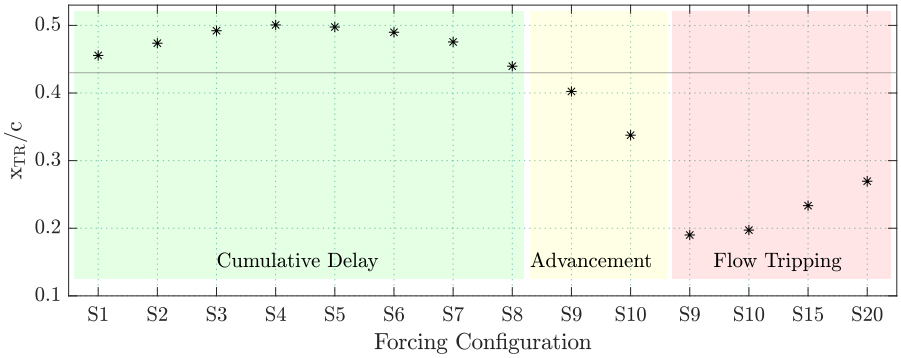

Figure 7.3: x_{TR}/c extracted from IR images for the baseline configuration (horizontal full gray line) and for the combination of the baseline configuration and the indicated number of stripes.

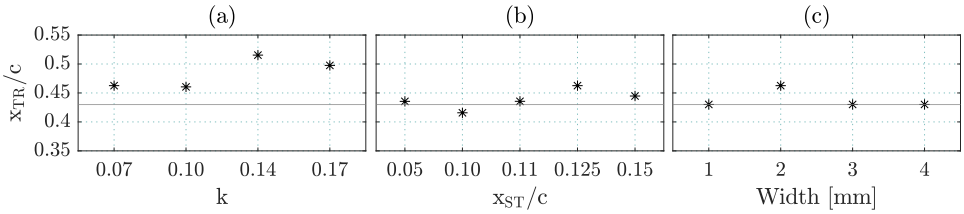

Figure 7.4: x_{TR}/c extracted from IR images for the combination of the baseline configuration (horizontal full gray line) with a control configuration featuring 5 stripes (a) with different DRE amplitude k (case C2), (b) at different chord location x_{ST}/c (case C3), (c) with different w_{ST} (case C4).

configuration C2-A_1-S5 for various forcing amplitude cases. All of the considered cases show significant transition delay, however a stripe amplitude of k_{ST}=0.140mm is capable of extending the laminar flow of almost 10% of chord.

The effects of modifications of the x_{ST}/c are investigated for a stripe height of k_{ST}=0.070mm (case C3) to avoid causing flow tripping at the more upstream chord locations considered. The resulting transition locations are shown in figure 7.4(b), indicating that both an upstream shift and a downstream shift of the control configuration are detrimental for its control capabilities. Furthermore, it is confirmed that x_{ST}/c=0.125 represents an optimal location for the control configuration. Finally, the effect of changes in the stripe width (C4) is shown in figure 7.4(c), indicating that w_{ST}=2mm, comparable to the DRE diameter, provides the highest transition delay.

Overall, the control configuration demonstrating stronger control capabilities is C2-A_1-S5 with roughness of height k_{ST}=0.140mm. Hence, as a last effort the control capabilities of this configuration in the presence a DRP (case D1) are investigated. Figure 7.5 shows the IR images and DIT images corresponding to case D1. The randomized boundary layer forcing provided by D_I, introduces some spanwise-irregularity in the boundary layer flow which reflects in a less uniform transition front (figure

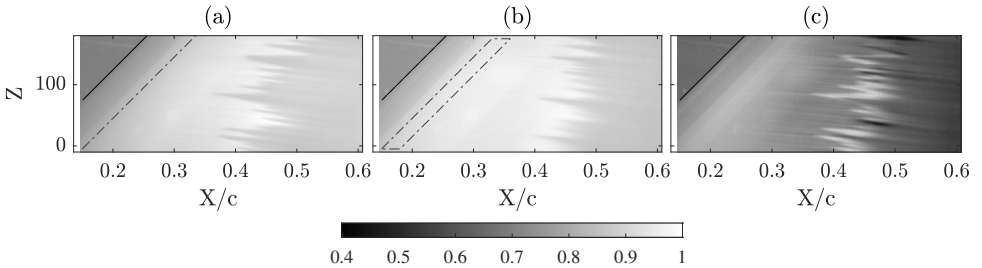

Figure 7.5: IR acquisitions at Re_{c_X}=2.17 $\times 10^6$ for forcing case D1. IR images for (a) D1-A_1-D_I, (b) D1-A_1-D_I-S5. (c) DIT image computed by subtracting D1-A_1-D_I-S5 case to C1-A_1-D_I. Wing leading edge (full black line); stripes location (dash-dot rectangle); DRP location (darker gray region in (b) and (c)); flow comes from the left.

7.5(b)). These characteristics persist also when the control configuration is applied (figure 7.5 (c)), nonetheless the multiple stripes configuration provides a transition delay in the order of 3% of chord with respect to the D1-A_1-D_I configuration (for the two cases x_{TR}/c=0.49 and 0.46 respectively). This is considered as a promising result, as the multiple stripes application effectively controls a realistic flight scenario embedding both enhanced distributed surface roughness, resulting for example from the wing surface finishing, as well as discrete roughness elements which can be representative for the deposition of material on the wing surface.

7

Recommendations

The preliminary results discussed beforehand provide interesting insights on the capabilities and possible application of control configurations based on the multiple stripes geometry. Nonetheless, the conducted investigation is only exploratory and is meant to outline the general behavior of the proposed technique but does not provide significant insights on the flow mechanisms dominating the superposition of the introduced disturbances. Therefore, two main objectives are identified and motivate further study of the multiple stripes technique.

On the one hand, to further investigate the control capabilities of the proposed technique the considered parameter range can be expanded. Numerous parameters are only marginally considered in this proof-of-concept experimental campaign. As an example, Re_{c_X} which is kept constant to avoid introducing excessive modifications of the baseflow scenario (i.e. a change in the dominant CFI mode wavelength). Comparably, the geometrical characteristics of the reference DRE array can be modified to investigate the interaction of different forcing amplitudes and wavelengths with the control capabilities of the multiple stripes configurations. In addition, the possibility of applying the stripes at an angle with respect to the leading edge can be explored, both keeping all the stripes parallel to each other (i.e. all inclined of same angle with respect to the wing leading edge) or varying the relative stripes inclination as well. At last, from the measured configurations it appears that the application of more than 5 consecutive stripes has marginal or even detrimental effect on the transition location. This aspect can be further investigated to determine whether it

relates to the chordwise location or amplitude of the individual stripes, or to other geometrical and flow-related parameters. Towards this, configurations with stripes of variable height can be considered, enhancing the heigh of the more downstream stripes in order to compensate for the thickening of the boundary layer.

On the other hand and of higher analytical interest, is the detailed investigation of the flow mechanisms underlying the control capabilities demonstrated by the multiple stripes configurations. To achieve this, dedicated experimental acquisitions employing high-resolution flow diagnostics are performed at the moment of delivery of this thesis, aiming at characterizing the local boundary layer flow features. This can clarify the processes dominating the interaction between the pre-existing instabilities and the applied control roughness configurations, outlining the type of mechanisms leading to the observed transition delay.

Further clarification of the aforementioned aspects can open the way to a whole new set of reliable and robust passive control methods, still based on the manipulation of the wing surface roughness.

Bibliography

[1] Acarlar, M. S. & Smith, C. R. 1987 A study of hairpin vortices in a laminar boundary layer. part 1. hairpin vortices generated by a hemisphere protuberance. *Journal of Fluid Mechanics* **175**, 1–41.

[2] Agüí, J. C. & Jiménez, J. 1987 On the performance of particle tracking. *Journal of Fluid Mechanics* **185**, 447–468.

[3] Airports Council International, (ACI) 2018 Preliminary world airport traffic rankings.

[4] Andersson, P., Berggren, M. & Henningson, D. S. 1999 Optimal disturbances and bypass transition in boundary layers. *Physics of Fluids* **11** (1), 134–150.

[5] Andersson, P., Brandt, L., Bottaro, A. & Henningson, D.s. 2001 On the breakdown of boundary layer streaks. *Journal of Fluid Mechanics* **428**, 29–60.

[6] Arnal, D. & Archambaud, J. P. 2008 Laminar-turbulent transition control: Nlf, lfc, hlfc. *Advances in Laminar-Turbulent Transition Modeling* .

[7] Arnal, D. & Casalis, G. 2000 Laminar-turbulent transition prediction in three-dimensional flows. *Progress in Aerospace Sciences* **36** (2), 173–191.

[8] Astarita, T. & Carlomagno, G. M. 2012 *Infrared thermography for thermo-fluid-dynamics*. Springer Science & Business Media.

[9] Baines, P. G., Majumdar, S. J. & Mitsudera, H. 1996 The mechanics of the tollmien-schlichting wave. *Journal of fluid mechanics* **312**, 107–124.

[10] Baker, C. J. 1979 The laminar horseshoe vortex. *Journal of fluid mechanics* **95** (2), 347–367.

[11] Baumann, M., Sturzebecher, D. & Nitsche, W. 2000 Active control of TS-instabilities on an unswept wing. In *Laminar-Turbulent Transition*, pp. 155–160. Springer Berlin Heidelberg.

[12] Berger, A. R., McMillan, M. N., White, E. B., Suryanarayanan, S. & Goldstein, D. B. 2017 Suppression of transition behind a discrete roughness element using a downstream element. In *Tenth International Symposium on Turbulence and Shear Flow Phenomena*. Begel House Inc.

[13] Berger, A. R. & White, E. B. 2020 Experimental study of the role of high- and low-speed streaks in turbulent wedge spreading. In *AIAA Scitech 2020 Forum*. American Institute of Aeronautics and Astronautics.

[14] Bertolotti, F. P. 1996 On the birth and evolution of disturbances in three-dimensional boundary layers. In *IUTAM Symposium on Nonlinear Instability and Transition in Three-Dimensional Boundary Layers*, pp. 247–256. Springer.

[15] Bertolotti, F. P., Herbert, T. H. & Spalart, P. R. 1992 Linear and nonlinear stability of the blasius boundary layer. *Journal of Fluid Mechanics* **242**, 441–474.

[16] Bippes, H. 1999 Basic experiments on transition in three-dimensional boundary layers dominated by crossflow instability. *Progress in Aerospace Sciences* (35), 363–412.

[17] Bippes, H. & Lerche, T. 1997 Transition prediction in three-dimensional boundary-layer flows unstable to crossflow instability. In *28th Fluid Dynamics Conference*, p. 1906.

[18] Böberg, L. & Brösa, U. 1988 Onset of turbulence in a pipe. *Zeitschrift für Naturforschung*

A **43** (8-9), 697–726.

[19] Bonfigli, G. & Kloker, M. 2007 Secondary instability of crossflow vortices: validation of the stability theory by direct numerical simulation. *Journal of Fluid Mechanics* **583**, 229–272.

[20] Breuer, K. S. & Kuraishi, T. 1994 Transient growth in two- and three-dimensional boundary layers. *Physics of Fluids* **6** (6), 1983–1993.

[21] Bruun, H. H. 1996 Hot-wire anemometry: principles and signal analysis.

[22] Brynjell-Rahkola, M., Schlatter, P., Hanifi, A. & Henningson, D. S. 2015 Global stability analysis of a roughness wake in a falkner-skan-cooke boundary layer. *Procedia IUTAM* **14**, 192–200.

[23] Brynjell-Rahkola, M., Shahriari, N., Schlatter, P., Hanifi, A. & Henningson, D. S. 2017 Stability and sensitivity of a cross-flow-dominated falkner–skan–cooke boundary layer with discrete surface roughness. *Journal of Fluid Mechanics* **826**, 830–850.

[24] Bucci, M. A., Cherubini, S., Loiseau, J. Ch. & Robinet, J. Ch. 2021 Influence of freestream turbulence on the flow over a wall roughness. *Physical Review Fluids* **6** (6).

[25] Bucci, M. A., Puckert, D. K., Andriano, C., Loiseau, J. Ch., Cherubini, S., Robinet, J. Ch. & Rist, U. 2017 Roughness-induced transition by quasi-resonance of a varicose global mode. *Journal of Fluid Mechanics* **836**, 167–191.

[26] Bushnell, Dennis M 1979 *Survey and bibliography on attainment of laminar flow control in air using pressure gradient and suction, volume 1*, , vol. 1. National Aeronautics and Space Administration, Scientific and Technical ....

[27] Butler, K. M. & Farrell, B. F. 1992 Three-dimensional optimal perturbations in viscous shear flow. *Physics of Fluids A: Fluid Dynamics* **4** (8), 1637–1650.

[28] Byström, M. G. 2007 Optimal disturbances in boundary layer flows. PhD thesis, Mekanik.

[29] Byström, M. G., Pralits, J. O., Hanifi, A., Luchini, P. & Henningson, D. S. 2007 Optimal disturbances in three-dimensional boundary-layer flows. In *6th ERCOFTAC SIG 33 workshop, Laminar-Turbulent Transition Mechanisms, Prediction and Control*.

[30] Carpenter, A. L., Saric, W. S. & Reed, H. L. 2010 Roughness receptivity in swept-wing boundary layers–experiments. *International Journal of Engineering Systems Modelling and Simulation* **2** (1-2), 128–138.

[31] Carpentier, J. 1901 Improvements in enlarging or like cameras. *Great Britain Patent* **1139**.

[32] Carrillo, Jr R. B., Reibert, M. S. & Saric, W. S. 1996 Distributed-roughness effects on stability and transition in swept-wing boundary layers. *NASA Center* .

[33] Casacuberta, J., Groot, K. J., Ye, Q. & Hickel, S. 2019 Transitional flow dynamics behind a micro-ramp. *Flow, Turbulence and Combustion* **104** (2-3), 533–552.

[34] Chernoray, V. G., Dovgal, A. V., Kozlov, V. V. & Loefdahl, L. 2005 Experiments on secondary instability of streamwise vortices in a swept-wing boundary layer. *Journal of Fluid Mechanics* **534**, 295.

[35] Cherubini, S., Tullio, M. D. De, Palma, P. De & Pascazio, G. 2013 Transient growth in the flow past a three-dimensional smooth roughness element. *Journal of Fluid Mechanics* **724**, 642–670.

[36] Chu, J. & Goldstein, D. 2012 Investigation of turbulent wedge spreading mechanism with comparison to turbulent spots. In *50th AIAA Aerospace Sciences Meeting including the New Horizons Forum and Aerospace Exposition*, p. 751.

[37] Cierpka, C., Lütke, B. & Kähler, C. J. 2013 Higher order multi-frame particle tracking

velocimetry. *Experiments in Fluids* **54** (5).

[38] Cohen, A 1994 Ten lectures on wavelets, cbms-nsf regional conference series in applied mathematics, vol. 61, i. daubechies, siam, 1992, xix+ 357 pp. *Journal of Approximation Theory* **78** (3), 460–461.

[39] Corbett, P. & Bottaro, A. 2001 Optimal linear growth in swept boundary layers. *Journal of Fluid Mechanics* **435**, 1.

[40] Dabiri, D. & Pecora, C. 2019 *Particle Tracking Velocimetry*. IOP Publishing.

[41] Dagenhart, J. R. & Saric, William S. 1999 Crossflow stability and transition experiments in swept-wing flow .

[42] Dagenhart, J. R., Stack, J., Saric, W. S. & Mousseux, M. 1989 Crossflow-vortex instability and transition on a 45 deg swept wing. In *20th Fluid Dynamics, Plasma Dynamics and Lasers Conference*, p. 1892.

[43] Denissen, N. A. & White, E. B. 2013 Secondary instability of roughness-induced transient growth. *Physics of Fluids* **25** (11), 114108.

[44] Deyhle, H. & Bippes, H. 1996 Disturbance growth in an unstable three-dimensional boundary layer and its dependence on environmental conditions. *Journal of Fluid Mechanics* **316**, 73–113.

[45] Dobbinga, E. & van Ghesel Grothe, J. A. 1955 De lage-snelheids windtunnel van de sub-afd. vliegtuig bouwkunde der technische hogeschool. *Technische Hogeschool Delft, Vliegtuigbouwkunde, Rapport VTH-77* .

[46] Doolittle, C. J., Drews, S. D. & Goldstein, D. B. 2014 Near-field flow structures about subcritical surface roughness. *Physics of Fluids* **26** (12), 124106.

[47] Downs, R. S. & White, E. B. 2013 Free-stream turbulence and the development of cross-flow disturbances. *Journal of Fluid Mechanics* **735**, 347–380.

[48] Downs, R. S., White, E. B. & Denissen, N. A. 2008 Transient growth and transition induced by random distributed roughness. *AIAA Journal* **46**, 451–462.

[49] Drews, S., Downs, R., Doolittle, C., Goldstein, D. & White, E. 2011 Direct numerical simulations of flow past random distributed roughness. In *49th AIAA Aerospace Sciences Meeting including the New Horizons Forum and Aerospace Exposition*. American Institute of Aeronautics and Astronautics.

[50] Drews, Scott David 2012 Direct numerical simulations of flow past quasi-random distributed roughness. Master's thesis.

[51] Elsinga, G. E., Scarano, F., Wieneke, B. & van Oudheusden, B. W. 2006 Tomographic particle image velocimetry. *Experiments in Fluids* **41** (6), 933–947.

[52] Ergin, F. G. & White, E. B. 2006 Unsteady and transitional flows behind roughness elements. *AIAA Journal* **44** (11), 2504–2514.

[53] Farrell, B. F. 1988 Optimal excitation of perturbations in viscous shear flow. *Physics of Fluids* **31** (8), 2093.

[54] Fischer, P. & Choudhari, M. 2004 Numerical simulation of roughness-induced transient growth in a laminar boundary layer. In *34th AIAA Fluid Dynamics Conference and Exhibit*. American Institute of Aeronautics and Astronautics.

[55] Fransson, J. H. M., Brandt, L., Talamelli, A. & Cossu, C. 2004 Experimental and theoretical investigation of the nonmodal growth of steady streaks in a flat plate boundary layer. *Physics of Fluids* **16** (10), 3627–3638.

[56] Fransson, J. H. M., Brandt, L., Talamelli, A. & Cossu, C. 2005 Experimental study of

the stabilization of tollmien–schlichting waves by finite amplitude streaks. *Physics of Fluids* **17** (5), 054110.

[57] Friederich, T. & Kloker, M. J. 2012 Control of the secondary cross-flow instability using localized suction. *Journal of Fluid Mechanics* **706**, 470–495.

[58] Gregory, N. T. & Walker, W. S. 1956 *The effect on transition of isolated surface excrescences in the boundary layer*. HM Stationery Office.

[59] Gulyaev, A. N., Kozlov, V. E., Kuznetsov, V. R., Mineev, B. I. & Sekundov, A. N. 1990 Interaction of a laminar boundary layer with external turbulence. *Fluid Dynamics* **24** (5), 700–710.

[60] Gustavsson, L. H. 1991 Energy growth of three-dimensional disturbances in plane poiseuille flow. *Journal of Fluid Mechanics* **224**, 241–260.

[61] Hanifi, A., Schmid, P. J. & Henningson, D. S. 1996 Transient growth in compressible boundary layer flow. *Physics of Fluids* **8** (3), 826–837.

[62] Haynes, T. S. & Reed, H. L. 2000 Simulation of swept-wing vortices using nonlinear parabolized stability equations. *Journal of Fluid Mechanics* **405**, 325–349.

[63] Henningson, D. S. 2006 Transient growth with application bypass transition to. In *IUTAM Symposium on Laminar-Turbulent Transition*, pp. 15–24. Springer.

[64] Henningson, D. S., Lundbladh, A. & Johansson, A. V. 1993 A mechanism for bypass transition from localized disturbances in wall-bounded shear flows. *Journal of Fluid Mechanics* **250**, 169–207.

[65] Herbert, T. 1993 Parabolized stability equations. *AGARD: Special Course on Progress in Transition Modelling, AGARD-R-d793* .

[66] Herbert, T. 1997 Parabolized stability equations. *Annual Review of Fluid Mechanics* **29** (1), 245–283.

[67] Hosseini, S. M., Tempelmann, D., Hanifi, A. & Henningson, D. S. 2013 Stabilization of a swept-wing boundary layer by distributed roughness elements. *Journal of Fluid Mechanics* **718**.

[68] Hultmark, M. & Smits, A. J. 2010 Temperature corrections for constant temperature and constant current hot-wire anemometers. *Measurement Science and Technology* **21** (10), 105404.

[69] Hunt, J. C. R., Wray, A. A. & Moin, P. 1988 Eddies streams and convergence zones in turbulent flows. *Studying Turbulence Using Numerical Simulation Databases-I1* p. 193.

[70] Hunt, L. & Saric, W. 2011 Boundary-layer receptivity of three-dimensional roughness arrays on a swept-wing. In *41st AIAA Fluid Dynamics Conference and Exhibit*, p. 3881.

[71] Janke, T. & Michaelis, D. 2021 Uncertainty quantification for PTV/LPT data and adaptive track filtering. *14th International Symposium on Particle Image Velocimetry* **1** (1).

[72] Joslin, Ronald D. 1998 AIRCRAFT LAMINAR FLOW CONTROL. *Annual Review of Fluid Mechanics* **30** (1), 1–29.

[73] Kachanov, Y. S. 1994 Physical mechanisms of laminar-boundary-layer transition. *Annual review of fluid mechanics* **26** (1), 411–482.

[74] Kendall, J. 1985 Experimental study of disturbances produced in a pre-transitional laminar boundary layer by weak freestream turbulence. In *18th Fluid Dynamics and Plasmadynamics and Lasers Conference*. American Institute of Aeronautics and Astronautics.

[75] Kendall, J. M. 1981 Laminar boundary layer velocity distortion by surface roughness: Effect upon stability. *AIAA paper* **195**, 1981.

[76] Klebanoff, P. S., Cleveland, W. G. & Tidstrom, K. D. 1992 On the evolution of a turbulent boundary layer induced by a three-dimensional roughness element. *Journal of Fluid Mechanics* **237**, 101–187.

[77] Koch, W. 2002 On the spatio-temporal stability of primary and secondary crossflow vortices in a three-dimensional boundary layer. *Journal of Fluid Mechanics* **456**, 85–111.

[78] Kotsonis, M., Giepman, R., Hulshoff, S. & Veldhuis, L. 2013 Numerical study of the control of tollmien–schlichting waves using plasma actuators. *AIAA Journal* **51** (10), 2353–2364.

[79] Kuester, M. S. & White, E. B. 2015 Roughness receptivity and shielding in a flat plate boundary layer. *Journal of Fluid Mechanics* **777**, 430–460.

[80] Kuester, M. S. & White, E. B. 2016 Structure of turbulent wedges created by isolated surface roughness. *Experiment in Fluids* **57**.

[81] Kulfan, Robert M & Howard, Weston M 1975 Application of advanced aerodynamic concepts to large subsonic transport airplanes. *Tech. Rep.*. BOEING COMMERCIAL AIRPLANE CO SEATTLE WASH.

[82] Kurian, T., Fransson, J. H. M. & Alfredsson, P. H. 2011 Boundary layer receptivity to free-stream turbulence and surface roughness over a swept flat plate. *Physics of Fluids* **23** (3), 034107.

[83] Kurz, H. B. E. & Kloker, M. J. 2014 Receptivity of a swept-wing boundary layer to micron-sized discrete roughness elements. *Journal of Fluid Mechanics* **755**, 62–82.

[84] Kurz, H. B. E. & Kloker, M. J. 2016 Mechanisms of flow tripping by discrete roughness elements in a swept-wing boundary layer. *Journal of Fluid Mechanics* **796**, 158–194.

[85] Kähler, C. J., Scharnowski, S. & Cierpka, C. 2012 On the uncertainty of digital PIV and PTV near walls. *Experiments in Fluids* **52** (6), 1641–1656.

[86] Ladd, D. M. 1990 Control of natural laminar instability waves on an axisymmetric body. *AIAA Journal* **28** (2), 367–369.

[87] Landahl, M. T. 1980 A note on an algebraic instability of inviscid parallel shear flows. *Journal of Fluid Mechanics* **98** (2), 243–251.

[88] Lemarechal, J., Costantini, M., Klein, C., Kloker, M. J., Würz, W., Kurz, H. B. E., Streit, T. & Schaber, S. 2019 Investigation of stationary-crossflow-instability induced transition with the temperature-sensitive paint method. *Experimental Thermal and Fluid Science* **109**, 109848.

[89] Lennart S., H. 1981 Algebraic growth of disturbances in a laminar boundary layer. *Physics of Fluids* **24** (6), 1000.

[90] Levin, O. & Henningson, D. S. 2003 Exponential vs algebraic growth and transition prediction in boundary layer flow. *Flow, Turbulence and Combustion* **70** (1-4), 183–210.

[91] Li, F., Choudhari, M. M. & Duan, L. 2016 Stationary crossflow breakdown due to mixed mode spectra of secondary instabilities. In *46th AIAA Fluid Dynamics Conference*, p. 3789.

[92] Liepmann, H. W., Brown, G. L. & Nosenchuck, D. M. 1982 Control of laminar-instability waves using a new technique. *Journal of Fluid Mechanics* **118** (-1), 187.

[93] Loiseau, J. Ch., Robinet, J. Ch., Cherubini, S. & Leriche, E. 2014 Investigation of the roughness-induced transition: global stability analyses and direct numerical simulations. *Journal of Fluid Mechanics* **760**, 175–211.

[94] Lomas, C. G. 2011 *Fundamentals of hot wire anemometry*. Cambridge University Press.

[95] Lucas, J. M. 2014 Spatial optimal perturbations for transient growth analysis in three-

dimensional boundary layers. PhD thesis, Universite de Toulouse.

[96] Luchini, P. 2000 Reynolds-number-independent instability of the boundary layer over a flat surface: optimal perturbations. *Journal of Fluid Mechanics* **404**, 289–309.

[97] Lumley, J. L. 1967 The structure of inhomogeneous turbulent flows. *Atmospheric turbulence and radio wave propagation* .

[98] Mack, L. M. 1984 Boundary-layer linear stability theory. *Tech. Rep.*. California Inst of Tech Pasadena Jet Propulsion Lab.

[99] Malik, Mujeeb R, Crouch, Jeffrey D, Saric, William S, Lin, John C, Whalen, Edward A, Brockley, R, Agarwal, R, Collier, F, Shaefer, A & Seabridge, A 2015 Application of drag reduction techniques to transport aircraft. *Green Aviation* pp. 53–62.

[100] Malik, M. R., Li, F., Choudari, M. M. & Chang, C. L. 1999 Secondary instability of crossflow vortices and swept-wing boundary-layer transition. *Journal of Fluid Mechanics* **399**, 85–115.

[101] Malik, N. A. & Dracos, T. 1993 Lagrangian ptv in 3d flows. *Applied Scientific Research* **51** (1), 161–166.

[102] Meelan, C. & Paul, F. 2005 Roughness-induced transient growth. In *35th AIAA Fluid Dynamics Conference and Exhibit*. American Institute of Aeronautics and Astronautics.

[103] Messing, R. & Kloker, M. J. 2010 Investigation of suction for laminar flow control of three-dimensional boundary layers. *Journal of Fluid Mechanics* **658**, 117–147.

[104] Michelis, T. 2017 Boundary layer separation: Diagnostics and control. PhD thesis.

[105] Milling, R. W. 1981 Tollmien–schlichting wave cancellation. *Physics of Fluids* **24** (5), 979.

[106] Mochizuki, M. 1961 Smoke observation on boundary layer transition caused by a spherical roughness element. *Journal of the Physical Society of Japan* **16** (5), 995–1008.

[107] Morkovin, M. V. 1969 On the many faces of transition. In *Viscous drag reduction*, pp. 1–31. Springer.

[108] Morkovin, M. V. 1994 Transition in open flow systems-a reassessment. *Bull. Am. Phys. Soc.* **39**, 1882.

[109] Müller, B. & Bippes, H. 1989 Experimental study of instability modes in a three-dimensional boundary layer. *AGARD CP, NATO AGARD* .

[110] Munaro, F. 2017 Mechanisms of boundary layer transition due to isolated roughness on swept wings: An experimental study.

[111] Ohmi, K. & Li, H.-Y. 2000 Particle-tracking velocimetry with new algorithms. *Measurement Science and Technology* **11** (6), 603.

[112] Orr, W. M'F. 1907 The stability or instability of the steady motions of a perfect liquid and of a viscous liquid. part ii: A viscous liquid. In *Proceedings of the Royal Irish Academy. Section A: Mathematical and Physical Sciences*, , vol. 27, pp. 69–138. JSTOR.

[113] Pereira, F., Stüer, H., Graff, E. C. & Gharib, M. 2006 Two-frame 3d particle tracking. *Measurement Science and Technology* **17** (7), 1680–1692.

[114] Prandtl, L. 1904 Über flussigkeitsbewegung bei sehr kleiner reibung. *Verhandl. III, Internat. Math.-Kong., Heidelberg, Teubner, Leipzig, 1904* pp. 484–491.

[115] Puckert, D. K. & Rist, U. 2018 Experiments on critical reynolds number and global instability in roughness-induced laminar–turbulent transition. *Journal of Fluid Mechanics* **844**, 878–904.

[116] Pupator, P. & Saric, W. 1989 Control of random disturbances in a boundary layer. In *2nd*

Shear Flow Conference. American Institute of Aeronautics and Astronautics.

[117] Radeztsky, R. H., Reibert, M. S. & Saric, W. S. 1999 Effect of isolated micron-sized roughness on transition in swept-wing flows. *AIAA Journal* **37** (11), 1370–1377.

[118] Raffel, M., Merz, C. B., Schwermer, T. & Richter, K. 2015 Differential infrared thermography for boundary layer transition detection on pitching rotor blade models. *Experiments in Fluids* **56** (2).

[119] Raffel, M., Willert, C. E., Scarano, F., Kähler, C. J., Wereley, S. T. & Kompenhans, J. 2018 *Particle Image Velocimetry*. Springer International Publishing.

[120] Ramesh, O. N., Dey, J. & Prabhu, A. 1996 Transitional intermittency distribution in a three-dimensional constant pressure diverging flow. *Experiments in Fluids* **21** (4), 259–263.

[121] Reddy, S. C. & Henningson, D. S. 1993 Energy growth in viscous channel flows. *Journal of Fluid Mechanics* **252**, 209–238.

[122] Reed, H. L. & Saric, W. S. 1989 Stability of three-dimensional boundary layers. *Annual Review of Fluid Mechanics* **21** (1), 235–284.

[123] Reibert, M., Saric, W. S., Carrillo, Jr. R. & Chapman, K. 1996 Experiments in nonlinear saturation of stationary crossflow vortices in a swept-wing boundary layer. In *34th Aerospace Sciences Meeting and Exhibit*. American Institute of Aeronautics and Astronautics.

[124] Reshotko, E. 2001 Transient growth: a factor in bypass transition. *Physics of Fluids* **13** (5), 1067–1075.

[125] Reshotko, E. & Leventhal, L. 1981 Preliminary experimental study of disturbances in a laminar boundary layer due to distributed surface roughness. In *14th Fluid and Plasma Dynamics Conference*. American Institute of Aeronautics and Astronautics.

[126] Reynolds, O. 1883 Xxix. an experimental investigation of the circumstances which determine whether the motion of water shall be direct or sinuous, and of the law of resistance in parallel channels. *Philosophical Transactions of the Royal society of London* (174), 935–982.

[127] Reynolds, O. 1901 On the extent and action of the heating surface of steam boilers. *Papers on Mechanical and Physical subjects* p. 81.

[128] Riedel, H. & Sitzmann, M. 1998 In-flight investigations of atmospheric turbulence. *Aerospace Science and technology* **2** (5), 301–319.

[129] Rius Vidales, A. F. 2022 Influence of a forward-facing step on crossflow instability and transition: An experimental study in a swept wing boundary-layer. PhD thesis.

[130] Rius Vidales, A. F. & Kotsonis, M. 2020 Influence of a forward-facing step surface irregularity on swept wing transition. *AIAA Journal* pp. 1–11.

[131] Rius Vidales, A. F., Kotsonis, M., Antunes, A. P. & Cosin, R. 2018 Effect of two-dimensional surface irregularities on swept wing transition: Forward facing steps. In *2018 Fluid Dynamics Conference*. American Institute of Aeronautics and Astronautics.

[132] Rizzetta, D. P. & Visbal, M. R. 2007 Direct numerical simulations of flow past an array of distributed roughness elements. *AIAA Journal* **45** (8), 1967–1976.

[133] Rizzetta, D. P., Visbal, M. R., Reed, H. L. & Saric, W. S. 2010 Direct numerical simulation of discrete roughness on a swept-wing leading edge. *AIAA journal* **48** (11), 2660–2673.

[134] Rosenfeld, A., Hummel, R. A. & Zucker, S. W. 1976 Scene labeling by relaxation operations. *IEEE Transactions on Systems, Man, and Cybernetics* (6), 420–433.

[135] Saric, W. S., Carpenter, A. L. & Reed, H. L. 2011 Passive control of transition in three-dimensional boundary layers, with emphasis on discrete roughness elements. *Philosophi-*

cal Transactions of the Royal Society A: Mathematical, Physical and Engineering Sciences **369** (1940), 1352–1364.

[136] Saric, W. S., Carrillo, R. & Reibert, M. 1998 Leading-edge roughness as a transition control mechanism.

[137] Saric, W. S., Reed, H. L. & White, E. B. 2003 Stability and transition of three dimensional boundary layers. *Annual Review of Fluid Mechanics* **35** (1), 413–440.

[138] Saric, W. S., West, D. E., Tufts, M. W. & Reed, H. L. 2019 Experiments on discrete roughness element technology for swept-wing laminar flow control. *AIAA Journal* **57** (2), 641–654.

[139] Scarano, F. 2001 Iterative image deformation methods in piv. *Measurement science and technology* **13** (1), R1.

[140] Schanz, D., Gesemann, S. & Schröder, A. 2016 Shake-the-box: Lagrangian particle tracking at high particle image densities. *Experiments in Fluids* **57** (5).

[141] Schanz, D., Gesemann, S., Schröder, A., Wieneke, B. & Novara, M. 2012 Non-uniform optical transfer functions in particle imaging: calibration and application to tomographic reconstruction. *Measurement Science and Technology* **24** (2), 024009.

[142] Scheimpflug, T. 1904 Improved method and apparatus for the systematic alteration or distortion of plane pictures and images by means of lenses and mirrors for photography and for other purposes. *GB patent* **1196**.

[143] Schlichting, H. & Gersten, K. 2017 *Boundary-Layer Theory*. Springer Berlin Heidelberg.

[144] Schmid, P. J. & Henningson, D. S. 2001 *Applied Mathematical Sciences*. Springer-Verlag, New York.

[145] Schrader, L. U., Brandt, L. & Henningson, D. S. 2009 Receptivity mechanisms in three-dimensional boundary-layer flows. *Journal of Fluid Mechanics* **618**, 209–241.

[146] Schrauf, G. 2005 Status and perspectives of laminar flow. *The Aeronautical Journal* **109** (1102), 639–644.

[147] Schubauer, G. B. & Klebanoff, P. S. 1956 Contributions on the mechanics of boundary-layer transition .

[148] Schubauer, G. B. & Skramstad, H. K. 1947 Laminar boundary-layer oscillations and transition on. *Journal of research of the National Bureau of Standards* **38**, 251.

[149] Sciacchitano, A. 2019 Uncertainty quantification in particle image velocimetry. *Measurement Science and Technology* **30** (9), 092001.

[150] Sciacchitano, A., Neal, D. R., Smith, B. L., Warner, S. O., Vlachos, P. P., Wieneke, B. & Scarano, F. 2015 Collaborative framework for PIV uncertainty quantification: comparative assessment of methods. *Measurement Science and Technology* **26** (7), 074004.

[151] Sequeira, A. D. 2022 Non-modal growth induced by discrete roughness elements in a swept wing boundary layer: Modelling and diagnostics. Master's thesis.

[152] Serpieri, J. 2018 Cross-flow instability. PhD thesis, Technische Universiteit Delft.

[153] Serpieri, J. & Kotsonis, M. 2015 Design of a swept wing wind tunnel model for study of cross-flow instability. In *33rd AIAA Applied Aerodynamics Conference*. American Institute of Aeronautics and Astronautics.

[154] Serpieri, J. & Kotsonis, M. 2016 Three-dimensional organisation of primary and secondary crossflow instability. *Journal of Fluid Mechanics* **799**, 200–245.

[155] Sharma, A., Drews, S., Kuester, M. S., Goldstein, D. B. & White, E. B. 2014 Evolution of disturbances due to distributed surface roughness in laminar boundary layers. In *52nd Aerospace Sciences Meeting*. American Institute of Aeronautics and Astronautics.

[156] Simen, M. 1992 Local and non-local stability theory of spatially varying flows. In *Instability, Transition, and Turbulence*, pp. 181–201. Springer.

[157] Sirovich, L. 1987 Turbulence and the dynamics of coherent structures part iii: Dynamics and scaling. *Quarterly of Applied Mathematics* **45** (3), 583–590.

[158] Smith, B. L., Neal, D. R., Feero, MarA. & Richards, G. 2018 Assessing the limitations of effective number of samples for finding the uncertainty of the mean of correlated data. *Measurement Science and Technology* **29** (12), 125304.

[159] Sturgeon, RF, Bennett, JA, Etchberger, FR, Ferrill, RS & Meade, LE 1976 Study of the application of advanced technologies to laminar-flow control systems for subsonic transports. volume 2: Analyses. *Tech. Rep.*.

[160] Sturzebecher, D. & Nitsche, W. 2002 Active control of tollmien-schlichting instabilities by multi-channel sensor actuator systems. In *New Results in Numerical and Experimental Fluid Mechanics III*, pp. 375–382. Springer.

[161] Sturzebecher, D. & Nitsche, W. 2003 Active cancellation of tollmien–schlichting instabilities on a wing using multi-channel sensor actuator systems. *International Journal of Heat and Fluid Flow* **24** (4), 572–583.

[162] Suryanarayanan, S., Goldstein, D. B., Berger, A. R., White, E. B. & Brown, G. L. 2020 Mechanisms of roughness-induced boundary-layer transition control by shielding. *AIAA Journal* **58** (7), 2951–2963.

[163] Tani, I. 1961 Effect of two-dimensional and isolated roughness on laminar flow. In *Boundary layer and flow control*, pp. 637–656. Elsevier.

[164] Tani, I. 1969 Boundary-layer transition. *Annual Review of Fluid Mechanics* **1** (1), 169–196.

[165] Tempelmann, D. & Hanifi, A.and Henningson, D. S. 2012 Spatial optimal growth in three-dimensional compressible boundary layers. *Journal of Fluid Mechanics* **704**, 251–279.

[166] Tempelmann, D., Schrader, L. U., Hanifi, A., Brandt, L. & Henningson, D. S. 2012 Swept wing boundary-layer receptivity to localized surface roughness. *Journal of Fluid Mechanics* **711**, 516–544.

[167] Thomas, T. R. 1981 Characterization of surface roughness. *Precision Engineering* **3** (2), 97–104.

[168] Tillmann, F. & Markus, K. 2011 Control of crossflow-vortex induced transition: DNS of pinpoint suction. In *41st AIAA Fluid Dynamics Conference and Exhibit*. American Institute of Aeronautics and Astronautics.

[169] Tol, H. J., Kotsonis, M. & Visser, C. C. De 2019 Pressure output feedback control of tollmien–schlichting waves in falkner–skan boundary layers. *AIAA Journal* **57** (4), 1538–1551.

[170] Tol, H. J., de Visser, C. C. & Kotsonis, M. 2019 Experimental model-based estimation and control of natural tollmien–schlichting waves. *AIAA Journal* **57** (6), 2344–2355.

[171] Tropea, C., Yarin, A. L., Foss, John F. & others 2007 *Springer handbook of experimental fluid mechanics*, , vol. 1. Springer.

[172] Tumin, A. & Ashpis, D. E. 2003 Optimal disturbances in boundary layers subject to streamwise pressure gradient. *AIAA Journal* **41** (11), 2297–2300.

[173] Von Doenhoff, A. E. & Braslow, A. l. 1961 The effect of surface roughness on laminar flow. In *Boundary Layer and Flow Control*, pp. 657–681. Elsevier.

[174] W., Bernhard 2012 Iterative reconstruction of volumetric particle distribution. *Measurement Science and Technology* **24** (2), 024008.

[175] Wassermann, P. & Kloker, M. 2002 Mechanisms and passive control of crossflow-vortex-induced transition in a three-dimensional boundary layer. *Journal of Fluid Mechanics* **456**, 49–84.

[176] Wassermann, P. & Kloker, M. J. 2000 DNS-investigations of the development and control of crossflow vortices in a 3-d boundary-layer flow. In *Laminar-Turbulent Transition*, pp. 565–570. Springer Berlin Heidelberg.

[177] Wassermann, P. & Kloker, M. J. 2003 Transition mechanisms induced by travelling crossflow vortices in a three-dimensional boundary layer. *Journal of Fluid Mechanics* **483**, 67–89.

[178] Weideman, J. A. & Reddy, S. C. 2000 A matlab differentiation matrix suite. *ACM Transactions on Mathematical Software (TOMS)* **26** (4), 465–519.

[179] Welch, P. 1967 The use of fast fourier transform for the estimation of power spectra: A method based on time averaging over short, modified periodograms. *IEEE Transactions on Audio and Electroacoustics* **15** (2), 70–73.

[180] Westerbeek, S. H. J. 2020 Development of a nonlinear parabolized stability equation (npse) analysis tool for spanwise invariant boundary layers. Msc thesis, Delft University of Technology.

[181] White, E., Saric, W. S., Gladden, R. & Gabet, P. 2001 Stages of swept-wing transition. In *39th Aerospace Sciences Meeting and Exhibit*, p. 271.

[182] White, E. B. & Ergin, F. G. 2003 Receptivity and transient growth of roughness induced disturbances. *33rd AIAA Fluids Dynamics Conference* .

[183] White, E. B., Rice, J. M. & Ergin, G. F. 2005 Receptivity of stationary transient disturbances to surface roughness. *Physics of Fluids* **17** (6), 064109.

[184] White, E. B. & Saric, W. S. 2005 Secondary instability of crossflow vortices. *Journal of Fluid Mechanics* **525**, 275–308.

[185] Wieneke, B. 2008 Volume self-calibration for 3d particle image velocimetry. *Experiments in Fluids* **45** (4), 549–556.

[186] Wieneke, B. 2015 PIV uncertainty quantification from correlation statistics. *Measurement Science and Technology* **26** (7), 074002.

[187] Wolf, C. C., Gardner, A. D. & Raffel, M. 2020 Infrared thermography for boundary layer transition measurements. *Measurement Science and Technology* **31** (11), 112002.

[188] Woodruff, M., Saric, W. & Reed, H. 2011 Receptivity measurements on a swept-wing model. In *41st AIAA Fluid Dynamics Conference and Exhibit*. American Institute of Aeronautics and Astronautics.

[189] Wu, Q. X. & Pairman, D. 1995 A relaxation labeling technique for computing sea surface velocities from sea surface temperature. *IEEE Transactions on Geoscience and Remote Sensing* **33** (1), 216–220.

[190] Ye, Q., Schrijer, F. F. J. & Scarano, F. 2016 Geometry effect of isolated roughness on boundary layer transition investigated by tomographic piv. *International Journal of Heat and Fluid Flow* **61**, 31–44.

[191] Zhou, L., Li, R., Hao, Z., Zaripov, D. & Yan, C. 2017 Improved k-ω-γ model for crossflow-induced transition prediction in hypersonic flow. *International Journal of Heat and Mass Transfer* **15**, 115–130.

[192] Zoppini, G., Michelis, T.and Ragni, D. & Kotsonis, M. 2022 Cancellation of crossflow instabilities through multiple discrete roughness elements forcing. *Physical Review Fluids*

7 (12).

[193] Zoppini, G., Michelis, T., Ragni, D. & Kotsonis, M. 2022 The near-wake of discrete roughness elements on swept wings: tomographic ptv measurements. In *12th International Symposium on Turbulence and Shear Flow Phenomena (TSFP12)*.

[194] Zoppini, G., Michelis, T., Ragni, D. & Kotsonis, M. 2023 The near wake of discrete roughness elements on swept wings. *Journal of Fluid Mechanics* **960**.

[195] Zoppini, G., Ragni, D. & Kotsonis, M. 2021 Experimental investigation on receptivity of crossflow instability to discrete roughness amplitude and location. In *AIAA Scitech 2021 Forum*. American Institute of Aeronautics and Astronautics.

[196] Zoppini, G., Ragni, D. & Kotsonis, M. 2022 Experimental investigation of isolated roughness induced transition in a swept wing boundary layer. In *AIAA SCITECH 2022 Forum*. American Institute of Aeronautics and Astronautics.

[197] Zoppini, G., Ragni, D. & Kotsonis, M. 2022 Transition due to isolated roughness in a swept wing boundary layer. *Physics of Fluids* **34** (8), 084113.

[198] Zoppini, G., Sequeira, A., Michelis, T., Ragni, D. & Kotsonis, M. 2023 The near-wake of super-critical discrete roughness elements on swept wings. In *AIAA SCITECH 2023 Forum*. American Institute of Aeronautics and Astronautics.

[199] Zoppini, G., Westerbeek, S., Ragni, D. & Kotsonis, M. 2022 Receptivity of crossflow instability to discrete roughness amplitude and location. *Journal of Fluid Mechanics* **939**.

A

Appendix A

A.1. Introduction

In Chapter 6 the multiple DRE array technique for stationary CFI suppression in 3D boundary layer was investigated. Despite performing well when applied on a smooth wing surface, the proposed suppression technique demonstrated reduced control capabilities when applied in the presence of enhanced distributed surface roughness. This can be associated with the excessive amplitude of the applied DRP and to a residual spanwise non-uniformity present in the BL due to the persistence of the weaker CFI modes induced by the DRP.

Therefore, an attempt to further characterize the interaction between the applied DRP and the reference DRE array is performed, aiming at clarifying the dominant mechanism and possibly improving the suppression capabilities of the proposed technique.

A.2. Methodology

The measurements presented hereafter are performed on the M3J swept wing model in the LTT (section §2.1.1) at a constant Reynolds number (Re_{cx}=2.17 $\times 10^6$) and angle of attack (α=-3.36°). DRP obtained from silicon carbide are applied on the wing surface (section §2.2.1), providing the baseline flow configuration (i.e. D_I located at x_{DRP}/c=0.035).

Critical and sub-critical DRE arrays (i.e. forcing wavelengths λ_1=8mm and $\lambda_{2/3}$=5mm respectively) are manufactured using a knife cutting procedure (section §2.2.3), and are applied at chord locations between x_{DRE}/c=0.10-0.2. The considered nominal DRE amplitudes are kk_1=0.075mm, kk_2=0.100mm, kk_3=0.140mm or kk_4=0.170mm.

The investigated cases are summarized in table A.1 where individual DRE arrays are indicated as A_n. Configurations combining DRP and DRE are indicated, for example, as D_I-A_1 which features DRP D_I and reference array A_1.

Infrared Thermography

The flow features are globally characterized by infrared thermography (section §2.3.1) providing an estimation of the transition front location. However, the various forcing

Case	DRE/DRP	kk [mm]	x_{DRE}/c	λ/λ_1
C1-	A_1, A_2, A_3, A_4	0.070	0.10, 0.125, 0.15, 0.20	1
	A_5, A_6, A_7, A_8	0.100	0.10, 0.125, 0.15, 0.20	1
	A_9, A_{10}, A_{11}, A_{12}	0.140	0.10, 0.125, 0.15, 0.20	1
	A_{13}, A_{14}, A_{14}, A_{15}	0.170	0.10, 0.125, 0.15, 0.20	1
	D_I	-	0.035	-
C2-	A_1, A_2	0.070	0.125, 0.15	2/3
	A_3, A_4, A_5, A_6	0.140	0.10, 0.125, 0.15, 0.20	2/3
	A_7, A_8	0.170	0.15, 0.20	2/3
	D_I	-	0.035	-

TABLE A.1: Geometrical parameters of measured forcing configurations. Case C1 features critical DRE arrays, while case C2 features sub-critical DRE arrays.

cases considered show only mild differences in transition location, hence, quantification of the flow characteristics is performed by estimating the laminar flow area variations (A_{lam}). Specifically, the DIT image is computed and the regions of advanced (i.e. darker regions) or delayed (i.e. brighter regions) transition are separated based on a threshold masking. The corresponding wing surface is then computed and the subtraction of these two regions provides a global estimate of the A_{lam} variation, expressed as a percentage of the laminar flow area in the baseline case (i.e. sole D_I forcing).

Planar Particle Image Velocimetry (PIV)
Planar Particle Image Velocimetry (PIV, §2.3.3) acquisitions are performed to incur the local BL characteristics at x/c=0.34. The wall-normal direction is non-dimensionalized as $y/\overline{\delta}^*$, ($\overline{\delta}^* \simeq 0.8$mm being natural BL displacement thickness). The main flow features are extracted as described in section §3.2.4.

Due to the application of the DRP, the investigated flow fields partially lose their spanwise periodicity and uniformity. As a consequence, the application of spatial FFT for the investigation of the BL spectral content is highly dependent on the signal shape and length. To obtain more reliable and repeatable characterization of the BL spectral content, at each y-coordinate the spanwise $\overline{w}$ signal is analysed by means of wavelets [38, 104]. The wavelet spectra is averaged along the spanwise direction at each y-location, providing a representative wavelet coefficient for each wavelength. This allows for comparing the various roughness configurations considered.

A.3. RESULTS AND DISCUSSION

Characterization of Reference DRP Baseflow
The flow field incurred by the baseline DRP forcing configuration D_I is described hereafter. Figure A.1(a) reports the corresponding IR image where the DRP is visible as the gray rectangle extending along the wing span. The sawtooth pattern of the transition front is rather irregular as a result of the simultaneous development of

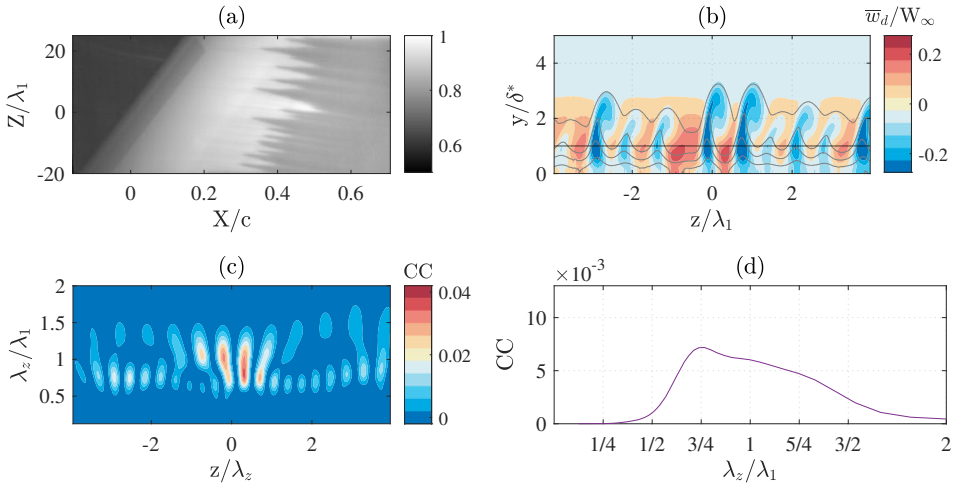

Figure A.1: (a) IR image acquired at Re_{c_X}=2.17 ×10^6 for baseline DRP forcing (D_I). (b) Contours of $\overline{w}_d$ acquired with PIV at x/c = 0.34; superposed contours of $\overline{w}$ every 20%W_∞ (black solid lines). (c, d) Spatial spectral analysis: (c) contours of wavelet correlation coefficients extracted at y/$\overline{\delta}^*$=1, (d) chordwise averaged wavelet correlation coefficients extracted at various chord locations.

multiple CFI modes with various wavelengths. The local BL disturbance velocity contours are shown in figure A.1(b), while figure A.1(c) shows the wavelet correlation coefficients at y/$\overline{\delta}^*$=1 (black line in figure A.1(b)). The coefficient peaks correspond to a broadband range of wavelength between $\lambda_{4/3}$-$\lambda_{2/3}$. This is confirmed by the representative spectral distribution reported in figure A.1(d).

Effect of a Critical DRE Array Superposition to DRP

The application of a critical DRE array downstream of the DRP does not substantially modify the BL transitional scenario. The modifications of the transitional sawtooth pattern (figure A.2(a)) are representative for a redistribution of the BL spectral energy, however A_{lam} is almost unaltered (or mildly reduced) for all the considered forcing cases (with the exception of the super-critical configuration C1-D_I-A_{13}, figure A.2(b)).

The spatial spectral analysis results in the wavelet correlation coefficients reported in figure A.3. The resulting trends show that the application of the DRE array focusses the BL development on a narrower range of modes, especially for cases with higher forcing amplitude (i.e. kk_2 in figure A.3(b)). Nonetheless, despite forcing the most critical wavelength λ_1=8mm in most cases the spectral energy corresponding to mode $\lambda_{4/3}$=6mm is comparable to (if not higher than) the energy pertaining to λ_1. In addition, a rather wide set of wavelength persists in the BL in the presence of the reference DRE array, albeit featuring lower spectral energy. The residual boundary layer spectral content further justifies the reduced control capability of the multiple arrays technique in the presence of DRP forcing (Chapter 6).

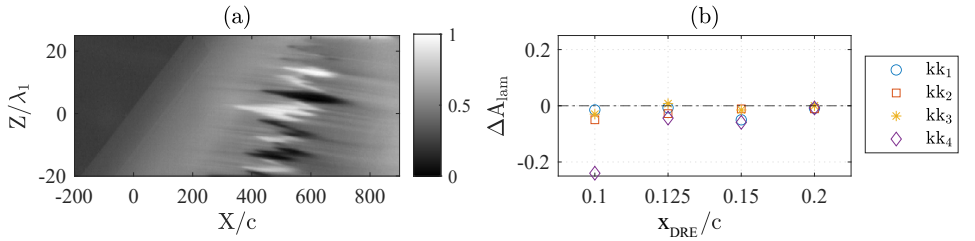

FIGURE A.2: (a) DIT IR image for case C1-D_I-A_{10}, obtained by subtracting the reference DRP case. (b) Variations of A_{lam} for forcing configurations of case C1.

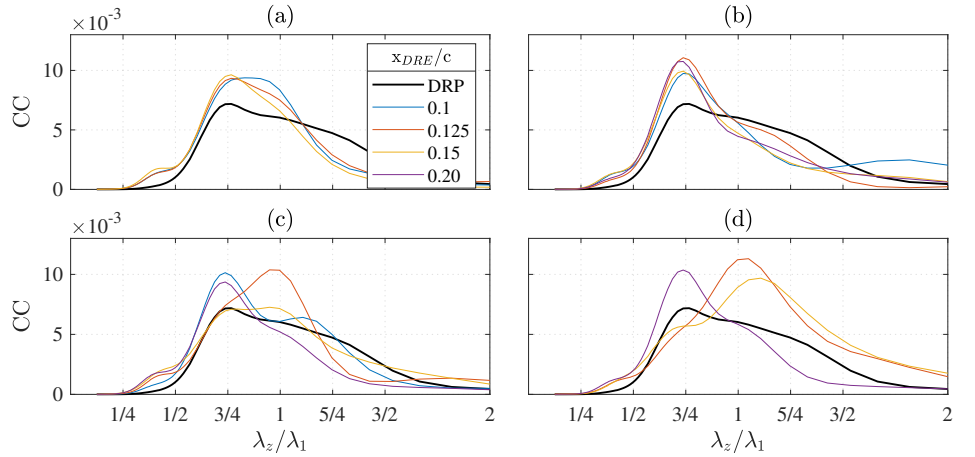

FIGURE A.3: Chordwise averaged wavelet correlation coefficients extracted for various forcing configurations of case C1 combining D_I and one DRE array of height (a) kk_1, (b) kk_2, (c) kk_3 and (d) kk_4.

Effect of a Sub-Critical DRE Array Superposition to DRP

When applying sub-critical DRE arrays in combination with D_I the BL flow development is still mostly unaltered for all the considered forcing configurations. The transition front modifications are minimal (figure A.4(a, b)), and mostly relate to a spectral energy redistribution. The wavelet correlation coefficients are reported in figure A.4(b, c) for DRE amplitudes of kk_2 and kk_3, and show comparable trends to what observed in the critical case. The DRE array reduces the range of excited CFI modes, enhancing the development of mode $\lambda_{4/3}$.

Discussion

Overall, no clear and complete focussing of the BL spectral content on λ_1 could be outlined from the acquired dataset. Almost all the considered forcing configurations show a rather broadband residual spectral content despite the application of a reference DRE array. Accordingly, the multiple DRE array forcing technique applied in the presence of D_I (not reported for the sake of brevity) did not provide significant

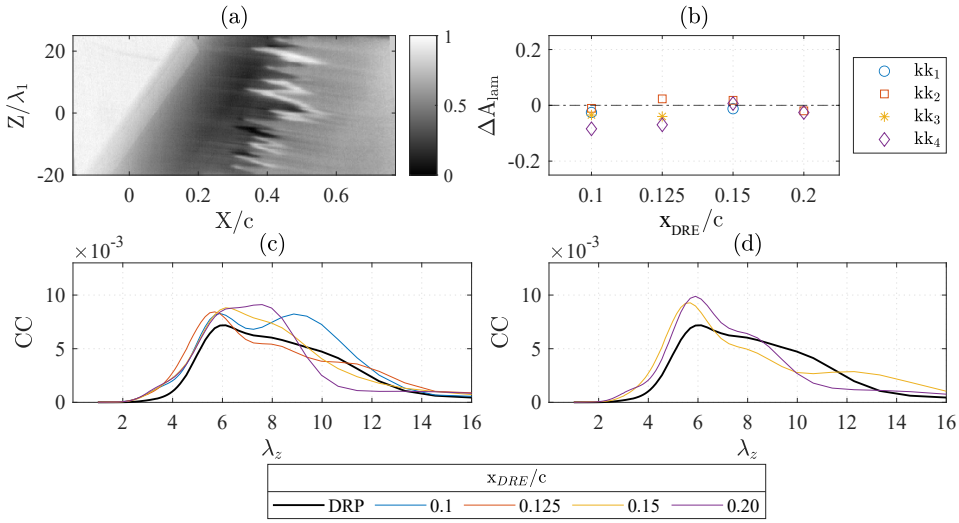

Figure A.4: (a) DIT IR image for case C2-D_I-A_4, obtained by subtracting the reference DRP case. (b) Variations of A_{lam} for various forcing configurations of case C2. (c, d) Chordwise averaged wavelet correlation coefficients extracted for various forcing configurations of case C2 combining D_I and one DRE array of amplitude (c) kk_2 or (d) kk_4.

transition modifications. Given the lack of a clear spectral behavior obtained by the superposition of the DRP and reference DRE arrays, no further improvement of the multiple DRE forcing technique could be investigated. As outlined in Chapter 7, the research interest moved towards spanwise invariant roughness configurations which proved to be less sensitive to the pre-existing instability field.

Bibliographical Note

Giulia was brought into this world in the enchanting town of Vicenza, Italy on the 5th of May, 1995. Growing up in the captivating hamlet of Dueville, nestled amidst picturesque hills and vineyards, her insatiable curiosity led her led her to dismantle dolls (especially those belonging to others) in search of their hidden secrets. Thankfully, as she matured, her inquisitive nature transitioned from dismembering playthings to a more noble pursuit of understanding the wonders of nature and the intriguing mechanics of the world.

During her travels, Giulia experienced the exhilaration of defying gravity aboard a metal box, evoking both terror and fascination. This captivating experience ignited her passion for the invisible forces of aerodynamics, propelling her towards a Bachelor's degree in Aerospace Engineering at the Universita di Padova. Continuing her journey, she pursued a Master's degree in Aeronautics at Politecnico di Milano, where she discovered a world of wind tunnels, vibrant flow visualization, and cutting-edge equipment in the Aerodynamics lab. Within this captivating environment, Giulia embarked on her first experimental escapade, shaping the trajectory of her academic journey that ultimately led to the pursuit of this PhD.

Alongside her scholarly pursuits, Giulia cherishes her leisure time, venturing into global escapades and finding solace in the majestic Italian mountains or along the picturesque seaside. When confined to a single location, she indulges in the delights of literature, culinary creations, harmonious melodies, theatrical spectacles, and the warm embrace of cherished friendships. Her experiences in the Netherlands have broadened her perspective, connecting her with people from diverse backgrounds and partially unraveling the tapestry of the world.

SUMMARISED CURRICULUM VITÆ

05-05-1995 Born in Vicenza, Italy.

EDUCATION

2013-2016 Bachelor in Aerospace Engineering
Università degli Studi di Padova, Italy

2016-2019 Masters in Aeronautical Engineering (Aerodynamics)
Politecnico di Milano, Italy

2019-2023 PhD. candidate in Aerodynamics
Delft University of Technology, Netherlands

OTHER EXPERIENCES

2022 Cyber Security for Business Leaders
Oxford Said Business School

2021 TUDelft TURBO AIR
Delft University of Technology

2019 Project Management Training
Leonardo at Politecnico di Milano

2016 Motorstudent Team
Università degli Studi di Padova

List of Publications

Journal Publications

5. ZOPPINI, G., MICHELIS, T., RAGNI, D., & KOTSONIS, M. 2022. The near-wake of discrete roughness elements on swept wings. *Journal of Fluid Mechanics*. [194]

4. ZOPPINI, G., MICHELIS, T., RAGNI, D. & KOTSONIS, M. 2022 Cancellation of crossflow instabilities through multiple discrete roughness elements forcing. *Physical Review Fluids* 7 (12). [192]

3. ZOPPINI, G., RAGNI, D., & KOTSONIS, M. 2022. Transition due to isolated roughness in a swept wing boundary layer. *Physics of Fluids* 34 (8), 084113. [197]

2. ZOPPINI, G., WESTERBEK S., RAGNI, D., & KOTSONIS, M. 2022. Receptivity of crossflow instability to discrete roughness amplitude and location. *Journal of Fluid Mechanics* 939. [199]

1. ZOPPINI, G., BELAN, M., ZANOTTI, A., DI VINCI, L., CAMPANARDI, G. 2020. Stall Control by Plasma Actuators: Characterization along the Airfoil Span. *Energies* 13, 1374.

Conference Proceedings

5. ZOPPINI, G., SEQUEIRA, A.D., MICHELIS, T., RAGNI, D., & KOTSONIS, M. 2023. The Near-Wake of Super-Critical Discrete Roughness Elements on Swept Wings. *AIAA, SiTech 2023 Forum*. [198]

4. ZOPPINI, G., MICHELIS, T., RAGNI, D., & KOTSONIS, M. 2022.The near-wake of discrete roughness elements on swept wings: tomographic PTV measurements. *12th International Symposium on Turbulence and Shear Flow Phenomena (TSFP12)*. [193]

3. ZOPPINI, G., RAGNI, D., & KOTSONIS, M. 2022. Experimental investigation of isolated roughness induced transition in a swept wing boundary layer. *AIAA SCITECH 2022 Forum*. [196]

2. ZOPPINI, G., RAGNI, D., & KOTSONIS, M. 2022. Experimental investigation on receptivity of crossflow instabilities to discrete roughness amplitude and location. *AIAA SCITECH 2021 Forum*. [195]

1. ZOPPINI, G., DI VINCI, L., CAMPANARDI, G., ZANOTTI, A., BELAN, M. 2019. PIV characterization of a separated flow controlled by a DBD actuator. *Journal of Physics: Conference Series*, 1249, XXVI AIVELA National Meeting.

Conference Abstracts and Posters

2. ZOPPINI, G., MICHELIS, T., RAGNI, D. & KOTSONIS, M. 2022. Control of stationary crossflow instabilities through destructive interference. *European Drag Reduction and Flow Control Meeting, EDRFCM 2022*.

1. ZOPPINI, G. 2022. Control of Crossflow Instabilities through Multiple DRE Forcing (Poster). *Burgers Symposium 2022*.